Doctoral Dissertation

Preparation of modified ZrO_2 nanoparticle and T-ZnO whisker hybrid reinforced Sn1.0Ag0.5Cu composite solder and soldering

Fupeng Huo

April 2022

Graduate School of Engineering

Osaka University

Supervisor

Professor Hiroshi Nishikawa, Ph. D.

Joining and Welding Research Institute

Osaka University

Doctoral Committee

Professor Hiroshi Nishikawa, Ph. D.

Joining and Welding Research Institute

Osaka University

Professor Shinji Fukumoto, Ph. D.

Division of Materials and Manufacturing Science, Graduate School of Engineering

Osaka University

Professor Keisuke Uenishi, Ph. D.

Division of Business Engineering, Graduate School of Engineering

Osaka University

Contents

List of figures

List of tables

Chapter 1 Research background

1.1 Solder interconnection in electronic packaging

Solder is widely used in the interconnection between chip/electronic components and integrated circuits in electronic packaging field. After more than 50 years of use of tin-lead (SnPb) solders, the global electronics manufacturing industry has made a critical transformation to lead-free solder materials and soldering technology. Therefore, developing new lead-free solder and soldering is a crucial research topic.

1.1.1 Develpoment of lead-free soldering

The traditional SnPb solder was widely used in the electronic packaging field due to the excellent performances and low price [1]. Due to the toxicity of Pb and the increasing awareness of environmental protection, many countries have passed legislation to prohibit the use of Pb [2-3]. In 1998, the environmental committee of the European Union (EU) issued a related statement on Waste Electrical and Electronic Equipment (WEEE) and the restriction of the use of Hazardous Substances (RoHS) [2]. This proposal called the ban on using heavy metals such as Pb, Hg, Cd, etc. In Japan, the legislative activities of the reclamation and recycling of electronics also have been proposed [3]. These legislations effectively drive lead-free solder development.

SnPb solder is inevitably used as a benchmark in the development process of lead-free solder. It is hoped that the performance of these alternatives are similar to or exceed SnPb solder. In general, some basic requirements of newly developed lead-free solder are listed as follows[4-6].

• Wettability. Candidate solders should have good wettability.

• IMC formation. An effective metallurgical bond should be formed; and the IMC should be thin and stable in the long-term service.

• Melting point. Ideally, the melting point of candidates should be as close as possible to SnPb solder, and the solid-liquid temperature range should be less than 30 °C.

• Mechanical properties. Lead-free solder joints shoul exhibit good mechanical properties and reliability during long-term service.

• Price. Alternative solders should have sufficient sources of raw materials and reasonable prices.

During the development program of lead-free solder, some mainstream alternative solders were appeared [7-12]. It mainly include binary lead-free solder: SnAg, SnCu, SnZn and SnBi series; and ternary lead-free solder: SnAgBi, SnBiZn, and SnAgCu series. The characteristics of several solders are as follows.

(a) Binary lead-free solder:

1. SnAg series: it has excellent thermal fatigue resistance, good oxidation resistance good creep resistance. However, the melting point of the SnAg series is high (221 °C), and shows normal level wettability. They were mainly used in reflow soldering.

2. SnCu series: it shows good thermal fatigue resistance, small melting-liquid temperature range, and low price, which is recommended by NEMI of America. The disadvantages of SnCu series solder were high melting temperature and low mechanical properties. They were mainly applied in wave soldering.

3. SnZn series: the eutectic melting point of SnZn was 198.5 °C, which is closest to the melting point of Sn37Pb solder. It also shows good thermal fatigue performance and low price. However, this kind of solder easily oxidizes and presents poor wettability.

4. SnBi series: the eutectic melting point is low to 139 °C, which is friendly to electronic products and shows good mechanical properties. However, its plasticity is poor.

(b) Ternary lead-free solder:

1. SnAgBi series: After adding Bi elements, it shows a lower melting point (200~210 °C) than SnAg solder. It also exhibited high UTS, excellent soldering processability, and good reliability: However, the plasticity of this kind of solder is poor.

2. SnBiZn series: Similar to SnBi solder, it still shows low melting points and excellent mechanical properties. But its corrosion resistance is poor.

3.SnAgCu series: The melting point of the eutectic composition is 217°C. It exhibited good wettability, solderablity and reliability. The solder joints have excellent fatigue resistance, and the fatigue life is more than three times that of Sn37Pb solder. Overall, it has good a comprehensive performance.

SnAgCu series solders are the best compromise of performance indicators such as melting point, UTS, plasticity and fatigue life among these lead-free solders. It is widely used in electronic products and internationally recognized as standard lead-free solders.

I have mentioned above that the melting point of eutectic SnAgCu solder alloy is 217 °C. The isothermic projection of the Sn-rich side of the Sn-Ag-Cu system is shown in Fig. 1-1 [13]. As observed in Fig. 1-1, the ternary eutectic point located in a range, the precise composition has not been obtained. The result indicates that the solidification mechanism of the solder alloy is very complicated, and the solidification temperature cannot be accurately determined according to thermodynamic calculations. The reported eutectic composition was Sn-(3~4)Ag-(0.5~0.9)Cu, and the eutectic microstructure was β-Sn+Ag_3Sn+Cu_6Sn_5[13,14]. The initial commercial solder included: Sn3.9Ag0.6Cu recommended by NEMI of America, Sn3.8Ag0.7Cu recommended by IDEALS of European Union, and Sn3.0Ag0.5Cu recommended by JEITA of Japan[15-17]. Considering the soldering performance and price, Sn3.0Ag0.5Cu is selected as the commercial solder in Japan.

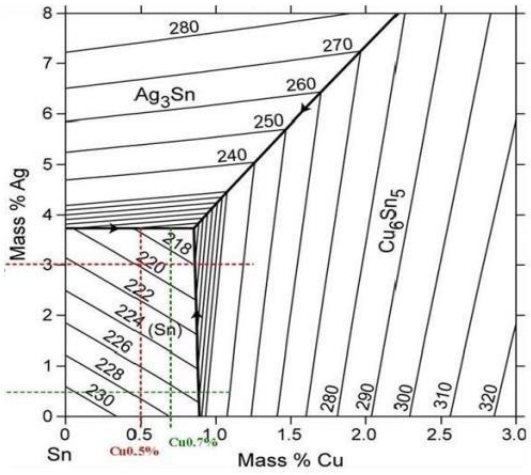

Fig. 1-1 Isothermic projection of Sn-rich side of Sn-Ag-Cu system [13].

However, the Ag content of these solders is above 3.0wt.%, which will increase the cost of solders. In addition, the high Ag content is easy to form a coarse slab-shaped Ag_3Sn in the solder joint, causing stress concentration and deteriorating the reliability of solder joints [18]. The toughness of the SnAgCu solder can be effectively improved after reducing the Ag contents, improving the drop impact resistance and thermal fatigue performance of the solder joint [19]. Therefore, it is a trends to develop SnAgCu series solders with low Ag contents.

1.1.2 Solder interconnection

Solder interconnection plays an important role in electronic packaging. It is a process in which the solder and substrate/metal layer of the die undergo a metallurgical reaction to achieve interatomic bonding [20]. Solder joint mainly plays four roles: mechanical support, transmission of electric energy, signal transmission, and heat dissipation channels [21]. With the trends in the harsh condition, multi-functional and miniaturization of electronic products, this promoted the development of electronic packaging toward miniaturization and high density. Fig.1-2 shows the trend of electronic packaging technologies[22]. From the original TO (Transistor Outline) and DIP (Double in-line Package) gradually developed to QFP (Quad Flat Package) and BGA (Ball Grid Array) technology, to the current advanced 3D Packaging and SiP (System in Package) technology. Specically for the most advanced electronic packaging techniques of 3D packaging, which is the solution of high-level integration and miniaturization. Fig. 1-3 shows a typical structure of 3D packaging [23]; dies are stacked vertically and connected using solder bumps or some other type of interconnect, corresponding to the solder joints with different forms and sizes. Therefore, the amount of Input/Output on the chip was increased, and the pitches of Input/Output decreased, corresponding to the demands for solder joints reliability also increased.

In this case, the traditional SnAgCu solder can no longer meet the needs of future electronic product development, so it is an urgent need to develop new high strength and ductility lead-free solders.

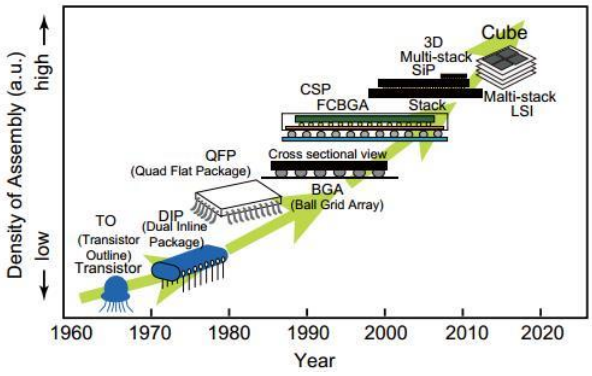

Fig.1-2 The trend of electronic packaging technologies [22].

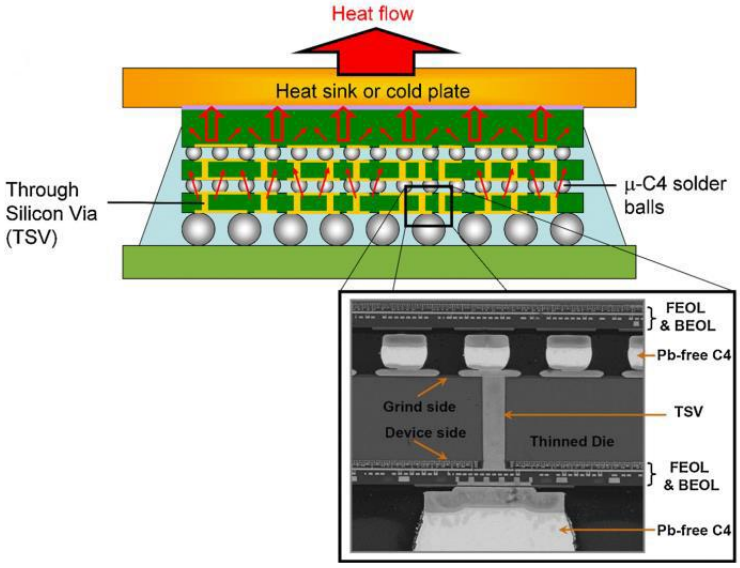

Fig.1-3 Illustrations of representative 3D chip stack lidless modules with select conceptual heat flow paths shown [23].

1.1.3 Improvement properties of lead-free solders

To further improve the performance of lead-free solder, two methods are main utilized: microalloying and composite solder methods.

(a) Microalloying method

Microalloying is a method to improve the performance of the solder by adding a small amount of alloying elements, such as Ni, Ti, Co [24-28]. The summary is shown in Table 1-1. These alloying elements are dissolved in the solder matrix and precipitate at the grain boundaries, or form nano-scale IMC with the solder matrix to improve the properties of the solder. Wang et al. [24] investigated the effect of Ni addition on the wettability and

Table 1-1 The effect of alloying elements on lead-free solder and joint.

Solder matrix	Alloying elements	Preparation methods	Produced effect	References
Sn2.5Ag0.7Cu 0.1RE	Ni	Arc melting	Improved wettability, the refined microstructure, and thinner interfacial IMC	[24]
Sn3.5Ag0.5Cu	Ti	vacuum arc melting	Narrower eutectic colony, increased microhardness, YS, and UTS; reduced elongation	[25]
Sn1.0Ag, Sn0.7Cu	Ti	injection molded solder	Ti_2Sn_3 networks can stabilize the morphology of β-Sn by retarding during thermal aging	[26]
Sn2.5Ag0.8Cu	Ni	Vibrating jet	Ni produced thinner Cu_3Sn layers, Ni addition higher than 0.01 wt.% could effectively retard the Cu_3Sn growth	[27]
Sn3.5Ag	Co	Vibrating jet	Interfacial IMC toughness of Sn-Ag-Co/Cu solder joint was higher than that of Sn-3.5Ag	[28]

microstructure of Sn2.5Ag0.7Cu0.1RE solder alloy. The results showed improved wettability, and the microstructure was also refined. Chuang et al. [25] reported the effects of a small amount of active Ti element additions on microstructure and property of Sn3.5Ag0.5Cu solder; the melting temperature and melting range of the SAC solder alloy can be slightly decreased. The eutectic colony becomes narrower with the addition of Ti into SAC, and the microhardness, YS, and UTS are significantly higher than those of the other commercially available SAC solder alloys. However, the benefits of elongation were reduced when exceeded Ti addition, which attributed to formation of coarse Ti_2Sn_3 in the eutectic colonies. Chen et al. [26] also investigated the effects of Ti addition to Sn–Ag and Sn–Cu solders, and similar results were obtained. In addition, for Ti-added solders, during the thermal aging, Ti_2Sn_3 networks can stabilize the morphology of β-Sn by retarding their grain growth and maintaining the strength of solders. Wang et al. [27] reported that reasonable Ni addition could suppress the Cu_3Sn IMC growth during reflow and thermal aging. Nishikawa et al. [28] studied the effect of Co element on the morphology and shear strength of Sn-Ag(-Co)/Cu solder joints. The results

showed that the toughness of Sn-Ag-Co/Cu solder joint was higher than that of Sn-3.5Ag, corresponding to the change of fracture mode.

(b) Composite solder method

It is a method to improve performance by adding a reinforcing phase that does not react with the solder matrix. These foreign reinforcements can improve the solder properties through several mechanisms such as Orowan strengthening, grain refinement, and load transfer mechanism. In addition, these reinforcements can inhibit the inter-diffusion between Cu and Sn atoms to reduce the IMC thickness, so as to improve the reliability of the solder joints. The summaryis shown in Table 1-2. Tsao et al. [29] investigated the effect of nano-TiO_2 on the microstructure and tensile properties of SnAgCu solder. The results showed that the grain size of β-Sn and Ag_3Sn were refined, the UTS was improved while the ductility was decreased. Chen et al. [30] prepared TiC reinforced Sn3.0Ag0.5Cu composite solder, which exhibited a suppressed growth rate of intermetallic compound (IMC) at the interface during isothermal aging, as well as improved shear strength compared to plain Sn3.0Ag0.5Cu solder. Kumar et al. [31] fabricated the SWCNT-reinforced solder alloy for ultra-fine pitch applications. The results showed that SWCNT addition results in finer grain size morphology of the solders, and SWCNTs are embedded deeply into the solder matrix. Moreover, the UTS and microhardness of the composite solders are improved with the addition of SWCNT compared to the unreinforced solders. However, the elongation of composite solder was decreased. To improve the interface between CNTs and solder matrix, Wang et al. [32] conducted surface modification for the CNTs, and explored the effects of Ni modified MWCNTs on the microstructural evolution and shear strength of Sn-3.0Ag-0.5Cu composite solder joints. The growth of the IMC layer of solder joints was significantly restrained after Ni-CNTs addition. The coarsening of IMC grains were significantly inhibited with Ni-CNTs in the solder, improving the shear strength of composite solder joints.

The microalloying method has been extensively studied in the past 20 years, and improved properties of solders were obtain with added alloy elements. However, this method has some microstructure stability problems, such as element segregation and IMC, deteriorating the

Table 1-2 The effect of reinforcements on lead-free solder and joint.

Solder matrix	Reinforce-ments	Preparation methods	Produced effect	References
Sn3.5Ag0.25Cu	Nano-TiO_2	mechanically dispersing	Refined grain size of β-Sn and Ag_3Sn; improved UTS, while decreased the ductility	[29]
Sn3.0Ag0.5Cu	Nano-TiC	Powder metallurgy	suppressed growth rate of interfacial IMC during isothermal aging, as well as improved shear strength	[30]
Sn3.8Ag0.7Cu	SWCNTs	Powder metallurgy	Refined grain size, increased UTS and microhardness; reduced elongation	[31]
Sn3.0Ag0.5Cu	Ni-CNTs	mechanically mixed	Inhibited IMC grains coarsening, enhanced shear strength, fracture mode changed from mixture fracture mode to ductile fracture	[32]

performance of the solder joints, leading to the failure of the them. Due to no react with solder matrix and no coarse of the reinforcement for the composite solder method, the composite solder presents good microstructure stability during the long-term service. Therefore, it has become a research hotspot in the development of novel lead-free solders in recent years. That is also the reason why the composite solder method is used in this study to prepare novel high-strength and ductility lead-free solders.

1.2 SnAgCu system lead-free composite solder

The design of SnAgCu system lead-free composite solder with high strength-ductility is a complex system engineering, including reasonable application of strengthening-ductility mechanism, the choice of reinforcements, preparation method of composite solder, and interface regulation between the reinforcements and solder matrix. Only by dealing with the above-mentioned problems simultaneously, can I successfully fabricate the high strength-ductility lead-free solder.

1.2.1 Strength-ductility mechanism of composite solder

The strength-ductility mechanism is the theoretical basis of the composite solders design, as well as the important basis of selection of reinforcements. Only by systematically mastering these mechanisms, can the design of composite solder be more effective. The main mechanisms is summarized as follows [33-37].

(a) Orowan strengthening effect [33,34]

The Orowan strengthening mechanism is the effect of the hard particles dispersed in the alloy on the hindering effect of dislocation movement. When dislocations on the slip surface encounter the hard particles, they would be blocked by the particle and bend. The dislocation bending intensifies as the external stress increases, causing the dislocation lines near the particle to meet on the left and right sides. The positive and negative dislocations cancel out, forming a dislocation ring surrounding the hard particles. The rest of the dislocation line continues to move forward. The schematic diagram of dislocations bypassing the second phase particles is shown in Fig. 1-4. This method of blocking dislocation movement by small-sized hard particles improves the strength and hardness of the materials.

(b) Grain refinement effect [35]

The smaller the grain size, the greater the number of grains per unit volume of the material; the larger the grain boundary area, the greater the resistance to plastic deformation of the material. Due to the grain boundaries, dislocations in deformed grains are blocked at the grain boundaries, and the slip band of each grain also ends near the grain boundaries; Meanwhile, multiple slips took place to coordinate the deformation due to different grain orientations, and

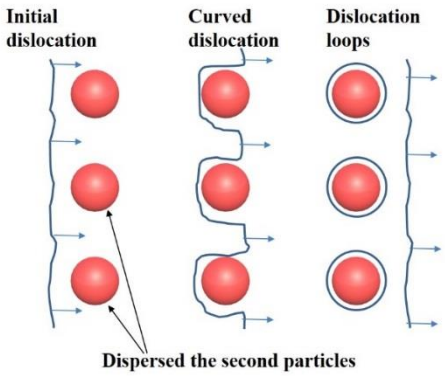

Fig. 1-4 The schematic diagram of dislocations bypassing the second phase particles.

dislocation intercross occurred during the multiple slips. The above two aspects increased the resistance of dislocation movement, improving the strength of the composite solder.

When the grains are small and uniform, the materials also exhibit good plasticity and toughness. Under the same deformation degree, the deformation is dispersed in much grain, resulting in much uniform deformation and less stress concentration, allowing it to withstand a larger amount of deformation before breaking.

(c) Thermal mismatch effect [36]

During the preparation or service of the composite solders, the different CTE between solder matrix and the reinforcement could produce lattice distortion. On the other hand, the high-density dislocation appears at the lattice distortion area.When slipping dislocations pass through the distortion area, dislocation delivery occurrs between moving dislocation and lattice distortion induced high density dislocation. Both of them could enhance the strength of materials.

(d) Load transfer effect [37]

Load transfer is a process where the load of the matrix material is transferred to the reinforcement phase through the interface. The interface is a key factor, and a good interface can achieve a synergistic improvement in strength and plasticity.

1.2.2 Choice of reinforcement

In part1.1.2, I had mentioned that a new high strength and ductility lead-free solder need to be developed. For this demand, it can be devided into two parts. The first part is a high strength, and the second part is high plasticity. Among the four kinds strengthen-ductility mechanisms mentioned in part 1.2.1, Orowan strengthening is the most effective mechanism [34]. Therefore, It is crucial to select suitable particle doping into the solder matrix to improve the strength of composite solder.

On the other hand, both grain refinement and load transfer effects can improve the ductility of solders. For the load transfer effect, the effective load transfer materials are mainly low-dimensional (whiskers, fibers, CNTs, GNS, etc.) rather than particle-shaped materials. Based on the above analysis, two types of reinforcement should be selected simultaneously to

increase strength and ductility. Namely, multi-component and multi-scale hybrid reinforced SnAgCu composite solder will be prepared.

(a) Choice of particle reinforcement

For the choice of particle reinforcement, firstly, the size of the reinforcement, microscale or nanoscale, needs to be determined, which profoundly affects the strengthening effect of the reinforcement. Zhang et al. [38] reported that 100 nm was the critical size for nanoparticulate-reinforced metal matrix nanocomposites (MMNCs) to produce excellent mechanical properties, compared to the counterpart of microparticulate-reinforced MMC. Therefore, nano-scaled reinforcement particles should be chosen to obtain excellent strengthening effect. In theory, the smaller the particle size, the more obvious the enhancement. Unfortunately, the smaller the nanoparticle size, the larger the specific surface area, which is easier to produce agglomeration. In the preparation of composite solders, these agglomerated nanoparticles cannot produce a strengthening effect, but could deteriorate the microstructure of solder and then reduce its performance. Therefore, based on the above analysis, the particle size should be slightly smaller than 100 nm.

After determining the size of the particles, the next step is to choose the appropriate candidate from several reinforcements. In part 1.1.3, it is mentioned that many kinds of materials can be used as the reinforcing phase of the composite solder, such as TiO_2, TiC, and CNTs [29-31]. The density and coefficient of thermal expansion (CTE) of SnAgCu solder and several nanomaterials are summarized in Table 1-3 [39-53]. As shown in the Table 1-3, ZrO_2 and Sn1.0Ag0.5Cu solder have a smaller density difference compared to other materials, which is conducive to the uniform distribution of ZrO_2 in the solder matrix. On the other hand, ZrO_2 and SnAgCu solder have smaller CTE differences, which are beneficial in reducing the thermal stress at the interface between the reinforcement and solder matrix. In summary, ZrO_2 nanoparticles are considered as a promising enhancement phase in SnAgCu solder.

Table 1-3 Density and CTE values of the SnAgCu solder and several reinforcements.

Materials	SnAgCu	SiC	Si_3N_4	TiC	Al_2O_3	GaAs	ZrO_2	GNS
Density (g/cm^3)	7.32	3.20[40]	3.18[42]	4.91[44]	3.96[46]	5.37[48]	5.85[50]	2.25[52]
CTE ($10^{-6}/K$)	25.0[39]	3.8[41]	1.2[43]	7.4[45]	7.4[47]	6.4[49]	9.6[51]	–8.0[53]

(b) Choice of whisker reinforcement

It is known that the composite materials with effective load transfer efficiency mainly include continuous fiber-reinforced composite and discontinuous reinforced composite [54]. The application of continuous fiber-reinforced composite materials is limited due to its high cost and complex preparation methods [55,56]. In addition, due to the miniaturization of flip chip and BGA solder joints, continuous fiber-reinforced composite solder is unsuitable for microelectronic connections [57]. Composite solders reinforced with discontinuous reinforcing phases mainly include short fiber reinforced, and whisker reinforced composite solders. The whisker reinforcement belongs to the single crystal with higher strength and smaller density difference compared with short fiber [58], so it is more suitable as a reinforcing phase for discontinuous composite solder. However, conventional whisker materials, such as SiC whisker and Al_2O_3 whisker, are mostly one-dimensional materials, making the prepared composite solders exhibit anisotropy. For composite solder, if there is anisotropy in performance, the stability and reliability of the solder joint cannot be guaranteed.

Among several whisker materials, tetra needle-like ZnO whisker (T-ZnO_w) is the only known whisker with a three-dimensional spatial structure [59,60]. T-ZnO_w has a four-corner needle shape, and four columnar single crystals extended from the core radial direction. The angle between any two needles is 109 °. The typical morphology of T-ZnO_w is shown in Fig. 1-5 [61]. This special structure not only allows load transfer, but also acts as the skeleton in a solder matrix to improve the mechanical properties. Moreover, the tetrahedral spatial

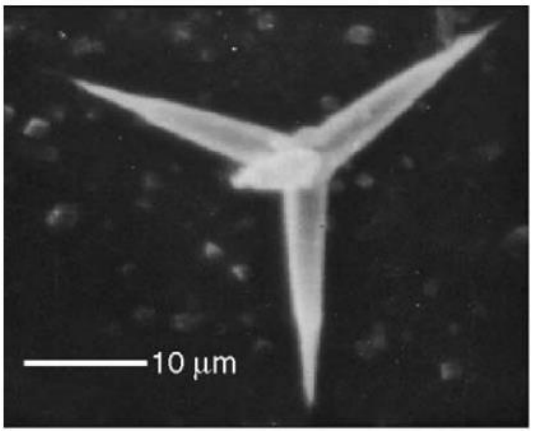

Fig. 1-5 The typical morphology of T-ZnO_w [61].

configuration of T-ZnO_w implies that the prepared composite solders have isotropic properties, which is not possible with other whisker materials.

In summary, among many reinforcing phases, nano-sized ZrO_2 and T-ZnO_w are selected as reinforcements to fabricate hybrid reinforced lead-free composite solders.

1.2.3 Surface modification of reinforcements

Despite its promising potential, some issues limit the application of ZrO_2 and T-ZnO_w in SnAgCu solder. This includes the poor wettability between reinforcements (ZrO_2 and T-ZnO_w) and SnAgCu, resulting in a weak bonding interface between the reinforcement and solder matrix. Thereby reducing the strengthening effect of the reinforcement. And the interface between whisker and matrix is the region controlling the load transfer efficiency from the matrix to the reinforcement [62]. Therefore, the weak bonding interface is also the reason for the decreased ductility of composite materials [63]. Furthermore, nano-ZrO_2 has a high specific surface area, causing the agglomeration trend, which is difficult to disperse in the solder matrix. Both the weak bonding and agglomeration could deteriorate the performance of composite solders. Therefore, it is important to develop systematic methods to solve these problems, which do not only ensure good interfacial bonding between reinforcements (ZrO_2 and T-ZnO_w) and SnAgCu solder matrix, but also obtain uniform distribution of reinforcements in Sn1.0Ag0.5Cu solder matrix, thereby simultaneously improving strength and ductility of the composite solders.

To improve the interface between the reinforcement and the solder matrix, the surface modification of the reinforcements has been considered to be an effective method. The current surface modification methods mainly include electroless plating, sol-gel, and magnetron sputtering.

(a) Electroless plating method

Electroless plating is a method in which metal ions are reduced to metal through a controllable oxidation-reduction reaction under the catalysis of metal and without an external current. The product is then deposited on the surface of various materials to form a dense coating [64]. It is widely utilized in the surface modification of materials. Yasin et al. [65]

synthesized the Ni/graphene composite coating on mild steel with the electroless plating method. The results showed that both the microhardness and corrosion resistance were improved. Wang et al. [66] reported that the nickel coating was formed on graphite by electroless plating to modify the interface of graphite/Cu composites. The mutual diffusion generated at the interface of Ni-Gr/Cu composites, and the interface type transferred from mechanical to metallurgy bonding. The Ni-Gr/Cu composites showed better mechanical properties than those without nickel coating. Zhang et al. [67] investigated the effects of whisker surface modification on microstructure, mechanical and thermal properties of β-Si_3N_4 whiskers reinforced Al matrix composites. The results showed that Ag-coated β-Si_3N_4 whiskers were successfully obtained by electroless plating(shown in Fig. 1-6). The β-Si_3N_4 whiskers were surrounded by an amorphous Ag enrichment layer and were well bonded with the Al matrix. Both the fracture toughness and the thermal conductivities of composites were effectively improved after surface modification. Xu et al. [68] prepared Ag nanoparticle-modified graphene/SnAgCu lead-free solder. The results exhibited that the wettability of the

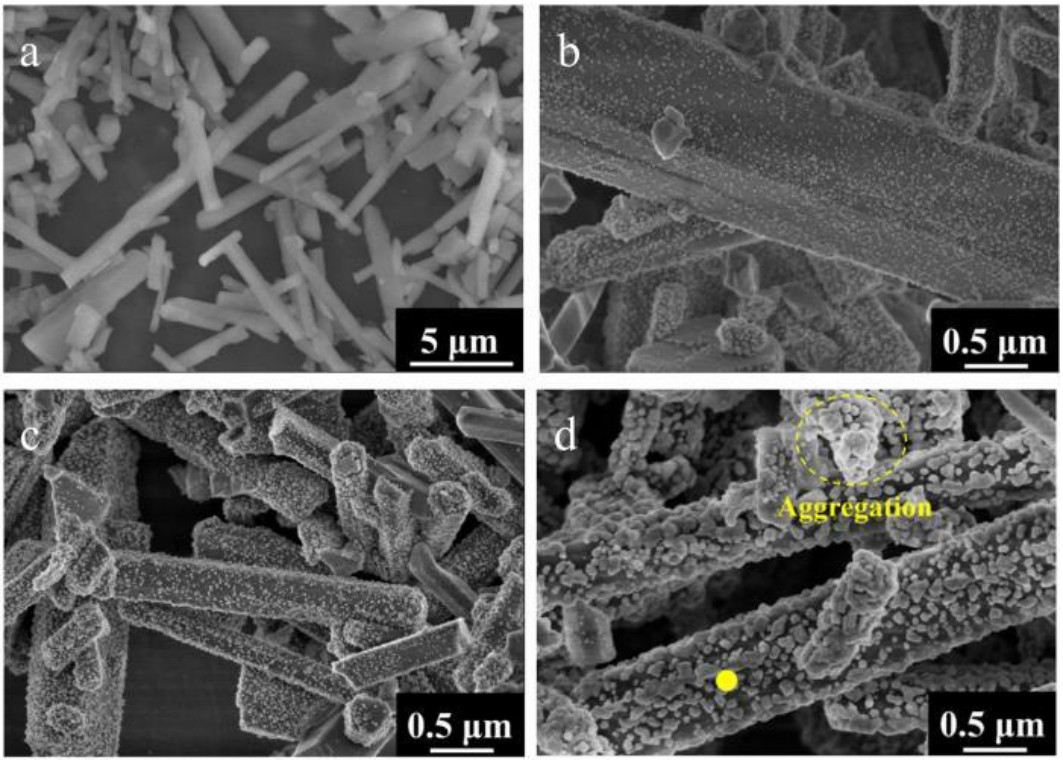

Fig. 1-6 SEM images of (a) as-prepared β-Si_3N_4w and Ag-coated β-Si_3N_4w with (b) 0.9 vol%, (c) 2.7 vol%, (d) 5.4 vol% Ag content [67].

composite solders was greatly increased, and the thickness of the IMC layer at the interface significantly decreased.

(b) Sol-gel method

The sol-gel method is a method in which compounds containing highly chemically active components are solidified through solutions, sols, and gels and then heated to form oxides or other compound solids [69]. Jin et al. [70] reported that the ZnO-coated $Mg_2B_2O_5$ whisker was prepared by a sol-gel method, and then the ZnO-coated $Mg_2B_2O_5$ reinforced AZ31B magnesium matrix composite was fabricated. The UTS increased from 181 MPa to 305 MPa. The result was 68.5% higher than plain AZ31B magnesium, which was attributed to improved interfacial bonding. Khramov et al. [71] reported surface modification of magnesium materials via the sol-gel route. The results indicated that the coat-magnesium AZ31B alloy demonstrates superior corrosion protection due to the chemical binding of phosphonate groups to the metal surface resulting in the enhanced hydrolytic stability of the formed P–O–Mg bonds. Ding et al. [72] investigated the sol-gel alumina coatings for aluminum borate whisker reinforced metal. The results showed that the coatings effectively controlled the interfacial reactions in aluminum borate whisker reinforced 6061Al composites by completely preventing the diffusion of magnesium from matrix to whisker. Wang et al. [73] systemically regulated the interface between Mg matrix and carbon fibers with the sol-gel method, resulting in a significant improvement of UTS of C_f/Mg composites.

(c) Magnetron sputtering

When the target is placed on the cathode, the collision between the electrons and the working gas occurs, splitting out the positive ions [74]. Under the action of the electric field, the positive ions bombarded the surface of the target material, and the atoms in the target material gained energy and cascaded collision. Finally, a sputtering phenomenon occurred to complete the coating [75]. This method is called magnetron sputtering. Ko ̈ck et al. [76] established the interlayer using magnetron sputtering between SiC fiber and Cu matrix to improve the fiber-matrix bonding. The results showed that pushout tests on these modified fibres exhibited a significant increase in adhesion compared to those fibres without interlayers.

Xin et al. [77] studied the effect of the W coatings prepared by the magnetron sputtering method on the stability of the thermal and mechanical properties of the Diamond/Al composites. After surface modification, the enhanced thermal conductivity and the bending strength stability were obtained, which was attributed to the formation of the continuous, stable and well bonded interfacial structure. Xu et al. [78] improved elevated temperature mechanical properties of Al-Si alloy deposited with Al-Si coating by magnetron sputtering. The results showed that the introduction of Al-Si coating on the Al-Si alloy surface could increase the mechanical properties of Al-Si material. The low friction coefficient of Al-Si coating was attributed to the Al and Si debris which react with thermal moisture to form aluminum and silicon oxide, serving as a lubricant between two contact counterparts. Cheng et al. [79] reported the microstructure and properties of SiC-coated carbon fibers prepared by radio frequency magnetron sputtering. The results showed that the coated carbon fibers have uniform, continuous, and flawless surfaces, corresponding to the enhanced mechanical properties.

Among the above methods, electroless plating is a widely used surface modification method to obtain a uniform coating with simple equipment. However, this process is complicated and cause pollution of heavy metal ions, which contradicts this study's purpose of environment-friendly solders. For the sol-gel method, the whole process is lengthly, and there are a lot of micropores in the gel, which makes the modified layer relatively loose. The thickness of the coating film prepared by the magnetron sputtering method is uniform and controllable, but the utilization rate of the target material is low. In addition, the equipment is expensive and requires harsh environmental conditions, such as no strong magnetic field, etc. Therefore, a convenient and green new surface modification method should be proposed.

1.2.4 Fabrication method of composite solder

After analyzing the selection and surface modification of the reinforcing phase, the next step is how to uniformly add the reinforcing phase to the solder matrix, that is, the preparation of the composite solder. The preparation methods of composite solder mainly include traditional casting, mechanical stirring, and powder metallurgy. These three methods were elaborated on respectively.

(a) traditional casting method

The traditional casting method refers to a method in which the solder matrix is melted, then the reinforcements is added to the moldten, and then simply mixed and poured into a mold to obtain a composite solder bulk. Shen et al. [80] prepared the nano ZrO_2 reinforced Sn3.5Ag lead-free composite solders with the casting method. Firstly, pure Sn and Ag bulk were melted in the vacuum arc furnace under a high purity argon atmosphere at 1073 K for half an hour. Afterwards, the alloy was remelted five times to homogenize the composition. After that, ZrO_2 nanoparticles, with an average size of 30 nm, were added into the solder molten while stirring. Finally, the composite mixtures were cooled down to room temperature on a water-cooled copper crucible with a cooling rate of~100K/s. Similarly, Xing et al. [81] fabricated the Sn9Zn-xAl_2O_3 composite alloys by melting pure metals (Sn: 99.95%, Zn: 99.95%, and Al_2O_3 nano-particles which the average particle size was 50nm and was wrapped in Zn foil) by high-frequency induction heating equipment in graphite crucibles at 500 °C for 3 min, and then the molten alloy was cast into a solder alloy rod with a diameter of 3 mm in the steel mould. Fawzy et al. [82] investigated the effect of ZnO nanoparticles addition on thermal, microstructure and tensile properties of Sn–3.5Ag–0.5 Cu (SAC355) solder alloy. The composite solder was prepared with the casting method. Afterwards, the solder ingots were cold drawn into a 0.8 mm diameter wire.

(b) mechanical stirring method

The reinforcing phase is mixed with solder powder or solder paste by mechanical stirring to achieve a relatively uniform distribution of the reinforcements. Gain et al. [83] prepared nano ZrO_2 reinforced SnAgCu composite solder with a mechanically dispersing method. ZrO_2 nano-particles were mixed with solder powder and stirred manually for at least 30 min to achieve a uniform distribution of nano-particles with a water-soluble flux; after that, the paste mixture was printed onto alumina substrates using a stainless steel stencil with a thickness of 0.15 mm and reflowed in a reflow oven to prepare 0.76 mm diameter solder balls. Yakymovych et al. [84] investigated the morphology and shear strength of lead-free solder joints with Sn3.0Ag0.5Cu solder paste reinforced with ceramic nanoparticles. Nanocomposite solder

pastes were prepared by manually mixing the SAC305 solder paste with SiO_2, TiO_2, and ZrO_2 nanopowders for at least 30 min to achieve a homogeneous nanoparticles distribution solder paste.

(c) Powder metallurgy method

First, the solder powder and the reinforcements are mixed to make these reinforcing phases uniformly distributed in the solder powder. Subsequently, the mixture was pressed and sintered to obtain composite solder bulk. Liu et al. [85] prepared graphene nanosheets (GNSs) reinforced Sn–Ag–Cu lead-free solder via powder metallurgy. Firstly, the solder powders and GNSs were mixed homogeneously in a V-blender. The mixture was uniaxially compacted, and the compacted billet was sintered in an inert argon atmosphere. Lastly, the billet was extruded into 6-mm-diameter rods at room temperature. Chen et al. [86] fabricated the fullerenes reinforced SnAgCu composite solder with the same method. In order to improve the interface between reinforcement and solder matrix, Han et al [87] prepared Ni-coated carbon nanotubes reinforced SnAgCu lead-free solders. The results revealed that with the addition of Ni-coated carbon nanotubes, the creep behaviour of composite solder improved significantly compared to that of the unreinforced solder alloy.

Among the above preparation methods, the casting method is a traditional for preparing solders, such as, microalloy typed solders. However, due to the surface tension of the molten solder, it is difficult to add the reinforcements to the solder matrix effectively. Even if partial nanoparticles are added, which are also difficult to disperse. Therefore, this method is unsuitable for preparing composite solders. The operation of the mechanical stirring method is simple, and the equipment is easy to be satisfied. This method can achieve effective dispersion for micro-scale reinforcements. However, it cannot produce an effective dispersion effect for the nano-scale reinforcements. Powder metallurgy is widely used in preparing high-temperature refractory materials, Still, the diffusion theory of sintering for low-melting composite materials (such as SnAgCu composite solder) is unclear. In previous studies, the microstructure and fracture of the solder fabricated by powder metallurgy method are significantly different from the typical solder structure.The plasticity of the solder by this

method is also relatively low. Therefore, it is unclear whether the powder metallurgy method is suitable for preparing SnAgCu composite solder. Overall, in order to prepare the composite solder with high performance, a fabrication method suitable for this study should be adopted.

1.3 Reliability concerns for solder joints

With the trend of miniaturization, high-density and harsh condition of electronic packaging, the number of solder joints per unit area is increasing, and the size of solder joints is decreasing. In this case, the service conditions of the solder joints in the electronic components are more severe, allowing higher requirements on the reliability of solder joints.

1.3.1 Challenges of solder joint during thermal aging

The reliability of solder joints is mainly determined by the performance of the solder joints and the working environment where the solder joints are located [88]. Reliability issues mainly include: thermal aging, creep, thermal fatigue and electromigration [89-92]. Among several reliability problems, thermal aging is the most common issue, which attributed to the low melting point of the SnAgCu solder alloy. Degradation of microstructure and properties of solder joints could occur even at room temperature. For example, coarsening of the solder seam microstructure and the growth of the interfacial IMC, etc., and the higher service temperature further accelerate the process [93,94]. The typical coarsening images are shown in Fig. 1-7 and Fig. 1-8, respectively. The coarsening of the solder microstructure and excessively thick interfacial IMC caused the failure of the solder joint. Therefore, it is of great significance to study the evolution principle of microstructure and mechanical properties of solder joints during thermal aging and seek effective ways to restrain the deterioration.

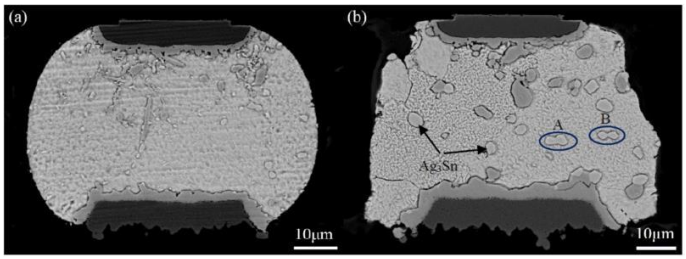

Fig. 1-7 Cross-sectional BSE images of SAC305 micro-joints in flip chip assembly: (a) After 500 h aging time; (b) after 2000 thermal shock (TS) cycles [93].

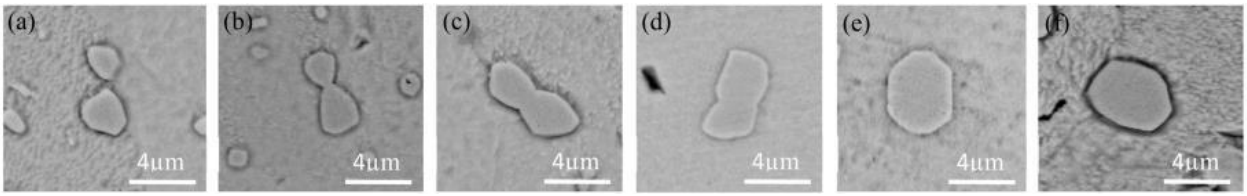

Fig. 1-8 Microstructure evolutions of the large Ag3Sn particles following necking coalescence: (a) theadjacent particles protruding towards each other; (b) two large particles bridged by a necking; (c–f) thenecking-shaped Ag_3Sn evolves to the uniform curvature [93].

Peng et al. [95]investigated the effect of thermal aging on the interfacial structure of SnAgCu solder joints on Cu. The results showed that Kirkendall voids formed at the Cu/Cu_3Sn interface and within the Cu_3Sn layer. The thickness of Cu_3Sn significantly increased with aging time, but that of Cu_6Sn_5 changed a little. The interfacial Cu_3Sn layer was found growing at the expense of Cu_6Sn_5. Liu et al. [96] reported the evolutions of the interface and shear strength between SnAgCu–xNi solder and Cu substrate during isothermal aging at 150 °C. The mean thickness of interfacial IMC layers increased linearly with the square root of the aging time for all the diffusion couples. The Cu_3Sn layer exhibited the fastest growth rate at the interface of the non-composite. The shear strength gradually decreased with thermal aging. The corresponding fracture mode also transformed from an initial ductile dimple in the solder layer to a mixed fracture near the interface. In order to furture investigate the microstructural evolution of interfacial IMC during thermal aging, Li et al. [97] designed a in situ quantitative study experiment. It found that the consumption of Cu substrate was not linear with the square root of aging time even though the growth of IMCs was diffusion-controlled. At the initial stage of solid-state aging, the Cu atoms to form IMCs were primarily from the supersaturated solder matrix. During the subsequent solid-state aging, the gaps between scallops were gradually blocked with the IMCs growing. For these IMCs, the Cu atoms were primarily from the Cu substrate. When the gaps disappeared, the consumption of Cu substrate slowed down.

In summary, two main problems were identified to reduce the reliability of the solder joints during thermal aging. The first is the coarsening of the microstructure consisting of solder layer and interfacial IMC, and the second is the decline of mechanical properties.

1.3.2 Microstructure coarsing

The coarsening of the microstructure of solder joints can be divided into two parts, one is the coarsening of the solder, and the other is the coarsening of the interfacial IMC.

The coarsening of the solder microstructure mainly refers to t coarse Ag_3Sn. These coarse Ag_3Sn will cause stress concentration to induce the generation of microcracks, causing failure of the solder joint [98]. The formation of the coarse Ag_3Sn is mainly attributed to the high Ag content. The Ag content should be reduced to overcome this problem. Zhao et al. [99] prepared low Ag solders, and the coarse Ag_3Sn was significantly reduced. In addition, the percentage failure in mechanical shock/drop tests for SAC105 solder joints was half that for SAC305 solder joints during thermal cycling [100]. On the other hands, During long-term service, the coarsening of Cu_6Sn_5 IMC in solder also occurred [101]. The Cu source of Cu_6Sn_5 IMC comes from the solder itself, and the other part comes from the Cu substrate. Therefore, some methods should be adopted to inhibit the diffusion of Cu atoms, reducing the formation of coarse Cu_6Sn_5 in the solder area.

The coarsening of the interfacial IMC is caused by the continuous diffusion between the Cu atoms from the Cu substrate and the Sn atoms in the soldering seam during the thermal aging, producing thicker interfacial IMC. Due to the inherently brittle of interfacial IMC, thicker IMC is more prone to cracks, which eventually lead to the failure of the solder joint. To effectively suppress the growth of the interfacial IMC, several studies have been carried out [102,103]. Nai et al. [102] reported the interfacial intermetallic growth and shear strength of CNTs reinforced SnAgCu composite solder joints. The results showed that the composite solder joints exhibited a lower diffusion coefficient, indicating that the presence of CNTs was effective in retarding the growth of the IMC layer. The schematic diagram of CNTs hindered the diffusion of Sn and Cu atoms is shown in Fig. 1-9. In addition, the shear strength of as-soldered and aged composite solder joints were higher than that of plain solder joints. Afolabi et al. [103] investigated the effect of isothermal aging on the morphology and shear strength of Sn-5Sb solder reinforced with carbon nanotubes. For the interfacial IMC layer evolution, appreciable retardation in IMC layer growth was observed in the composite solder joints

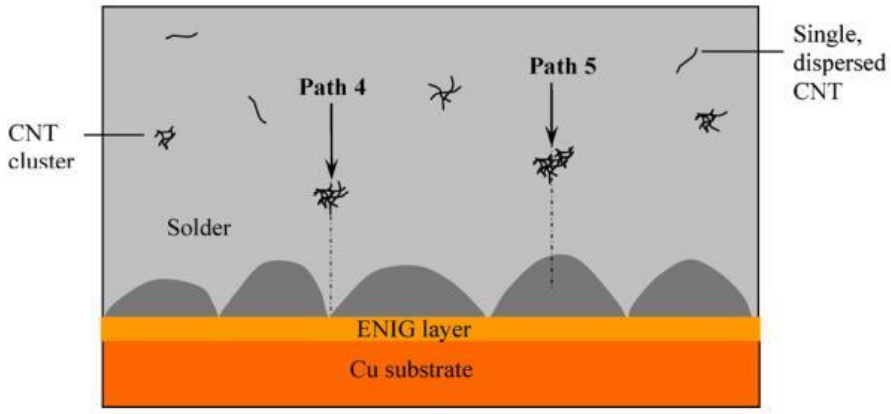

Fig. 1-9 Schematic diagram of CNTs hindered the diffusion of Sn and Cu atoms [102].

against the plain solder joint. And the composite solder joints showed better shear strength due to the exceptional mechanical properties of CNTs and the proper dispersion of CNTs in the solder matrix.

In summary, the microstructure coarsening of the solder joint is mainly attributed to the high Ag content and fast Cu-Sn interdiffusion rate. In order to obtain a good microstructure of solder joint, the newly developed solder should be a composite solder that has low Ag and can effectively inhibit Cu-Sn interdiffusion.

1.3.3 Mechanical limitation

Due to the microstructure coarsening of the solder joint, correspondingly, the mechanical properties are also decreased. Zhao et al. [99] reported the thermal aging behavior of SnAgCu solder joints. The results showed that the shear strength of solder joint was decreased with the increase of aging time. After reasonable addition of nano Fe_2O_3, the reliability of composite solder joint was better than that of plain solder, which would be attributed to the suppressed IMC growth. Similarly, Anah et al. [101] reported that the shear strength of SnAg solder joint exhibited a decreased trend as the aging time increased. In addition, the fracture of the solder joint partly occurred near the solder/Cu interface and partly inside the solder. After 1000 h aging, the fracture occurred completely near the solder/Cu interface. To solve the issue that the shear strength was declined during aging, some reinforcements were tried to added. The CNTs reinforced SnAgCu solder joint shows a better shear strength after reflow than the plain solder

joint. After thermal aging, the shear strength of aged solder joints decreased, while still higher than than that of plain solder joints.

Therefore, to obtain high reliability of solder joint, I need to obtain refined microstructure of solder joint after reflow and maintain the microstructure stability during long-term thermal aging.

1.4 Research strategy

To solve the issues mentioned above, the experiments in this study were systematically designed. In this part, several ideas were proposed, and corresponding experiments were conducted.

1.4.1 Interface regulation between reinforcements and SnAgCu solder matrix

Interface design between the reinforcement and solder matrix is important for obtaining composites with excellent performance. It is vital to understand the reinforcement-matrix interface in a metal matrix composite (MMC) because this interface is the region controlling the efficiency of load transfer from the matrix to the reinforcement [62]. In part1.2.3, I had mentioned that the poor wettability between reinforcements (ZrO_2 and T-ZnO_w) and SnAgCu results in a weak bonding interface between the reinforcement and solder matrix, reducing the strengthening effect of the reinforcement.

To improve the interface between the reinforcement and the solder matrix, the surface modification of the reinforcement has been considered to be an effective method. And it is known that an ideal interface of composites should have effectively combination and without coarse brittle IMC generated between them [70,104,105]. The interface composed of the solder matrix, modified layer, and reinforcement should also meet the same requirements. Therefore, it is imperative to choose an appropriately modified layer.

For the interface between ZrO_2 and SnAgCu solder matrix, a potentially modified layer is the transition metal oxide NiO. The Ni^{2+} in NiO can be partially substituted with Zr^{4+} of ZrO_2, forming a ZrO_2–NiO solid solution [106]. This suggests that ZrO_2 and NiO can wet each other and have a good interfacial binding ability. Moreover, Sn can be doped into the crystal lattice

of NiO [107,108], which also means the partially solid solution between NiO and Sn. This is conducive to the wetting between the SnAgCu solder and NiO. The above results suggest that NiO can not only wetting and solid solution with ZrO_2, but also with SnAgCu solder. Therefore, the Sn/NiO/ZrO_2 interface system based on mutual solid solution was ingeniously designed. In summart, it can be inferred that NiO is an ideal choice for the surface modification. Additionally, NiO has a CTE of 13.8×10^{-6}/K [109], which is between that of ZrO_2 and SnAgCu solder (CTE(ZrO_2)=9.6×10^{-6}/K, CTE(SnAgCu)=25.0×10^{-6}/K). The moderate CTE value of NiO is conducive to regulate the thermal mismatch of the interface.

After determining the material of the modified layer, the next step is to confirm which surface modification method will be adopted. In part 1.2.3, the surface modification methods mainly include electroless plating, sol-gel, and magnetron sputtering. However, most of these methods are costly, difficult for mass production, and cumbersome. Therefore, a convenient and green new surface modification method should be proposed.

Pyrolysis can be used to prepare nanomaterials and nanocomposites due to its convenience and low cost [110–112]. Lin et al. reported the preparation of graphene-basednanocomposite using pyrolysis [113]. Normally the surface of ZrO_2 is smooth and lacks functional groups, i.e., there are few active sites on the surface of ZrO_2. However, to produce NiO/ZrO_2 by pyrolysis, many active sites are required on the ZrO_2 surface. Among the active treatment methods, the ball milling method was considered to be a green and effective method. Since defects on the surface are introduced by ball milling, these defects can act as active sites [114,115]. Amade et al. [115] reported defect formation during high-energy ball milling in TiO_2, and increased photocatalytic activity was obtained. But the research on the activation of ball milling in the preparation of nanocomposites is limited. Inspired by this, the ball milling process was used to generate active sites on the surface of ZrO_2, and was combined with the pyrolysis method. Hence, the ball milling-pyrolysis method for NiO/ZrO_2 preparation was proposed.

Based on the same interface design principle, the surface modification of T-ZnO_w was carried out with the similar method. Due to the special three-dimensional space structure (Fig. 1-5) of T-ZnO_w, the ball milling-pyrolysis method should be appropriately changed. The

needles of the whisker will be broken if the ball milling process is applied. In order to ensure the integrity of the space structure of T-ZnO_w, the ball milling process was cancelled. Therefore, the surface modification method of T-ZnO_w was a pyrolysis method based on self-assembly.

1.4.2 Dispersed distribution of reinforcement assisted with ultrasonic agitation

The dispersed distribution of the reinforcements in the solder matrix is the key to obtain high-performance composite solder. However, neither the traditional casting nor the powder metallurgy method can dispersely add the nano-scale reinforcing phase to the solder matrix, as mentioned in part 1.2.4.

To solve this problem, an ultrasonic stirring is introduced into the casting method. When ultrasonic vibration is applied to the melt, the cavitation effect and the acoustic flow effect occur. The cavitation effect refers to the formation of cavitation bubbles in the melt under alternating positive and negative pressures of ultrasonic vibration [116]. The cavitation bubble expands rapidly and bursts. During the process, instantaneous high pressure impact force is generated, which can make the agglomerated particles dispersed [117]. At the same time, ultrasonic vibration can also produce acoustic streaming effects [118]. The eddy current effect produced by the acoustic current can effectively homogenize the processed melt. Based on the above characteristics, ultrasonic vibration is considered to be an effective method to homogenize the enhanced phase. It has been successfully applied to prepare composite materials [119-121]. Nie et al. [119] fabricated SiC particles-reinforced magnesium matrix composite by ultrasonic vibration. The UTS, yield strength and elongation of the SiCp/AZ91 composites were simultaneously improved compared with the as-cast AZ91 alloy. Kai et al [120] investigated the effects of ultrasonic

vibration on the microstructure and tensile properties of the nano ZrB_2/2024Al composites. The results showed that the large clusters of the agglomeration could be divided into dispersed particles and uniformly distributed in the matrix. At the same time, the ultrasonic treatment also has a significant degassing effect and results in fewer defects and mechanical property enhancement of the nanocomposites. The yield stress and elongation of the composite were 77% and 10% higher than that of the composites without ultrasonic processing, respectively. Gao et

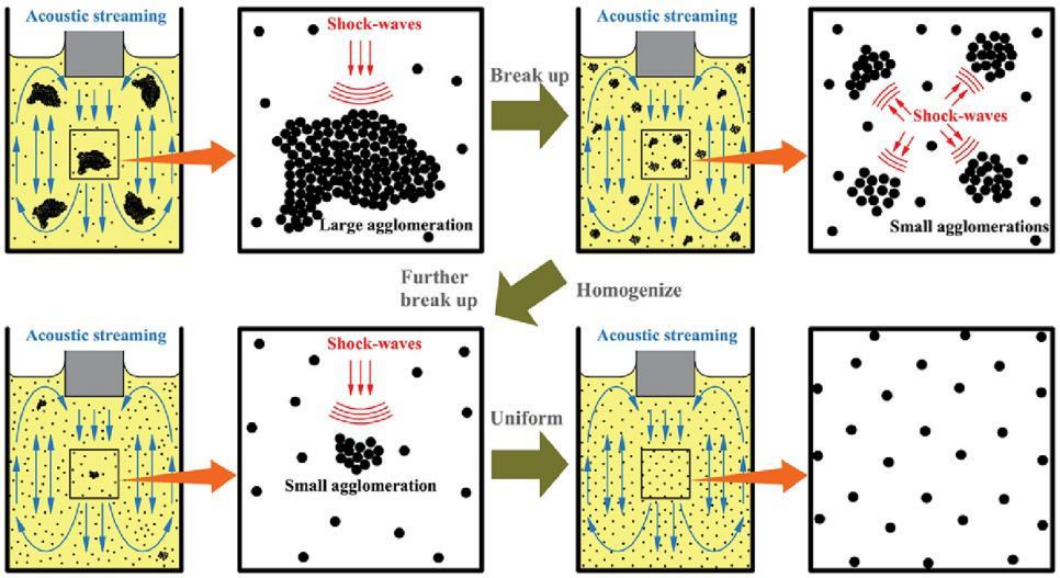

Fig. 1-10 The sketch of effects of ultrasonic cavitation and acoustic streaming on distribution of particles [121].

al. [121] reported improvement of particles distribution of in-situ 5 vol% TiB_2 particulates reinforced Al-4.5Cu alloy matrix composites with ultrasonic vibration treatment. The particulate distribution was effectively improved, uniformly distributed along grain boundary area. The yield strength of the composite was improved by 114% and 61% compared with base metal and untreated composite, respectively. In addition, the ultrasonic vibration mechanism was illustrated, and the sketch of the effects of ultrasonic cavitation and acoustic streaming on the distribution of particles is shown in Fig. 1-10. However, ultrasonic stirring is rarely used in the preparation of composite solders. Therefore, the ultrasonic stirring method is applied to obtain the dispersed distribution of the reinforcements in the solder matrix.

1.4.3 The design concept of multi-phase and multi-scale hybrid reinforced composite solder

The development of new lead-free solders mainly includes microalloying and composite solders methods. For the microalloying method, the design and preparation of alloy components are mature due to long-term development. For example, based on phase diagram software and thermodynamic software, the best alloy composition can be calculated and then combined with experiments, the best performance solder alloy can be obtained. In recent years,

the design and preparation of composite solders have gradually become a hot research topic. Various reinforcements are added to the solder matrix; some could improve the performance of plain solder, whereas some worsen the performance. In this case, the development efficiency of the composite solder is very low, wasting time and financial resources. This is mainly due to the relatively short development time of composite solders, and the design criteria and principles of composite solders are unclear. These design criteria and principles are urgently needed to guide the design of composite solders.

In this study, through the design and preparation of multi-phase and multi-scale hybrid reinforced composite solders, I systematically elaborated how to select the appropriate reinforcing phase, how to regulate the interface between the reinforcement and the solder matrix, and how to construct a multi-phase and multi-scale hybrid reinforced composite system based on the strengthening-ductility mechanism. I hope that this information from this study can provide some support for the improvement of the design criterion and principle of composite solder.

1.5 Research purpose and outline of this study

This study aims to develop a Sn1.0Ag0.5Cu solder with high strength-ductility, and obtain high reliability of Sn1.0Ag0.5Cu solder joints. To improve the strength and plasticity synergistically, the design concept of multi-phase and multi-scale hybrid enhancement is proposed. In addition, a new surface modification method, the ball milling-pyrolysis method, is proposed. In this study, the surface modification of the reinforcements, preparation of the composite solder, the interface regulation between the reinforcements and solder matrix, strengthening-ductility behavior of composite solders, and the reliability of composite solder joints were systematically designed. This research is expected to provide theoretical and experimental basis for the development of high strength-ductility lead-free solders. The outline of the dissertation is as follows:

In chapter 1, briefly illustrated the solder interconnection in electronic packaging, the development of lead-free solders, and reliability concerns for solder joints. The problems

existing in the development of composite solder are pointed out. Some ideas and methods to solve these problems are proposed.

In chapter 2, a new surface modification method, ball milling-pyrolysis method, is proposed. The proposed method is successfully applied to the surface modification of ZrO_2 nanoparticles and T-ZnO_w. The attachment of NiO on ZrO_2 could be regulated by controlling the ball milling time and Ni/Zr molar ratios. In addition, the formation mechanism of NiO/ZrO_2(NiO/T-ZnO_w) are explored using in-situ transmission electron microscopy (TEM). The interface relationship between the reinforcements and the modified layer NiO are also studied.

In chapter 3, NiO/ZrO_2-reinforced Sn1.0Ag0.5Cu composite solder is prepared with ultrasonic stirring. The microstructure evolution and refinement mechanism of composite solders are systematically investigated. The Sn/NiO/ZrO_2 interface system based on mutual solid solution is designed. In addition, the melting point and mechanical properties of composite solders are also studied.

In chapter 4, NiO/T-ZnO_w-reinforced Sn1.0Ag0.5Cu composite solder is prepared with ultrasonic stirring. The microstructure evolution and refinement mechanism of composite solders are systematically investigated. Sn/NiO/T-ZnOw interface system is designed. Moreover, the strengthening-ductility of composite solder was investigated.

In chapter 5, NiO/ZrO_2 and NiO/T-ZnO_w hybrid reinforced Sn1.0Ag0.5Cu composite solder is prepared with ultrasonic stirring. The microstructure evolution and mechanical properties of composite solders are systematically investigated. Morever, the thermal stability of composite solder is also investigated.

In chapter 6, the wetting performance of NiO/ZrO_2 and NiO/T-ZnO_w hybrid reinforced Sn1.0Ag0.5Cu composite solder is conducted. The composite solder/Cu solder joints with reflow are prepared, and the microstructure and shear strength of solder joints are investigated. Reliability of solder joints were also studied during thermal aging.

In Conclusion, brief achievements and results of each chapter in this thesis are summarized. The future plan is listed as well.

References

[1] K.N. Tu, K. Zeng, Tin-lead (SnPb) solder reaction in flip chip technology, Mater. Sci. Eng. R Reports. 34 (2001) 1–58. https://doi.org/10.1016/S0927-796X(01)00029-8.

[2] Stevels, Huisman, An industry vision on the implementation of WEEE and RoHS, (2014) 9–16. https://doi.org/10.1109/ecodim.2003.1322631.

[3] M. Fuse, K. Tsunemi, Assessment of the effects of the Japanese shift to lead-free solders and its impact on material substitution and environmental emissions by a dynamic material flow analysis, Sci. Total Environ. 438 (2012) 49–58. https://doi.org/10.1016/j.scitotenv.2012.08.017.

[4] M. Abtew, G. Selvaduray, Lead-free solders in microelectronics, Mater. Sci. Eng. R Reports. 27 (2000) 95–141. https://doi.org/10.1016/S0927-796X(00)00010-3.

[5] T. Laurila, V. Vuorinen, M. Paulasto-Kröckel, Impurity and alloying effects on interfacial reaction layers in Pb-free soldering, Mater. Sci. Eng. R Reports. 68 (2010) 1–38. https://doi.org/10.1016/j.mser.2009.12.001.

[6] T. Laurila, V. Vuorinen, J.K. Kivilahti, Interfacial reactions between lead-free solders and common base materials, Mater. Sci. Eng. R Reports. 49 (2005) 1–60. https://doi.org/10.1016/j.mser.2005.03.001.

[7] J. Keller, D. Baither, U. Wilke, G. Schmitz, Mechanical properties of Pb-free SnAg solder joints, Acta Mater. 59 (2011) 2731–2741. https://doi.org/10.1016/j.actamat.2011.01.012.

[8] W.Y. Chen, T.C. Chiu, K.L. Lin, A.T. Wu, W.L. Jang, C.L. Dong, H.Y. Lee, Anisotropic dissolution behavior of the second phase in SnCu solder alloys under current stress, Scr. Mater. 68 (2013) 317–320. https://doi.org/10.1016/j.scriptamat.2012.11.001.

[9] G. Ren, I.J. Wilding, M.N. Collins, Alloying influences on low melt temperature SnZn and SnBi solder alloys for electronic interconnections, J. Alloys Compd. 665 (2016) 251–260. https://doi.org/10.1016/j.jallcom.2016.01.006.

[10] A.T. Wu, M.H. Chen, C.H. Huang, Formation of intermetallic compounds in SnAgBiIn solder systems on Cu substrates, J. Alloys Compd. 476 (2009) 436–440. https://doi.org/10.1016/j.jallcom.2008.09.001.

[11] Z.H. Chen, Z. Wei, F.Q. Zu, X.B. Zhu, Y.F. Sun, Influence of liquid structure change on microstructure and properties of SnZnBi solder alloy, Adv. Mater. Res. 463–464 (2012) 489–493. https://doi.org/10.4028/www.scientific.net/AMR.463-464.489.

[12] H. Nishikawa, N. Iwata, Formation and growth of intermetallic compound layers at the interface during laser soldering using Sn-Ag-Cu solder on a Cu Pad, J. Mater. Process. Technol. 215 (2015) 6–11. https://doi.org/10.1016/j.jmatprotec.2014.08.007.

[13] K.W. Moon, W.J. Boettinger, U.R. Kattner, F.S. Biancaniello, C.A. Handwerker, Experimental and thermodynamic assessment of Sn-Ag-Cu solder alloys, J. Electron. Mater. 29 (2000) 1122–1136. https://doi.org/10.1007/s11664-000-0003-x.

[14] Y.-D. Tsai, C.-C. Hu, Composition Control of the Eutectic Sn-Based Alloys: Sn-Ag, Sn-Cu, Sn-Ag-Cu, From Simple Plating Baths, J. Electrochem. Soc. 158 (2011) D527. https://doi.org/10.1149/1.3601877.

[15] Q. Xiao, W.D. Armstrong, Tensile creep and microstructural characterization of bulk Sn3.9Ag0.6Cu lead-free solder, J. Electron. Mater. 34 (2005) 196–211. https://doi.org/10.1007/s11664-005-0233-z.

[16] J.P. Tucker, D.K. Chan, G. Subbarayan, C.A. Handwerker, Maximum entropy fracture model and its use for predicting cyclic hysteresis in Sn3.8Ag0.7Cu and Sn3.0Ag0.5 solder alloys, Microelectron. Reliab. 54 (2014) 2513–2522. https://doi.org/10.1016/j.microrel.2014.04.012.

[17] K.S. Kim, S.H. Huh, K. Suganuma, Effects of intermetallic compounds on properties of Sn-Ag-Cu lead-free soldered joints, J. Alloys Compd. 352 (2003) 226–236. https://doi.org/10.1016/S0925-8388(02)01166-0.

[18] T. Luo, Z. Chen, A. Hu, M. Li, Study on melt properties, microstructure, tensile properties of low Ag content Sn-Ag-Zn Lead-free solders, Mater. Sci. Eng. A. 556 (2012) 885–890. https://doi.org/10.1016/j.msea.2012.07.086.

[19] M. Sona, K.N. Prabhu, Review on microstructure evolution in Sn-Ag-Cu solders and its effect on mechanical integrity of solder joints, J. Mater. Sci. Mater. Electron. 24 (2013) 3149–3169. https://doi.org/10.1007/s10854-013-1240-0.

[20] J.S. Jeong, N. Park, C. Han, Field failure mechanism study of solder interconnection for crystalline silicon photovoltaic module, Microelectron. Reliab. 52 (2012) 2326–2330. https://doi.org/10.1016/j.microrel.2012.06.027.

[21] H. Ma, J.C. Suhling, A review of mechanical properties of lead-free solders for electronic packaging, J. Mater. Sci. 44 (2009) 1141–1158. https://doi.org/10.1007/s10853-008-3125-9.

[22] T. Yasuo, M. Masakatsu, Environmentally Friendly Low Temperature Solid State Micro-joining, Trans. JWRI. 40 (2011) 1–7.

[23] A.L. Moore, L. Shi, Emerging challenges and materials for thermal management of electronics, Mater. Today. 17 (2014) 163–174. https://doi.org/10.1016/j.mattod.2014.04.003.

[24] Y. Wang, G. Wang, K. Song, K. Zhang, Effect of Ni addition on the wettability and microstructure of Sn2.5Ag0.7Cu0.1RE solder alloy, Mater. Des. 119 (2017) 219–224. https://doi.org/10.1016/j.matdes.2017.01.046.

[25] C.L. Chuang, L.C. Tsao, H.K. Lin, L.P. Feng, Effects of small amount of active Ti element additions on microstructure and property of Sn3.5Ag0.5Cu solder, Mater. Sci. Eng. A. 558 (2012) 478–484. https://doi.org/10.1016/j.msea.2012.08.031.

[26] W.M. Chen, S.K. Kang, C.R. Kao, Effects of Ti addition to Sn-Ag and Sn-Cu solders, J. Alloys Compd. 520 (2012) 244–249. https://doi.org/10.1016/j.jallcom.2012.01.032.

[27] Y.W. Wang, C.C. Chang, C.R. Kao, Minimum effective Ni addition to SnAgCu solders for retarding Cu_3Sn growth, J. Alloys Compd. 478 (2009) L1. https://doi.org/10.1016/j.jallcom.2008.11.027.

[28] H. Nishikawa, A. Komatsu, T. Takemoto, Morphology and pull strength of Sn-Ag(-Co) solder joint with copper pad, J. Electron. Mater. 36 (2007) 1137–1143. https://doi.org/10.1007/s11664-007-0148-y.

[29] L.C. Tsao, S.Y. Chang, Effects of Nano-TiO2 additions on thermal analysis, microstructure and tensile properties of Sn3.5Ag0.25Cu solder, Mater. Des. 31 (2010) 990–993. https://doi.org/10.1016/j.matdes.2009.08.008.

[30] G. Chen, H. Peng, V. V. Silberschmidt, Y.C. Chan, C. Liu, F. Wu, Performance of Sn-3.0Ag-0.5Cu composite solder with TiC reinforcement: Physical properties, solderability and microstructural evolution under isothermal ageing, J. Alloys Compd. 685 (2016) 680–689. https://doi.org/10.1016/j.jallcom.2016.05.245.

[31] K.M. Kumar, V. Kripesh, L. Shen, A.A.O. Tay, Study on the microstructure and mechanical properties of a novel SWCNT-reinforced solder alloy for ultra-fine pitch applications, Thin Solid Films. 504 (2006) 371–378. https://doi.org/10.1016/j.tsf.2005.09.072.

[32] H. Wang, X. Hu, X. Jiang, Effects of Ni modified MWCNTs on the microstructural evolution and shear strength of Sn-3.0Ag-0.5Cu composite solder joints, Mater. Charact. 163 (2020). https://doi.org/10.1016/j.matchar.2020.110287.

[33] S. Queyreau, G. Monnet, B. Devincre, Orowan strengthening and forest hardening superposition examined by dislocation dynamics simulations, Acta Mater. 58 (2010) 5586–5595. https://doi.org/10.1016/j.actamat.2010.06.028.

[34] Y. Geng, Y. Ban, X. Li, Y. Zhang, Y. Jia, B. Tian, M. Zhou, Y. Liu, A.A. Volinsky, K. Song, S. Tang, Excellent mechanical properties and high electrical conductivity of Cu-Co-Si-Ti alloy due to multiple strengthening, Mater. Sci. Eng. A. 821 (2021). https://doi.org/10.1016/j.msea.2021.141639.

[35] J.H. Martin, B. Yahata, J. Mayer, R. Mone, E. Stonkevitch, J. Miller, M.R. O'Masta, T. Schaedler, J. Hundley, P. Callahan, T. Pollock, Grain refinement mechanisms in additively manufactured nano-functionalized aluminum, Acta Mater. 200 (2020) 1022–1037. https://doi.org/10.1016/j.actamat.2020.09.043.

[36] Y.N. Hou, K.M. Yang, J. Song, H. Wang, Y. Liu, T.X. Fan, A crystal plasticity model for metal matrix composites considering thermal mismatch stress induced dislocations and twins, Sci. Rep. 11 (2021) 1–13. https://doi.org/10.1038/s41598-021-95439-z.

[37] Z. Peng, X. Wang, Z. Wu, A bundle-based shear-lag model for tensile failure prediction of unidirectional fiber-reinforced polymer composites, Mater. Des. 196 (2020) 109103. https://doi.org/10.1016/j.matdes.2020.109103.

[38] Z. Zhang, D.L. Chen, Consideration of Orowan strengthening effect in particulate-reinforced metal matrix nanocomposites: A model for predicting their yield strength, Scr. Mater. 54 (2006) 1321–1326. https://doi.org/10.1016/j.scriptamat.2005.12.017.

[39] Y. Wen, X. Zhao, Z. Chen, Y. Gu, Y. Wang, Z. Chen, X. Wang, Reliability enhancement of Sn-1.0Ag-0.5Cu nano-composite solders by adding multiple sizes of TiO_2 nanoparticles, J. Alloys Compd. 696 (2017) 799–807. https://doi.org/10.1016/j.jallcom.2016.12.037.

[40] J. Li, X. Ren, Y. Zhang, H. Hou, Significant improvements of the relative density, microhardness, and fracture toughness of SiC via the addition of Ni_3Al and Mg_2Si, Ceram. Int. 47 (2021) 1472–1477. https://doi.org/10.1016/j.ceramint.2020.08.240.

[41] T. Huber, H.P. Degischer, G. Lefranc, T. Schmitt, Thermal expansion studies on aluminium-matrix composites with different reinforcement architecture of SiC particles, Compos. Sci. Technol. 66 (2006) 2206–2217. https://doi.org/10.1016/j.compscitech.2005.12.012.

[42] B.L. Turner-Adomatis, N.N. Thadhani, Shock-enhanced alpha to beta phase transformation in Si_3N_4 powders, Mater. Sci. Eng. A. 256 (1998) 289–300. https://doi.org/10.1016/s0921-5093(98)00805-3.

[43] J. Diani, K. Gall, Study on High-Performance Poly(etheretherketone)/Si3N4 Nanocomposites: New Electronic Substrate Materials, Polym. Eng. Sci. 51 (2011) 509–517. https://doi.org/10.1002/pen.21837.

[44] Y. Wang, P. Shen, R.F. Guo, Z.J. Hu, Q.C. Jiang, Developing high toughness and strength Al/TiC composites using ice-templating and pressure infiltration, Ceram. Int. 43 (2017) 3831–3838. https://doi.org/10.1016/j.ceramint.2016.12.038.

[45] X.C. Li, J. Stampfl, F.B. Prinz, Mechanical and thermal expansion behavior of laser deposited metal matrix composites of Invar and TiC, Mater. Sci. Eng. A. 282 (2000) 86–90. https://doi.org/10.1016/s0921-5093(99)00781-9.

[46] A. Rokanopoulou, P. Skarvelis, G.D. Papadimitriou, Microstructure and wear properties of the surface of 2205 duplex stainless steel reinforced with Al_2O_3 particles by the plasma

transferred arc technique, Surf. Coatings Technol. 254 (2014) 376–381. https://doi.org/10.1016/j.surfcoat.2014.06.047.

[47] L.C. Sim, S.R. Ramanan, H. Ismail, K.N. Seetharamu, T.J. Goh, Thermal characterization of Al_2O_3 and ZnO reinforced silicone rubber as thermal pads for heat dissipation purposes, Thermochim. Acta. 430 (2005) 155–165. https://doi.org/10.1016/j.tca.2004.12.024.

[48] B. Krummheuer, V.M. Axt, T. Kuhn, I. D'Amico, F. Rossi, Pure dephasing and phonon dynamics in GaAs- and GaN-based quantum dot structures: Interplay between material parameters and geometry, Phys. Rev. B - Condens. Matter Mater. Phys. 71 (2005) 1–13. https://doi.org/10.1103/PhysRevB.71.235329.

[49] S. Gao, N. Zhao, Q. Liu, Y. Li, G. Xu, X. Cheng, J. Yang, Sc2W3O12/Cu composites with low thermal expansion coefficient and high thermal conductivity for efficient cooling of electronics, J. Alloys Compd. 779 (2019) 108–114. https://doi.org/10.1016/j.jallcom.2018.11.131.

[50] N. Li, M. Suzuki, Y. Abe, M. Kawamura, K. Sasaki, H. Itoh, T. Suzuki, Effects of substrate temperature on the ion conductivity of hydrated ZrO_2 thin films prepared by reactive sputtering in H_2O atmosphere, Sol. Energy Mater. Sol. Cells. 99 (2012) 160–165. https://doi.org/10.1016/j.solmat.2011.03.037.

[51] X. Yang, J. Xu, H. Li, X. Cheng, X. Yan, In situ synthesis of ZrO_2/ZrW_2O_8 composites with near-zero thermal expansion, J. Am. Ceram. Soc. 90 (2007) 1953–1955. https://doi.org/10.1111/j.1551-2916.2007.01718.x.

[52] Y. Wei, J. Chen, S. Wang, X. Zhong, R. Xiong, L. Gan, Y. Ma, T. Zhai, H. Li, Wrapping Sb_2Te_3 with a Graphite Layer toward High Volumetric Energy and Long Cycle Li-Ion Batteries, ACS Appl. Mater. Interfaces. 12 (2020) 16264–16275. https://doi.org/10.1021/acsami.9b22346.

[53] D. Yoon, Y. Son, H. Cheong, Negative Thermal Expansion Coefficient of Graphene Measured by Raman Spectroscopy, Nano Lett. 11 (2011) 3227–3231. https://doi.org/10.1021/nl201488g.

[54] B. Ren, C.T. Wu, P. Seleson, D. Zeng, D. Lyu, A peridynamic failure analysis of fiber-reinforced composite laminates using finite element discontinuous Galerkin approximations, Int. J. Fract. 214 (2018) 49–68. https://doi.org/10.1007/s10704-018-0317-4.

[55] H. Zhang, T. Huang, Q. Jiang, L. He, A. Bismarck, Q. Hu, Recent progress of 3D printed continuous fiber reinforced polymer composites based on fused deposition modeling: a review, J. Mater. Sci. 56 (2021) 12999–13022. https://doi.org/10.1007/s10853-021-06111-w.

[56] H. Zhao, X. Liu, W. Zhao, G. Wang, B. Liu, An Overview of Research on FDM 3D Printing Process of Continuous Fiber Reinforced Composites, J. Phys. Conf. Ser. 1213 (2019). https://doi.org/10.1088/1742-6596/1213/5/052037.

[57] P. Zhang, S. Xue, J. Wang, New challenges of miniaturization of electronic devices: Electromigration and thermomigration in lead-free solder joints, Mater. Des. 192 (2020) 108726. https://doi.org/10.1016/j.matdes.2020.108726.

[58] H. Huang, Y.Q. Wu, S.L. Wang, Y.H. He, J. Zou, B.Y. Huang, C.T. Liu, Mechanical properties of single crystal tungsten microwhiskers characterized by nanoindentation, Mater. Sci. Eng. A. 523 (2009) 193–198. https://doi.org/10.1016/j.msea.2009.05.060.

[59] Y.C. Zhao, J. Wang, J.F. Liu, Z.G. Song, X.L. Xi, Prediction of microwave absorption properties of tetrapod-needle zinc oxide whisker radar absorbing material without prior knowledge, J. Appl. Phys. 122 (2017). https://doi.org/10.1063/1.4993191.

[60] C. Ge, L. Wang, G. Liu, T. Wang, H. Chen, Synthesis of core–shell structured tetra-needle ZnO whisker and Fe composite with excellent electromagnetic properties, Mater. Lett. 238 (2019) 126–129. https://doi.org/10.1016/j.matlet.2018.11.166.

[61] Z. Zhou, L. Chu, S. Hu, Microwave absorption behaviors of tetra-needle-like ZnO whiskers, Mater. Sci. Eng. B Solid-State Mater. Adv. Technol. 126 (2006) 93–96. https://doi.org/10.1016/j.mseb.2005.09.009.

[62] B.A. Feldhoff, E. Pippel, J. Woltersdorf, Interface Engineering of Carbon- Fiber Reinforced Mg ± Al Alloys, Adv. Eng. Mater. (2000) 471–480. https://doi.org/10.1002/1527-2648(200008)2:8<471::AID-ADEM471>3.0.CO;2-S.

[63] S. Nambu, M. Michiuchi, J. Inoue, T. Koseki, Effect of interfacial bonding strength on tensile ductility of multilayered steel composites, Compos. Sci. Technol. 69 (2009) 1936–1941. https://doi.org/10.1016/j.compscitech.2009.04.013.

[64] G.P. Ling, Y. Li, Influencing factors on the uniformity of copper coated nano-Al_2O_3 powders prepared by electroless plating, Mater. Lett. 59 (2005) 1610–1613. https://doi.org/10.1016/j.matlet.2004.12.054.

[65] G. Yasin, M.A. Khan, M. Arif, M. Shakeel, T.M. Hassan, W.Q. Khan, R.M. Korai, Z. Abbas, Y. Zuo, Synthesis of spheres-like Ni/graphene nanocomposite as an efficient anti-corrosive coating; effect of graphene content on its morphology and mechanical properties, J. Alloys Compd. 755 (2018) 79–88. https://doi.org/10.1016/j.jallcom.2018.04.321.

[66] Y. Wang, Y. Gao, Y. Li, C. Zhang, L. Sun, W. Zhai, Research on nickel modified graphite/Cu composites interface, Surf. Coatings Technol. 328 (2017) 70–79. https://doi.org/10.1016/j.surfcoat.2017.08.036.

[67] C. Zhang, D. Yao, J. Yin, K. Zuo, Y. Xia, H. Liang, Y.P. Zeng, Effects of whisker surface modification on microstructures, mechanical and thermal properties of β-Si_3N_4 whiskers reinforced Al matrix composites, Mater. Des. 159 (2018) 117–126. https://doi.org/10.1016/j.matdes.2018.08.055.

[68] L. Xu, X. Chen, H. Jing, L. Wang, J. Wei, Y. Han, Design and performance of Ag nanoparticle-modified graphene/SnAgCu lead-free solders, Mater. Sci. Eng. A. 667 (2016) 87–96. https://doi.org/10.1016/j.msea.2016.04.084.

[69] U.G. Akpan, B.H. Hameed, The advancements in sol-gel method of doped-TiO_2 photocatalysts, Appl. Catal. A Gen. 375 (2010) 1–11. https://doi.org/10.1016/j.apcata.2009.12.023.

[70] P. Jin, L. Han, S. Chen, J. Wang, Y. Zhu, Microstructure and tensile properties of ZnO-coated magnesium borate whisker reinforced AZ31B composite, Mater. Sci. Eng. A. 554 (2012) 48–52. https://doi.org/10.1016/j.msea.2012.06.008.

[71] A.N. Khramov, V.N. Balbyshev, L.S. Kasten, R.A. Mantz, Sol-gel coatings with phosphonate functionalities for surface modification of magnesium alloys, Thin Solid Films. 514 (2006) 174–181. https://doi.org/10.1016/j.tsf.2006.02.023.

[72] D.Y. Ding, J.C. Rao, D.Z. Wang, Z.Y. Ma, L. Geng, C.K. Yao, Sol-gel alumina coatings for whisker reinforced metal matrix composites, Mater. Sci. Eng. A. 279 (2000) 138–141. https://doi.org/10.1016/S0921-5093(99)00619-X.

[73] W.G. Wang, B.L. Xiao, Z.Y. Ma, Interfacial reaction and nanostructures in Mg matrix composites reinforced with carbon fibers modified by sol-gel method, Compos. Sci. Technol. 87 (2013) 69–76. https://doi.org/10.1016/j.compscitech.2013.07.027.

[74] P.J. Kelly, R.D. Arnell, Magnetron sputtering: A review of recent developments and applications, Vacuum. 56 (2000) 159–172. https://doi.org/10.1016/S0042-207X(99)00189-X.

[75] X.Q. Tan, J.Y. Liu, J.R. Niu, J.Y. Liu, J.Y. Tian, Recent progress in magnetron sputtering technology used on fabrics, Materials (Basel). 11 (2018). https://doi.org/10.3390/ma11101953.

[76] T. Köck, A. Brendel, H. Bolt, Interface reactions between silicon carbide and interlayers in silicon carbide-copper metal-matrix composites, J. Nucl. Mater. 362 (2007) 197–201. https://doi.org/10.1016/j.jnucmat.2007.01.022.

[77] L. Xin, X. Tian, W. Yang, G. Chen, J. Qiao, F. Hu, Q. Zhang, G. Wu, Enhanced stability of the Diamond/Al composites by W coatings prepared by the magnetron sputtering method, J. Alloys Compd. 763 (2018) 305–313. https://doi.org/10.1016/j.jallcom.2018.05.310.

[78] F. Xu, D. Gong, Improved the elevated temperature mechanical properties of Al-Si alloy deposited with Al-Si coating by magnetron sputtering, Vacuum. 150 (2018) 1–7. https://doi.org/10.1016/j.vacuum.2018.01.013.

[79] Y. Cheng, X. Huang, Z. Du, J. Xiao, S. Zhou, Y. Wei, Microstructure and properties of SiC-coated carbon fibers prepared by radio frequency magnetron sputtering, Appl. Surf. Sci. 369 (2016) 196–200. https://doi.org/10.1016/j.apsusc.2016.02.070.

[80] J. Shen, Y. Liu, D. Wang, H. Gao, Nano ZrO_2 Particulate-reinforced Lead-Free Solder Composite, 22 (2006) 529–532.

[81] W. qing Xing, X. ye Yu, H. Li, L. Ma, W. Zuo, P. Dong, W. xian Wang, M. Ding, Effect of nano Al_2O_3 additions on the interfacial behavior and mechanical properties of eutectic Sn-9Zn solder on low temperature wetting and soldering of 6061 aluminum alloys, J. Alloys Compd. 695 (2017) 574–582. https://doi.org/10.1016/j.jallcom.2016.11.136.

[82] A. Fawzy, S.A. Fayek, M. Sobhy, E. Nassr, M.M. Mousa, G. Saad, Effect of ZnO nanoparticles addition on thermal, microstructure and tensile properties of Sn-3.5 Ag-0.5 Cu (SAC355) solder alloy, J. Mater. Sci. Mater. Electron. 24 (2013) 3210–3218. https://doi.org/10.1007/s10854-013-1230-2.

[83] A.K. Gain, Y.C. Chan, Growth mechanism of intermetallic compounds and damping properties of Sn-Ag-Cu-1wt% nano-ZrO_2 composite solders, Microelectron. Reliab. 54 (2014) 945–955. https://doi.org/10.1016/j.microrel.2014.01.026.

[84] A. Yakymovych, Y. Plevachuk, P. Švec, P. Švec, D. Janičkovič, P. Šebo, N. Beronská, A. Roshanghias, H. Ipser, Morphology and Shear Strength of Lead-Free Solder Joints with Sn3.0Ag0.5Cu Solder Paste Reinforced with Ceramic Nanoparticles, J. Electron. Mater. 45 (2016) 6143–6149. https://doi.org/10.1007/s11664-016-4832-7.

[85] X.D. Liu, Y.D. Han, H.Y. Jing, J. Wei, L.Y. Xu, Effect of graphene nanosheets reinforcement on the performance of SnAgCu lead-free solder, Mater. Sci. Eng. A. 562 (2013) 25–32. https://doi.org/10.1016/j.msea.2012.10.079.

[86] G. Chen, F. Wu, C. Liu, W. Xia, H. Liu, Effects of fullerenes reinforcement on the performance of 96.5Sn-3Ag-0.5Cu lead-free solder, Mater. Sci. Eng. A. 636 (2015) 484–492. https://doi.org/10.1016/j.msea.2015.03.106.

[87] Y.D. Han, H.Y. Jing, S.M.L. Na, L.Y. Xu, C.M. Tan, J. Wei, Creep mitigation in Sn-Ag-Cu composite solder with Ni-coated carbon nanotubes, J. Mater. Sci. Mater. Electron. 23 (2012) 1108–1115. https://doi.org/10.1007/s10854-011-0557-9.

[88] K. Zeng, K.N. Tu, Six cases of reliability study of Pb-free solder joints in electronic packaging technology, Mater. Sci. Eng. R Reports. 38 (2002) 55–105. https://doi.org/10.1016/s0927-796x(02)00007-4.

[89] M.A. Rabiatul Adawiyah, O. Saliza Azlina, Comparative study on the isothermal aging of bare Cu and ENImAg surface finish for Sn-Ag-Cu solder joints, J. Alloys Compd. 740 (2018) 958–966. https://doi.org/10.1016/j.jallcom.2018.01.054.

[90] X. Long, X. He, Y. Yao, An improved unified creep-plasticity model for SnAgCu solder under a wide range of strain rates, J. Mater. Sci. 52 (2017) 6120–6137. https://doi.org/10.1007/s10853-017-0851-x.

[91] P. Borgesen, L. Wentlent, S. Hamasha, S. Khasawneh, S. Shirazi, D. Schmitz, T. Alghoul, C. Greene, L. Yin, A Mechanistic Thermal Fatigue Model for SnAgCu Solder Joints, J. Electron. Mater. 47 (2018) 2526–2544. https://doi.org/10.1007/s11664-018-6121-0.

[92] H. Madanipour, Y.R. Kim, C.U. Kim, D. Mishra, P. Thompson, Study of electromigration in Sn-Ag-Cu micro solder joint with Ni interfacial layer, J. Alloys Compd. 862 (2021) 158043. https://doi.org/10.1016/j.jallcom.2020.158043.

[93] Y. Tian, N. Ren, Z. Zhao, F. Wu, S.K. Sitaraman, Ag_3Sn compounds coarsening behaviors in micro-joints, Materials (Basel). 10 (2018) 1–12. https://doi.org/10.3390/ma11122509.

[94] D. Zhao, K. Zhang, N. Ma, S. Li, C. Yin, F. Huo, Dynamic Observation of Interfacial IMC Evolution, Materials (Basel). (2020) 1–13.

[95] W. Peng, E. Monlevade, M.E. Marques, Effect of thermal aging on the interfacial structure of SnAgCu solder joints on Cu, Microelectron. Reliab. 47 (2007) 2161–2168. https://doi.org/10.1016/j.microrel.2006.12.006.

[96] P. Liu, P. Yao, J. Liu, Evolutions of the interface and shear strength between SnAgCu-xNi solder and Cu substrate during isothermal aging at 150 ℃, J. Alloys Compd. 486 (2009) 474–479. https://doi.org/10.1016/j.jallcom.2009.06.171.

[97] H. Li, R. An, C. Wang, Z. Jiang, In situ quantitative study of microstructural evolution at the interface of Sn3.0Ag0.5Cu/Cu solder joint during solid state aging, J. Alloys Compd. 634 (2015) 94–98. https://doi.org/10.1016/j.jallcom.2015.02.088.

[98] H. Chen, T.T. Chou, C. Fleshman, J.G. Duh, Investigating the Effect of Ag Content on Mechanical Properties of Sn-Ag-Cu Micro-BGA Joints, J. Electron. Mater. 48 (2019) 6866–6871. https://doi.org/10.1007/s11664-019-07428-8.

[99] X. Zhao, Y. Wen, Y. Li, Y. Liu, Y. Wang, Effect of γ-Fe2O3 nanoparticles size on the properties of Sn-1.0Ag-0.5Cu nano-composite solders and joints, J. Alloys Compd. 662 (2016) 272–282. https://doi.org/10.1016/j.jallcom.2015.11.213.

[100] H. Ji, Y. Ma, M. Li, C. Wang, Effect of the Silver Content of SnAgCu Solder on the Interfacial Reaction and on the Reliability of Angle Joints Fabricated by Laser-Jet Soldering, J. Electron. Mater. 44 (2015) 733–743. https://doi.org/10.1007/s11664-014-3516-4.

[101] S. Ahat, M. Sheng, L. Luo, Microstructure and shear strength evolution of SnAg/Cu surface mount solder joint during aging, J. Electron. Mater. 30 (2001) 1317–1322. https://doi.org/10.1007/s11664-001-0118-8.

[102] S.M.L. Nai, J. Wei, M. Gupta, Interfacial intermetallic growth and shear strength of lead-free composite solder joints, J. Alloys Compd. 473 (2009) 100–106. https://doi.org/10.1016/j.jallcom.2008.05.070.

[103] T.T. Dele-Afolabi, M.A. Azmah Hanim, M. Norkhairunnisa, H.M. Yusoff, M.T. Suraya, Investigating the effect of isothermal aging on the morphology and shear strength of Sn-5Sb solder reinforced with carbon nanotubes, J. Alloys Compd. 649 (2015) 368–374. https://doi.org/10.1016/j.jallcom.2015.07.036.

[104] S.H. Chen, P.P. Jin, G. Schumacher, N. Wanderka, Microstructure and interface characterization of a cast Mg_2B_2O5 whisker reinforced AZ91D magnesium alloy composite, Compos. Sci. Technol. 70 (2010) 123–129. https://doi.org/10.1016/j.compscitech.2009.09.015.

[105]S. Li, K. Kondoh, H. Imai, B. Chen, L. Jia, J. Umeda, Y. Fu, Strengthening behavior of in situ-synthesized (TiC-TiB)/Ti composites by powder metallurgy and hot extrusion, Mater. Des. 95 (2016) 127–132. https://doi.org/10.1016/j.matdes.2016.01.092.

[106]C. Angeles-Chavez, D.A. Prado-Chay, M.A. Cortes-Jacome, J.A. Antonio-Toledo, Structural Analysis of HR-TEM Images of Ni-doped Zirconia Nanoparticles, Microsc. Microanal. 25 (2019) 2112–2113. https://doi.org/10.1017/s1431927619011292.

[107]B.Y. Kim, J.W. Yoon, J.K. Kim, Y.C. Kang, J.H. Lee, Dual Role of Multiroom-Structured Sn-Doped NiO Microspheres for Ultrasensitive and Highly Selective Detection of Xylene, ACS Appl. Mater. Interfaces. 10 (2018) 16605–16612. https://doi.org/10.1021/acsami.8b02412.

[108]M.H. Mamat, N. Parimon, A.S. Ismail, I.B. Shameem Banu, S. Sathik Basha, R.A. Rani, A.S. Zoolfakar, M.F. Malek, A.B. Suriani, M.K. Ahmad, M. Rusop, Synthesis, structural and optical properties of mesostructured, X-doped NiO (x = Zn, Sn, Fe) nanoflake network films, Mater. Res. Bull. 127 (2020). https://doi.org/10.1016/j.materresbull.2020.110860.

[109]C.R. He, W.G. Wang, J. Wang, Y. Xue, Effect of alumina on the curvature, Young's modulus, thermal expansion coefficient and residual stress of planar solid oxide fuel cells, J. Power Sources. 196 (2011) 7639–7644. https://doi.org/10.1016/j.jpowsour.2011.05.025.

[110]M. Unni, A.M. Uhl, S. Savliwala, B.H. Savitzky, R. Dhavalikar, N. Garraud, D.P. Arnold, L.F. Kourkoutis, J.S. Andrew, C. Rinaldi, Thermal Decomposition Synthesis of Iron Oxide Nanoparticles with Diminished Magnetic Dead Layer by Controlled Addition of Oxygen, ACS Nano. 11 (2017) 2284–2303. https://doi.org/10.1021/acsnano.7b00609.

[111]C. Wen, M. Shao, S. Zhuo, Z. Lin, Z. Kang, Silver/graphene nanocomposite: Thermal decomposition preparation and its catalytic performance, Mater. Chem. Phys. 135 (2012) 780–785. https://doi.org/10.1016/j.matchemphys.2012.05.058.

[112]B.M. Abu-Zied, A.M. Asiri, An investigation of the thermal decomposition of silver acetate as a precursor for nano-sized Ag-catalyst, Thermochim. Acta. 581 (2014) 110–117. https://doi.org/10.1016/j.tca.2014.02.020.

[113]Y. Lin, K.A. Watson, M.J. Fallbach, S. Ghose, J.G. Smith, D.M. Delozier, W. Cao, R.E. Crooks, J.W. Connell, Rapid, solventless, bulk preparation of metal nanoparticle-decorated carbon nanotubes, ACS Nano. 3 (2009) 871–884. https://doi.org/10.1021/nn8009097.

[114]Y. Lin, T. V. Williams, W. Cao, H.E. Elsayed-Ali, J.W. Connell, Defect functionalization of hexagonal boron nitride nanosheets, J. Phys. Chem. C. 114 (2010) 17434–17439. https://doi.org/10.1021/jp105454w.

[115]R. Amade, P. Heitjans, S. Indris, M. Finger, A. Haeger, D. Hesse, Defect formation during high-energy ball milling in TiO_2 and its relation to the photocatalytic activity, J. Photochem. Photobiol. A Chem. 207 (2009) 231–235. https://doi.org/10.1016/j.jphotochem.2009.07.015.

[116]R. Feng, Y. Zhao, C. Zhu, T.J. Mason, Enhancement of ultrasonic cavitation yield by multi-frequency sonication, Ultrason. Sonochem. 9 (2002) 231–236. https://doi.org/10.1016/S1350-4177(02)00083-4.

[117]S. Sumitomo, H. Koizumi, M.A. Uddin, Y. Kato, Comparison of dispersion behavior of agglomerated particles in liquid between ultrasonic irradiation and mechanical stirring, Ultrason. Sonochem. 40 (2018) 822–831. https://doi.org/10.1016/j.ultsonch.2017.08.023.

[118]E. Riedel, M. Liepe, S. Scharf, Simulation of ultrasonic induced cavitation and acoustic streaming in liquid and solidifying aluminum, Metals (Basel). 10 (2020). https://doi.org/10.3390/met10040476.

[119]K.B. Nie, X.J. Wang, K. Wu, L. Xu, M.Y. Zheng, X.S. Hu, Fabrication of SiC particles-reinforced magnesium matrix composite by ultrasonic vibration, J. Mater. Sci. 47 (2012) 138–144. https://doi.org/10.1007/s10853-011-5780-5.

[120]X. Kai, K. Tian, C. Wang, L. Jiao, G. Chen, Y. Zhao, Effects of ultrasonic vibration on the microstructure and tensile properties of the nano ZrB_2/2024Al composites synthesized by direct melt reaction, J. Alloys Compd. 668 (2016) 121–127. https://doi.org/10.1016/j.jallcom.2016.01.152.

[121]Q. Gao, S. Wu, S. Lü, X. Xiong, R. Du, P. An, Improvement of particles distribution of in-situ 5vol% TiB_2 particulates reinforced Al-4.5Cu alloy matrix composites with ultrasonic vibration treatment, J. Alloys Compd. 692 (2017) 1–9. https://doi.org/10.1016/j.jallcom.2016.09.013.

Chapter 2 Surface modification of ZrO_2 nanoparticles and T-ZnO_w

2.1 Introduction

In chapter 1, ZrO_2 nanoparticles and tetra-needle like ZnO whisker (T-ZnO_w) have been selected as the reinforcements for the composite solder preparation. However, the poor wettability between reinforcements (ZrO_2 and T-ZnO_w) and SnAgCu resulted in a weak bonding interface between the reinforcement and solder matrix. The problem limited the application of ZrO_2 and T-ZnO_w in SnAgCu solder. To improve the interface between the reinforcements and the solder matrix, the surface modification of the reinforcement has been considered to be an effective method. In part 1.2.3, I had mentioned that surface modification methods mainly include electroless plating, sol-gel, and magnetron sputtering. However, most of these methods are expensive, difficult for mass production, and cumbersome. Therefore, a convenient and green new surface modification method should be proposed.

In this chapter, a new surface modification method, ball milling-pyrolysis method based on self-assembly, was proposed. And successfully applied to the surface modification of ZrO_2 nanoparticles and T-ZnO_w. The attachment of NiO on ZrO_2 was regulated by controlling the ball milling time and Ni/Zr molar ratios. In addition, the formation mechanism of NiO/ZrO_2 (NiO/T-ZnO_w) were explored using in-situ transmission electron microscopy (TEM). The interface relationship between the reinforcements and the modified layer NiO also studied. Based on the same interface design principle, the surface modification of T-ZnO_w was carried out with pyrolysis method based on self-assembly method.

2.2 Experimental procedure

2.2.1 Materials

The size of commercial ZrO_2 (HW NANO, China) particle was in the range 60–120 nm; the length and dimension of T-ZnO_w (TY Company, China) were in the range of 5–20 and 0.5–3 μm, respectively. $Ni(CH_3COO)_2 \cdot 4H_2O$ powder of 99.9% purity was obtained from Wako Pure Chemical Industries, Ltd. Japan.

2.2.2 Preparation of NiO/ZrO_2 and $NiO/T\text{-}ZnO_w$

(a) Preparation of NiO/ZrO_2

Commercial ZrO_2 (HW NANO, China) was milled at 400 rpm for 1, 5, 10, and 20 h using a planetary ball mill (Tencan XQM-0.4L, China). The phase and crystalline structure of the raw and milled ZrO_2 were characterized by X-ray diffraction (XRD, Ultima IV, Rigaku, Japan) using Cu-kα radiation in the 2θ range 10–80°. The raw and milled ZrO_2 powder was placed in the groove of holder, and then scanning was started.

Milled ZrO_2 and $Ni(CH_3COO)_2 \cdot 4H_2O$ powder were mixed at a constant molar ratio (Ni/Zr = 10%) in ethanolic solution, stirred and subjected to ultrasonication. $Ni(CH_3COO)_2 \cdot 4H_2O$ dissolved in the ethanolic solution, while ZrO_2 remained in a solid-dispersed state. Subsequently, this mixed solution was stirred and heated to 70 ℃ and maintained at this temperature until all the ethanol was evaporated. During the evaporation period, $Ni(CH_3COO)_2 \cdot 4H_2O$ gradually crystallized again and was supported on the ZrO_2 surface, which acted as nucleation sites. This phenomenon represents self-assembly between ZrO_2 and $Ni(CH_3COO)_2 \cdot 4H_2O$. Finally, NiO/ZrO_2 composites were obtained after heating the self-assembly system ($Ni(CH_3COO)_2 \cdot 4H_2O/ZrO_2$) in a furnace in a N_2 atmosphere at 500 ℃ (heating rate of 20 ℃/min and holding time of 5 min) and allowing them to cool naturally in the furnace. For the pyrolysis temperature of 500 °C, according to the previous research [1], the thermal decomposition temperature was about 400 °C. Based on this data, the temperature parameters of preparation of NiO/ZrO_2 were further optimized, so as to guarteen the precursor ($Ni(CH_3COO)_2 \cdot 4H_2O$ completely decomposed, as well as ensure the homogenization and crystallization of NiO particles. Therefore, in this study, the final optimized pyrolysis temperature of 500 °C was directly presented in the experimental part. Other NiO/ZrO_2 composites with different Ni/Zr molar ratios were fabricated using the same process. The schematic illustration of preparation process of NiO/ZrO_2 is shown in Fig. 2-1. Their solid phase and crystal structure were characterized by XRD.

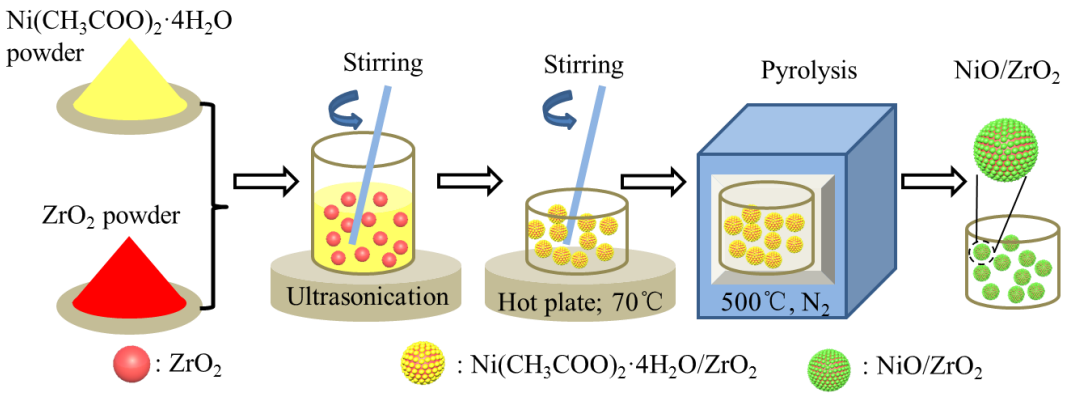

Fig. 2-1 The schematic illustration of preparation process of NiO/ZrO_2.

Temperature programmed desorption–mass spectrometry (TPD-MS) was used to measure the gas generated during the pyrolysis process. TPD measurements were conducted on the BELCAT-II (MicrotracBEL Corp.) instrument. The sample(100 mg), the mixture of ZrO_2 and precursor, was mounted in a quartz reactor, and then heated up to 500 °C at 20 °C/min in the N_2 atmosphere. And the produced gases of pyrolysis were detected with BELMass (MicrotracBEL Corp.) mass spectrometer (MS) instrument. According to the reference [2], the signals at m/e=14, 16, 18, 28, 31, 44, 46, 58 and 60 was related to the ketene (CH_2CO), methane (CH_4), Water (H_2O), carbon monoxide (CO), ethanol(C_2H_5OH), carbon dioxide (CO_2), formic acid(HCOOH), acetone(CH_3COCH_3), and acetic acid(CH_3COOH), respectively.

XPS was used in this study with the aim of analyzing state chemical bonding and elemental composition. The spectrometer was Axis Ultra, Kratos Analytical Company. The base pressure during spectra acquisition was better than 4×10^{-9} achieved by Tubrbo-Molecular Pump. Residual gas analysis revealed that the main background gases in the analysis chamber were N_2. The excitation source was Al Kα and a monochromator was used operated at 150 W. The recorded spectra include core levels. The spectra were acquired sequentially mode. With the selected scan parameters, the energy resolution was 1.0 eV, FWHM of the Ag $3d_{5/2}$. The electron emission angle was 30 °, and the size of the analyzed sample area was about 0.165 mm^2. Complementary work function measurements were performed by UPS with He-I radiation (21.22 eV). The samples were prepared by ball milling-pyrolysis method and stored for two weeks in atmospheric pressure and temperature of 25 ℃ prior to loading into the spectrometer. The transfer procedure within the spectrometer includes exposure to vacuum

level of 5×10^{-8} achived by Tubrbo-Molecular Pump for over night prior to XPS analyses. The charge neutralizer didn't use in all experiments. For the traditional binding energy referencing method, aligning the spectra to the C 1s peak of adventitious carbon was a highly risky procedure and was recently shown to lead to unphysical results [3,4]. G. Greczynski and L. Hultman [5,6] found that the binding energy of C 1s peak E_B^F is closely correlated to the sample work function $\emptyset_{SA}$, such that the sum $E_B^F+\emptyset_{SA}$ is constant. Hence, all binding energies were calibrated by setting the C 1s peak at $289.58-\emptyset_{SA}$. In this study, the measured work function $\emptyset_{SA}$ was 4.62 eV, binding energy of C 1s peak was calibrated at 289.58–4.62= 284.96 eV. The binding energy of each peak was calculated with CasaXPS software.

Transmission electron microscopy TEM (JEOL JEM 2100F) equipped with energy dispersive spectroscopy (EDS) was conducted to observe the defects on the surface of the milled ZrO_2, sample morphology, size and elemental distribution in NiO attached to ZrO_2 surface. Digital Micrograph software was used to obtain the fast Fourier transformed (FFT) diffractogram of HRTEM images. Statistical analysis of NiO nanoparticle size was carried out using Nano Measure Software.

(b) Preparation of NiO/T-ZnO_w

T-ZnO_w was subjected to ultrasonic treatment in an ethanol solution for 10 min to improve its dispersion. Raw $Ni(CH_3COO)_2{\cdot}4H_2O$ powder was manually ground in an agate mortar and then mixed with T-ZnO_w (Ni/Zn molar ratios: 5%, 10%, 20%, and 40%) in an ethanol solutions. After the mixture was ultrasonicated and thoroughly stirred, $Ni(CH_3COO)_2{\cdot}4H_2O$ was dissolved while T-ZnO_w maintained its original state. The mixture was then heated to 70 °C and stirred with a glass rod until the ethanol evaporated. In this process, $Ni(CH_3COO)_2{\cdot}4H_2O$ crystallized on the surface of T-ZnO_w. The self-assembled $Ni(CH_3COO)_2{\cdot}4H_2O$/T-$ZnO_w$ system was heated to 500 °C (heating rate: 20 °C/min, holding time: 5 min) in a furnace with N_2 atmosphere, and then cooled in the furnace, so the NiO/T-ZnO_w was obtained. The phase and crystalline structures of raw and modified T-ZnO_w were characterized using X-ray diffraction (XRD, Ultima IV, Rigaku, Japan). Scanning electron microscopy (SEM, SU-70, Hitachi, Japan) equipped with energy dispersive X-ray spectroscopy (EDS) was used to

observe the morphology, size, and elemental distribution of NiO/T-ZnO_w. The interfacial structure between NiO and T-ZnO_w was investigated using TEM.

2.2.3 In-situ TEM analysis of the formation of NiO/ZrO_2 and NiO/T-ZnO_w

(a) In-situ TEM analysis of the formation of NiO/ZrO_2

In-situ TEM observation using electron beam irradiation was an effective method to explore the mechanism of material synthesis and microstructure transformation [7,8]. On one hand, the irradiation effect of the electron beam increased the temperature of the sample (thermal effect); on the other hand, radiation damage effects were performed [9,10]. There are three main mechanisms of radiation damage, namely: knock-on displacement, radiolysis and electrostatic charging effects. Among them, the latter two mainly effected to poorly conducting samples. Since the $Ni(CH_3COO)_2{\cdot}4H_2O$ belonged to the poorly conducting sample, the main radiation damage mechanisms were radiolysis and electrostatic charging effects. Therefore, in this study, thermal effect, radiolysis, and electrostatic charging effects of electron beam were used to investigate the formation mechanism of NiO/ZrO_2 composites. The mixed solution, consisting of the $Ni(CH_3COO)_2{\cdot}4H_2O$/$ZrO_2$ and ethanol solution, was dropped onto a Cu grid. After the mixed solution drops onto the Cu grid, waited for about 20 minutes. During this period, the alcohol was gradually volatilized and the precursor crystallized on the surface of ZrO_2. And then the Cu grid was loaded into the TEM chamber. The morphologies of composites were observed every 10 min. The schematic illustration of in-situ TEM observation

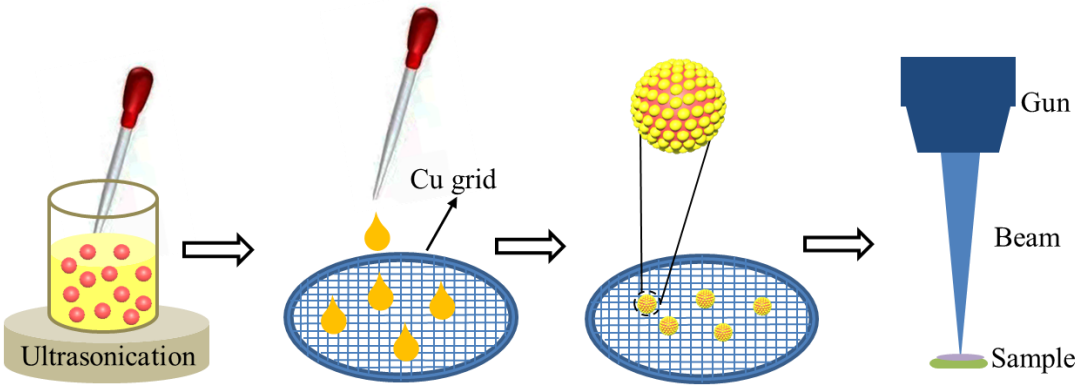

Fig. 2-2 The schematic illustration of in-situ TEM observation

is shown in Fig. 2-2. Digital Micrograph software was used to analysis the HRTEM images. Here, the electron beam is at an accelerated voltage of 200 kV, emission current of 150 μA.

(b) In-situ TEM analysis of the formation of NiO/T-ZnO_w

Similarly, to explore the surface modification mechanism of T-ZnO_w with nano-NiO, in-situ TEM observation based on electron beam irradiation damage was conducted. Here, the TEM was operated at an acceleration voltage of 200 kV. The specific operation program was as follows. A mixed solution containing T-ZnO_w and the precursor was dropped onto the Cu grid, which was then transferred to the TEM chamber. High-resolution TEM images were obtained every 10 min of beam irradiation. Digital Micrograph software was used to analyze the images.

2.3 Morphology of ZrO_2 and NiO/ZrO_2

To observe the morphology of ZrO_2 and NiO/ZrO_2, as well as their crystallographic information, TEM analysis was conducted. Fig. 2-3 shows the TEM, high-resolution TEM (HRTEM) and EDS images of initial ZrO_2 and NiO/ZrO_2. Pristine ZrO_2 particles were either ellipsoidal or polyhedral in shape, with a size range of 30–120 nm (average size of 84 nm), as shown in Fig. 2-3(a). The selected area diffraction (SAED) pattern of area 1 indicated in Fig. 2-3(a) shows the $(1\bar{1}0)$, (012), and (102) planes of ZrO_2 along the $[22\bar{1}]$ axis. Fig. 2-3(b) and (c) show the HRTEM images at areas 2 and 3 indicated in Fig. 2-3(a), and corresponded FFT diffractograms are inserted to the upper right corner of HRTEM images, respectively. In the former, the (012) interplanar spacing was found to be 0.234 nm according to the index of FFT diffractogram, while the latter shows a $(1\bar{1}0)$ interplanar spacing of 0.364 nm. These observations suggest a monoclinic crystal structure phase for ZrO_2, without misaligned or disordered atoms. Fig. 2-3(d) shows a TEM images of the NiO/ZrO_2 (Ni/Zr = 10%) composite; a number of small particles were observed to be attached to the surface of the large sphere. The corresponding higher magnification image in Fig. 2-3(e) shows that these small particles were evenly distributed on the surface; their average particle size was 8.7 nm and most were

spherical in shape, while some were tapered or rod-shaped. In area 4, the (100), (002), and (102) planes of ZrO_2 and NiO were identified, as shown in the SAED pattern in the inset of Fig. 2-3(d). FFT diffractogram inserted to the HRTEM image in Fig. 2-3(f) (of area 5) indicated the ZrO_2 (002) interplanner of 0.262 nm and NiO (101) interplanar spacing of 0.241 nm. The composites structure consisted of small NiO particles attached on a ZrO_2 serving as a carrier. This observation was supported by EDS. Fig. 2-3(g) and (h) show the Ni and Zr distribution by EDS maps, respectively, on the surface of the composite. Fig. 2-3(i) presents an EDS

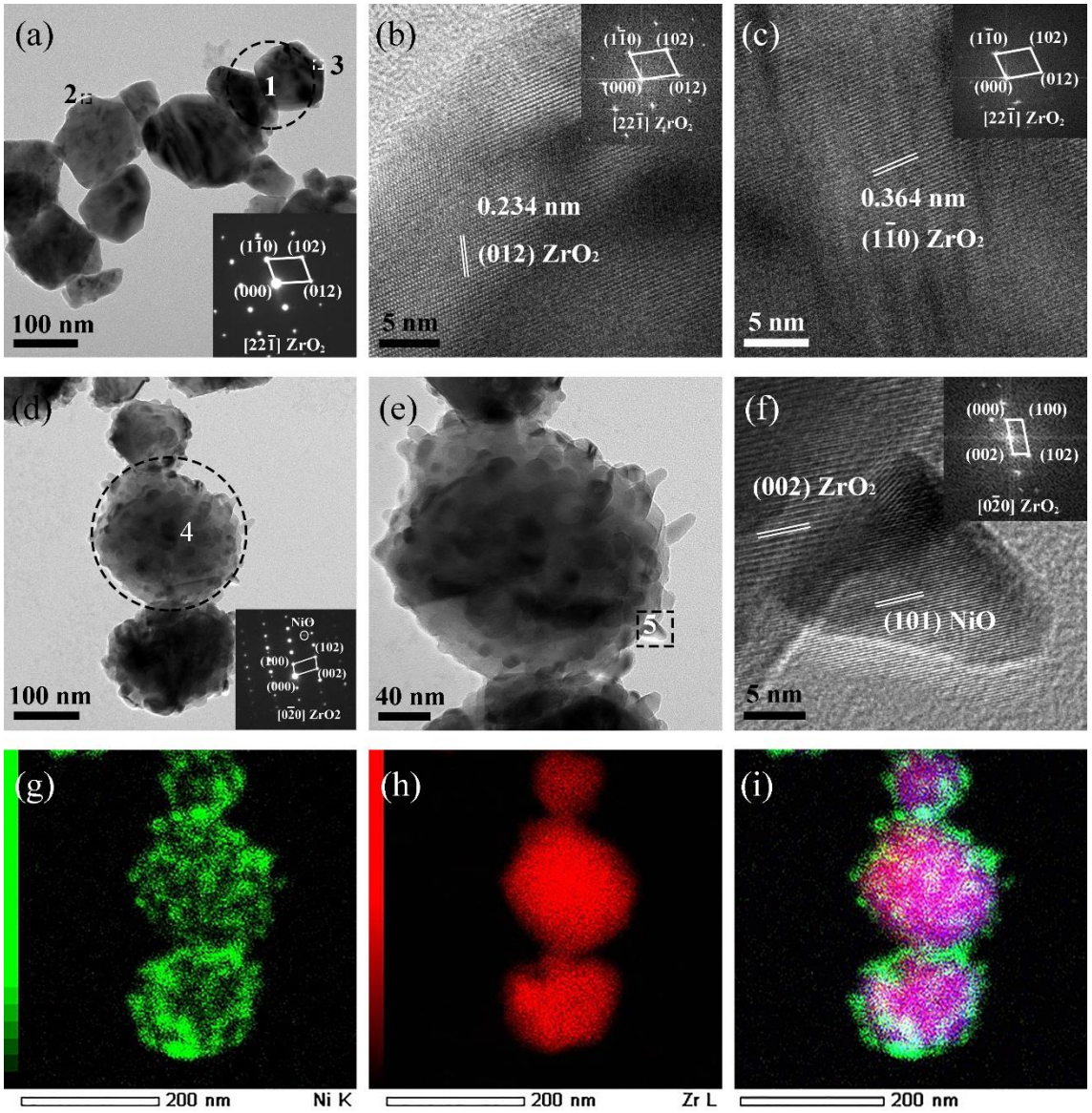

Fig. 2-3 TEM and HRTEM images of ZrO_2 and NiO/ZrO_2. (a)–(c) ZrO_2, (d)–(f) NiO/ZrO_2. EDS maps of (g) Ni, (h) Zr, and (i) their overlay.

overlay of Zr and Ni distributions. These images clearly demonstrate that NiO/ZrO_2 was successfully prepared by the ball milling-pyrolysis method.

Above, I had analyzed the final solid product (NiO/ZrO_2) of pyrolysis of precursor/ZrO_2 by TEM. In order to further systematically investigate the pyrolysis process of precursor/ZrO_2, especially the gas products in the dynamic pyrolysis process, TPD-MS test was conducted. For the TPD-MS system, TPD is acting as a furnace, its function is to thermal decompose the sample by heating, and the function of MS is to detect the composition of these gases. Fig. 2-4 exhibits the TPD-MS analysis of precursor/ZrO_2. Fig. 2-4(a) shows the TPD-MS spectra

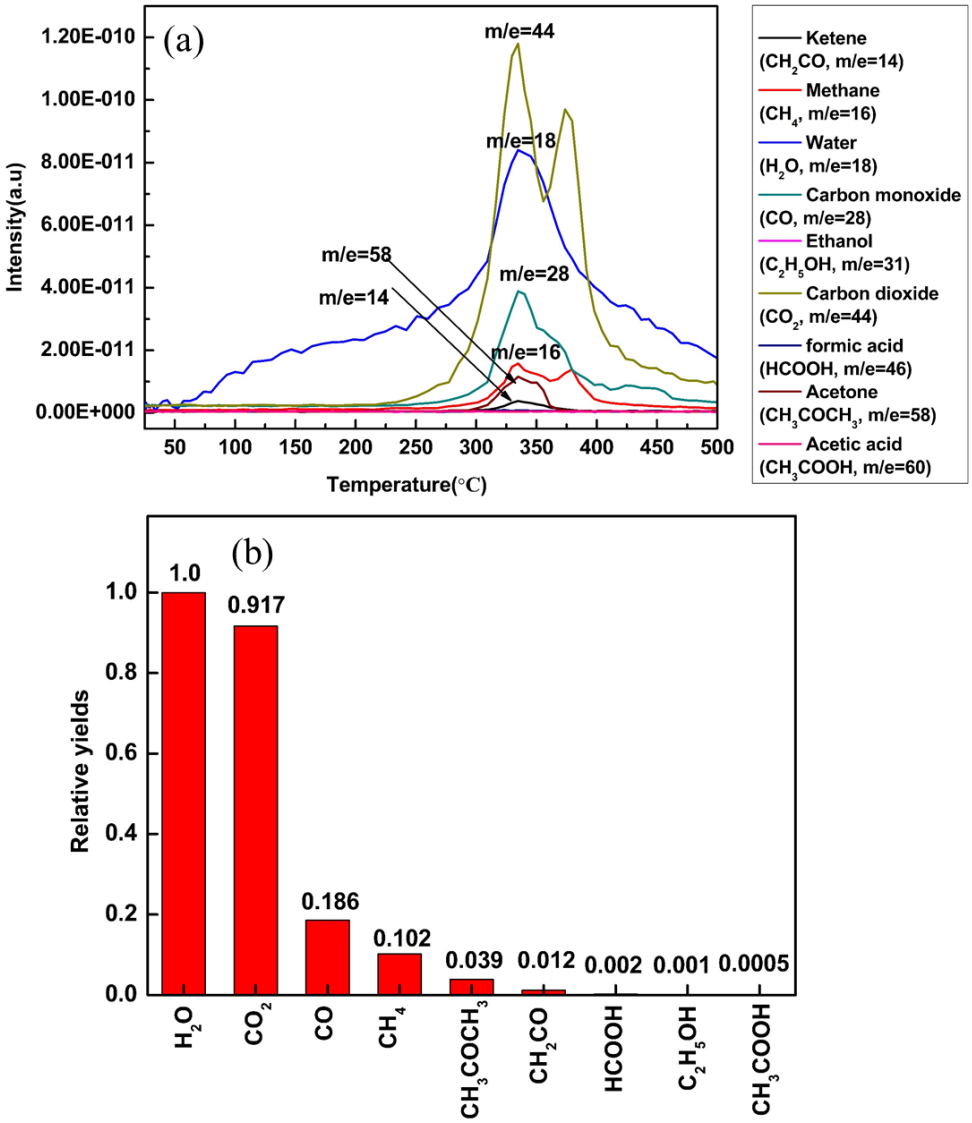

Fig. 2-4 TPD-MS analysis of precursor/ZrO_2. (a) TPD-MS spectra collected during the pyrolysis of the mixture of ZrO_2 and precursor. (b) relative yields of the gases.

collected during the pyrolysis of the mixture of ZrO_2 and precursor. It can be seen that several gases were produced during the pyrolysis process. They are Ketene (CH_2CO, m/e=14), Methane (CH_4, m/e=16), Water (H_2O, m/e=18), Carbon monoxide (CO, m/e=28), Ethanol (C_2H_5OH, m/e=31), Carbon dioxide (CO_2, m/e=44), formic acid (HCOOH, m/e=46), Acetone (CH_3COCH_3, m/e=58), and Acetic acid (CH_3COOH, m/e=60), respectively. Among them, due to the low contents of HCOOH, C_2H_5OH and CH_3COOH, no obvious peaks (m/e=46,31,60) were displayed. On the other hand, it also can be seen that H_2O and CO_2 were the main gases during the pyrolysis process. In addition, in order to assess the relative yields of the gases generated, the relative product yields, based on the calibration of the TPD peak areas after correcting for coincident m/e values and conversion to partial pressures [1], were depicted in Fig. 2-4(b). As can be seen from Fig. 2-4(b), the major gas products were H_2O and CO_2, the minor gas products included CO, CH_4, CH_3COCH_3 and CH_2CO, and the trace gas product included HCOOH, C_2H_5OH, and CH_3COOH.

2.4 Regulation of attachment of NiO on ZrO_2

2.4.1 NiO/ZrO_2 produced at different milling times

In order to determine the phase of milled ZrO_2 and NiO/ZrO_2, and to evaluate the defect density of ZrO_2 milled with different times, XRD tests were carried out. Fig. 2-5 shows the XRD analysis of ZrO_2 and NiO/ZrO_2 milled with different times. From the XRD patterns of Fig. 2-5(a), it was confirmed that ZrO_2 exhibited a monoclinic structure with characteristic plans at (100), (011), ($\bar{1}$10), ($\bar{1}$11), (111), (022), and ($\bar{2}$20); *d* spacing were calculated using Bragg's equation [11] (Eq. (2-1)) to be 0.508, 0.369, 0.364, 0.316, 0.284, 0.185, and 0.182 nm, respectively.

$$2d\sin\theta=n\lambda \quad (2\text{-}1)$$

Here, *d* represents the the interplanar spacing, θ is the diffraction angle, n = 1, and λ is the X-ray wavelength used (0.154056 nm). The d spacing of the ($\bar{1}$10) plane calculated by XRD (0.364 nm) was quite similar to that (0.362 nm) observed in the HRTEM image in Fig. 2-3(c).

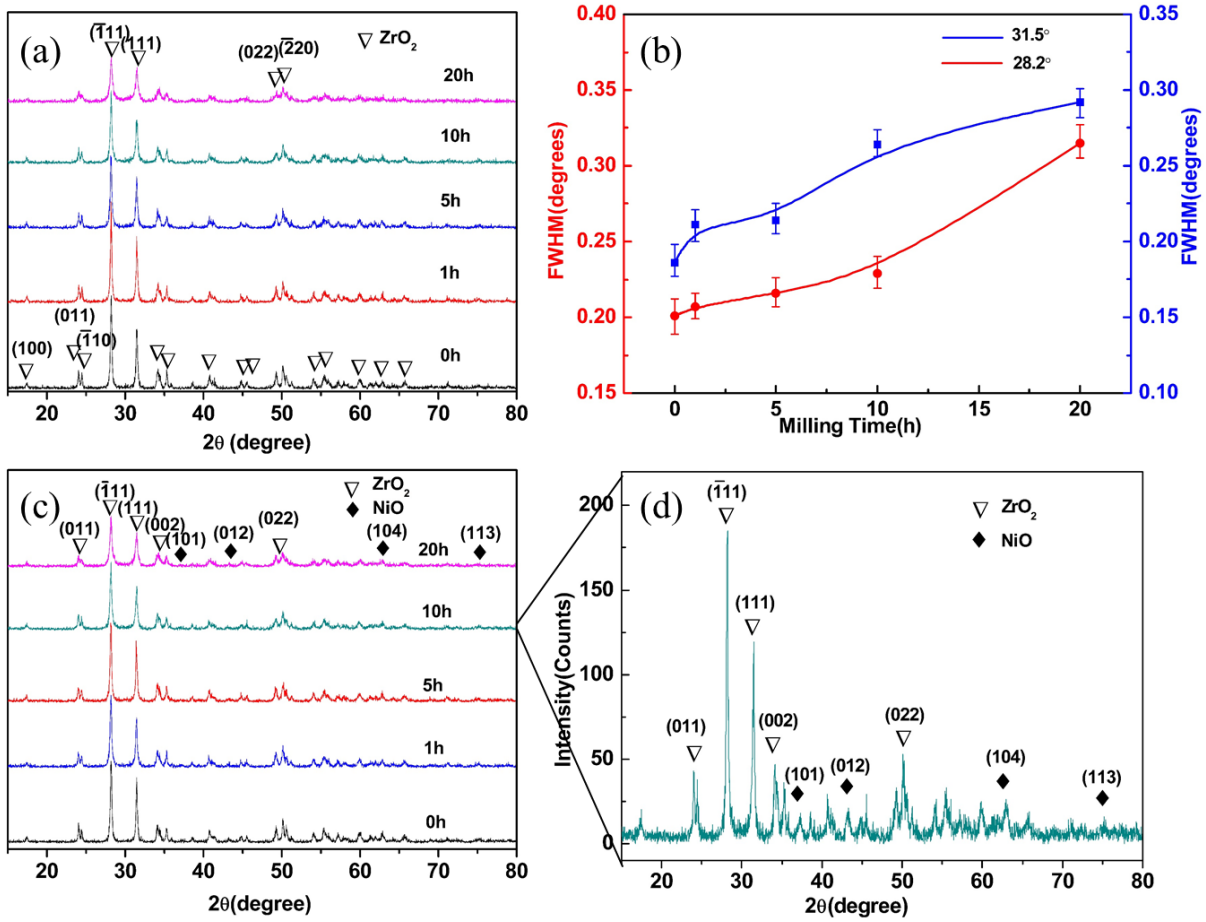

Fig. 2-5 XRD analysis of ZrO_2 and NiO/ZrO_2 milled with different times. (a) XRD patterns of ZrO_2, (b) FWHM of ZrO_2, (c) NiO/ZrO_2 milled for different time periods, and (d) magnified view of NiO/ZrO_2 milled for 10h.

Meanwhile, ZrO_2 samples milled for different durations exhibited similar diffraction peaks (2θ values), indicating that their crystal structure did not change during the ball milling process; however, the full width at half maximum (FWHM) of the characteristic peaks increased with an increase in the milling duration. Fig. 2-5(b) shows the FWHM of two characteristic peaks (28.2° and 31.5°) at different milling times. In the case of the peak at 28.2°, for the milling time of 0 h, the FWHM was 0.201 and this value increased to 0.315 as the milling time was increased. In the case of the peak at 31.5°, although the FWHM values were different compared with peak at 28.2°, they followed a similar trend. Such changes in the FWHM can be attributed to the strain, changes in grain size, and lattice distortion [12]. The relation between grain size and FWHM can be expressed using Scherrer's equation [13]:

$$D = K\lambda/B\cos\theta \qquad (2\text{-}2)$$

where D is the grain size, λ is X-ray wavelength (0.154056 nm), B is the FWHM of the diffraction peak, and θ is the angle of X-ray incidence. The average grain size was calculated using the following relationship:

$$D_{avg} = \frac{\sum_{i=1}^{N} D_i}{N} \tag{2-3}$$

where D_{avg} is the average grain size and N is the number of planes.

According to Eqs. (2-2) and (2-3), the average grain size of pristine ZrO_2 was calculated to be 35.5 nm. At grain size smaller than 100 nm, the peak broadening due to stress is almost negligible when compared to broadening induced by grain size. Morever, the initial ZrO_2 grain size was very small and minimal changes occurred during the ball milling process. This result indicates that the energy of ball milling does not generate strain or reduce the grain size; instead, it introduces lattice distortion to generate defects such as vacancies, dislocations, or stacking faults. The increase in defect density may be attributed to the impacts and friction generated during the ball milling process. These characteristics will be analyzed in detail later in this study.

Fig. 2-5(c) shows the XRD patterns of NiO/ZrO_2 milled for different periods of time. In addition to the characteristic peaks of ZrO_2, new peaks were observed at 37.2°, 43.3°, 62.9°, and 75.3° corresponding to the NiO (101), (012), (104) and (113) crystal planes, respectively, with interplanar distances of 0.241, 0.209, 0.148, and 0.126 nm (according to Eq. (2-1)). Fig. 2-5(d) shows the magnified view of NiO/ZrO_2 milled for 10h, where the peaks of NiO can be observed obviously. This indicates that the final product from pyrolysis of the precursor was NiO.

Fig. 2-6 show the morphologies of NiO/ZrO_2 composites milled for 0–20 h. Although ellipsoidal or spherical NiO particles were attached to ZrO_2 before milling, some exposed ZrO_2 surfaces were observed (Fig. 2-6(a)). Additionally, the attachment density of NiO nanoparticles increased with an increase in the milling time, as shown in Fig. 2-6(b)–(e). This trend can be easily inferred from Table 2-1, which lists the NiO size ranges and their averages corresponding to Fig. 2-6(a)–(e). Without milling, the NiO particle size was 5.0–22.8 nm (average of 13.2 nm). After milling for 1, 5, 10, and 20 h, the average particle size was reduced to 10.3, 9.3, 8.5,

Table 2-1 Size ranges and average sizes of NiO nanoparticles at different ball milling times.

Milling times	0h	1 h	5 h	10 h	20h
Size range (nm)	5.0-22.8	3.7-17.5	4.0-20.6	3.2-13.3	3.9-15.3
Average size (nm)	13.2	10.3	9.3	8.5	8.3

and 8.3 nm, respectively. Statistical analyses (figure inset) also indicated that the size ranges were narrowed; in other words, the sizes of the NiO attached to ZrO_2 tended to become more uniform. The smaller the size of NiO particles, the large the number of nucleation sites on ZrO_2. Therefore, the attached ability of ellipsoidal or spherical NiO nanoparticle to the ZrO_2 was enhanced with an increase of milling time.

Fig. 2-6(f) shows the correlation between the average NiO particle size and ball milling time. Initially, the NiO nanoparticles size decreased sharply with an increase in the ball milling time. Subsequently, the absolute value of the slope of the curve tangent reduced gradually until it was almost zero. This is because the number of active sites on the surface of ZrO_2 gradually increased as ball milling progressed, corresponding the the number of NiO also increased. When the total content of NiO was constant, the size of each NiO was decreased. With the extension of the ball milling time, the final number of activation sits gradually stabilized and they were almost no further changes in the size of NiO. For example, at ball milling times of 10 and 20 h, NiO particle sizes were 8.5 and 8.3 nm, respectively; almost equal. Using the nonlinear curve fit function in the origin software, based on the Allometric1 model, the relationship between the average size of NiO nanoparticles and ball milling time can be obtained as follows:

$$y = \mathrm{K}t^{\mathrm{m}} \tag{2-4}$$

where y is the average particle size (nm), K is a constant, t is the ball milling time (h), and m is the ball milling index.

In the experimental conditions used here, K was 10.310 and m was –0.076. Therefore, the kinetic relationship between the average size of NiO nanoparticles and ball milling time can be described as follows:

$$y = 10.310t^{-0.076} \tag{2-5}$$

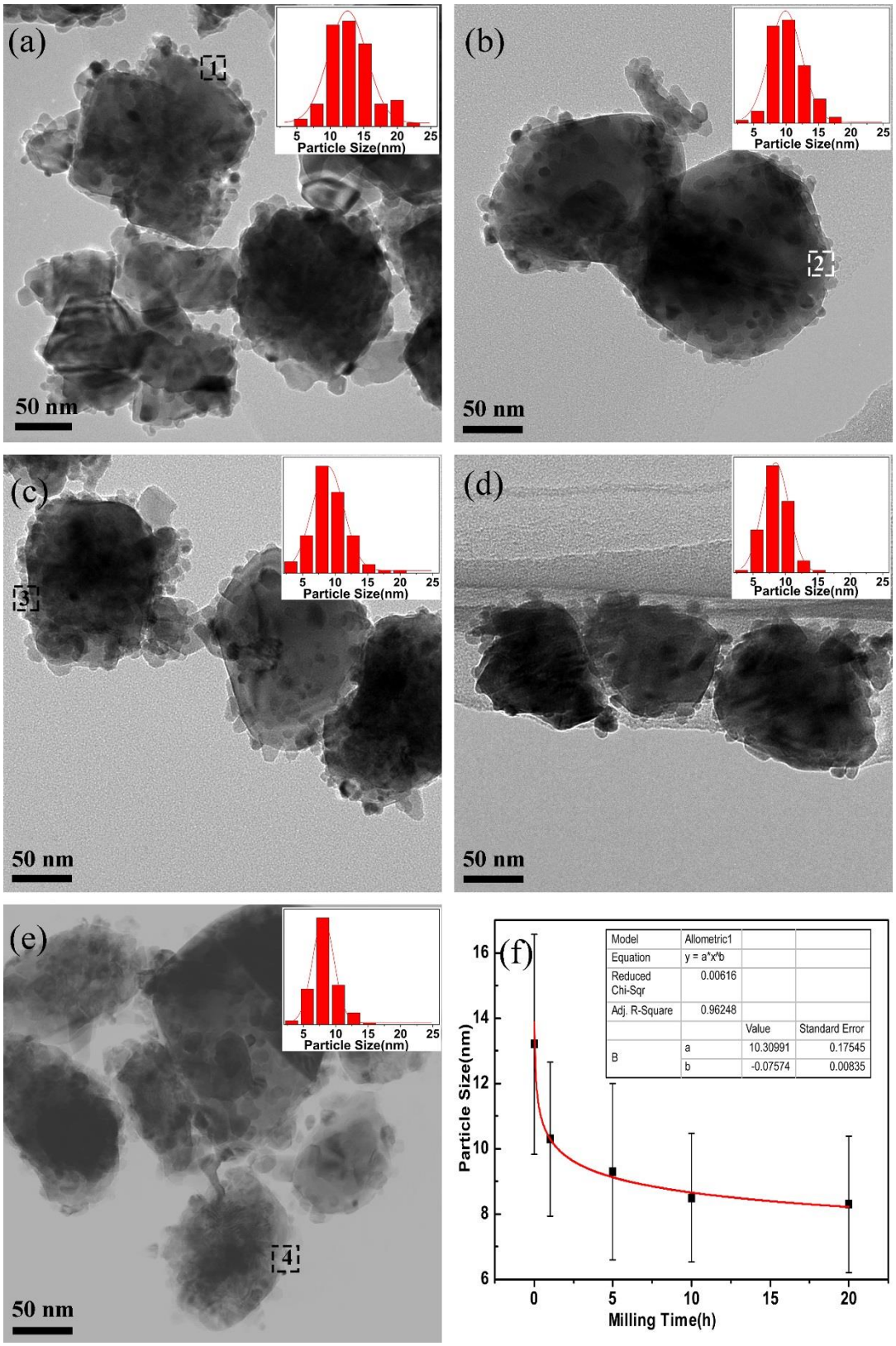

Fig. 2-6 TEM images of NiO/ZrO_2 milled for (a) 0, (b) 1, (c) 5, (d) 10, and (e) 20 h. (f) Fitting kinetic curves of NiO particle size vs. ball milling time.

The above results suggest that milling generates a large number of defects on the surface of ZrO_2, making the materials rough and enabling NiO nanoparticles to be supported on the surfaces. Similar result was mentioned in literature [14].This theory was supported by HRTEM analysis of the defects close to the NiO/ZrO_2interface, Fig. 2-7(a)–(d) show HRTEM of area 1–4, respectively, indicated in Fig. 2-6. As shown in Fig. 2-7(a) (corresponding to area 1 in Fig. 2-6(a)), the NiO/ZrO_2 interface can be divided into three parts; ZrO_2, NiO, and transition zone, denoted as part 1, 2, and 3, respectively. In the ZrO_2 zone, the ZrO_2 lattice was periodically arranged as it was not subjected to any ball milling treatment; further, no atomic misalignment or other defects were present. Thus, this presents normal lattice fringes. In the NiO zone, NiO was arranged on the surface of ZrO_2 in an ellipsoidal or spherical shape. These nanoparticles were arranged next to each other, but the orientation of lattice fringes of adjacent grains was different. The transition zone represents the overlapping region of the lattice fringes of ZrO_2 and NiO. Lattice distortion was introduced due to the differences in lattice fringe spacings and orientations of ZrO_2 and NiO. Therefore, the transition zone can also be called the lattice distortion area. After 1 h of milling (Fig. 2-7(b)), the ZrO_2 carrier exhibited a small number of defects (dislocations and stacking faults) close to the interface with NiO. After 5 h of milling, other types of defect could be observed in Fig. 2-7(c), with ellipsoidal NiO nanoparticles (indicated by dotted circles) attached to the ZrO_2 surface. On the right side of the NiO nanoparticles, ZrO_2 exhibited an irregular atomic arrangement. Inverse FFT image of area 1 in Fig. 2-7(c) was inserted in the bottom right corner, where an atom was found to be missing in this region, indicating the vacancy point defects. After 20 h of milling, a large number of dislocations and stacking faults appeared close to the NiO/ZrO_2 interface (Fig. 2-7(d)). In addition, lattice and atomic distortions were observed. Due to these defects, a local high-energy area was generated during the transformation from $Ni(CH_3COO)_2 \cdot 4H_2O$ to NiO. The high-energy defects zones acted as the activation sites for heterogeneous nucleation, thus enhancing the attachment ability of NiO nanoparticles. Therefore, the attachment ability of NiO on ZrO_2 surface of can be improved by increasing the ball milling time. However, excessive ball milling destroyed the crystalline structure of the nanomaterials leading to an amorphous, as shown in

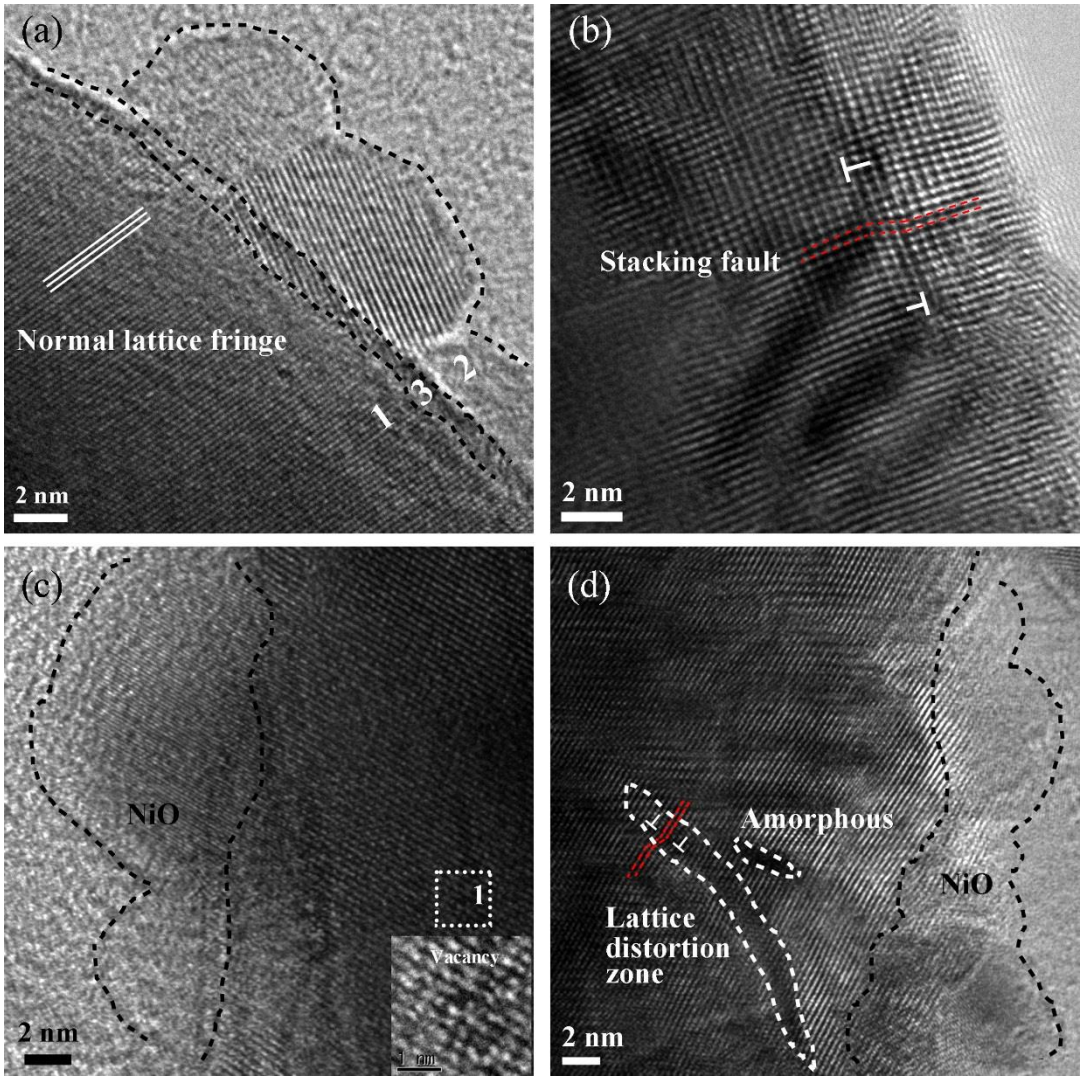

Fig. 2-7 HRTEM images of NiO/ZrO_2 milled for (a) 0, (b) 1, (c) 5, and (d) 20 h.

Fig. 2-7(d). On the one hand, in terms of thermodynamics, the huge energy generated during the ball milling increased the free energy of the ZrO_2. When the free energy of the ZrO_2 crystal phase was higher than that of the amorphous phase, the amorphous transformation was occurred. On the other hand, defects were generated on the surface of ZrO_2 due to the huge impact and friction generated during the ball milling. And as the milling time increased, the defect density also increased, which has been mentioned in Fig. 2-5(b). With the increase of the ball milling time, when the crystal defects cannot withstand the defect stress caused by ball milling, the ZrO_2 lattice system became unstable and collapsed to form amorphous. The typical feature was the disordered arrangement of atoms, which was appeared in Fig. 2-7(d). Furthermore, as the NiO particle size produced after 10 h of milling was quite similar to that

after 20 h. Here I chose a duration of 10 h to prepare NiO/ZrO_2 composites by the ball milling-pyrolysis method.

To better understand why the nucleation sites are formed, the force analysis diagram of planetary ball milling is conducted. Fig. 2-8 (a) and (b) show the force analysis diagram of the planetary ball mill, where the gravity of the ball is smaller than the rest of the force, so it can be ignored. When the ball was in the centrifugal zone (Fig. 2-8 (a)), the centrifugal force generated by the revolution and rotation caused the ball to press against the wall of the cylinder, and it was unlikely to break away from the wall of the cylinder. When the grinding ball attached with the wall of the cylinder turn to the centripetal area, it may be thrown away from the barrel wall, especially the location in Fig. 2-8 (b) has the greatest possibility. Therefore, this position can be used as the critical position for grinding ball detach with the barrel wall to obtain the critical speed.

When the ball is in the position of Fig. 2-8(b) [15]:

$$G_r = mrW_r^2 \tag{2-6}$$

$$G_R = m(R-r)W_R^2 \tag{2-7}$$

$$G_K = 2mrWrW_R \tag{2-8}$$

Where m is the mass of the ball, g, W_R is the angular velocity of revolution, rad, W_r is the angular velocity of rotation, rad, G_r is the centrifugal force caused by rotation, N, G_R is the centrifugal force caused by revolution, N, and G_K is the Coriolis force caused by the combined action of rotation and revolution, N.

If the grinding ball is separated from the cylinder wall at this position, $G_R+G_K \geq G_r$ must

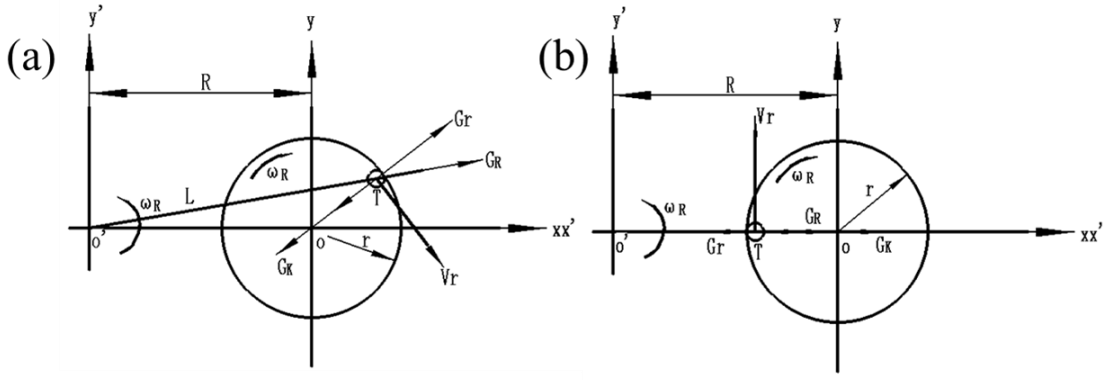

Fig. 2-8 Force analysis diagram of the planetary ball mill. (a) Centrifugal zone, (b) Centripetal zone.

be satisfied, that is

$$m(R-r)W_R^2+2mrW_RW_r \geq mrW_r^2 \quad (2\text{-}9)$$

When Eq. (2-9) is taken"="

$$\Rightarrow W_r=[\pm (R/r)0.5 -1]W_R \quad (2\text{-}10)$$

Eq. (2-10) shows the critical condition for the grinding ball to be separated from the wall of the cylinder.

The XQM-0.4Lplanetary ball mill instrument was used in this experiment, R=75 mm, r=25 mm. Substituting into Eq. (2-10), I get $W_{critical} = W_r = 2.73\ W_R$.

When the rotation angular velocity is 2.73 times the revolution angular velocity, the grinding ball will not leave the cylinder wall. The designed ratio of the rotation angular velocity to the revolution angular velocity of the planetary ball mill used in the experiment is 2: 1, which is less than 2.73. Therefore, there are two movement states of the grinding ball during the ball grinding process: one is the rotation movement state around the cylinder wall, and the other is the falling movement state when it is separated from the cylinder wall. While in the motion state of rotating around the cylinder wall, there is friction between particles or between particles and balls, which makes the surface of the particles crush, that is, friction crushing. While in the falling motion state of the grinding ball, due to the separation from the cylinder wall, shearing and impact of the grinding ball on the ZrO_2 particles was conducted, which called impact compression crushing. In the process of ball milling, ZrO_2 was not only subjected to friction from particles or between particles and balls, but also by the shearing and impact of the grinding balls. Then, the periodic arrangement of local atoms is changed, resulting in a large number of defects such as vacancies, dislocations and stacking fault (as shown in Fig. 2-7).

2.4.2 NiO/ZrO_2 produced with different Ni/Zr ratios

In section 2.4.1, I had demonstrated the effect of ball milling time on the attached ability of NiO on ZrO_2, and defined the 10 h was the best ball milling time. However, the effect of Ni/Zr ratio on the microstructures of NiO/ZrO_2 composite powder was not understood. Based on this, after ZrO_2 milled for 10 h, NiO/ZrO_2 composites with varying Ni/Zr molar ratios were examined by XRD and TEM.

Fig. 2-9 shows the XRD patterns of NiO/ZrO_2 with varying Ni/Zr molar ratios. The phases present in NiO and ZrO_2 were independent of the Ni/Zr ratio, indicating that the final pyrolysis products of the mixture (ZrO_2 and precursor) were NiO and ZrO_2. The intensities of the peaks at 37.2°, 43.3°, and 62.9° corresponding to the (101), (012), and (104) of NiO increased as the Ni/Zr ratio increased.

The surface morphologies of NiO/ZrO_2 composites produced with different molar Ni/Zr ratio are shown in Fig. 2-10. At 5% Ni/Zr ratio (Fig. 2-10(a)), most of the surface of ZrO_2 was bare because of the low NiO content. In Fig. 2-10(b) and (c) (5% Ni/Zr and 10% Ni/Zr, respectively), the NiO particles on the ZrO_2 surface gradually became larger and denser. At a Ni/Zr ratio of 40%, considerably dense NiO particles were distributed on ZrO_2. Such high density led to the formation of two layers of NiO (lower circle) and NiO agglomeration (upper circle) on the ZrO_2 carrier, as shown in Fig. 2-10(d). The size ranges and average size of NiO in Fig. 2-10(a)–(d) are summarized in Table 2-2. The average NiO particle size increased from 5.9 nm at a Ni/Zr ratio of 5% to 8.2 nm a 10% Ni/Zr ratio. When the Ni/Zr ratio was further increased to 20%, the particle size was just 1 nm larger than that of 10%. However, when the Ni/Zr ratio reached 40%, the size increased significantly. This is likely because almost the nucleation sites on the surface of the ZrO_2 were exhausted. At the same milling time of 10 h, the number of nucleation sites was constant. When the Ni/Zr ratios were between 5%–20%, a sufficient number of nucleation sites were present for NiO nucleation. Therefore, even when the NiO content was doubled, the particle size did not increase significantly. However, when

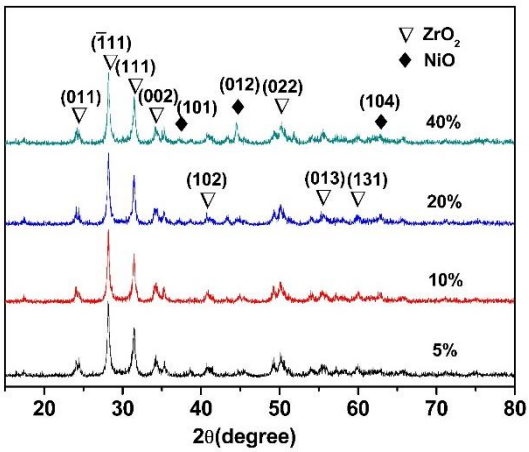

Fig. 2-9 XRD patterns of NiO/ZrO_2 with different Ni/Zr molar ratios.

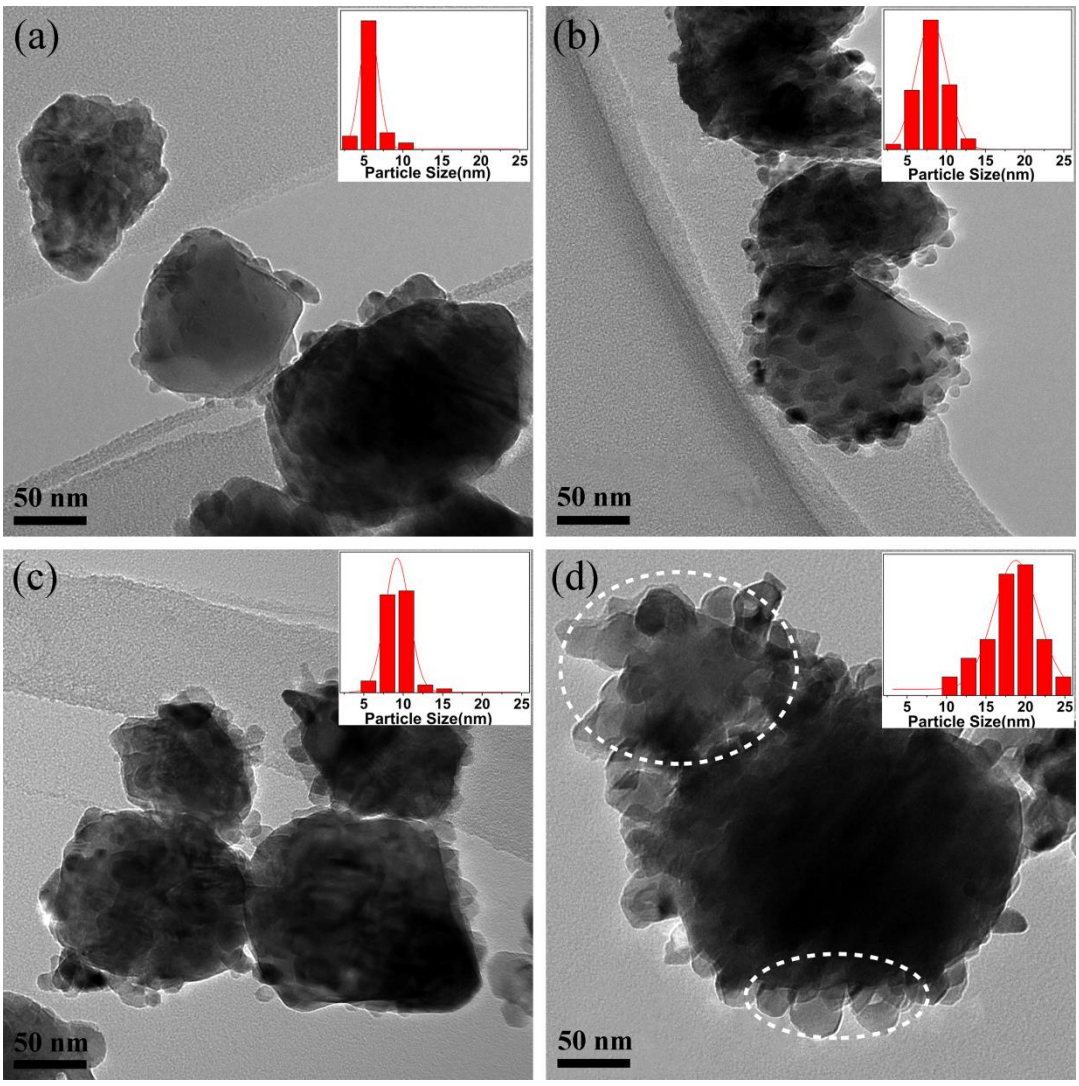

Fig. 2-10 TEM images of NiO/ZrO_2 with Ni/Zr molar ratios of (a) 5%, (b) 10%, (c) 20%, and (d) 40%.

Table 2-2 Size ranges and average particle sizes of NiO with different Ni/Zr molar ratios

Ni/Zr ratios	5 %	10 %	20 %	40 %
Size range (nm)	1.1-10.6	4.0-12.1	5.6-14.1	9.7-28.9
Average size (nm)	5.9	8.2	9.2	18.7

most of the activation sites on ZrO_2 were exhaust, which means the surface of ZrO_2 was almost completely covered. Continue to increase the content of NiO, the volume of a single NiO increased significantly, corresponding the size of NiO nanoparticles increased obviously.

To further evaluate the cover degree of NiO to ZrO_2, the coverage rate of NiO to ZrO_2 were measured. At 5% Ni/Zr (Fig. 2-10(a)), the coverage rate was 54.1%. With the increase the Ni/Zr molar ratio, the coverage rate gradually increased. when the Ni/Zr molar ratio reached

10% (Fig. 2-10(b)), the coverage rate was 80.4%. At 20% Ni/Zr (Fig. 2-10(c)), ZrO_2 were fully cover with NiO (coverage rate almost was 100%), and the NiO size didn't increase significantly. However, when the Ni/Zr molar ratio reached 40%, ZrO_2 were completely covered by NiO, but the NiO size was dramatically increased, and agglomeration was occurred, shown in Fig. 2-10(d).

Fig. 2-11 presents the TEM and corresponded EDS images of NiO/ZrO_2 with 20% Ni/Zr molar ratio. Fig. 2-11(a) exhibit the TEM image of NiO/ZrO_2 with 20% Ni/Zr molar ratio. Fig. 2-11(b) and (c) show the Ni and Zr EDS maps, respectively, of NiO/ZrO_2 composites with the Ni/Zr molar ratio of 20 %. From the overlay of the Ni and Zr EDS maps in Fig. 2-11(d), it can be observed that the carrier surface was almost completely covered by the Ni-based compounds. This implies that Ni-based compounds started to aggregate at a Ni/Zr ratio beyond 20 %. That was the reason why 40% Ni/Zr ratio had much larger NiO particle sizes.

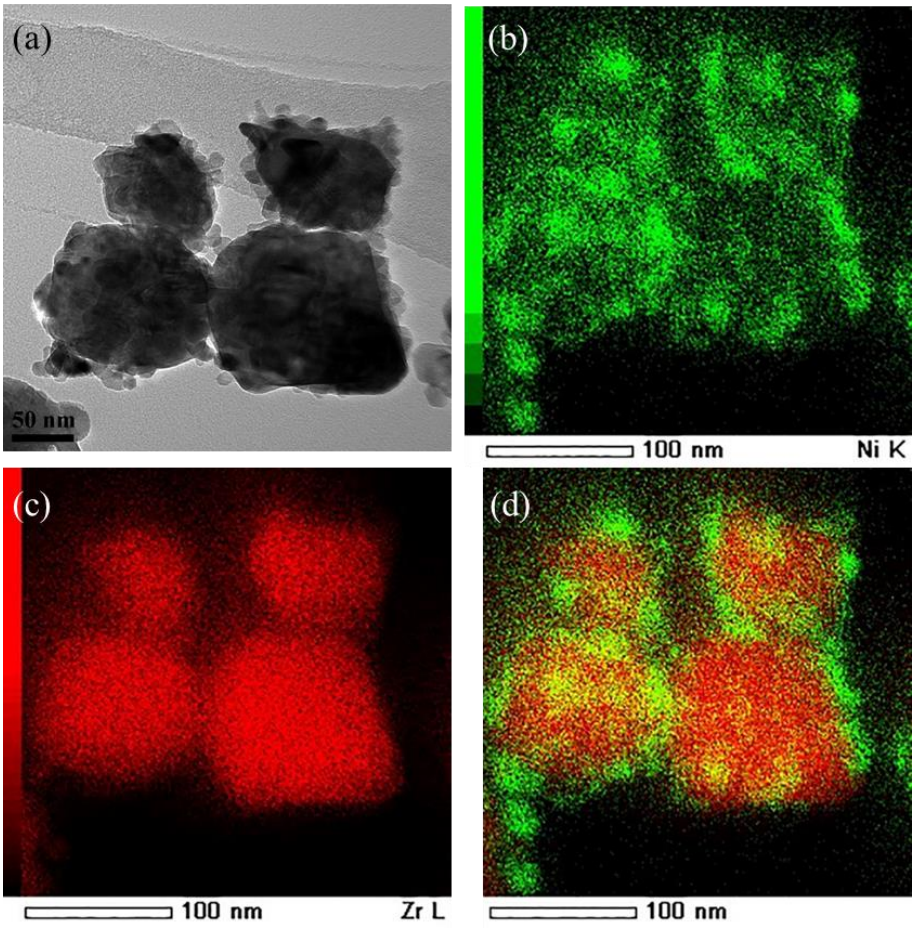

Fig. 2-11 TEM and corresponded EDS images of NiO/ZrO_2 with 20% Ni/Zr molar ratio. (a) TEM image. EDS of (b) Ni, (c) Zr, and (c) overlay of (b) and (c).

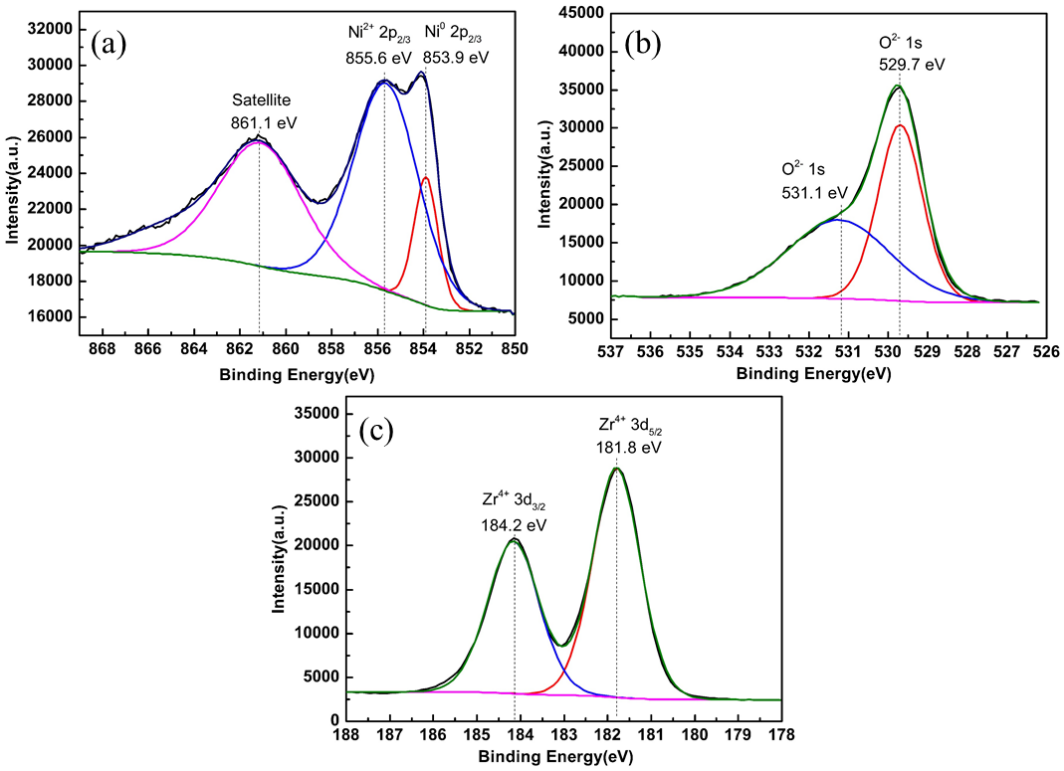

Fig. 2-12 XPS spectrum of NiO/ZrO_2 nanocomposite. (a) Ni 2p, (b) O 1s, and (c) Zr 3d.

To further study the surface composition and valence states of NiO/ZrO_2 nanocomposite (Ni/Zr ratio was 20 %), XPS analysis was carried out, and the results were shown in Fig. 2-12. Fig. 2-12(a) shows the high resolution scans of Ni 2p peak, it can be fitted into four peaks. The peaks at 853.89 eV and 855.57 eV corresponded to the Ni-O bond and surface states of NiO [16]. The peaks at 860.99 eV and 864.47 eV can be assigned to the satellite peaks of NiO [17,18]. The result was consistent with the XRD result in Fig. 2-9. Fig. 2-12(b) shows the high resolution scans of the O1s peak for NiO/ZrO_2 nanocomposite. It can be separated into two peaks. The peak at 531.66 eV attributed to the surface adsorbed oxygen (O_α); the peak at 529.71 eV was the lattice oxygen (O_β) [19,20]. High resolution scans of the Zr 3d peaks were shown in Fig. 2-12(c), characteristic peaks appeared at 181.90 eV (Zr $3d_{5/2}$) and 184.27 eV (Zr $3d_{3/2}$) indicated that the valence of zirconium was +4. The results were in agreement with the reported for ZrO_2 [21].

Finally, XRD, TEM, EDS and XPS analyses indicated that I successfully fabricated composites composed of ZrO_2 with dense NiO present. As demonstrated in section 2.4.1 and

section 2.4.2, the morphologies of NiO/ZrO_2 composites can be regulated by controlling ball milling time and the Ni/Zr molar ratio.

2.5 Calculation of the interfacial mismatch between NiO and ZrO_2

In this study, NiO/ZrO_2 composites were obtained using ball milling-pyrolysis method. It is well known that in a composite, the interface of composite materials is critical. Therefore, I studied the interface binding ability of the prepared NiO/ZrO_2 composites to evaluate their application potential. In this section, typical interfaces between NiO and ZrO_2 were analyzed using HRTEM.

Fig. 2-13 shows the HRTEM images of the typical ZrO_2/NiO interfaces. The ZrO_2/NiO interface in Fig. 2-13(a) can be assigned to the $ZrO_2(012)$/NiO(101) interface, where $d_{ZrO2(012)}$=0.234 nm and $d_{NiO(101)}$=0.241nm. There presented a lattice distortion zone at the junction of the two surfaces, a similar phenomenon also observed in Fig. 2-7(a). According to the mismatch Eq. (2-11),

$$\varepsilon=(d_\alpha-d_\beta)/d_\alpha \tag{2-11}$$

where ε is the mismatch between the two interfaces, d_α is the interplanar spacing of interface α (nm), d_β is the interplanar spacing of interface β, (nm). According to the literature [22], an interface is considered coherent if $\varepsilon < 0.05$, semi-coherent if $\varepsilon = 0.05–0.25$, and incoherent if $\varepsilon > 0.25$.

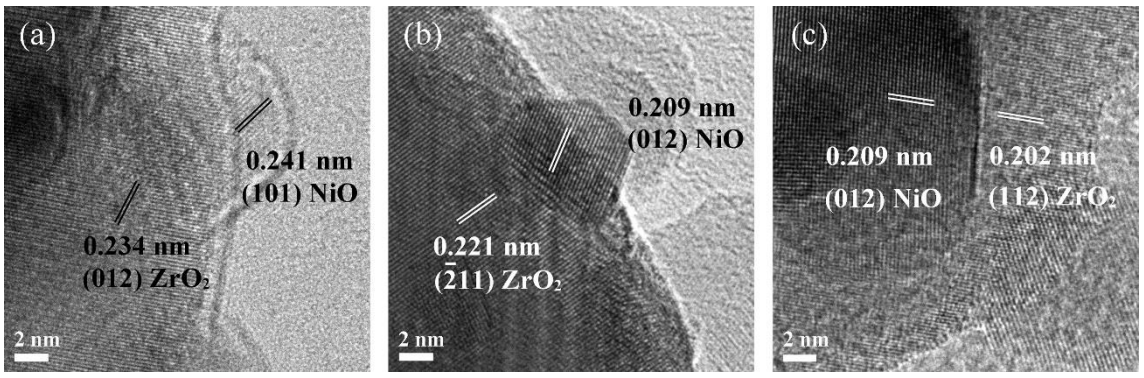

Fig. 2-13 HRTEM images of the (a) $ZrO_2(012)$/NiO(101), (b) $ZrO_2(\bar{2}11)$/NiO(012) and (c) $ZrO_2(112)$/NiO(012) interfaces.

The value of ε of ZrO_2(012)/NiO(101) interface was 0.029, lower than 0.25; this implies that the interface is coherent. The lower the value of mismatch, the stronger the binding between the two interfaces. The ZrO_2/NiO interface in Fig. 2-13(b) can be assigned to the $ZrO_2(\bar{2}11)$/NiO(012) interface, where $d_{ZrO2(\bar{2}11)}$ = 0.221nm and $d_{NiO(012)}$ = 0.209nm. Using Eq. (2-11), ε was calculated to be 0.054, indicating that this interface belongs to a semi-coherent interface. The ZrO_2/NiO interface in Fig. 2-13(c) can be assigned to the ZrO_2(112)/NiO(012) interface, where $d_{ZrO2(112)}$ = 0.202 nm and $d_{NiO(012)}$ = 0.209 nm. Eq. (2-11) was used to calculated ε = 0.033, which is less than 0.05. This result indicates that this interface is coherent.

In summary, interfacial mismatch value was found to be 0.029–0.054, indicating the semi-coherent and coherent interfaces, which indicated the good combination between NiO and ZrO_2.

2.6 In-situ TEM observation of the formation of NiO/ZrO_2

In-situ TEM observation, the thermal effect, radiolysis, and electrostatic charging effects of electron beam facilitated the decomposition of precursor, was conducted to explore the mechanisms of the NiO/ZrO_2 composite formation. Fig. 2-14 shows the TEM and HRTEM images of the transformation from precursor/ZrO_2 to NiO/ZrO_2 at different irradiation times. Fig. 2-14 (a) shows the TEM image of the self-assembled precursor/ZrO_2. As the surface of ZrO_2 was covered with the precursor, the original morphology of ZrO_2 could not be determined; in this case, the self-assemble system of precursor and ZrO_2 was approximately quadrilateral in shape. There were several semicirclar and ellip particles attached to the edge of the quadrilateral. Self-assembly refers to a technique in which basic structural units (such as molecules, nanomaterials, or materials on a micrometer or larger scale) spontaneously form an ordered structure. In this process, the structural units spontaneously organize or gather through non-covalent interaction to form a stable structure with a certain geometric shape [23,24]. In this study, I used a templated self-assembly mode, in which ZrO_2 acted as the template, and the precursor was automatically adsorbed on the surface of ZrO_2 during the evaporation process. Due to the mutual mobility of the precursors, driven by the minimization of thermodynamic energy, ZrO_2 was uniformly coated with the precursor. Fig. 2-14(b) shows the TEM image of

the self-assembled system irradiated for 10 min. While there was minimal change in the overall shape, but some particles at the edge (indicated by the dotted frame) transformed into smaller particles, which indicates that the precursor starts to decompose. With the increase of the irradiation time, some interesting phenomena occurred when the irradiation reached 30 min (Fig. 2-14(d)). The primary split particles (particles undergoing decomposition) did not continue to split. On the contrary, they grew and merged to new particles. At an irradiation time of 40 min (Fig. 2-14(e)), the particles that previously merged, once again began to split into smaller particles. At 50 min (Fig. 2-14(f)), the small particles in Fig. 2-14(e) merged into larger particles. At this moment, the overall contour of the self-assembled system changed; the four corners of the initial quadrilateral gradually disappeared, which may be a result of the gradual decomposition of the precursor. When the irradiation time was 60–90 min (Fig. 2-14(g) and (h)), the particles began to merge with their neighbors and further growth occurred.

To analyze the pyrolysis process and monitor the phase evolution during irradiation, the corresponding HRTEM observation was also conducted. When the irradiation time was 0 min (Fig. 2-14(i)), many nanoparticles were attached to the edge; their lattice fringe spacings were 0.225, 0.254, and 0.268 nm, corresponding to the (330), (041), and (221) planes of $Ni(CH_3COO)_2{\cdot}4H_2O$, respectively, which indicated that the precursor was indeed $Ni(CH_3COO)_2{\cdot}4H_2O$. When the irradiation time was 10 min (Fig. 2-14(j)), the (041) plane of $Ni(CH_3COO)_2{\cdot}4H_2O$ began to decompose into two nanoparticles, exhibiting the same interplanar spacing but different orientations.

According to the literature [1,25], the main pyrolysis reaction of $Ni(CH_3COO)_2{\cdot}4H_2O$ can be described as follows.

$$Ni(CH_3COO)_2{\cdot}4H_2O \rightarrow 0.86Ni(CH_3COO)_2{\cdot}0.14Ni(OH)_2+0.28CH_3COOH+3.72H_2O \quad (2\text{-}12)$$

$$Ni(CH_3COO)_2 \rightarrow NiCO_3+CH_3COCH_3 \quad (2\text{-}13)$$

$$NiCO_3 \rightarrow NiO+CO_2 \quad (2\text{-}14)$$

$$Ni(OH)_2 \rightarrow NiO+H_2O \quad (2\text{-}15)$$

It can be seen from the Eqs. (2-12)-(2-15) that in the initial stage, the $Ni(CH_3COO)_2{\cdot}4H_2O$ precursor decomposed into $Ni(CH_3COO)_2$, $Ni(OH)_2$, CH_3COOH, and H_2O upon the electron

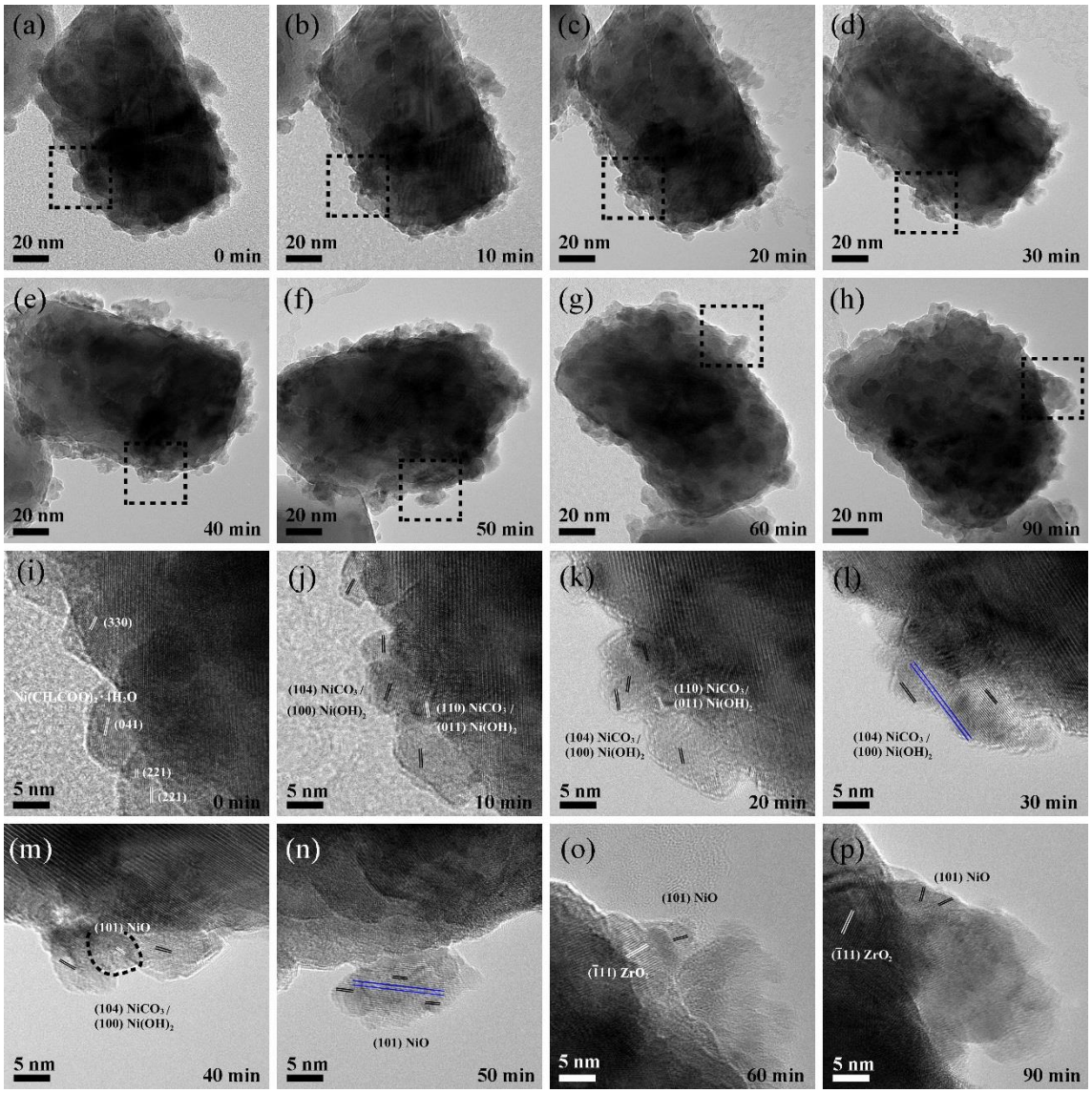

Fig. 2-14 In-situ TEM observation of transformation from precursor/ZrO_2 to NiO/ZrO_2. (a)–(h) TEM and (i)–(p) HRTEM images of the precursor/ZrO_2 transformed into NiO/ZrO_2 at different irradiation times (0–90 min). The HRTEM images correspond to areas indicated by the dotted line in (a)–(h).

beam irradiation; CH_3COOH and H_2O were pumped away from the chamber by the vacuum system of TEM. In the second stage, $Ni(CH_3COO)_2$ rapidly decomposed into $NiCO_3$ and other gaseous species upon continuous irradiation. Therefore, at the end of the second stage, the remaining products were $NiCO_3$ or $Ni(OH)_2$ or a mixture of these. When the irradiation time was 10 min (Fig. 2-14(j)), the lattice fringe spacing of the decomposition product was 0.272 nm, which can be assigned to $NiCO_3$ (104), $Ni(OH)_2$ (100), or the mixture of these ($NiCO_3$(104)/$Ni(OH)_2$(100)). However, in this study, our focus is on the final pyrolysis product

NiO and its formation on the ZrO_2 surface. Combining Eqs. (2-14)−(2-15), whether it was $NiCO_3$ or $Ni(OH)_2$, they are intermediate products in the pyrolysis process, so they were collectively referred to as intermediate products $NiCO_3/Ni(OH)_2$. In other words, after irradiation for 10 min, the $Ni(CH_3COO)_2{\cdot}4H_2O$ (041) plane evolved to intermediate products $NiCO_3$(104)/$Ni(OH)_2$(100) plane. Similarly, $Ni(CH_3COO)_2{\cdot}4H_2O$(221) plane transformed into the intermediate products $NiCO_3$(104)/$Ni(OH)_2$(100) and $NiCO_3$(110)/$Ni(OH)_2$(011) planes.

When the irradiation time was increased to 20 min (Fig. 2-14(k)), although there was no phase transition, the particle size of the intermediate product $NiCO_3$(104)/$Ni(OH)_2$(100) increased and the particles were in close proximity, In the process, the orientation of adjacent grains was also constantly adjusting itself. Additionally, the $NiCO_3$(110)/$Ni(OH)_2$(011) grains at the middle were squeezed away by the $NiCO_3$(104)/$Ni(OH)_2$(100) grains on top and bottom sides. This may be because grain boundaries with the same plane were easier to migrate. When the irradiation time increased to 30 min (Fig. 2-14(l)), several small particles on the upper side merged into one grain that once again merged with the particles on the lower side to form one grain. The parallel blue lines show that they have the same orientation, indicating that they have merged into one grain. With the further increase in the irradiate time to 40 min (Fig. 2-14(m)), $NiCO_3$(104)/$Ni(OH)_2$(100), which merged into large particles, started to decompose into small particles again. The decomposition process was initiated at the concave position in the middle of grain. There was a tip at this position, which acted as a high-energy area, and hence it was the first to undergo decomposition during irradiation. The interplanar spacing of this small particle in the middle was 0.241 nm, corresponding to NiO (101), indicating that the intermediate product began to decompose into NiO. At 50 min irradiation (Fig. 2-14(n)), the intermediate product completely transformed into NiO and merged into a large grain after the grain orientation adjustment. At 60 min irradiation (Fig. 2-14(o)), the combined large grain NiO in Fig. 2-14(n) started to approach and merge with adjacent grains, but no phase transformation occurred. Furthermore, some ZrO_2 surfaces were observed on the left, with a lattice fringe spacing of 0.316 nm (ZrO_2 ($\bar{1}11$)). At 90 min irradiation (Fig. 2-14(p)), there was

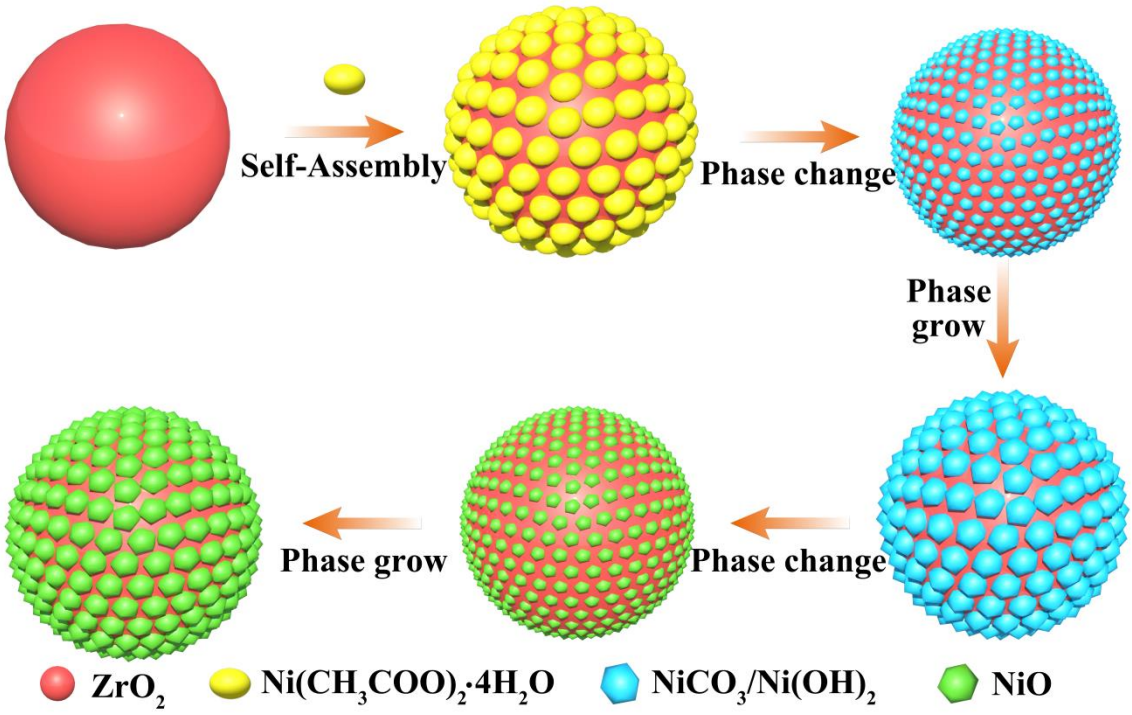

Fig. 2-15 Schematic illustration of evolution from precursor/ZrO_2 to NiO/ZrO_2 composite by milling-pyrolysis method.

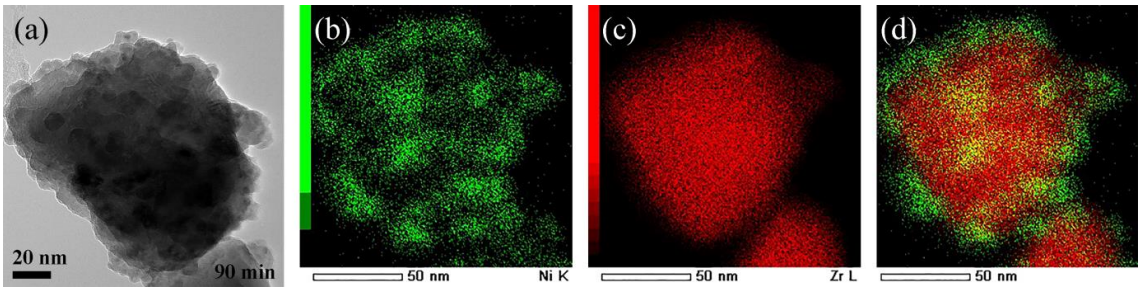

Fig. 2-16 TEM and EDS images of the NiO/ZrO_2 composite subjected to 90min of irradiation. (a) TEM image, EDS maps of (b) Ni, (c) Zr, and (d) the overlay of (b) and (c).

no other change except for continuous merging between NiO and other grains. The final decomposition product was NiO. Similar evolutions also occurred in other locations in Fig. 2-14(a). Therefore, the evolution map of the composite product by milling-pyrolysis method can be charted in Fig. 2-15. Firstly, $Ni(CH_3COO)_2{\cdot}4H_2O$ precursor was attached to the ZrO_2 nanoparticles forming the precursor/ZrO_2 system through self-assembly. Secondly, the precursor was decomposed into intermediate product $NiCO_3/Ni(OH)_2$ under electron beam irradiation. Thirdly, with continuous irradiation, these intermediate products merged, grew at the ZrO_2 surface, but no phase change occurred. Fourthly, intermediate product decomposed

into the final product NiO. Finally, no phase changed, but NiO particles merged and grew gradually.

Fig. 2-16 shows the TEM and EDS images of the NiO/ZrO_2 composite subjected to 90min of irradiation. Ni element was found to be evenly distributed around Zr. Together, these results suggest that the final NiO product was uniformly and densely attached to the surface of ZrO_2 yield a NiO/ZrO_2 composite.

2.7 Morphology of raw T-ZnO_w and NiO/ZnO_w

Fig. 2-17 shows the XRD patterns of raw T-ZnO_w and modified T-ZnO_w. The pattern of raw T-ZnO_w (downside with black color) exhibited sharp characteristic peaks at 31.8°, 34.4°, 36.3°, 47.5°, 56.6°, 62.8°, 66.4°, 68.0°, and 69.1°, corresponding to the ZnO (100), (002), (101), (102), (110), (103), (200), (112), and (201) planes of monoclinic crystalline structure, respectively. The pattern of modified T-ZnO_w (upside with red color) showed not only the characteristic peaks of ZnO, but also two new peaks observed at 37.2° and 43.3°, corresponding to the NiO (101) and (012) planes, respectively. In addition, the characteristic peak of NiO (104) at 62.9° was not evident because it overlapped with that of ZnO (103) at 62.8°.

Fig. 2-18 shows the SEM images of raw T-ZnO_w and NiO/T-ZnO_w. In the three-dimensional structure of raw T-ZnO_w (Fig. 2-18(a)), the length of the whisker needles was 5–20 μm, and their diameter was in the range of 0.5–2 μm. In addition, nanotips were observed at the top of the whisker needles. The EDS result for area A in Fig. 2-18(a) are presented in

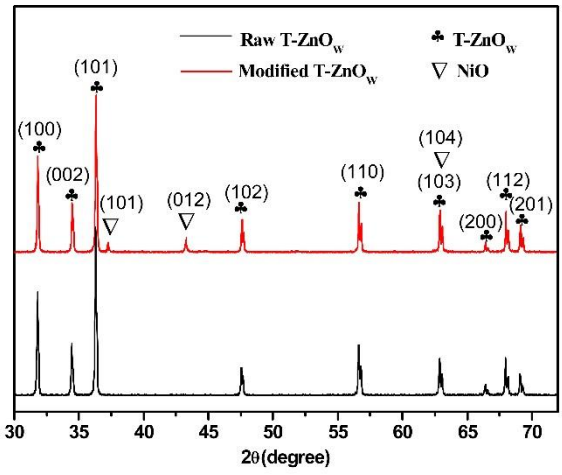

Fig. 2-17 XRD patterns of raw T-ZnO_w and modified T-ZnO_w.

Table 2-3. Zn and O were detected, which is consistent with the XRD results shown in Fig. 2-17. Fig. 2-18(b), which is a magnified view of Fig. 2-18(a), indicates that the surface was smooth and clean without attached impurities. In the modified T-ZnO_w (Fig. 2-18(c)), the special spatial structure of the whisker was maintained except for the broken nanotips, suggesting that our modification method caused little damage to the original material. The high magnification view (Fig. 2-18(d)) shows that many nano-sized particles were uniformly attached to the T-ZnO_w surface. The EDS results for area B in Fig. 2-18(c) are also presented in Table 2-3. Zn, Ni, and O were detected. The combined EDS results in Table 2-3 and the XRD patterns in Fig. 2-17 suggest that these nano-sized particles were NiO. Therefore, NiO was successfully coated on T-ZnO_w.

Table 2-3 EDS results for raw T-ZnO_w and NiO/T-ZnO_w in Fig. 2-18 (at. %)

Location	Zn	Ni	O
A	48.91	-	51.09
B	40.72	2.91	56.26

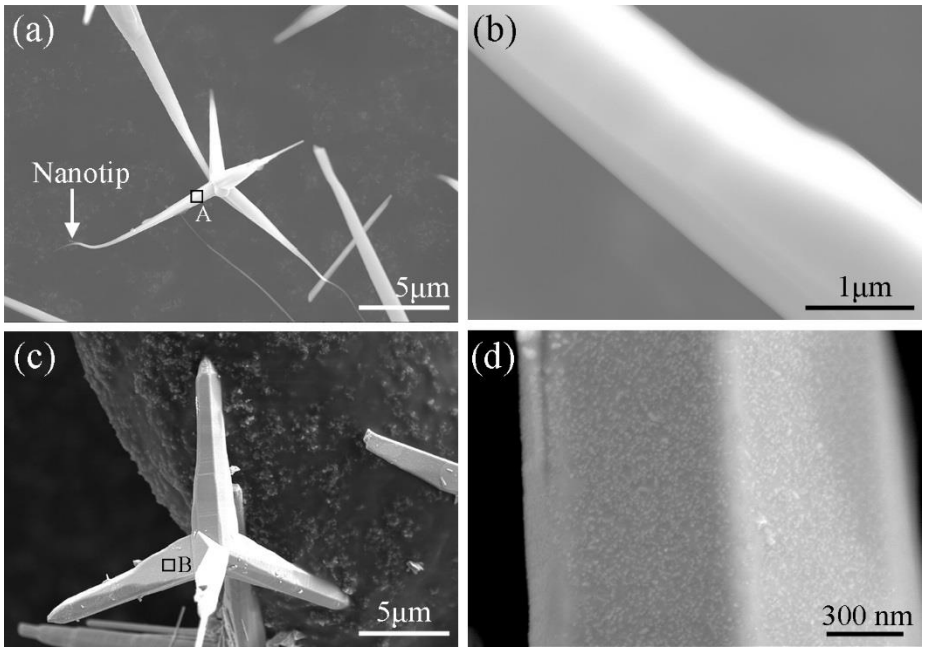

Fig. 2-18 SEM images of (a) raw T-ZnO_w and (c) NiO/T-ZnO_w. (b) and (d) are magnified views of (a) and (c), respectively.

2.8 The effect of Ni/Zn ratio on the morphology of NiO/T-ZnO_w

To investigate the influence of NiO loading on surface modification, NiO/T-ZnO_w samples with different Ni/Zn molar ratios were prepared. Fig. 2-19 shows the SEM images of NiO/T-ZnO_w with different Ni/Zn molar ratios. At a 5% Ni/Zn molar ratio (Fig. 2-19(a)), NiO nanoparticles were uniformly distributed on the surface of T-ZnO_w, but most of the surface remained exposed because of the low Ni/Zn molar ratio. At Ni/Zn = 10% (Fig. 2-19(b)), the size of NiO nanoparticles showed little change while their number increased significantly. Thus, the uniformly distributed NiO nanoparticles covered most of the T-ZnO_w surface. When Ni/Zn ratio increased to 20% (Fig. 2-19(c)), the average size of NiO particles increased significantly, and some of them were considerably coarsened. Stacking phenomena were also observed. At Ni/Zn = 40% (Fig. 2-19(d)), coarse NiO particles were layered on the T-ZnO_w surface and formed aggregates in some areas (dotted circle). A comparison of Fig. 2-19(a)–(d) shows that the NiO particle size gradually increased with increasing Ni/Zn molar ratio. However, the size increase was negligible when Ni/Zn = 5%–10% and more significant when Ni/Zn > 10%. This can be explained as follows. The $Ni(CH_3COO)_2{\cdot}4H_2O$ precursor was attached to the surface of T-ZnO_w after self-assembly, and then T-ZnO_w acted as heterogeneous nucleation sites during

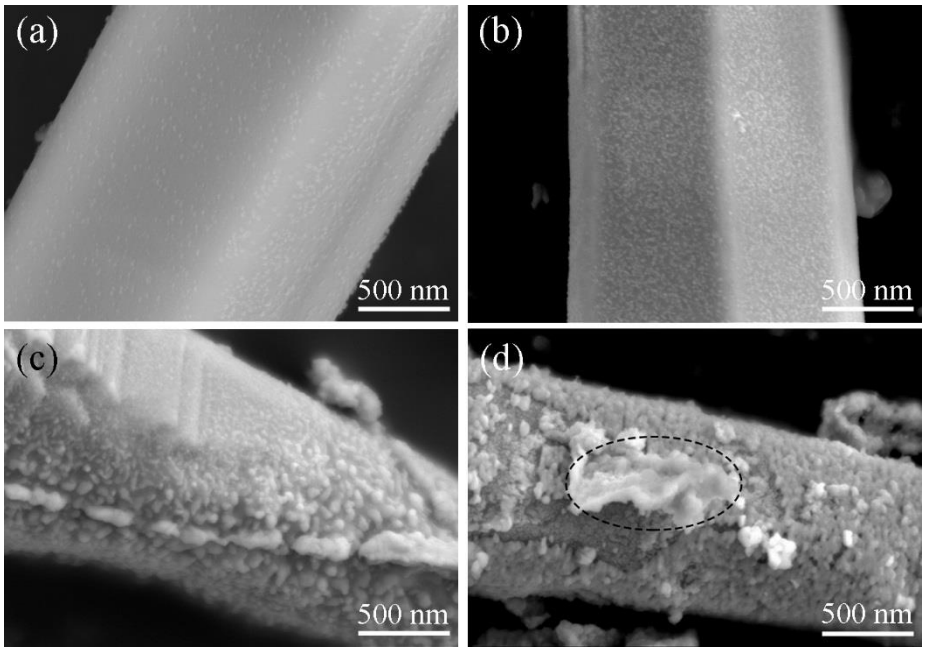

Fig. 2-19 SEM images of NiO/T-ZnO_w with different Ni/Zn molar ratios: (a) 5%, (b) 10%, (c) 20%, and (d) 40%.

pyrolysis of the precursor. When the loaded NiO was less than or equal to 10%, there was enough area for NiO nucleation, and therefore the size of NiO did not increase markedly when Ni/Zn increased from 5% to 10%. However, when the surface of T-ZnO_w was almost covered (Ni/Zn > 10%), the nucleation and growth of newly formed NiO could only occur on other NiO particles, resulting in a significant increase in particle size. Finally, a layered NiO structure composed of coarse particles was formed when the Ni/Zn ratio increased to 40%. Such a thick modified layer composed of coarse particles could reduce the tensile properties, as confirmed by Zhang's research [26]. In summary, a Ni/Zn molar ratio of 10% was recommended for the surface modification of T-ZnO_w by the pyrolysis method based on self-assembly.

2.9 Interface between NiO and T-ZnO_w

TEM observations were conducted to further explore the loading of NiO nanoparticles on the surface of T-ZnO_w and the resultant interface. Fig. 2-20 shows the TEM and high-resolution TEM (HRTEM) images of NiO/T-ZnO_w with Ni/Zn = 10%. In Fig. 2-20(a), the NiO particles were distributed almost continuously on the T-ZnO_w surface. The overall morphology shows a jagged shape, which is conducive to the micromechanical interlocking between the reinforcement and the matrix [27]. This jagged shape may be attributed to the merging and growth of neighboring NiO nanoparticles. Fig. 2-20(b) shows the selected area electron diffraction (SAED) pattern corresponding to Fig. 2-20(a). Diffraction points and rings can be observed at the same time. The diffraction points can be assigned to the (002), (110), and (112) planes of T-ZnO_w along the $[\bar{2}20]$ axis, while the rings were calibrated as the (101), (012), and (110) planes of NiO. These results are consistent with the XRD patterns in Fig 2-17. A highly magnified view of area 1 in Fig. 2-20(a) is shown in Fig. 2-20(c), where NiO particles were densely arranged close to each other with an average size of approximately 17.1 nm. This result is similar to that observed by SEM in Fig. 2-19(b). Fig. 2-20(d) shows the HRTEM image of area 2 in Fig. 2-20(c), where the lattice fringe spacing on the left side was 0.283 nm, corresponding to the (100) plane of T-ZnO_w, while the right side indicates the NiO (101) plane with a lattice spacing of 0.242 nm. Therefore, the interface of NiO/T-ZnO_w could be divided

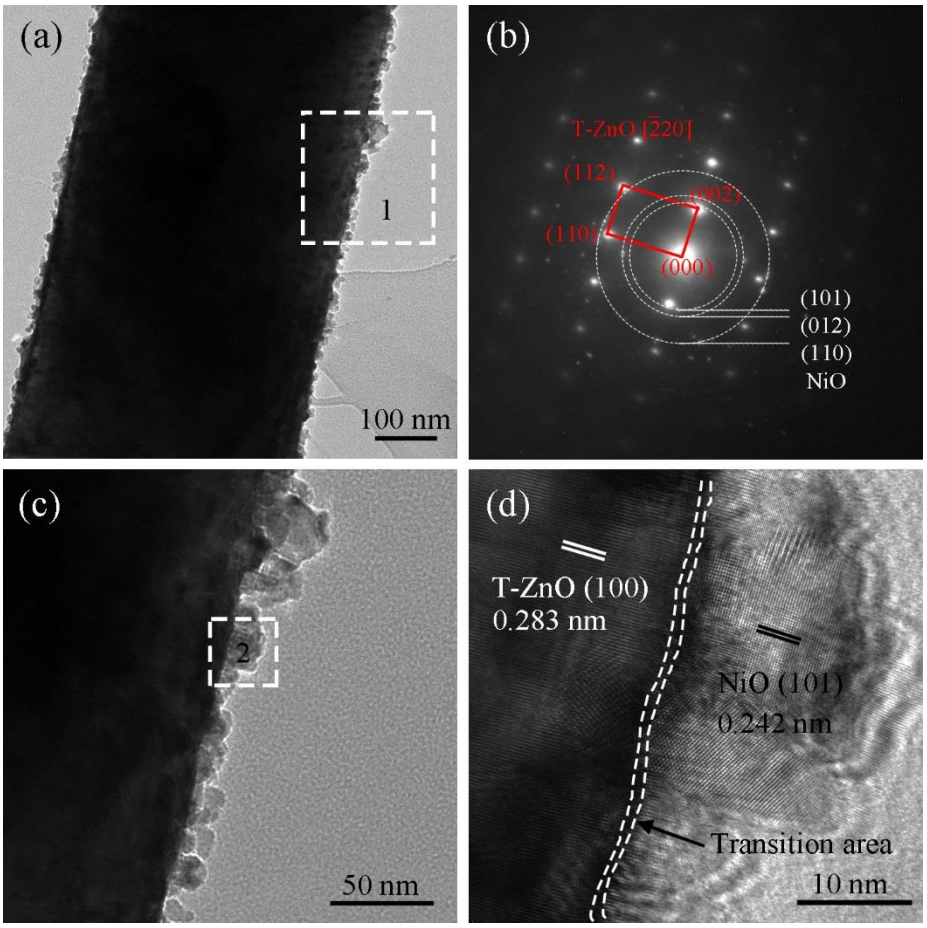

Fig. 2-20 TEM and HRTEM images of NiO/T-ZnO_w with Ni/Zn molar ratio of 10%. (a) NiO/T-ZnO_w, (b) SAED pattern of (a), (c) high-magnification view of area 1, (d) HRTEM imagine of area 2.

into three parts: the T-ZnO_w area, transition area, and NiO area. In the transition area, there are overlapping lattice fringes of T-ZnOw and NiO. The misfit of the T-ZnOw/NiO interface (e) can be calculated using the following Eq. (2-11).

The ε value of T-ZnO(100)/NiO(101) interface is 0.145, lower than 0.25, indicating a semi-coherent interface. This suggestes that the NiO nanoparticles and T-ZnO_w combined well at the atomic scale.

2.10 In-situ observation of mechanism of surface modification of T-ZnO_w

In-situ TEM observation was conducted to investigate the mechanism of surface modification of T-ZnO_w with nano NiO. Fig. 2-21(a) shows the $Ni(CH_3COO)_2{\cdot}4H_2O$/T-$ZnO_w$ system produced by self-assembly. The dark phase on the bottom side was T-ZnO_w, and the hemispherical phase on the upper side was the precursor $Ni(CH_3COO)_2{\cdot}4H_2O$. With electron

beam irradiation, changes first occured at the interface between T-ZnO_w and $Ni(CH_3COO)_2{\cdot}4H_2O$. In Fig. 2-21(b) (10 min irradiation), some disordered atoms and lattice distortion regions (dotted frame) appeared at the interface. The interface zone has a higher energy compared with other locations, and the atomic arrangement is less stable [28,29]. So it was easier to be in the active state under the irradiation of external energy. When the irradiation time increased to 20min (Fig. 2-21(c)), several small particles were formed at the interface.

The decomposition process of the precursor had mentioned in Eqs. (2-12)–(2-15).

First, the precursor $Ni(CH_3COO)_2{\cdot}4H_2O$ decomposed into solid products ($Ni(CH_3COO)_2$ and $Ni(OH)_2$) and gas products (CH_3COOH and H_2O). The gas products were pumped away by the vacuum system of the TEM. Subsequently, $Ni(CH_3COO)_2$ decomposed into $NiCO_3$ and CH_3COCH_3 gas, and the letter was also vacuumed away. Therefore, at the end of the second stage, the intermediate solid product was a mixture of $NiCO_3$ and $Ni(OH)_2$. For convenient description, I refer to them as the intermediate products $NiCO_3/Ni(OH)_2$.

Therefore, when the irradiation time reached 20 min (Fig. 2-21(c)), the formed small particles were $NiCO_3/Ni(OH)_2$ but with different crystal planes. The three sets of crystal planes were $NiCO_3(024)/Ni(OH)_2(012)$, $NiCO_3(113)/Ni(OH)_2(011)$, and $NiCO_3(113)/ Ni(OH)_2(011)$, respectively. After extending the irradiation time to 30min (Fig. 2-21(d)), these small particles of intermediate product at the interface gradually grew into large particles. At the same time, new particles were generated on the top side of these large particles. According to FFT analysis of Fig. 2-21(d), these small particles can be identified as $NiCO_3(113)/Ni(OH)_2(011)$. On the one hand, the top side of the large particles is the interface between the precursor and the intermediate product, and this location has higher energy and is easier to induce phase transition. On the other hand, the previously generated intermediate product could act as nucleation sites for forming new particles. When the irradiation time reached 40 min (Fig. 2-21(e)), the $NiCO_3/Ni(OH)_2$ particles in the second layer gradually grew up, and new intermediate products were formed at the top side of the second layer. When the irradiation time was 50 min (Fig. 2-21(f)), no further noticeable changes were observed, except that the intermediate product in the

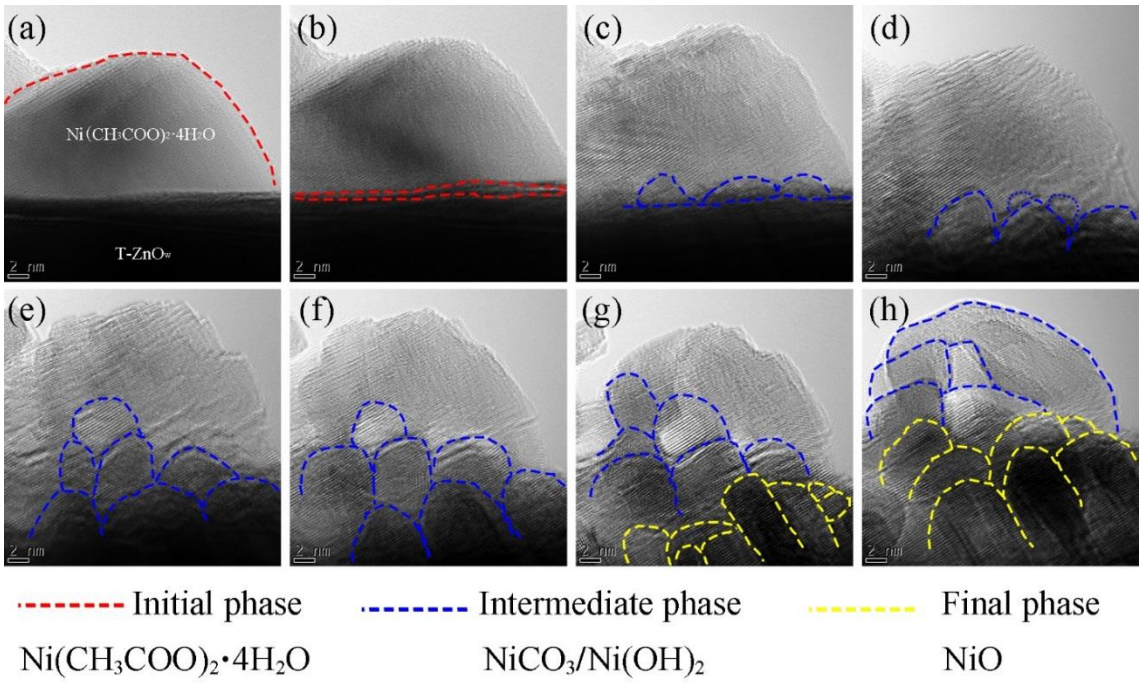

Fig. 2-21 In-situ HRTEM images of the transformation from $Ni(CH_3COO)_2 \cdot 4H_2O$/T-$ZnO_w$ to NiO/ T-ZnO_w at various irradiation times: (a) 0, (b) 10, (c) 20, (d) 30, (e) 40, (f) 50, (g) 60, and (h) 70min.

second layer continued to grow. After 60 min of irradiation (Fig. 2-21(g)), the new phase change was occurred, in which the large-sized intermediate product $NiCO_3$(104)/$Ni(OH)_2$(100) in the first layer began to transform into the small-sized final product NiO (100) but with the different plane orientations. When the irradiation time reached 70 min (Fig. 2-21(h)), the NiO particles in the first layer gradually merged and grew. At the same time, the intermediate product in the second layer began to transform into NiO nanoparticles as the final product. Furthermore, the unconverted precursor $Ni(CH_3COO)_2 \cdot 4H_2O$ in Fig. 2-21(g) also started to transform into the intermediate product $NiCO_3/Ni(OH)_2$. Finally, NiO was attached to the surface of T-ZnO_w in a stacked manner, thereby completing the surface modification of T-ZnO_w with NiO nanoparticles.

A schematic diagram for the surface modification of T-ZnO_w is shown in Fig. 2-22. In Fig. 2-22(a), the precursor $Ni(CH_3COO)_2 \cdot 4H_2O$ was first attached to the surface of T-ZnO_w through self-assembly. Next (Fig. 2-22(b)), the precursor at the interface were first activated under beam irradiation, and precursor at the interface began to transform into the intermediate products $NiCO_3/Ni(OH)_2$. Third, as shown in Fig. 2-22(c), the initially formed intermediate

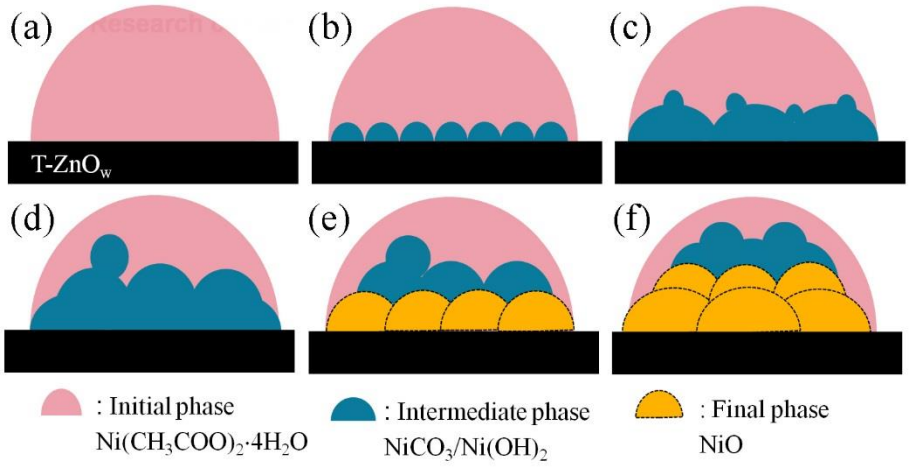

Fig. 2-22 Schematic diagram of surface modification of T-ZnO_w with pyrolysis method.

product further grew, while a new intermediate product was formed on top of it. Next, the intermediate products continued to grow under the effect of beam irradiation (Fig. 2-22(d)). Then, in Fig. 2-22(e), the aged intermediate product $NiCO_3$/ $Ni(OH)_2$ began to transform into the final NiO particles. Eventually, the final NiO particles grew gradually (Fig. 2-22(f)). At the same time, intermediate products in other areas gradually transformed into NiO, and the precursor was also gradually converted into intermediate products.

By comparing the surface modification process of ZrO_2 and T-ZnO_w (Fig. 2-15, 2-21), similarities and differences exist simultaneously. In terms of phase transition, there is little difference. Both of them are transformed from the precursor $Ni(CH_3COO)_2·4H_2O$ to the intermediate phase $NiCO_3/Ni(OH)_2$, and then to the final product NiO. During the process, the growth and merger of the phases are also carried out at the same time. On the other hand, different aspects are mainly shown in the following aspects. The transition from precursor/ZrO_2 to NiO/ZrO_2 is monolayer, while the transformation from precursor/T-ZnO_w to NiO/T-ZnO_w occurs layer by layer, and NiO is attached to the surface of T-ZnO_w in a stacked manner. This may be due to the difference in morphology and size between ZrO_2 and T-ZnO_w. The needle of T-ZnO_w belongs to micrometer-scale in the length direction, which allows it to take on larger volumes of precursors, resulting in a stacked-form pyrolysis of the precursors $Ni(CH_3COO)_2·4H_2O$.

2.11 Conclusion

In this chapter, a new surface modification method, ball milling-pyrolysis method based on self-assembly, was proposed. And systemically illustrated the surface modification of ZrO_2 and T-ZnO_w.

The NiO/ZrO_2 successfully prepared using the ball milling-pyrolysis method, and the synthesis of NiO/ZrO_2 can be regulated by controlling ball milling time and Ni/Zr molar ratio. As the the ball milling time increased, the surface defects of ZrO_2 were increased, facilitating the attachment of NiO nanaoparticles. I drived an expression to describle the relationship between the NiO particle size (y) and the ball milling time (t), $y = 10.310t^{-0.076}$. Meanwhile, as the Ni/Zr molar ratio increased in the range of 5–20 %, the NiO particle size slighly increased.

The transformation from precursor/ZrO_2 into NiO/ZrO_2 under beam irradiation was explored by in-situ TEM. Initially, the precursor was attached to ZrO_2 surface as a result of a self-assembly reaction with ZrO_2. Subsequently, it decomposed into intermediate $NiCO_3$/$Ni(OH)_2$ products. With continuous irradiation, these intermediate products merged, grew, and finally transformed into NiO. The mismatch of the typical interfaces was found to be 0.029–0.054, indicating semi-coherent and coherent interfaces.

Similarly, T-ZnO_w was successfully modified by NiO nanoparticles via a pyrolysis method based on self-assembly. When the Ni/Zn molar ratio reached 10%, NiO nanoparticles were densely and evenly distributed on the surface of T-ZnO_w. The interfacial relationship between T-ZnO_w (100) and NiO (101) plane was semi-coherent interface with the misfit of 0.145, indicating the good adhesion. In-situ TEM observation showed that NiO attached to the surface of T-ZnO_w in a stacked manner.

References

[1] J.C. De Jesus, I. González, A. Quevedo, T. Puerta, Thermal decomposition of nickel acetate tetrahydrate: An integrated study by TGA, QMS and XPS techniques, J. Mol. Catal. A Chem. 228 (2005) 283–291. https://doi.org/10.1016/j.molcata.2004.09.065.

[2] M.L.M. Bonati, R.W. Joyner, M. Stockenhuber, A temperature programmed desorption study of the interaction of acetic anhydride with zeolite beta (BEA), Catal. Today. 81 (2003) 653–658. https://doi.org/10.1016/S0920-5861(03)00163-9.

[3] G. Greczynski, L. Hultman, C 1s Peak of Adventitious Carbon Aligns to the Vacuum Level: Dire Consequences for Material's Bonding Assignment by Photoelectron Spectroscopy, ChemPhysChem. 18 (2017) 1507–1512. https://doi.org/10.1002/cphc.201700126.

[4] G. Greczynski, L. Hultman, Compromising Science by Ignorant Instrument Calibration—Need to Revisit Half a Century of Published XPS Data, Angew. Chemie. 132 (2020) 5034–5038. https://doi.org/10.1002/ange.201916000.

[5] G. Greczynski, L. Hultman, Reliable determination of chemical state in x-ray photoelectron spectroscopy based on sample-work-function referencing to adventitious carbon: Resolving the myth of apparent constant binding energy of the C 1s peak, Appl. Surf. Sci. 451 (2018) 99–103. https://doi.org/10.1016/j.apsusc.2018.04.226.

[6] G. Greczynski, L. Hultman, X-ray photoelectron spectroscopy: Towards reliable binding energy referencing, Prog. Mater. Sci. 107 (2020) 100591. https://doi.org/10.1016/j.pmatsci.2019.100591.

[7] J. Liu, A.H. Mir, G. He, M. Danaie, J. Hinks, S. Donnelly, H. Nordin, S. Lozano-Perez, C.R.M. Grovenor, In-situ TEM study of irradiation-induced damage mechanisms in monoclinic-ZrO_2, Acta Mater. 199 (2020) 429–442. https://doi.org/10.1016/j.actamat.2020.08.064.

[8] J. Liu, D. Kaoumi, Use of in-situ TEM to characterize the deformation-induced martensitic transformation in 304 stainless steel at cryogenic temperature, Mater. Charact. 136 (2018) 331–336. https://doi.org/10.1016/j.matchar.2017.12.005.

[9**]** R.F. Egerton, Control of radiation damage in the TEM, Ultramicroscopy. 127 (2013) 100–108. https://doi.org/10.1016/j.ultramic.2012.07.006.

[10**]** R.F. Egerton, Radiation damage to organic and inorganic specimens in the TEM, Micron. 119 (2019) 72–87. https://doi.org/10.1016/j.micron.2019.01.005.

[11] F. Huo, K. Zhang, M. Zhang, H. Wang, The Interfacial Intermetallic and Shear Strength of Ni Nanoparticle-Decorated Reduced Graphene Oxide Reinforced Sn2.5Ag0.5Cu Lead-Free Composite Soldering Joints, Adv. Eng. Mater. 20 (2018) 1–8. https://doi.org/10.1002/adem.201800147.

[12] Y. Pang, Y. Liu, X. Zhang, M. Gao, H. Pan, Role of particle size, grain size, microstrain and lattice distortion in improved dehydrogenation properties of the ball-milled $Mg(AlH_4)_2$, Int. J. Hydrogen Energy. 38 (2013) 1460–1468. https://doi.org/10.1016/j.ijhydene.2012.11.006.

[13] F.T.L. Muniz, M.A.R. Miranda, C. Morilla Dos Santos, J.M. Sasaki, The Scherrer equation and the dynamical theory of X-ray diffraction, Acta Crystallogr. Sect. A Found. Adv. 72 (2016) 385–390. https://doi.org/10.1107/S205327331600365X.

[14] R. Amade, P. Heitjans, S. Indris, M. Finger, A. Haeger, D. Hesse, Defect formation during high-energy ball milling in TiO_2 and its relation to the photocatalytic activity, J. Photochem. Photobiol. A Chem. 207 (2009) 231–235. https://doi.org/10.1016/j.jphotochem.2009.07.015.

[15] H. T. Sun, Y. Fang, Y. M. Wan, Study on ball movement law in planetary ball mill, Metal Mine. 10 (2007) 104-107.

[16] P. Liu, J. Ran, B. Xia, S. Xi, D. Gao, J. Wang, Bifunctional Oxygen Electrocatalyst of Mesoporous Ni/NiO Nanosheets for Flexible Rechargeable Zn–Air Batteries, Nano-Micro Lett. 12 (2020) 1–12. https://doi.org/10.1007/s40820-020-0406-6.

[17] M.A. Peck, M.A. Langell, Comparison of nanoscaled and bulk NiO structural and environmental characteristics by XRD, XAFS, and XPS, Chem. Mater. 24 (2012) 4483–4490. https://doi.org/10.1021/cm300739y.

[18] S. Uhlenbrock, C. Scharfschwerdt, M. Neumann, G. Illing, H.J. Freund, The influence of defects on the Ni 2p and O 1s XPS of NiO, J. Phys. Condens. Matter. 4 (1992) 7973–7978. https://doi.org/10.1088/0953-8984/4/40/009.

[19] C. Rameshan, H. Li, K. Anic, M. Roiaz, V. Pramhaas, R. Rameshan, R. Blume, M. Hävecker, J. Knudsen, A. Knop-Gericke, G. Rupprechter, In situ NAP-XPS spectroscopy during methane dry reforming on ZrO_2/Pt(1 1 1) inverse model catalyst, J. Phys. Condens. Matter. 30 (2018). https://doi.org/10.1088/1361-648X/aac6ff.

[20] W. Zhu, A. Fujiwara, N. Nishiike, S. Nakashima, H. Gu, E. Marin, N. Sugano, G. Pezzotti, Mechanisms induced by transition metal contaminants and their effect on the hydrothermal stability of zirconia-containing bioceramics: An XPS study, Phys. Chem. Chem. Phys. 20 (2018) 28929–28940. https://doi.org/10.1039/c8cp06027d.

[21] S. Velu, K. Suzuki, C.S. Gopinath, H. Yoshida, T. Hattori, XPS, XANES and EXAFS investigations of CuO/ZnO/Al_2O_3/ZrO_2 mixed oxide catalysts, Phys. Chem. Chem. Phys. 4 (2002) 1990–1999. https://doi.org/10.1039/b109766k.

[22] J. Yang, L. Xu, K. Zhu, R. Wang, L. Zhou, W. Wang, Improvement of HAZ Toughness of Steel Plate for High Heat Input Welding by Inclusion Control with Mg Deoxidation, Steel Res. Int. 86 (2015) 619–625. https://doi.org/10.1002/srin.201400313.

[23] J. Hendricks, M.J. Patitz, T.A. Rogers, S.M. Summers, The power of duples (in self-assembly): It's not so hip to be square, Theor. Comput. Sci. 743 (2018) 148–166. https://doi.org/10.1016/j.tcs.2015.12.008.

[24] X. Tang, G. Wen, Y. Song, Stable silicon/3D porous N-doped graphene composite for lithium-ion battery anodes with self-assembly, Appl. Surf. Sci. 436 (2018) 398–404. https://doi.org/10.1016/j.apsusc.2017.12.068.

[25] M.A. Mohamed, S.A. Halawy, M.M. Ebrahim, Non-isothermal decomposition of nickel acetate tetrahydrate, J. Anal. Appl. Pyrolysis. 27 (1993) 109–110. https://doi.org/10.1016/0165-2370(93)80002-H.

[26] C. Zhang, D. Yao, J. Yin, K. Zuo, Y. Xia, H. Liang, Y.P. Zeng, Effects of whisker surface modification on microstructures, mechanical and thermal properties of β-Si_3N_4 whiskers

reinforced Al matrix composites, Mater. Des. 159 (2018) 117–126. https://doi.org/10.1016/j.matdes.2018.08.055.

[27] B. Qiu, T. Sun, M. Li, Y. Chen, S. Zhou, M. Liang, H. Zou, High micromechanical interlocking graphene oxide/carboxymethyl cellulose composite architectures for enhancing the interface adhesion between carbon fiber and epoxy, Compos. Part A Appl. Sci. Manuf. 139 (2020) 106092. https://doi.org/10.1016/j.compositesa.2020.106092.

[28] M.D. Scafetta, Z. Yang, S.R. Spurgeon, M.E. Bowden, T.C. Kaspar, S.M. Heald, S.A. Chambers, Epitaxial growth and atomic arrangement in Fe_2CrO_4 on crystal symmetry matched (001) $MgAl_2O_4$, J. Vac. Sci. Technol. A. 37 (2019) 031511. https://doi.org/10.1116/1.5093537.

[29] Y. Zheng, T. Zhou, X. Zhao, W.K. Pang, H. Gao, S. Li, Z. Zhou, H. Liu, Z. Guo, Atomic Interface Engineering and Electric-Field Effect in Ultrathin Bi_2MoO_6 Nanosheets for Superior Lithium Ion Storage, Adv. Mater. 29 (2017) 1–8. https://doi.org/10.1002/adma.201700396.

Chapter 3 Microstructure and mechanical properties of NiO/ZrO_2 reinforced Sn1.0Ag0.5Cu composite solders

3.1 Introduction

Previous chapter mentioned that the NiO/ZrO_2 and $NiO/T\text{-}ZnO_w$ hybrid reinforced Sn1.0Ag0.5Cu composite solders would be prepared. But before the fabrication of hybrid reinforced composite solder, single reinforcement enhanced composite solder needed to prepare. The effect of single reinforcement on the melting points, microstructure, and mechanical properties of composite solders are investigated. These data can provide a foundation for the further design of hybrid reinforced composite solders.

In this chapter, NiO/ZrO_2–reinforced Sn1.0Ag0.5Cu composite solder was prepared with ultrasonic stirring. The microstructure evolution and refinement mechanism of composite solders were systematically investigated. The $Sn/NiO/ZrO_2$ interface system based on mutual solid solution was designed. In addition, the melting point and mechanical properties of composite solders were also studied.

3.2 Experimental procedure

3.2.1 Materials

The reinforcement of NiO/ZrO_2 was prepared with the ball milling-pyrolysis method. Based on the results of chapter 2, the optimized process parameters are as follows: 10 h milled at a speed of 400 rpm and the 20% Ni/Zr molar ratio. The detailed fabrication program and morphology of NiO/ZrO_2 were shown in chapter 2. So this chapter will not elaborate. The commercial Sn1.0Ag0.5Cu solder bar was provided by Senju Metal Industry Co. Ltd. Japan.

3.2.2 Fabrication of composite solders using ultrasonic stirring

A commercial Sn1.0Ag0.5Cu solder bar was melted at 380 °C in a furnace. Subsequently, different mass fractions (0, 0.05, 0.1, 0.3, and 0.5 mass%) of the NiO/ZrO_2 reinforcement were added to the molten solder, respectively. Then, ultrasonic vibration-assisted agitation was

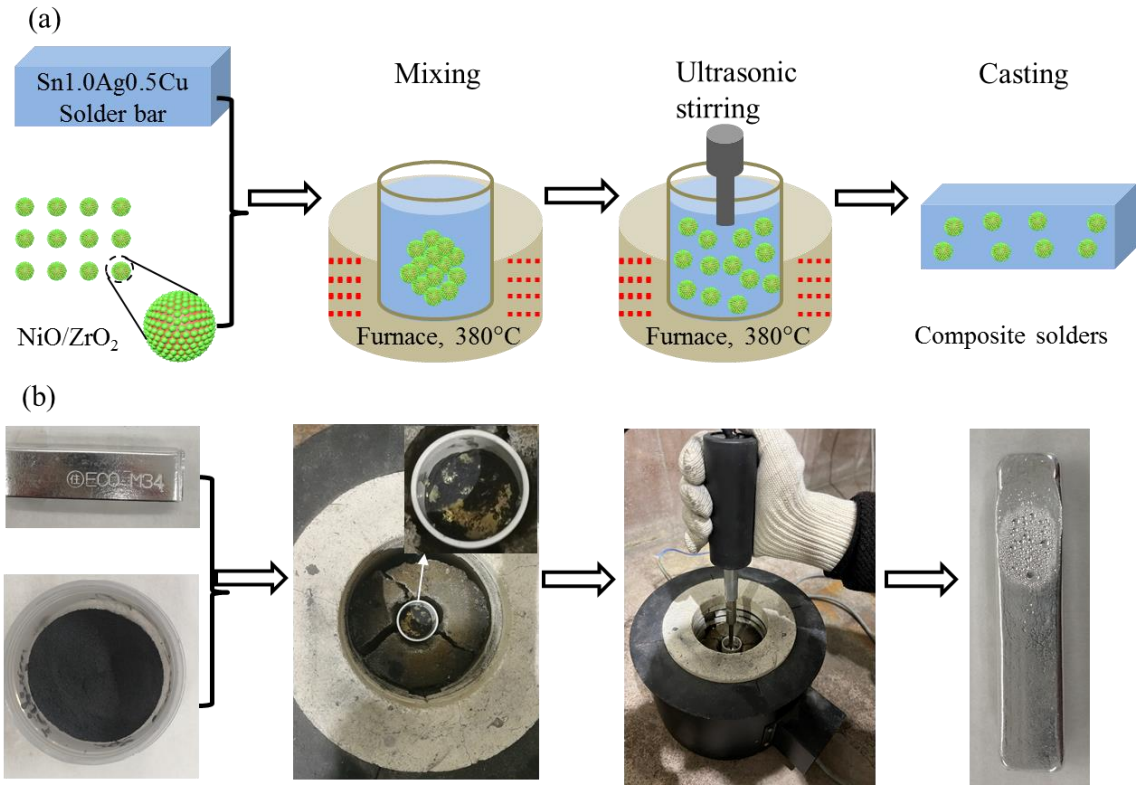

Fig. 3-1 The fabrication process of NiO/ZrO_2 reinforced Sn1.0Ag0.5Cu composite solder. (a) schematic illustration, (b) actual image.

applied to the mixture. The applied ultrasonic power and time were 80 W and 240 s, respectively. Finally, the oxide film on the surface of the molten solder was removed and quickly cast molten into a stainless steel mold with the size of 50 mm × 10 mm × 5 mm (L × W × H). The schematic illustration and actual image of fabrication process of NiO/ZrO_2 reinforced Sn1.0Ag0.5Cu composite solder are shown in Fig. 3-1.

3.2.3 Characterization and testing

X-ray diffraction (XRD, Ultima IV, Rigaku, Japan) was used to characterize the phase and crystalline structures of the NiO/ZrO_2 reinforced Sn1.0Ag0.5Cu composite solders. Scanning electron microscopy (SEM, SU-70, Hitachi, Japan) equipped with energy-dispersive X-ray spectroscopy (EDS) was used to observe the microstructure and fracture surface of the composite solders. The size of these phases was measured with Nano Measurer software. Fig. 3-2 shows the typical example used for the measurement. Three SEM images were selected for each composition, and about 30 β-Sn and 100 IMC phases were measured for each composition,

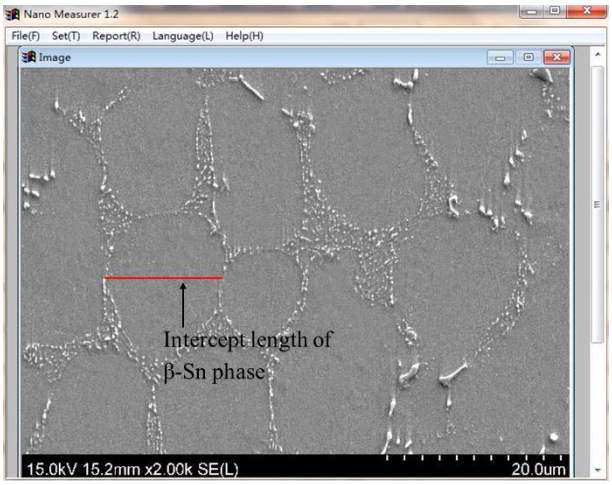

Fig. 3-2 Typical example of the mean intercept length measurement.

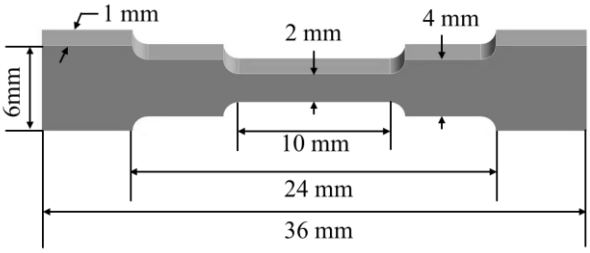

Fig. 3-3 The schematic diagram of the tensile test sample.

respectively. The distribution of NiO/ZrO_2 in solder matrix, and the interface between reinforcement and solder matrix were investigated using transmission electron microscopy (TEM, JEOL JEM 2100F) equipped with EDS. The acceleration voltage of TEM was 200 kV. The TEM samples of the composite solder were prepared with a focused ion beam (FIB, HITACHI FB-2000A).

The melting behavior of composite solder was examined by differential scanning calorimetry (DSC; 7020 clinical analyzer, Hitachi, Japan) under a constant flow of N_2 in the range of 25–300 °C at a rate of approximately 10 °C/min. These composite solder bars were formed into the tensile test samples using an electrical discharge machine (AG360L). The schematic diagram of the tensile test sample is shown in Fig. 3-3. The sample gauge length was 10 mm, and the width and thickness were 2 mm and 1 mm, respectively. The tensile tests were performed using a universal electrical tensile tester (Autograph AG-X Shimazu, Japan) with a strain rate of 0.0005/s. The experimental results were the average values of four tensile samples.

3.3 Microstructure of composite solders

3.3.1 Microstructure evolution of composite solders with various NiO/ZrO_2 additions

To detect the phase of the composite solder and determine whether NiO/ZrO_2 is added to the solder matrix, XRD analysis were carried out. Fig. 3-4 shows the XRD patterns of the plain Sn1.0Ag0.5Cu solder and composite solder with various NiO/ZrO_2 additions. According to the PDF cards (PDF#04-0673, 04-0800, 45-1888, 36-0420), the characteristic peaks of β-Sn at 30.6 °,32.0 °,44.9 °, 55.3 °, 62.5 °, 64.5 °, and 79.4 ° correspond to the (200), (101), (211), (301), (112), (321), and (312) planes, respectively. Similarly, the characteristic peaks of Ag_3Sn appeared at 37.6 ° and 72.9 °, corresponding to the (002) and (220) planes, respectively. The characteristic peaks of Cu_6Sn_5 appeared at 62.6 °, corresponding to the $(22\bar{6})$ plane. In addition, weak characteristic peaks of ZrO_2 can be observed at 28.2 ° and 31.5 °, corresponding to the $(\bar{1}11)$ and (111) planes, respectively. However, the characteristic peaks could not be detected for the 0.05 mass% and 0.1 mass% NiO/ZrO_2 reinforced composite solders, which may be attributed to the fact that the reinforcement contents are too small to be detected. Fig. 3-4(b) shows the high magnification view of 0.3 mass% and 0.5 mass% NiO/ZrO_2 reinforced composite solders. As shown in Fig. 3-4(b), the characteristic peaks of ZrO_2 can be clearly

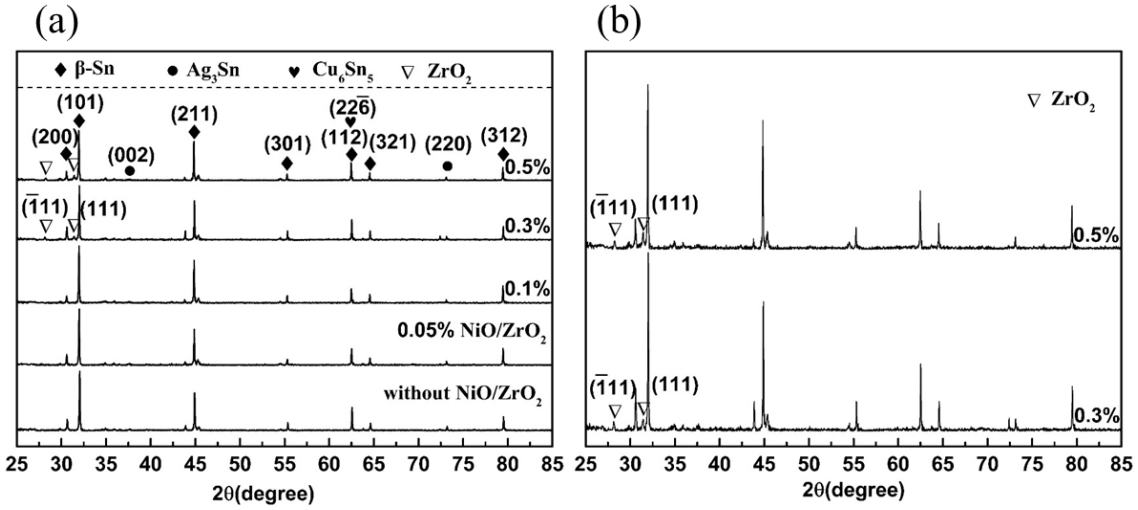

Fig. 3-4 XRD patterns of (a) plain Sn1.0Ag0.5Cu solder and composite solder with various NiO/ZrO_2 addition contents, (b) high magnification view of (a).

observed, whereas the peaks of NiO are not clearly visible, which can also be ascribed to the low NiO contents. Therefore, other characterization method should be utilized to detect the existence of NiO, which will be discussed later. Overall, according to the XRD results, it can be inferred that the NiO/ZrO_2 is successfully added to the Sn1.0Ag0.5Cu solder matrix.

To investigate the effect of NiO/ZrO_2 on the microstructure of composite solders, as well as the phases distribution of composite solders, SEM and TEM observation were conducted. Fig. 3-5 shows the typical microstructure of Sn1.0Ag0.5Cu solder. During the cooling process of the molten solder, the primary β-Sn is first formed (Eq. (3-1)) [1], followed by the net-like eutectic microstructure. The SEM image of Sn1.0Ag0.5Cu solder is shown in Fig. 3-5(a). During the formation of eutectic structure, the reaction represented by Eq. (3-2) first occurred and an isolated Cu_6Sn_5 IMC is formed. With the decrease in melt temperature, the eutectic reaction represented by Eq. (3-3) subsequently occurred, which included β-Sn and separated Ag_3Sn. Finally, the ternary eutectic reaction occurred (Eq. (3-4)), where Cu_6Sn_5 and Ag_3Sn IMCs are generated simultaneously. Fig. 3-5(b) and (c)–(f) show the TEM image and

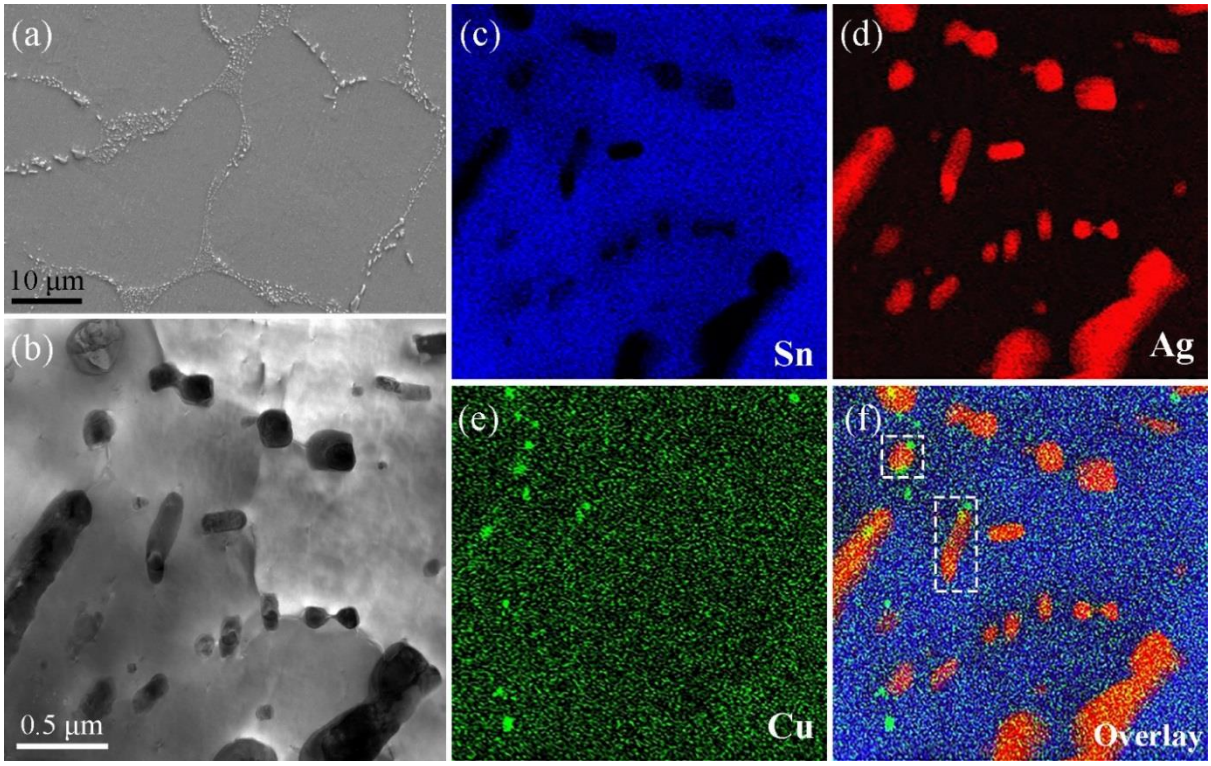

Fig. 3-5 Typical microstructure of Sn1.0Ag0.5Cu solder. (a) SEM image of Sn1.0Ag0.5Cu, (b) TEM image of eutectic area. EDS mappings of (c) Sn, (d) Ag, (e) Cu, and (f) their overlay.

corresponding EDS mappings of the eutectic structure, respectively. The precipitates with various shapes and sizes can be observed in Fig. 3-5(b). According to the above solidification process and XRD results shown in Fig. 3-4, it can be inferred that the small granular IMCs existed alone are Cu_6Sn_5, whereas the short rod and large sized granular IMC are Ag_3Sn, which corresponds to the binary eutectic reaction of Eq. (3-2) and (3-3), respectively. Additionally, interdependent Cu_6Sn_5 and Ag_3Sn IMCs (marked with dotted frames in Fig. 3-5(f)) can also be observed in the eutectic area, which can be explained by the ternary eutectic reaction depicted in Eq. (3-4).

$$L \rightarrow \beta\text{-Sn (232 °C)} \quad (3\text{-}1)$$

$$L \rightarrow \beta\text{-Sn} + Cu_6Sn_5 \text{ (227 °C)} \quad (3\text{-}2)$$

$$L \rightarrow \beta\text{-Sn} + Ag_3Sn \text{ (221 °C)} \quad (3\text{-}3)$$

$$L \rightarrow \beta\text{-Sn} + Cu_6Sn_5 + Ag_3Sn \text{ (217 °C)} \quad (3\text{-}4)$$

Fig. 3-6 shows the microstructure evolution of Sn1.0Ag0.5Cu composite solders reinforced with various NiO/ZrO_2 addition. For the plain Sn1.0Ag0.5Cu solder (Fig. 3-6 (a)), β-Sn with a size of 21.7 μm and some coarse eutectic structures are observed, where IMC average size in eutectic area is 0.9 μm. With 0.05 mass% NiO/ZrO_2, the size of β-Sn slightly decreased. With an increase in the amount of added NiO/ZrO_2, the β-Sn size gradually decreased, the proportion of the eutectic structure increased, and the coarse eutectic structure is also refined. When the addition amounts reached 0.3 mass%, the β-Sn transformed from elliptical to round shapes. In addition, the size of β-Sn and eutectic microstructure are refined compared to those in Fig. 3-6(a). The average size of β-Sn and IMC are 12.5 and 0.5 μm, respectively. However, the refined microstructure disappeared and microstructure defects (area 1 in Fig. 3-6(e)) are observed when the amount of reinforcement addition reached to 0.5 mass%. The high magnification view of area 1 in Fig. 3-6(e) is shown in Fig. 3-6(f). According to the EDS results of areas A, B, and C (shown in Table 3-1) and XRD in Fig. 3-4, these agglomerated particles are NiO/ZrO_2. When excessive NiO/ZrO_2 is added to the solder matrix, although partial reinforcements are dispersed in the solder matrix assisted by ultrasonic stirring, other

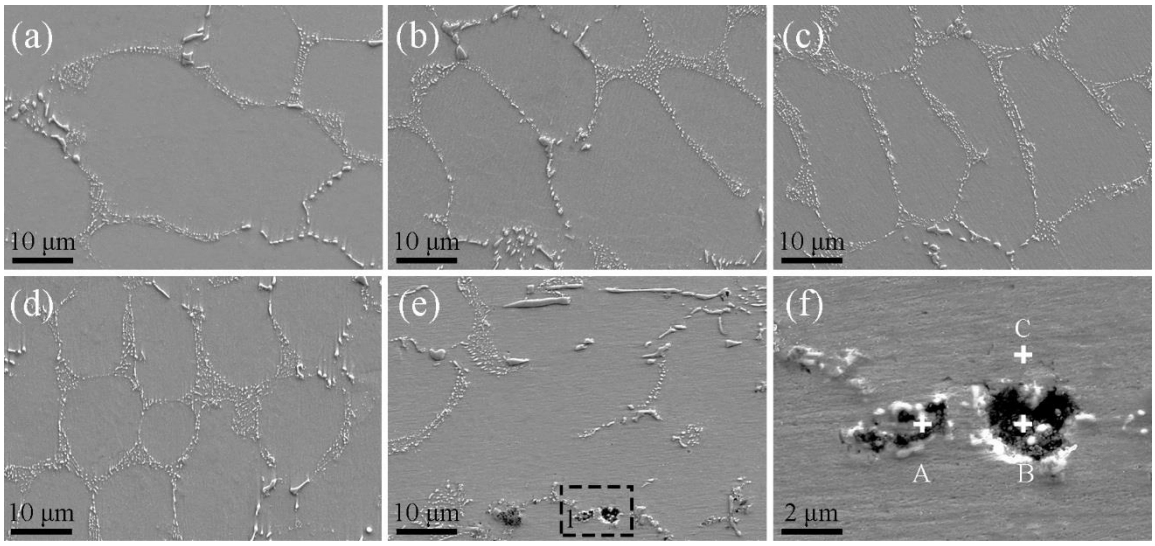

Fig. 3-6 Microstructure evolution of Sn1.0Ag0.5Cu composite solders reinforced with various NiO/ZrO_2 addition. (a) 0 mass%, (b) 0.05 mass%, (c) 0.1 mass%, (d) 0.3 mass%, (e) 0.5 mass%, (f) high magnification view of area 1 in (e).

Table 3-1. EDS results of Fig. 3-6(f) (at. %)

Location	Sn	Ag	Cu	Zr	Ni	O
A	33.5	12.1	-	18.2	3.1	33.1
B	6.4	-	-	26.8	5.8	61.0
C	100.0	-	-	-	-	-

agglomerated NiO/ZrO_2 deteriorated the microstructure. Therefore, it can be inferred that an appropriate NiO/ZrO_2 addition can obtain the refined microstructure, whereas excessive addition causes microstructure defects. These defects will deteriorate the mechanical properties of composite solders, which will be discussed later.

3.3.2 Microstructure refinement mechanism of NiO/ZrO_2

In section 3.3.1, I showed that the appropriate addition of NiO/ZrO_2 refined the microstructure of the composite solders. To further explore the refinement mechanism of NiO/ZrO_2 on the microstructure, I performed TEM observations on the 0.3mass% NiO/ZrO_2 reinforced Sn1.0Ag0.5Cu composite solder.

Fig. 3-7 shows the TEM and EDS mapping images of the composite solder. Several phases with different morphologies can be observed in Fig. 3-7(a). Combining the EDS (Fig. 3-7(b)–(e)) and XRD results in Fig. 3-4, it can be inferred that ZrO_2 (marked with the dashed circles), Ag_3Sn, and Cu_6Sn_5 phases are existed in Fig. 3-7 (a), which belongs to the eutectic area. The reinforcements are located in the eutectic area, which can be explained by the solidification process of the composite solder. In the initial stage of the solidification process, primary β-Sn is formed (Eq. (3-1)), while it did not react with the reinforcements. So the reinforcements are pushed to the front of solid–liquid interface. As the temperature gradually decrease, the reinforcements are finally located in eutectic area (Eq. (3-2)–(3-4)). In addition, the reinforcements are relatively dispersed and evenly distributed in the eutectic microstructure area, and no holes or gaps are found at the interface between the reinforcement and solder matrix. The good results can be attributed to two aspects. First, the ultrasonic stirring introduced during the preparation of composite solder could disperse the agglomerated nanoparticles. Second, the surface modification of ZrO_2 was conducted with NiO. As mentioned before, NiO can be solid solute with ZrO_2 and Sn at the same time, so it can act as a transition layer to improve the wetting between the ZrO_2 and solder matrix. The above two reasons make the reinforcements could be dispersed in the solder matrix and achieve a good

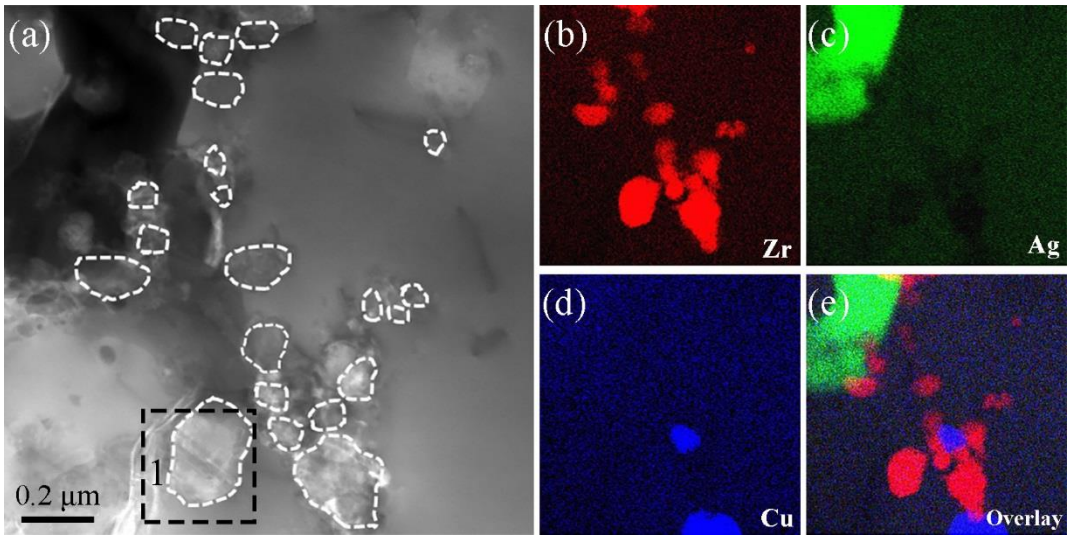

Fig. 3-7 TEM and EDS images of 0.3 mass% NiO/ZrO_2 reinforced Sn1.0Ag0.5Cu composite solder. (a) TEM image. EDS mappings of (b) Zr, (c) Ag, (d) Cu, and (e) their overlay. ZrO_2 are marked by the dashed circles.

interface between solder matrix and reinforcements. Moreover, these dispersed reinforcements can act as heterogeneous nuclear sites in the eutectic area. For example, in Fig. 3-7(e), the formation of Ag_3Sn and Cu_6Sn_5 was dependent on ZrO_2. This is also one of the reasons why the eutectic microstructure in Fig. 3-6 was refined after the addition of reinforcements. In addition, these dispersed nano reinforcements can produce Orowan strengthening effect, which is one of the reasons for the improved mechanical properties of the composite solders. This part will be discussed later.

A good interface is important in promoting the load transfer efficiency and improving the mechanical properties of composites [2]. Therefore, the interface between the reinforcements and solder matrix was also explored. Fig. 3-8 shows the magnified view of area 1 in Fig. 3-7(a). As shown in Fig. 3-8(a), the reinforcement is tightly embedded in the solder matrix, and no micropore or de-bond was found at the interface between the reinforcement and solder matrix, indicating a good combination. The SAED result of area 1 in Fig. 3-8(a) is shown in Fig. 3-8(b), where two sets of diffraction points and a set of diffraction rings can be observed simultaneously. One set of diffraction points can be assigned to the (111), ($\bar{1}$02), and (013) planes of ZrO_2 along the [2$\bar{3}$1] axis, and another set of diffraction points can be calibrated to the (200) plane of β-Sn (marked by the yellow circle). While the diffraction rings can be indexed as the (101), (012), and (110) planes of NiO. The SAED results indicate that NiO is still attached to the ZrO_2 surface, then the Sn/NiO/ZrO_2 interface system is formed. The EDS results shown in Fig. 3-8(c)–(f) further confirmed the result. NiO/ZrO_2 was added to the molten solder with ultrasonic stirring, then casting. During the preparation process of the composite solder, NiO is still fastened to the ZrO_2 surface, indicating the good attachment ability of them. This good attachment ability is attributed to the semi-coherent and coherent interface relationship between ZrO_2 and NiO, which have already mentioned in Fig. 3. Moreover, the NiO nanoparticles are uniformly attached to the ZrO_2 surface, resulting in the increased roughness of the ZrO_2 surface. This rough surface could increase the contact area between the solder matrix and reinforcements. Meanwhile, the protruding NiO nanoparticles could act as wedges, which are conductive to the formation of micro-mechanical locking between the

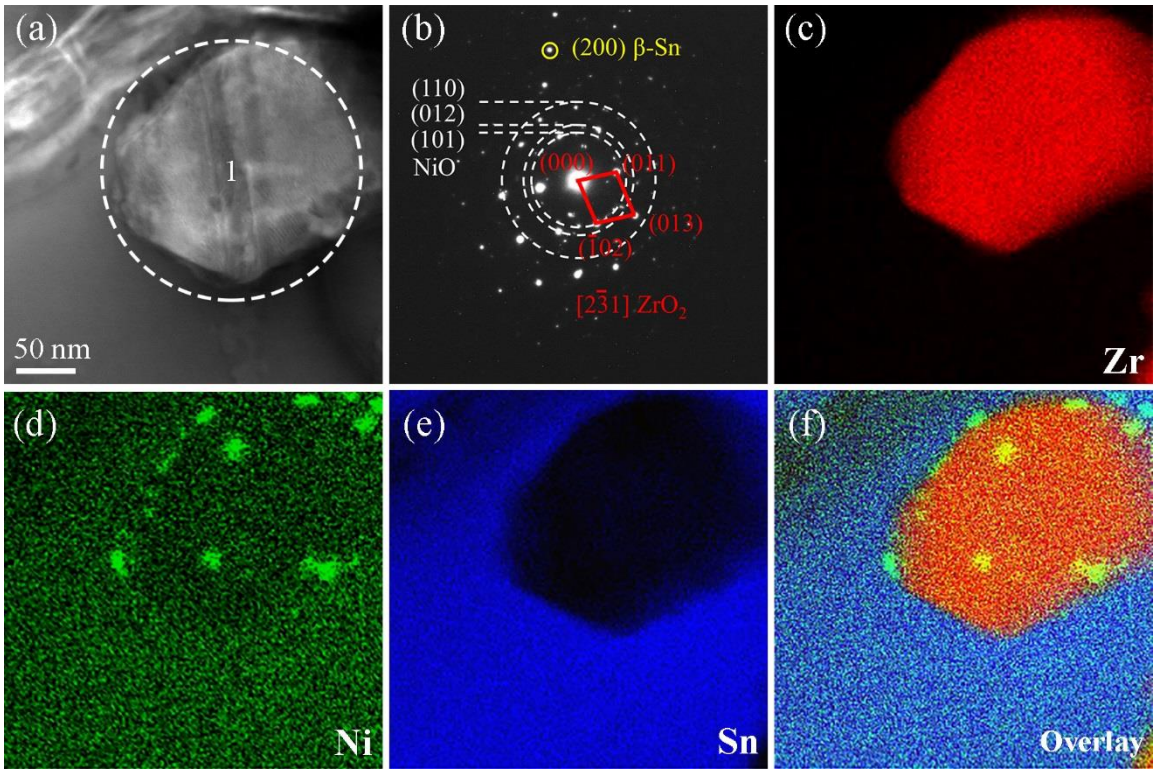

Fig. 3-8 Magnified view of area 1 in Fig. 3-7(a). (a) TEM image of the interface between the reinforcements and solder matrix, (b) SAED patterns of area 1 in Fig. 3-8(a). EDS mappings of (c) Zr, (d) Ni, (e) Sn, and (f) their overlay.

NiO/ZrO_2 and solder matrix. Both of the two factors can improve the load transfer efficiency of the reinforcements in solder matrix.

In addition, from SAED results in Fig. 3-8 (b), there are no other new phases detected, except for β-Sn, ZrO_2, and NiO. The results suggest that no interfacial reaction occurred between the reinforcements and solder matrix to produce a brittle interfacial IMC, which will deteriorate the performance of composites. Hence, it indicates that the interface between the NiO/ZrO_2 and solder matrix has a clean interface, belonging to the ideal interface in the composites. In summary, a micro-mechanical lock and non-micropored clean interface was formed between NiO/ZrO_2 and the solder matrix. The $Sn/NiO/ZrO_2$ interface system based on mutual solid solution was ingeniously designed.

In Fig. 3-7, I had illustrated that the dispersed NiO/ZrO_2 could act as nucleation sites for the molten solder, resulting in a refined microstructure of composite solder. In this part, the NiO/ZrO_2 located at the grain boundary can also produce positive effects. The detailed analysis

is as follows. Fig. 3-9 shows the TEM and SAED images of the 0.3mass% NiO/ZrO_2 reinforced composite solder. As shown in Fig. 3-9(a), several brightly colored nano-sized particles are distributed in the grain boundary areas. In order to detect the phase of them, SAED was conducted. Fig. 3-9(b) shows the SAED images of area 1 in Fig. 3-9(a), of which the diffraction spots can be assigned to the $(\bar{1}11)$, (101), and (012) planes of ZrO_2 along the $[12\bar{1}]$ axis, whereas the rings can be indexed to the (101), (012), and (110) planes of NiO. Similarly, the SAED image of area 2 in Fig. 3-9(a) is shown in Fig. 3-9(c), which can be calibrated to the (002), (201), and (203) planes of Cu_6Sn_5 along the [040] axis. The above results indicate that NiO/ZrO_2 is located in the grain boundary and the growth of Cu_6Sn_5 leaned on the NiO/ZrO_2. According to these results, it can be inferred that NiO/ZrO_2 could act as nucleation sites of IMC, which has already mentioned in Fig. 3-7. In addition, NiO/ZrO_2 is distributed at the grain boundary locations, which can produce pin effects on the grain boundary, thereby inhibiting the migration of the grain boundary. From a kinetic perspective, grain growth is achieved through grain boundary migration [3]. Therefore, the added NiO/ZrO_2 can inhibit the migration of grain boundaries, resulting in a refined microstructure of composite solders. Moreover, the influence of the reinforcement on the grain growth is related to the particle radius (r) and volume fraction (φ) of the reinforcements [4]. The qualitative relationship between the grain size (D), r, and φ can be expressed as the followed formula (3-5),

$$D \propto 4r/3\varphi \tag{3-5}$$

This formula indicates that when the size of the reinforcement remains constant, increased volume fraction of the reinforcement results in a smaller grain size, indicating a stronger ability

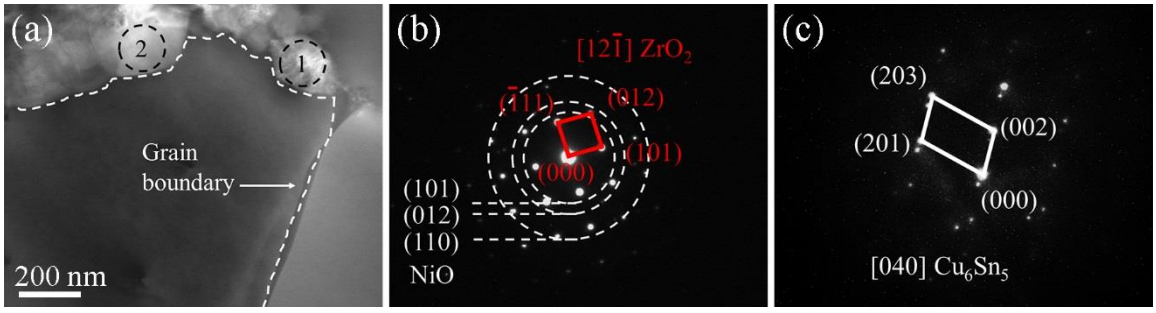

Fig. 3-9 TEM and SAED images of 0.3 mass% NiO/ZrO_2 reinforced Sn1.0Ag0.5Cu composite solder. (a) TEM image, (b) SAED pattern of area 1 in (a), (c) SAED pattern of area 2 in (a).

to hinder the grain growth. This is also the reason why the microstructure is gradually refined with the increase of the addition amount of NiO/ZrO_2 in the range 0–0.3 mass% (shown in Fig. 3-6).

In summary, the above results systematically investigate the refinement mechanism of NiO/ZrO_2 on the microstructure, with a focus on two aspects. The first one is to promote the nucleation. The addition of NiO/ZrO_2 increased the nucleation sites of solder molten, resulting in the refined microstructure of composite solders. The second one is to suppress the growth of grain. NiO/ZrO_2 distributed at the grain boundary can hinder the migration of grain boundary, producing the refined grains of composite solders. Fig. 3-10 shows the schematic illustration of solidification process of plain and composite solders. In particular, Fig. 3-10(b) illustrates why the grain size of composite solder is refined after NiO/ZrO_2 addition. In addition, for the interface between the reinforcements and Sn1.0Ag0.5Cu solder matrix, a micro-mechanical lock and non-micropored clean interface was formed between NiO/ZrO_2 and the solder matrix. The $Sn/NiO/ZrO_2$ interface system based on mutual solid solution was ingeniously designed.

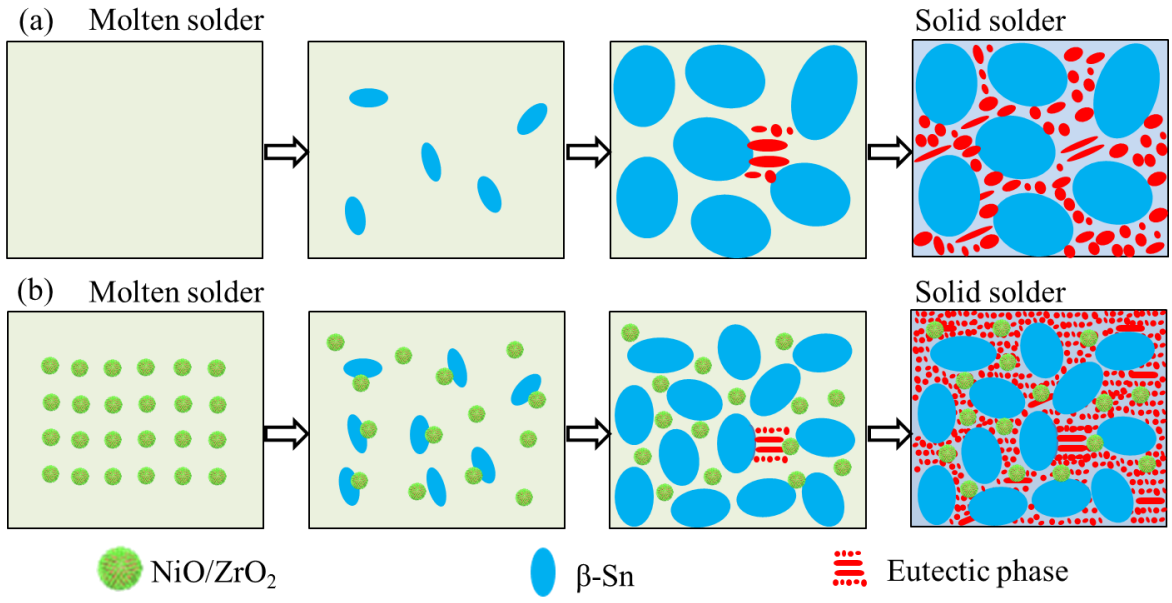

Fig. 3-10 Schematic illustration of solidification process of solders. (a) Plain Sn1.0Ag0.5Cu solder, (b) NiO/ZrO_2 reinforced Sn1.0Ag0.5Cu composite solder.

3.4. Melting properties of the composite solders

Melting property is one of the important properties of solder, since it mainly determines the process temperature. In this study, endset temperature during heating was defined as the melting point, and the pasty temperature refers to the difference between endset and onset during heating [5,6]. Fig. 3-11 shows the DSC curves of plain SAC105 and NiO/ZrO_2 reinforced SAC105 composite solders. The critical data were summarized in Table 3-2. Two endothermic peaks can be observed during heating process, corresponding to the melting of eutectic microstructure and primary β-Sn [7]. With increase of NiO/ ZrO_2 addition, T_{Onset} and T_{Endset} have little changes during heating process, which indicated the melting points of composite solder have little difference compared with plain solder. The melting points of composite solders were in the range of 226.6-228.0 °C. Generally, the melting property is an inherent physical property, which is determined by inter-atomic distance and the atomic mean-square displacements. A small amount of addition of reinforcement has little influence on melting temperature [8]. The results are similar to the previous report [9,10]. In addition, the pasty range also has no significant difference; the result is similar with 11.5 °C of SnPb solder [10]. The summarized melting properties from previous reports are shown in Table 3-3.

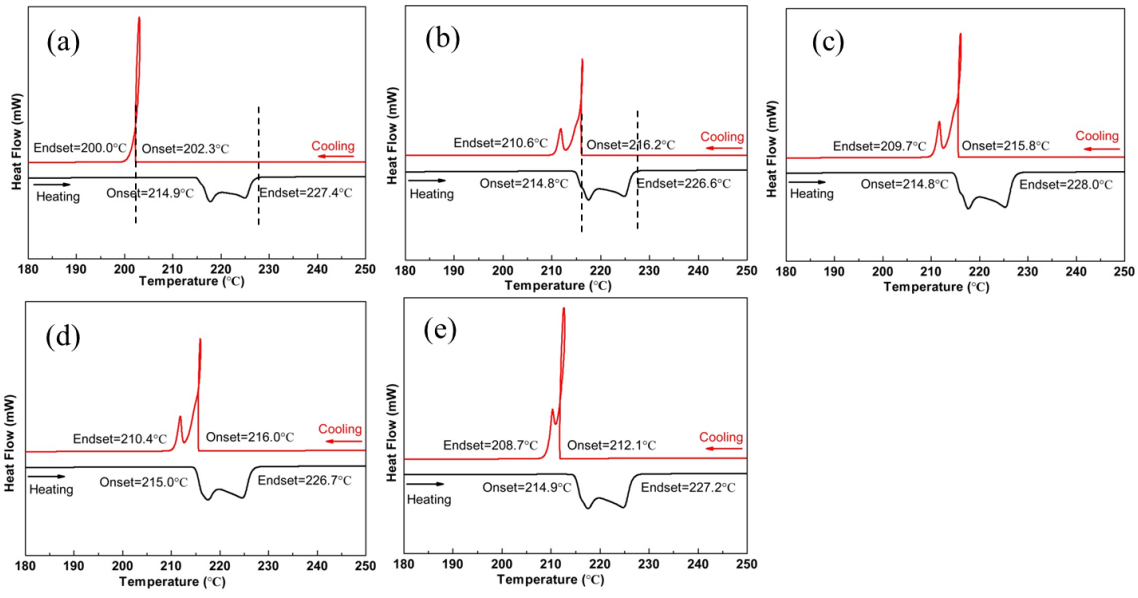

Fig. 3-11 DSC curves of composite solders with different NiO/ZrO_2 additions: (a) 0 wt%; (b) 0.05 wt%; (c) 0.1 wt%; (d) 0. 3 wt%; (e) 0.5 wt%.

Table 3-2 Information from heating curves of Fig. 3-11

NiO/ZrO_2 additions	Onset (°C)	Endset (°C)	Paste range (°C)	Melting point (°C)
0	214.9	227.4	12.5	227.4
0.05 wt%	214.8	226.6	11.8	226.6
0.1 wt%	214.8	228.0	13.2	228.0
0.3 wt%	215.0	226.7	11.7	226.7
0.5 wt%	214.9	227.2	12.3	227.2

Table 3-3 Melting properties in previous reports [8-11]

Solder matrix	Reinforcement	Paste range (°C)	Melting point range (°C)	References
Sn3.0Ag0.5Cu	Ni-GNS (0%, 0.05%, 0.10%, 0.20 mass %)	7.08-8.58	219.25-220.12	[8]
Sn3.5Ag0.7Cu	Ni-CNT (0%, 0.05%, 0.10%, 0.30 mass %)	-	219.4-220.8	[9]
Sn3.0Ag0.5Cu	ZnO nanoparticles (0, 0.7%)	6.4-7.7	220.3-220.5	[10]
Sn1.0Ag0.5Cu	SiC nanoparticles (0, 0.7%)	9.7-11.5	226.5-227.3	[11]

Table 3-4 Undercooling degree of plain and composite solders

NiO/ZrO_2 additions	Heating Endset (°C)	Cooling Onset (°C)	Undercooling (°C)
0	227.4	202.3	25.1
0.05 wt%	226.6	216.2	10.4
0.1 wt%	228.0	215.8	12.1
0.3 wt%	226.7	216.0	10.7
0.5 wt%	227.2	212.1	15.1

[Note: Undercooling= Heating Endset– Cooling Onset]

On the other hand, undercooling was also analyzed in this study. Undercooling was defined as the difference gaps between the liquidus temperature (T_{Endset}) at heating and actual solidification temperature (T_{Onset}) during cooling [12]. Table 3-4 shows that the undercooling values decreased from 25.1 to 10.4 °C with the NiO/ZrO_2 addition. The decrease of undercooling degree suggested that NiO/ZrO_2 reinforced composite solder molten is easier to solidify than plain solder molten. This is because the NiO/ZrO_2 reinforcements can act as nucleation sites, thus promoting solidificatio. It can be inferred that the rate of solidification of β-Sn is faster compared with plain solder, and then less time for IMC to grow up. In the thermodynamic, the larger the undercooling cause, the larger the driving force for the IMCs growth [11]. Therefore, the decreased undercooling could suppress the growth of IMC. This is one of the reasons why the microstructure was refined in Fig. 3-6.

3.5. Mechanical properties of NiO/ZrO_2 reinforced Sn1.0Ag0.5Cu composite solders

3.5.1 Tensile properties and fracture surface

In order to obtain the mechanical properties of composite solders, tensile test was conducted. Fig. 3-12(a) shows the representative stress-strain curves of samples, and Fig. 3-12(b) shows the UTS and elongation of Sn1.0Ag0.5Cu composite solders reinforced with various NiO/ZrO_2 addition. With an increase in the amount of NiO/ZrO_2 addition, the UTS of the NiO/ZrO_2 reinforced Sn1.0Ag0.5Cu composite solder clearly increases and then decreases. And the corresponding elongations exhibit a similar trend. For the plain Sn1.0Ag0.5Cu solder, the UTS and elongation are 27.9 MPa and 21.6%, respectively. With the addition of 0.05 mass% NiO/ZrO_2, the UTS and elongation increase to 29.9 MPa and 22.4%, respectively. With the increase of the addition amount, the tensile strength and elongation gradually increased. When the NiO/ZrO_2 addition reached 0.3 mass%, the mechanical properties of composite solder got their maximum value with a tensile strength and elongation of 34.8 MPa and 27.9%, respectively. This result is an increase of 24.7% and 29.2%, respectively, compared to the plain solder. While continue to increase the addition amounts to 0.5 mass%, the UTS and elongation decreased to 30.4 MPa and 24.1%, respectively. This is due to the excessive addition of

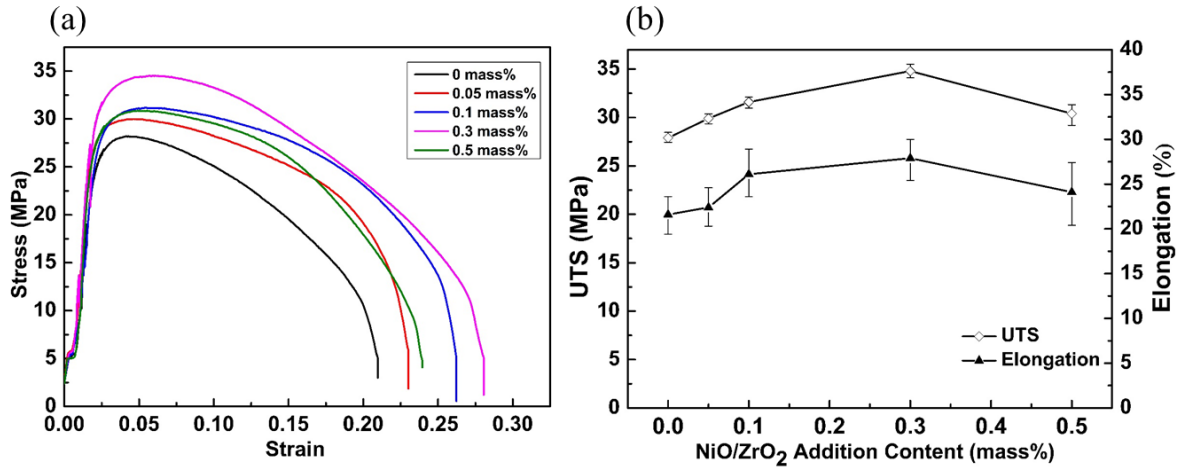

Fig. 3-12 Mechanical properties of Sn1.0Ag0.5Cu composite solders reinforced with various NiO/ZrO_2 addition. (a) Representative stress-strain curves, (b) UTS and elongation.

Table 3-5 Mechanical properties in previous reports [11, 13, 14]

Solder	UTS (MPa)	Elongation (%)	References
Sn1.0Ag0.5Cu composite solder	27.3	19.6	[11]
Plain Sn3.0Ag0.5Cu	34.5	30.5	[13]
Plain Sn1.0Ag0.5Cu	28.6	7.5	[14]

NiO/ZrO_2 to produce partially aggregated NiO/ZrO_2. It could deteriorate the microstructure of the solder, which had mentioned in Fig. 3-6. In summary, when 0.3 mass% NiO/ZrO_2 was added, the UTS and elongation (34.8 MPa and 27.9%) of the composite solder reached their maximum values simultaneously, which are better than those of previously reported nanomaterials reinforced Sn1.0Ag0.5Cu composite solder [11]. The summarized mechanical properties from previous reports are shown in Table 3-5. Meanwhile, compared with commercial Sn3.0Ag0.5Cu [13,14], the UTS result is basically the same, and the elongation is higher than that of commercial Sn3.0Ag0.5Cu. These results suggest that a novel lead-free solder with high strength and ductility can be obtained.

In order to better understand the evolution of mechanical properties and fracture behavior of composite solders, fracture surfaces were observed. Fig. 3-13 shows the photographs of the composite solder samples with various NiO/ZrO_2 addition after tensile tests. And Fig. 3-14 shows the SEM images of fracture surfaces of composite solders reinforced with various

amounts of added NiO/ZrO_2. Fig. 3-14(a) presents the fracture surface of plain Sn1.0Ag0.5Cu solder, which is composed of dimples and cleavage facets, with a ductile–brittle mixed fracture mode. With an increase in the amount of added NiO/ZrO_2, a higher density of dimples is appeared, and the depths of dimple also increased, which mean a large degree of plastic

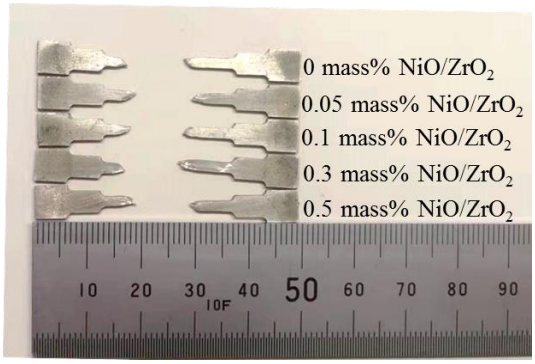

Fig. 3-13 Photographs of the composite solder samples with various NiO/ZrO_2 addition after tensile tests.

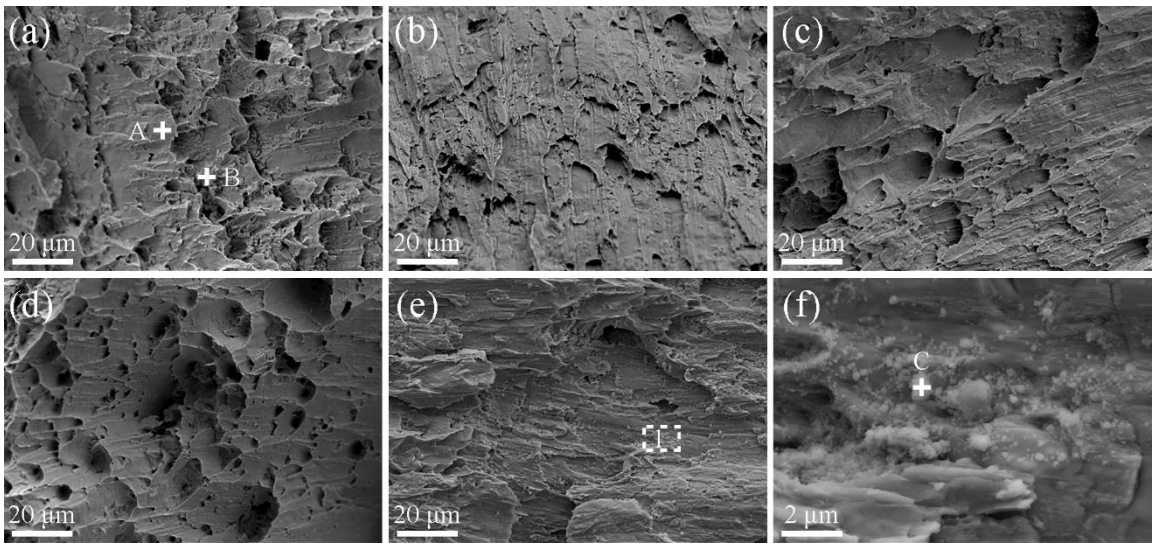

Fig. 3-14 Fracture surfaces of Sn1.0Ag0.5Cu composite solders reinforced with various amounts of added NiO/ZrO_2. (a) 0 mass%, (b) 0.05 mass%, (c) 0.1 mass%, (d) 0.3 mass%, (e) 0.5 mass%, (f) high magnification view of area 1 in (e).

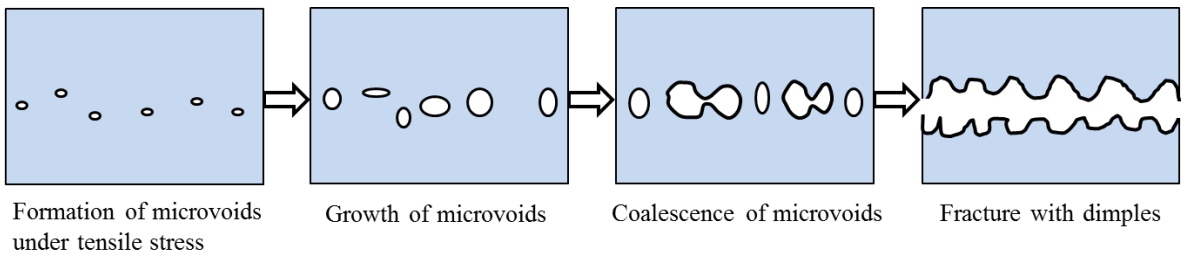

Fig. 3-15 Schematic illustration of formation of microvoid coalescence fracture.

Table 3-6. EDS results of Fig. 3-14 (at. %)

Location	Sn	Ag	Cu	Zr	Ni	O
A	100	-	-	-	-	-
B	92.3	5.2	2.5	-	-	-
C	14.2	-	-	14.7	2.3	68.8

deformation of composite solders. In addition, the proportion of the cleavage surface is reduced. Table 3-6 shows the EDS results of areas A and B in Fig. 3-14(a), which suggests that area A is β-Sn, while area B belongs to the eutectic microstructure. Combining the composition analysis and local fracture morphology, it can be inferred that area A exhibits a microvoid coalescence fracture, where the schematic illustration of formation of microvoid coalescence fracture is shown in Fig. 3-15. whereas the area B exhibits the microvoid coalescence fracture of β-Sn in the eutectic microstructure and cleavage fracture of the IMC (Ag_3Sn and Cu_6Sn_5). With an increase in the NiO/ZrO_2 contents, the number of dimples increased, the cleavage fracture area decreased, and the degree of fracture deformation increased. This is attributed to the refinement of the microstructure of the composite solder, especially the gradual reduction or disappearance of coarse IMCs (shown in Fig. 3-6) after the addition of NiO/ZrO_2. Meanwhile, a micro-mechanical lock and non-micropored clean interface are formed between NiO/ZrO_2 and the solder matrix. Therefore, the effective load transfer can be carried out, which allows the composite solder to withstand a higher degree of strain. This is also the reason for the improvement of the elongation of the composite solder in Fig. 3-12. Therefore, when the amount of reinforcement added reached 0.3 mass% (Fig. 3-14(d)), the fracture surface presents uniform dimples. The fracture mode also transformed from a ductile–brittle mixed fracture consisting of dimples and cleavage planes to the ductile fracture dominated by dimples. The Schematic illustration of evolution of fracture mode is shown in Fig. 3-16.

However, when the amount of reinforcement added reached 0.5 mass% (Fig. 3-14(e)), the number of dimples significantly decreased, indicating a dramatic decrease in the degree of plastic deformation. Fig. 3-14(f) shows the high magnification image of area 1 in Fig. 3-14(e), where some agglomerated particles are distributed on the fracture surface. EDS results (Table

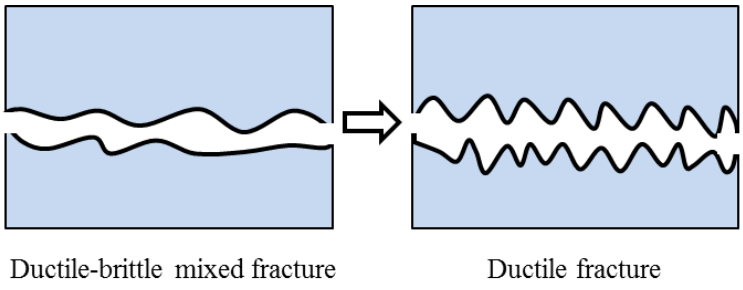

Fig. 3-16 Schematic illustration of evolution of fracture mode.

3-6) of area C in Fig. 3-14(f) suggest that these reunited particles are NiO/ZrO_2. In Fig. 3-6, it had mentioned that excessive NiO/ZrO_2 addition could cause microstructure defects, such as agglomerated enhancement phase (shown in Fig. 3-6(f)). When the tensile sample is subjected to external loads, stress concentration tends to occur at the defect locations, where cracks are generally prone to initiation and propagation, leading to failure of the samples. So agglomerated NiO/ZrO_2 is observed at the fracture surface (Fig. 3-14 (f)). This is also the reason why the mechanical properties of composite solder were decreased when NiO/ZrO_2 added excessively.

In summary, when the addition amount of NiO/ZrO_2 is within a certain range (0–0.3mass%), the mechanical properties of the composite solder gradually increased with an increase in the addition amount, and the corresponding fracture mechanism also transformed from a ductile–brittle mixed fracture consisting of dimples and cleavage planes to the ductile fracture dominated by dimples. While excessive NiO/ZrO_2 addition could deteriorate the microstructure of the composite solder, thereby reducing the mechanical properties.

3.5.2 Strengthening-ductility mechanism

In this study, the mechanical properties of NiO/ZrO_2 reinforced Sn1.0Ag0.5Cu composite solder were improved compared with the plain solder. The strengthening-ductility mechanism can be summarized as Orowan strengthening effect, grain refinement effect, and thermal misfit dislocation effect.

Among the three mechanisms, Orowan strengthening mechanism was the main strengthening mechanism in improving the mechanical properties of composite solders [15]. The effective implementation of the Orowan strengthening mechanism is mainly attributed to

the appropriate choice of reinforcement and its dispersed distribution. In this study, ZrO_2 was selected as the reinforcement among many candidates, its advantages have mentioned in introduction part. Moreover, the size of ZrO_2 belongs to nano-sized level, which could produce a significant strengthening effect [16]. On the other hands, these nanoparticles were dispersed in a solder matrix assisted by ultrasonic stirring, which has mentioned in Fig. 3-7. Compared with previous studies [11,14], better results was obtained, which were mainly attributed to the design of Sn/NiO/ZrO_2 interface system based on mutual solid solution, forming a micro-mechanical lock and non-micropored clean interface between NiO/ZrO_2 and the Sn1.0Ag0.5Cu solder matrix. Thus, the lead-free solder with high strength and ductility was obtained.

3.6 Conclusions

The effects of NiO/ZrO_2 addition on the microstructure, melting behaviors and mechanical properties of composite solder were systematically investigated. The major findings are as follows:

1. An appropriate addition amount (0–0.3 mass%) of NiO/ZrO_2 can improve the microstructure of composite solders, which the eutectic and β-Sn were refined. The refinement mechanism of NiO/ZrO_2 on the microstructure was investigated with the TEM observation. NiO/ZrO_2 were relatively dispersed and uniformly distributed in the eutectic microstructure area, acting as the heterogeneous nuclear sites in eutectic area. On the other hand, reinforcements distributed at the grain boundary can hinder the grain boundary migration by the pinning effect.
2. A micro-mechanical lock and non-micropored clean interface was formed between NiO/ZrO_2 and Sn1.0Ag0.5Cu solder matrix. The Sn/NiO/ZrO_2 interface system based on mutual solid solution was ingenious designed.
3. In a certain addition range of NiO/ZrO_2 (0–0.3 mass%), the mechanical properties of the composite solder gradually increased. The fracture mechanism also transformed from the ductile–brittle mixed fracture consisting of dimples and cleavage planes to the ductile fracture dominated by dimples. When the NiO/ZrO_2 addition reached 0.3 mass%, the

maximum tensile strength and elongation of 34.8 MPa and 27.9%, respectively, were obtained. This result is an increase of 24.7% and 29.2%, respectively, compared to the plain Sn1.0Ag0.5Cu solder.

References

[1] F. Wang, M. O'Keefe, B. Brinkmeyer, Microstructural evolution and tensile properties of Sn-Ag-Cu mixed with Sn-Pb solder alloys, J. Alloys Compd. 477 (2009) 267–273. https://doi.org/10.1016/j.jallcom.2008.10.141.

[2] B.A. Feldhoff, E. Pippel, J. Woltersdorf, Interface Engineering of Carbon-Fiber Reinforced Mg ± Al Alloys, 2 (2000) 471–480. https://doi.org/10.1002/1527-2648(200008)2:8<471::AID-ADEM471>3.0.CO;2-S.

[3] N. Barreau, T. Painchaud, F. Couzini é-Devy, L. Arzel, J. Kessler, Recrystallization of CIGSe layers grown by three-step processes: A model based on grain boundary migration, Acta Mater. 58 (2010) 5572–5577. https://doi.org/10.1016/j.actamat.2010.06.025.

[4] H. Che, X. Jiang, N. Qiao, X. Liu, Effects of Er/Sr/Cu additions on the microstructure and mechanical properties of Al–Mg alloy during hot extrusion, J. Alloys Compd. 708 (2017) 662–670. https://doi.org/10.1016/j.jallcom.2017.01.039.

[5] C. Villada, F. Jaramillo, J.G. Casta ño, F. Echeverr á, F. Bol ívar, Design and development of nitrate-nitrite based molten salts for concentrating solar power applications, Sol. Energy. 188 (2019) 291–299. https://doi.org/10.1016/j.solener.2019.06.010.

[6] A. Bonk, S. Sau, N. Uranga, M. Hernaiz, T. Bauer, Advanced heat transfer fluids for direct molten salt line-focusing CSP plants, Prog. Energy Combust. Sci. 67 (2018) 69–87. https://doi.org/10.1016/j.pecs.2018.02.002.

[7] A.A. El-Daly, A.E. Hammad, G.S. Al-Ganainy, M. Ragab, Influence of Zn addition on the microstructure, melt properties and creep behavior of low Ag-content Sn-Ag-Cu lead-free solders, Mater. Sci. Eng. A. 608 (2014) 130–138. https://doi.org/10.1016/j.msea.2014.04.070.

[8] G. Chen, F. Wu, C. Liu, V. V. Silberschmidt, Y.C. Chan, Microstructures and properties of new Sn-Ag-Cu lead-free solder reinforced with Ni-coated graphene nanosheets, J. Alloys Compd. 656 (2016) 500–509. https://doi.org/10.1016/j.jallcom.2015.09.178.

[9] Y.D. Han, S.M.L. Nai, H.Y. Jing, L.Y. Xu, C.M. Tan, J. Wei, Development of a Sn-Ag-Cu solder reinforced with Ni-coated carbon nanotubes, J. Mater. Sci. Mater. Electron. 22 (2011) 315–322. https://doi.org/10.1007/s10854-010-0135-6.

[10] A.A. El-Daly, T.A. Elmosalami, W.M. Desoky, M.G. El-Shaarawy, A.M. Abdraboh, Tensile deformation behavior and melting property of nano-sized ZnO particles reinforced Sn-3.0Ag-0.5Cu lead-free solder, Mater. Sci. Eng. A. 618 (2014) 389–397. https://doi.org/10.1016/j.msea.2014.09.028.

[11] A.A. El-Daly, A. Fawzy, S.F. Mansour, M.J. Younis, Novel SiC nanoparticles-containing Sn-1.0Ag-0.5Cu solder with good drop impact performance, Mater. Sci. Eng. A. 578 (2013) 62–71. https://doi.org/10.1016/j.msea.2013.04.022.

[12] R. Abbaschian, M.D. Lipschutz, Eutectic solidification processing via bulk melt undercooling, Mater. Sci. Eng. A. 226–228 (1997) 13–21. https://doi.org/10.1016/s0921-5093(97)80022-6.

[13] F.X. Che, E.C. Poh, W.H. Zhu, B.S. Xiong, Ag content effect on mechanical properties of Sn–xAg–0.5Cu solders, Proc. Electron. Packag. Technol. Conf. EPTC. (2007) 713–718. https://doi.org/10.1109/EPTC.2007.4469808.

[14] Z. Yang, W. Zhou, P. Wu, Effects of Ni-coated carbon nanotubes addition on the microstructure and mechanical properties of Sn-Ag-Cu solder alloys, Mater. Sci. Eng. A. 590 (2014) 295–300. https://doi.org/10.1016/j.msea.2013.10.008.

[15] Y. Geng, Y. Ban, X. Li, Y. Zhang, Y. Jia, B. Tian, M. Zhou, Y. Liu, A.A. Volinsky, K. Song, S. Tang, Excellent mechanical properties and high electrical conductivity of Cu-Co-Si-Ti alloy due to multiple strengthening, Mater. Sci. Eng. A. 821 (2021). https://doi.org/10.1016/j.msea.2021.141639.

[16] Z. Zhang, D.L. Chen, Consideration of Orowan strengthening effect in particulate-reinforced metal matrix nanocomposites: A model for predicting their yield strength, Scr. Mater. 54 (2006) 1321–1326. https://doi.org/10.1016/j.scriptamat.2005.12.017.

Chapter 4 Microstructure and properties of NiO/T-ZnO_w reinforced Sn1.0Ag0.5Cu composite solders

4.1 Introduction

In chapter 3, the NiO/ZrO_2 reinforced Sn1.0Ag0.5Cu composite solder was prepared via the ultrasonic stirring method. And the effect of NiO/ZrO_2 on the microstructure and properties of composite solder were systematically investigated. In this chapter, the effect of single reinforcement NiO/T-ZnO_w on the microstructure and properties of composite solder were investigated. NiO/T-ZnO_w reinforced Sn1.0Ag0.5Cu composite solder was prepared with ultrasonic stirring. The microstructure evolution of composite solders was systematically investigated. The interface between reinforcement and solder matrix was also explored. Moreover, the melting point and mechanical properties of composite solders were also studied.

4.2 Experimental procedure

4.2.1 Materials

The reinforcement of NiO/T-ZnO_w was prepared with the pyrolysis method based on the self-assembly. According to the chapter 2, 20% Ni/Zn molar ratio was the the optimized surface modification process parameter. The detailed fabrication program and morphology of NiO/T-ZnO_w are shown in chapter 2. The commercial Sn1.0Ag0.5Cu solder bar was provided by Senju Metal Industry Co. Ltd. Japan.

4.2.2 Fabrication of composite solders using ultrasonic stirring

A commercial Sn1.0Ag0.5Cu solder bar was melted at 380 °C in a furnace. Subsequently, different mass fractions (0, 0.05, 0.1, 0.3, 0.5, and 0.7 mass%) of the NiO/T-ZnO_w reinforcement were added to the molten solder, respectively. Due to the surface tension of the molten solder, the reinforcement could not be well dispersed. Ultrasonic vibration-assisted stirring was applied to the mixture at the ultrasonic power of 80 W for 4 min, respectively. After ultrasonic vibration, the oxide film on the surface of the molten solder was removed and

quickly cast molten into a stainless steel mold with the size of 50 mm × 10 mm × 5 mm (L × W × H).

4.2.3 Characterization and testing

X-ray diffraction (XRD, Ultima IV, Rigaku, Japan) was used to characterize the phase and crystalline structures of the NiO/T-ZnO_w reinforced Sn1.0Ag0.5Cu composite solders. Scanning electron microscopy (SEM, SU-70, Hitachi, Japan) equipped with energy-dispersive X-ray spectroscopy (EDS) was used to observe the microstructure and fracture surface of the composite solders. The size of these phases was measured with Nano Measurer software. Fig. 4-1 shows the typical example used for the measurement. Three SEM images were selected for each composition, and about 30 β-Sn and 100 IMC phases were measured for each composition, respectively. The interface between reinforcement and solder matrix were investigated using transmission electron microscopy (TEM, JEOL JEM 2100F) equipped with EDS at an acceleration voltage of 200 kV. The TEM samples of the composite solder were prepared with the focused ion beam (FIB, HITACHI FB-2000A).

The melting behavior of composite solder was examined by differential scanning calorimetry (DSC; 7020 clinical analyzer, Hitachi, Japan) under a constant flow of N_2 in the range of 25–300 °C at a rate of approximately 10 °C/min. These composite solder bars were formed into the tensile test samples using an electrical discharge machine (AG360L). The

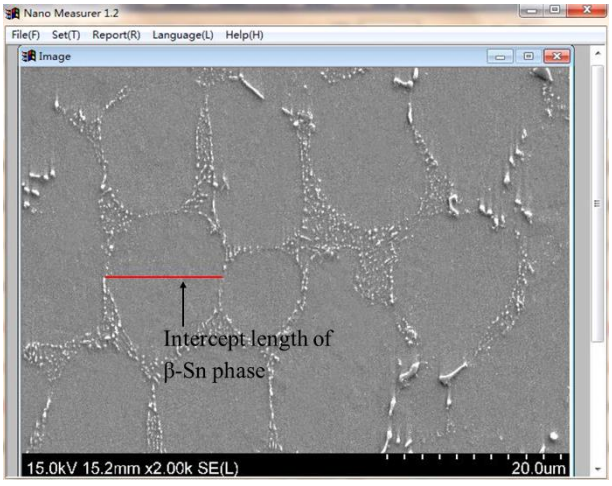

Fig. 4-1 Typical example of the mean intercept length measurement.

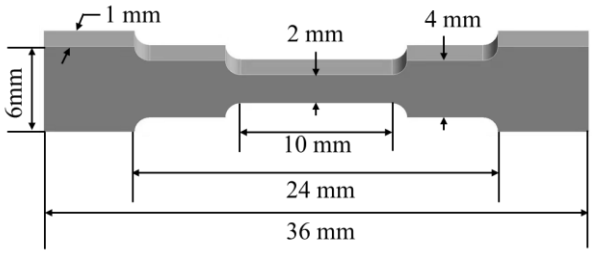

Fig. 4-2 The schematic diagram of the tensile test sample.

schematic diagram of the tensile test sample is shown in Fig. 4-2. The sample gauge length was 10 mm, and the width and thickness were 2 mm and 1 mm, respectively. The tensile tests were performed using a universal electrical tensile tester (Autograph AG-X Shimazu, Japan) with a strain rate of 0.0005/s. The experimental results were the average values of four tensile samples.

4.3 Microstructure evolution of composite solders reinforced with various NiO/T-ZnO_w additions

Fig. 4-3 shows the XRD patterns of the plain Sn1.0Ag0.5Cu and 0.3 mass% NiO/T-ZnO_w reinforced Sn1.0Ag0.5Cu composite solders. For the plain solder (downside with black color), characteristic peaks of β-Sn, Ag_3Sn and Cu_6Sn_5 were observed at 30.6°, 32.0°, 43.9°, 44.9°, 55.3°, 62.5°, 64.6° and 79.5°, 34.6°, and 62.6°, corresponding to the (200), (101), (220), (211), (301), (112), (321), and (312) planes of β-Sn, (111) planes of Ag_3Sn, and $(22\bar{6})$ planes of Cu_6Sn_5, respectively. Meanwhile, in addition to the characteristic peaks of the above three phases, the characteristic peaks of T-ZnO_w were detected at 31.8° and 34.4° for the composite solder (upside with red color), corresponding to the (100) and (101) planes of T-ZnO_w. However, characteristic peaks of NiO were not detected due to its low content. These XRD results indicate that the reinforcement was successfully added to the solder matrix.

Fig. 4-4 shows SEM images of the Sn1.0Ag0.5Cu plain solder and composite solders reinforced with various NiO/T-ZnO_w additions. As seen in Fig. 4-4(a), the microstructure of plain Sn1.0Ag0.5Cu solder was composed of β-Sn and eutectic structure; β-Sn presented round or elliptical shape, while the eutectic structure was distributed in a network structure. A magnified view of the eutectic structure (area 1) in Fig. 4-4(a) is shown in Fig. 4-5(a), including the binary eutectic consisting of β–Sn+Cu_6Sn_5, β–Sn+Ag_3Sn, and ternary eutectic consisting

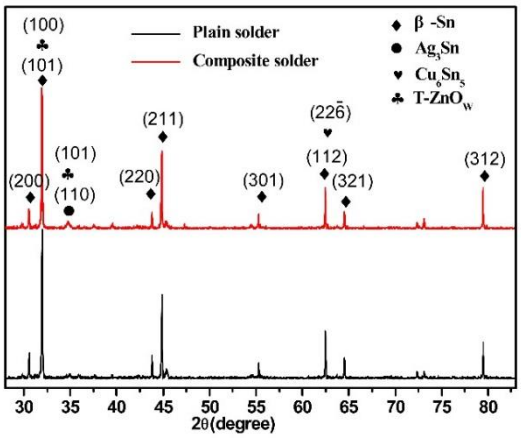

Fig. 4-3 XRD patterns of plain Sn1.0Ag0.5Cu and 0.3 mass% NiO/T-ZnO_w reinforced Sn1.0Ag0.5Cu composite solder.

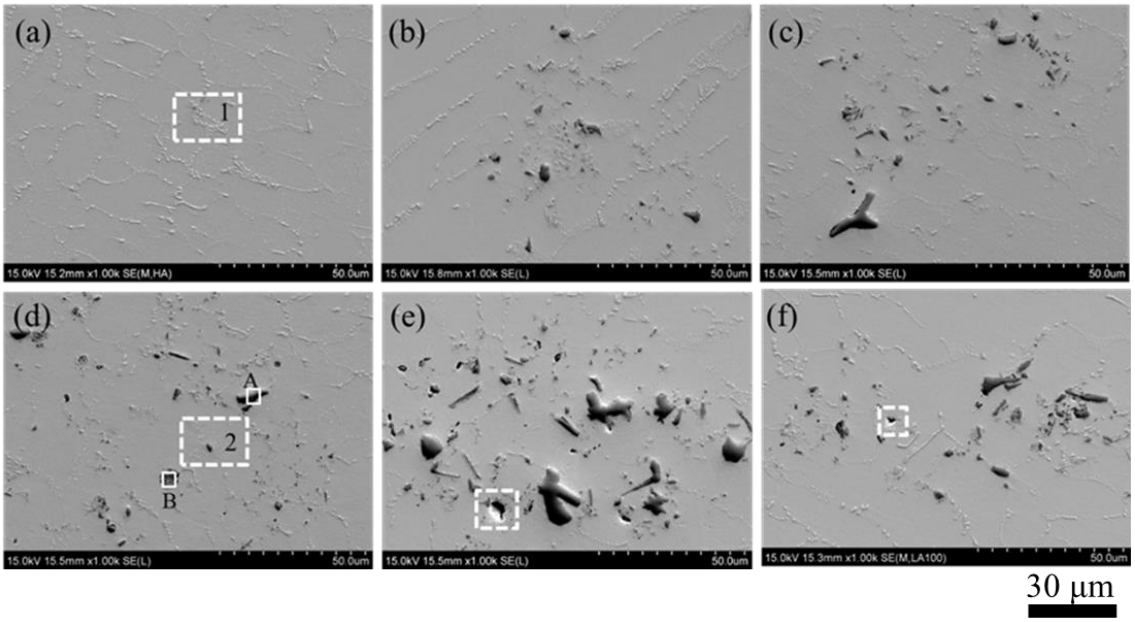

Fig. 4-4 SEM images of plain Sn1.0Ag0.5Cu and composite solders with different NiO/T-ZnO_w additions. (a) 0 mass%; (b) 0.05 mass%; (c) 0.1 mass%; (d) 0. 3 mass%; (e) 0.5 mass%; (f) 0.7 mass%.

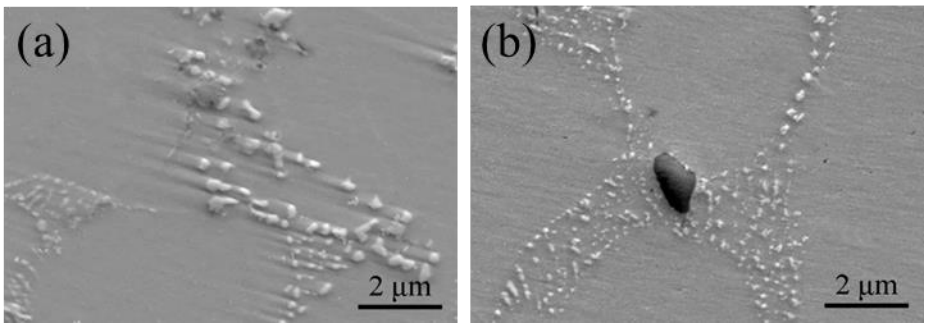

Fig. 4-5 Magnified view of the eutectic structure. (a) magnified views of area 1 in Fig. 4-4(a), (b) magnified views of area 2 in Fig. 4-4(d).

Table 4-1. EDS results of the black phase in Fig. 4-4 (at. %)

Location	Sn	Zn	Ni	O
A	2.73	45.22	1.03	51.02
B	8.44	41.41	1.21	48.94

of β–Sn+Cu_6Sn_5+Ag_3Sn [1]. The average size of β-Sn was about 21.2 μm with an aspect ratio of about 1.9. And the average size of IMC (Ag_3Sn and Cu_6Sn_5) in eutectic area was about 0.2 μm. But the morphology and size of Ag_3Sn and Cu_6Sn_5 cannot be distinguished clearly using SEM. However, it is very important to understand the formation, morphology and size of Ag_3Sn and Cu_6Sn_5 to study the mechanical properties of the solder and its joint [2,3]. Therefore, the TEM observation will be conducted below.

Fig. 4-4(b)-(f) show SEM images of composite solders reinforced with various NiO/T-ZnO_w additions. Many dark coloured phases can be observed; related EDS results are shown in Table 4-1. Combining the EDS and XRD results, these black phases were inferred to be T-ZnO_w. In addition, Ni was also detected, indicating that the NiO nanoparticles remained attached to the surface of T-ZnO_w. Overall, the reinforcing phases are evenly distributed in the solder matrix, and neither gaps nor micropores were found at the interface, indicating a good combination. The dispersed distribution of NiO/T-ZnO_w is attributed to the application of ultrasonic vibration. When ultrasonic vibration was applied to the melt, the cavitation effect and the acoustic flow effect occurred. The cavitation effect refers to the formation of cavitation bubbles in the melt under alternating positive and negative pressures of ultrasonic vibration [4]. The cavitation bubble expands rapidly and bursts. During the process, instantaneous high pressure impact force is generated, which can make the agglomerated NiO/T-ZnO_w dispersed. In addition, ultrasonic vibration can also produce acoustic streaming effects [5]. The eddy current effect produced by the acoustic current can effectively homogenize the processed melt. Moreover, in the range of 0-0.5 mass%, with the increase of reinforcing phase addition, the amount of black phase in the SEM image gradually increases, indicating that the reinforcements were effectively added to the solder matrix. The observed reinforcement presented needle-like, round-like, dot-like, and Y-like shapes, attributed to the random

distribution of NiO/T-ZnO_w in the solder matrix. The random distribution of NiO/T-ZnO_w and its unique three-dimensional structure ensured isotropic properties in the NiO/T-ZnO_w reinforced Sn1.0Ag0.5Cu composite solder, which was unavailable in composite solders reinforced by other whiskers.

When the added contents of NiO/T-ZnO_w reached 0.05 mass%, NiO/T-ZnO_w is sparsely distributed in the solder matrix. The size of β-Sn is slightly reduced. And the size of IMC in eutectic microstructure wasalso refined where the reinforcements were enriched because NiO/T-ZnO_w can act as heterogeneous nucleation sites. With the increase of the addition amount, the size of β-Sn gradually decreases, the proportion of eutectic structure increases, and the size of IMC in the eutectic structure becomes smaller than plain Sn1.0Ag0.5Cu. When NiO/T-ZnO_w reaches 0.3 mass%, The shape of β-Sn changes from long strip to ellipse. The average size of β-Sn was about 16.4 μm. A magnified view of the eutectic structure (area 2) in Fig. 4-4(d) is shown in Fig. 4-5(b), the IMC size was significantly decreased to 0.1 μm, which is reduced by 50.0% compared with plain Sn1.0Ag0.5Cu solder. When the addition amount reaches 0.5 mass %, the NiO/T-ZnO_w is densely distributed in the solder matrix with different shapes, but some micropores (marked with dotted frame) were observed. This may be due to excessive addition of reinforcements. Excessive addition could reduce the fluidity of composite solder, causing micropores to be formed during the solidification process. These defects could deteriorate the microstructure, thereby reducing the mechanical properties of composite solders. Similarly, the content of 0.7 mass% NiO/T-ZnO_w addition was too high to add to the solder matrix effectively. This is also the reason why the number of enhancement phases in Fig. 4-4(f) is less than that in Fig. 4-4(e). In summary, the proper addition of the reinforcements can effectively improve the microstructure of the composite solders. In contrast, excessive addition could cause structural defects, which may weaken the enhancing effect of the reinforcements.

Additionally, some interesting phenomena should be noted. NiO/T-ZnO_w was mainly distributed in the eutectic zone. This is because the reinforcements remained in the solid state during the solidification process. In the early stage of solidification, solid β-Sn was first generated, and then NiO/T-ZnO_w was pushed to the front of the solid–liquid interface

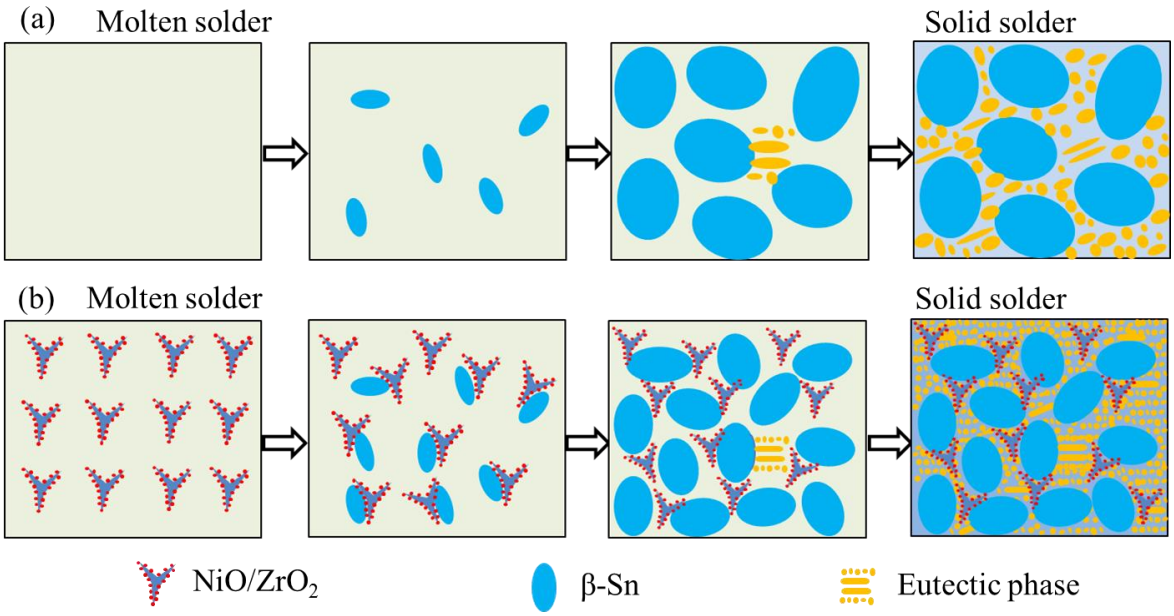

Fig. 4-6 Schematic illustration of solidification process of solders. (a) Plain Sn1.0Ag0.5Cu solder, (b) NiO/T-ZnO_w reinforced Sn1.0Ag0.5Cu composite solder.

composed of β-Sn and liquid solder. As the molten solder cooled, the reinforcement was finally located in the eutectic area with a low melting point. In the later stage of solidification, the eutectic structure was formed. the schematic illustration of solidification process of plain and composite solders is shown in Fig. 4-6. On the one hand, the solid NiO/T-ZnO_w reinforcements acted as heterogeneous nucleation sites for the eutectic, thereby achieving the grain refinement effect; on the other hands, the grain growth was achieved through grain boundary migration [6], and the NiO/T-ZnO_w could hinder the grain boundary movement owing to its pinning effect. Both of the two factors could reduce the grain size of IMC in the eutectic structure, as confirmed by the smaller IMC with the addition of NiO/T-ZnO_w (Fig. 4-5(b)). This is also one of the reasons for the improved mechanical properties in the composite solder.

To better understand the formation, morphology and size of Ag_3Sn and Cu_6Sn_5, the TEM observation was conducted. Fig. 4-7 shows the TEM, SAED, and EDS images of plain Sn1.0Ag0.5Cu solder. From Fig. 4-7(a), IMCs with different shapes such as granules, short rods, and needles were distributed in the β-Sn matrix. These IMCs in β-Sn can be roughly divided into two types depending on their locations: inside the β-Sn grains (such as area 1 in Fig. 4-7(a)) and at the grain boundary of β-Sn (such as areas 2 and 3 in Fig. 4-7(a)). The former

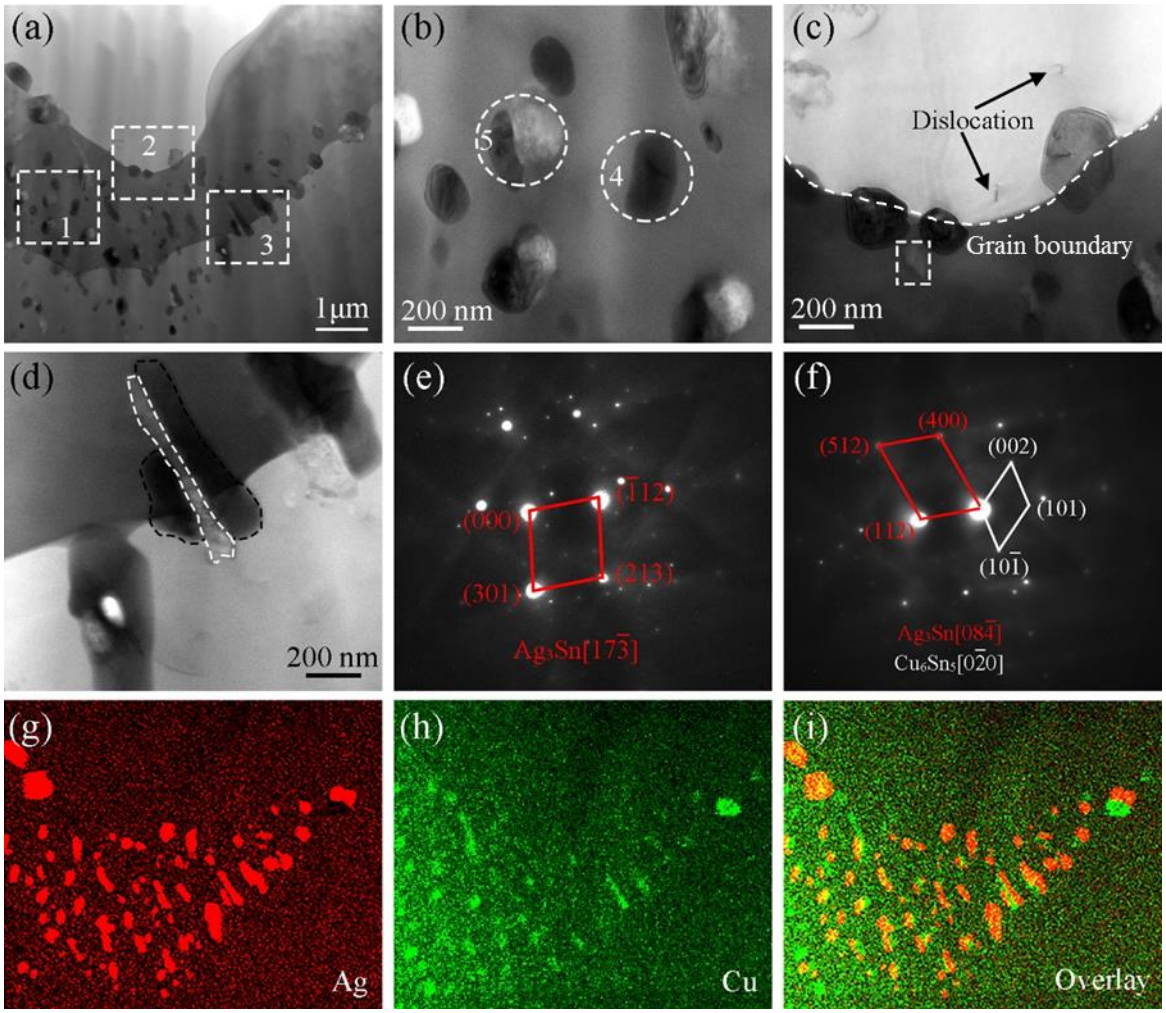

Fig. 4-7 TEM images of (a) plain Sn1.0Ag0.5Cu solder, (b) magnified view of area 1, (c) magnified view of area 2, (d) magnified view of area 3. (e) SAED of area 4, (f) SAED of area 5. EDS maps of (g) Ag, (h) Cu, and (i) their overlay.

type of IMC has a smaller average size than the latter. This was because there was a higher energy at the grain boundary than inside the grain [7], which is more conducive to the nucleation of IMC. Additionally, the size of IMC located at the grain boundaries also differ among themselves. Those precipitated at sharp corners of the grain boundary had a larger size, which is attributed to the higher energy at those locations compared with the flat locations.

Fig. 4-7(b) is a magnified view of area 1 in Fig. 4-7(a), where two types of IMC particles with black and bright colors were distributed in β-Sn. Some of the dark-colored IMC existed alone, whereas others were attached to bright IMC. In contrast, most of the bright-colored IMCs were attached to the black ones and rarely existed alone. To detect the phases of dark and

bright-colored IMC, SAED analysis was conducted. The SAED pattern of area 4 in Fig. 4-7(b) is shown in Fig. 4-7(e), which can be assigned to the ($\bar{1}$12), (301) and (213) planes of Ag_3Sn along the [17$\bar{3}$] axis, indicating that the dark-colored phase was Ag_3Sn. Similarly, the SAED pattern of area 5 in Fig. 4-7(b) is shown in Fig. 4-7(f), with two phases detected according to the diffraction spot. These phases can be assigned to the Ag_3Sn (112), (400), and (512) planes along the [08$\bar{4}$] axis; and Cu_6Sn_5 (10$\bar{1}$), (002), and (101) planes along the [0$\bar{2}$0] axis. Combining the results in Fig. 4-7(e), it can be inferred that the bright phase was Cu_6Sn_5. In addition, the EDS results in Figs. 4-5(g)-(i) show that the dark-colored phase contained Ag element and the bright-colored one contained Cu, which further prove that the phase with dark color and bright color were Ag_3Sn and Cu_6Sn_5, respectively.

The magnified image of area 2 in Fig. 4-7(a) is shown in Fig. 4-7(c). Ag_3Sn (IMC with dark color) was precipitated at the grain boundary, and an isolated Cu_6Sn_5 IMC was also observed near the Ag_3Sn (marked with a dashed frame). In addition, a few dislocations were observed near the grain boundary, which may be attributed to the different coefficients of thermal expansion (CTE) between Ag_3Sn and β-Sn ($CTE_{(Ag3Sn)} = 18.29 \times 10^{-6}$/K and $CTE_{(\beta\text{-}Sn)} = 14.96 \times 10^{-6}$/K [8]). Fig. 4-7(d) shows the magnified image of area 3 in Fig. 4-7(a), where needle-shaped Ag_3Sn and Cu_6Sn_5 grew depending on each other. For example, a sandwich structure of $Ag_3Sn/Cu_6Sn_5/Ag_3Sn$ (marked with a dashed line) was formed at the grain boundary.

The existence of Ag_3Sn and Cu_6Sn_5, either separately or in mutual dependence, can be explained by Eqs. (4-1)–(4-4) [9]:

$$L \rightarrow \beta\text{-}Sn\ (231.9\ °C) \quad (4\text{-}1)$$

$$L \rightarrow \beta\text{-}Sn + Cu_6Sn_5\ (227\ °C) \quad (4\text{-}2)$$

$$L \rightarrow \beta\text{-}Sn + Ag_3Sn\ (221\ °C) \quad (4\text{-}3)$$

$$L \rightarrow \beta\text{-}Sn + Cu_6Sn_5 + Ag_3Sn\ (217\ °C) \quad (4\text{-}4)$$

Eq. (4-2) occurred after the crystallization of primary β-Sn was completed (Eq. (4-1)), and the Cu_6Sn_5 (marked with dashed box in Fig. 4-7(c)) was generated at this stage. Subsequently,

the eutectic reaction (Eq. (4-3)) produced β-Sn and Ag_3Sn, corresponding to isolated Ag_3Sn that existed in β-Sn of Fig. 4-7(b) and at the grain boundary in Fig. 4-7(c). Finally, the ternary eutectic reaction occurred (Eq. (4-4)), and Ag_3Sn and Cu_6Sn_5 that are interdependent in Fig. 4-7(b) and Fig. 4-7(d) were formed at this stage.

These IMCs in the β-Sn and at the grain boundary could play a role of dispersion strengthening and pinning effect, which are the reasons why the Sn based solder has a higher strength than that of pure Sn [10]. However, IMC will grow in the SnAgCu solder during long-term service, which weakens the strengthening effect and reduces plasticity due to the inherent brittleness of IMC [11,12]. Therefore, it is a suitable choice to improve the mechanical properties of the solder by adding the reinforcement that does not react with the matrix and does not grew during long service period.

4.4 Interface of NiO/T-ZnO_w reinforced Sn1.0Ag0.5Cu composite solder

In order to investigate the interface between the solder matrix and reinforcement, high magnified SEM image was conducted. Fig. 4-8 shows the interface of the NiO/T-ZnO_w reinforced Sn1.0Ag0.5Cu composite solder. As can be seen from Fig. 4-8(a), T-ZnO_w was tightly embedded in the solder matrix and no gaps or micropores were observed at the interface, indicating that the solder matrix and reinforcement were well bonded at the micrometer scale. Magnified views of areas 1 and 2 in Fig. 4-8(a) are shown in Fig. 4-8(b) and Fig. 4-8(c), respectively. No micropores appeared, but some small-sized IMCs (marked by dashed frame) were generated at the interface. This is because the NiO/T-ZnO_w reinforcement could act as heterogeneous nucleation sites for IMC during solidification, similar to the results presented in Fig. 4-4(d).

TEM observation was conducted to further explore the interfacial relationship between the solder matrix and reinforcement at the nanometer scale and to check whether new phase was formed at the interface. Fig. 4-9 shows the TEM, EDS, and SAED images of the NiO/T-ZnOw reinforced Sn1.0Ag0.5Cu composite solder. In Fig. 4-9(a)–(e), the phase on the upper side is T-ZnO_w, the lower side is the solder matrix, and a thin NiO transition layer exists between them. The thickness of the transition layer was approximately 16.2 nm, which is

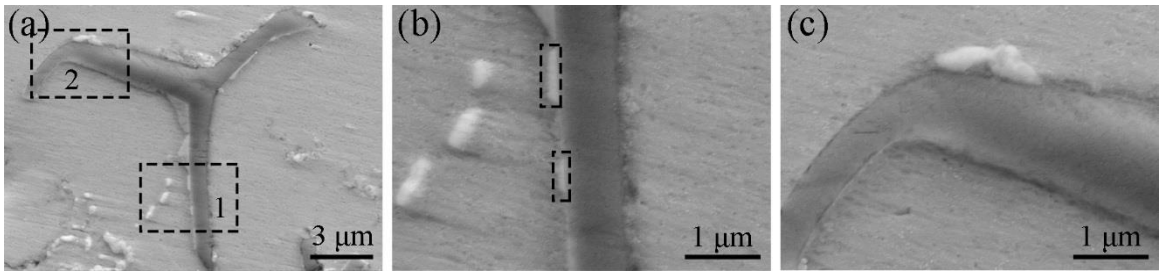

Fig. 4-8 SEM images of (a) the interface of NiO/T-ZnO_w reinforced Sn1.0Ag0.5Cu composite solder, (b) magnified views of area 1, (c) magnified view of area 2.

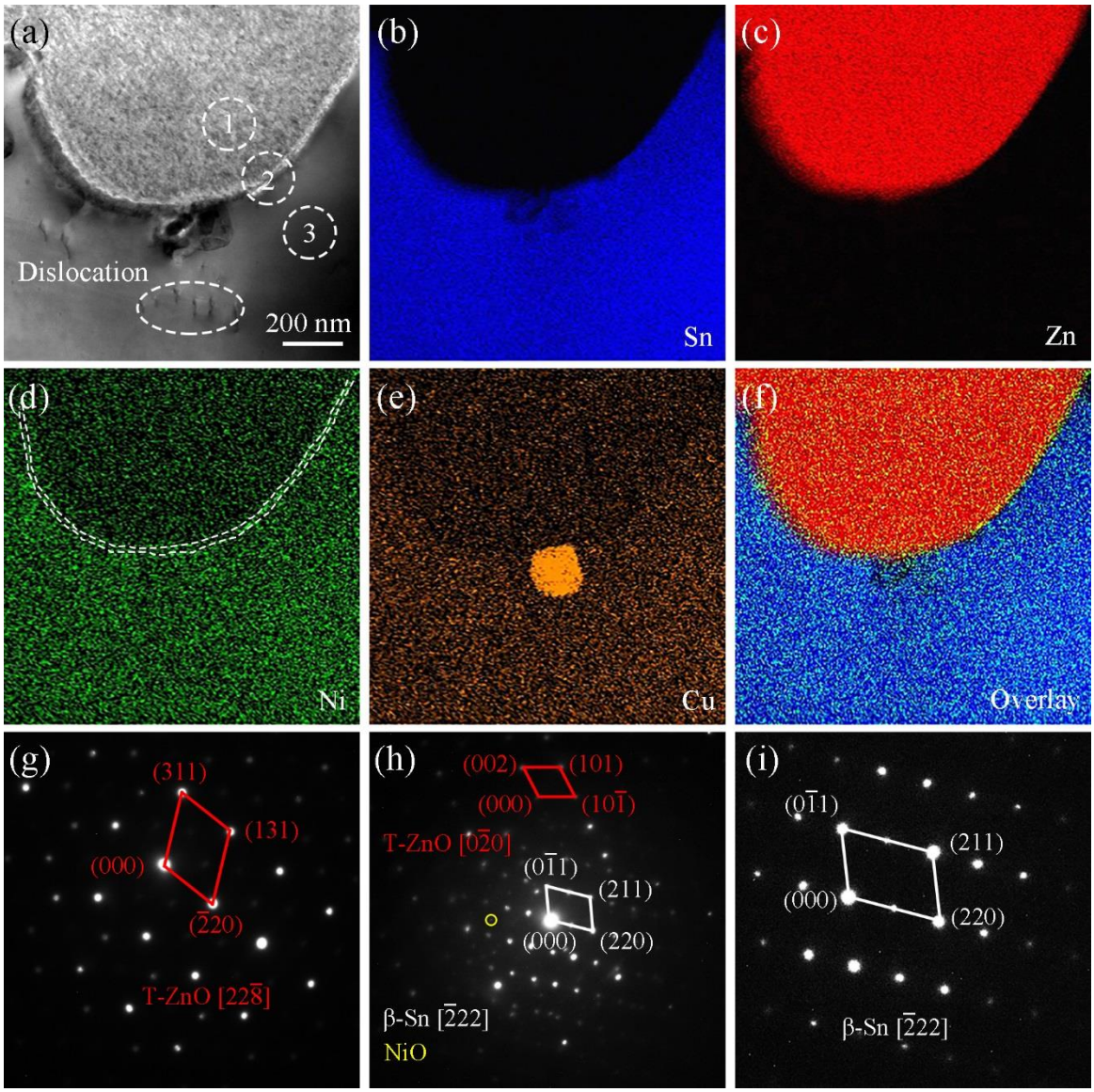

Fig. 4-9 TEM images of (a) the interface of NiO/T-ZnO_w reinforced Sn1.0Ag0.5Cu composite solder. EDS maps of (b) Sn, (c) Zn, (d) Ni, (e) Cu, and (f) the overlay of Sn, Zn, and Ni. SAED patterns of (g) area 1, (h) area 2, and (i) area 3 in Fig. 4-9(a).

basically consistent with the results observed in Fig. 2-19(a) in chapter 2. Additionally, neither nanogaps nor nanopores were found at the interface. Fig. 4-9(f) shows the overlay of Sn, Zn, and Ni mappings, indicating that both Sn and Zn elements existed in the NiO layer area. Thus, atomic inter-diffusion occurred at the interface, constituting an effective way of bonding. In addition, NiO can be found at the interface of the composite solder, indicating its relative stability during the preparation process of the composite solder and also suggesting good bonding between NiO and T-ZnO_w.

An ideal interface needs to avoid not only gaps and pores but also the reaction between NiO/T-ZnO_w and the solder matrix to form brittle IMC at the interface, which will deteriorate the performance of the composite solder. SEAD was conducted to detect whether new phase was formed. First, the selected area aperture was located at the T-ZnO_w zone (area 1 of Fig. 4-9(a)) to obtain diffraction spots, and then the selected area was continuously moved until it passed through the interface and reached the solder matrix. Three representative zones (area1, area2, and area3 of Fig. 4-9(a)) are displayed here. Fig. 4-9(g) shows the pattern of area 1 in Fig. 4-9(a), which can be calibrated as T-ZnO_w ($\bar{2}20$), (311), and (131) planes with the [$22\bar{8}$] axis. The SAED pattern of area 2 is shown in Fig. 4-9(h), through which three phases, T-ZnO_w, β-Sn, and NiO, can be identified. Similarly, the SAED pattern of area 3 shows the ($0\bar{1}1$), (220), and (211) planes of β-Sn along the [$\bar{2}22$] axis. According to the above SAED results, it can be inferred that no other phases were detected except for Sn1.0Ag0.5Cu, NiO, ZnO. In other words, no new phases were generated, and the clean interface was obtained. In summary, no gaps, no micropores, and no new phases was generated at the interface of NiO/T-ZnO_w reinforced Sn1.0Ag0.5Cu composite solder, which suggest that the Sn1.0Ag0.5Cu/NiO/T-ZnO_w composite interface structure was well designed. This interface is an important factor in the strengthening and ductility of the composite solder.

In addition, it can be seen from Fig. 4-9(a) and Fig. 4-9(e) that Cu_6Sn_5 IMC with small size is observed near the interface. This is because NiO/T-ZnO_w could act as heterogeneous nucleation sites during the solidification process, as similar results were observed in Fig. 4-

5(b) and Fig. 4-8(b). On the lower side of Cu_6Sn_5 (Fig. 4-9(a)), dislocation was observed, which was caused by the different coefficients of thermal expansion of Sn1.0Ag0.5Cu, NiO and T-ZnO_w (($CTE_{(Sn1.0Ag0.5Cu)}$ = 25.0 × 10^{-6}/K [13], ($CTE_{(NiO)}$ = 13.8 × 10^{-6}/K [14], and $CTE_{(ZnO)}$ = 2.0 × 10^{-6}/K [15]). Thermal misfit dislocations were also one of the reasons for the increased strength of the composite solder [16].

4.5 Melting properties of the composite solders

Melting property is one of the important properties of solder, since it mainly determines the process temperature. In this study, endset temperature during heating was defined as the melting point, and the pasty temperature refers to the difference between endset and onset during heating [17,18]. Fig. 4-10 shows the DSC curves of plain SAC105 and NiO/T-ZnO_w reinforced SAC105 composite solders. And critical data are summarized in Table 4-2. two endothermic peaks can be observed during heating process, corresponding to the melting of eutectic microstructure and primary β-Sn [19]. With the increase of NiO/T-ZnO_w addition, T_{Onset} and T_{Endset} have little changes during heating process, which indicated the melting points of composite solder have little difference compared with plain solder. The melting points of composite solders were in the range of 226.7-227.4 °C. Generally, the melting property is an

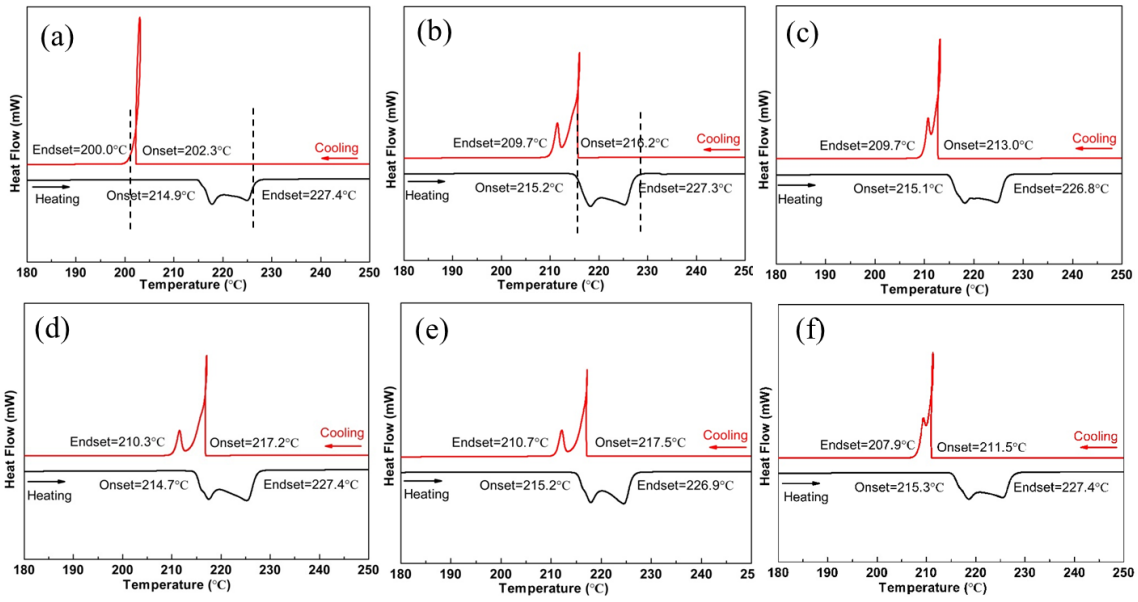

Fig. 4-10 DSC curves of composite solders with different NiO/T-ZnO_w additions. (a) 0 mass%; (b) 0.05 mass%; (c) 0.1 mass%; (d) 0. 3 mass%; (e) 0.5 mass%; (f) 0.7 mass%.

Table 4-2 Melting properties obtained from heating curves of Fig. 4-10

NiO/ZnO_w additions	Onset (°C)	Endset (°C)	Paste range (°C)	Melting point (°C)
0	214.9	227.4	12.5	227.4
0.05 wt%	215.2	227.3	12.1	227.3
0.1 wt%	215.1	226.8	11.7	226.8
0.3 wt%	214.7	227.4	12.7	227.4
0.5 wt%	215.2	226.9	11.7	226.7
0.7 wt%	215.3	227.4	12.1	227.4

Table 4-3 Melting properties in previous reports [20-23]

Solder matrix	Reinforcement	Paste range (°C)	Melting point range (°C)	References
Sn3.0Ag0.5Cu	Ni-GNS (0%, 0.05%, 0.10%, 0.20 mass %)	7.08-8.58	219.25-220.12	[20]
Sn3.5Ag0.7Cu	Ni-CNT (0%, 0.05%, 0.10%, 0.30 mass %)	-	219.4-220.8	[21]
Sn3.0Ag0.5Cu	ZnO nanoparticles (0, 0.7%)	6.4-7.7	220.3-220.5	[22]
Sn1.0Ag0.5Cu	SiC nanoparticles (0, 0.7%)	9.7-11.5	226.5-227.3	[23]

Table 4-4 Undercooling degree of plain and composite solders

$NiO/T\text{-}ZnO_w$ additions	Heating Endset (°C)	Cooling Onset (°C)	Undercooling (°C)
0	227.4	202.3	25.1
0.05 wt%	227.3	216.2	11.1
0.1 wt%	226.8	213.0	13.8
0.3 wt%	227.4	217.2	10.2
0.5 wt%	226.9	217.5	9.4
0.7 wt%	227.4	211.5	15.9

[Note: Undercooling= Heating Endset– Cooling Onset]

inherent physical property, which is determined by inter-atomic distance and the atomic mean-square displacements. Adding a small amount of reinforcement does not significantly influence on the melting temperature [20]. The results are similar to previous report for SAC composite solders [21]. In addition, the pasty range also has little difference. The result is similar to 11.5 °C of SnPb solder [22]. The summarized melting properties from previous reports are shown in Table 4-3.

On the other hands, undercooling was also analyzed in this study. Undercooling was defined as the difference gaps between the liquidus temperature (T_{Endset}) at heating and actual solidification temperature (T_{Onset}) during cooling [24]. As seen from Table 4-4, the undercooling values decreased from 25.1 to 9.4 °C with the NiO/T-ZnO_w addition. The decrease of undercooling degree suggested that NiO/T-ZnO_w reinforced composite solder molten is easier to solidify than plain solder molten. This is because the NiO/T-ZnO_w reinforcements can act as a nucleation sites, thus promoting the solidification process. It can be inferred that the rate of solidification of β-Sn is faster compared with plain solder, and take less time for IMC to grow up [25]. From the thermodynamic prospective, the larger the undercooling is, the larger the driving force for the IMCs growth [23]. Therefore, the decreased undercooling could suppress the growth of IMC. This is one of the reasons why the microstructure was refined in Fig. 4-4 and 4-5.

4.6 Mechanical properties of NiO/T-ZnO_w reinforced Sn1.0Ag0.5Cu composite solders

4.6.1 Tensile properties and fracture surface

In order to obtain the mechanical properties of composite solders, tensile test was conducted. Fig. 4-11(a) shows the representative stress-strain curves of samples, and Fig. 4-11(b) shows the UTS and elongation of Sn1.0Ag0.5Cu composite solders reinforced with various NiO/T-ZnO_w addition. With an increase in the amount of NiO/T-ZnO_w addition, the UTS of the NiO/T-ZnO_w reinforced Sn1.0Ag0.5Cu composite solder gradually increases and then decreases. While the corresponding elongations sharply increases and then also decreases. For the plain Sn1.0Ag0.5Cu solder, the UTS and elongation are 27.3 MPa and 20.8%,

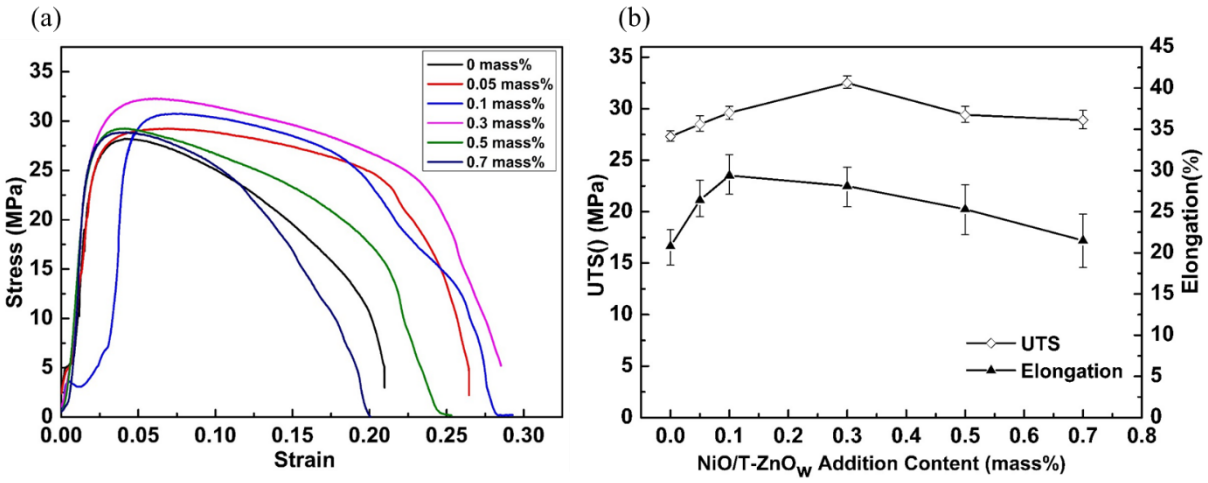

Fig. 4-11 Mechanical properties of Sn1.0Ag0.5Cu composite solders reinforced with various NiO/T-ZnO_w addition. (a) Representative stress-strain curves, (b) UTS and elongation.

respectively. With the addition of 0.05 mass% NiO/T-ZnO_w, the UTS slightly increase to 28.5 MPa, and the elongation increase to 26.4%. With the increase of the addition amount to 0.1%, UTS gets a modest increase; while the corresponded elongation gets to the maximum value of 29.4%, which is 30% higher than plain Sn1.0Ag0.5Cu solder. When the NiO/T-ZnO_w addition reached 0.3 mass%, the UTS of composite solder got their maximum value of 32.5 MPa, which is an increase of 19.0% compared to the plain solder. The corresponding elongation of composite solder is 28.1%. While continue to increase the addition amounts to 0.5 mass%, the UTS and elongation decreased to 29.4 MPa and 25.3%, respectively. This is due to the excessive addition of NiO/T-ZnO_w to produce microstructure defects, which had mentioned in Fig. 4-4. In summary, with the appropriate addition of NiO/T-ZnO_w, the improvements of UTS and elongation of the composite solder can be obtained simultaneously, which are better than those of previously reported nanomaterials reinforced Sn1.0Ag0.5Cu composite solder [23].

In order to better understand the evolution of mechanical properties and fracture behavior of composite solders, fracture surfaces were observed. Fig. 4-12 shows the photographs of the composite solder samples with various NiO/ZrO_2 addition after tensile tests. Fig. 4-13 shows the fracture surfaces of composite solders reinforced with various amounts of added NiO/T-ZnO_w. Fig. 4-13(a) presents the fracture surface of plain Sn1.0Ag0.5Cu solder, which is composed of dimples and cleavage facets, with a ductile–brittle mixed fracture mode. The

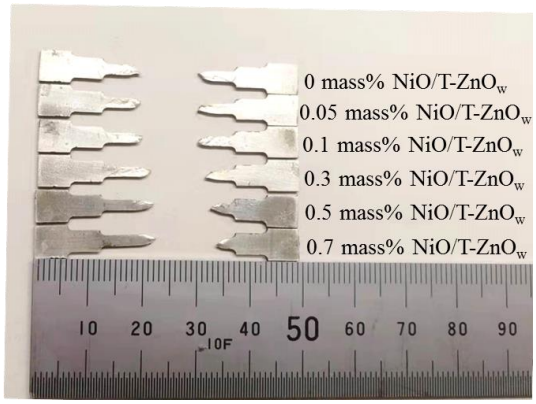

Fig. 4-12 Photographs of the composite solder samples with various NiO/T-ZnO_w addition after tensile tests.

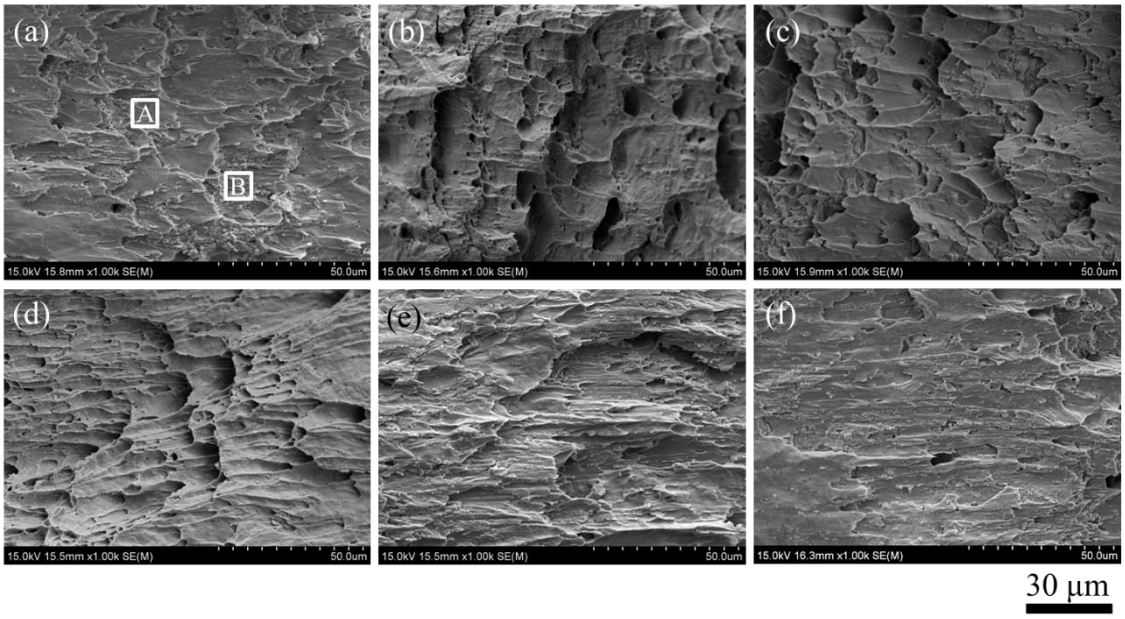

Fig. 4-13 Fracture surfaces of Sn1.0Ag0.5Cu composite solders reinforced with various amounts of added NiO/T-ZnO_w. (a) 0 mass%, (b) 0.05 mass%, (c) 0.1 mass%, (d) 0.3 mass%, (e) 0.5 mass%, (f) 0.7 mass%.

Table 4-5. EDS results for the fracture surface in Fig. 4-13 (at. %)

Location	Sn	Ag	Cu
A	98.41	0.93	0.81
B	36.29	42.14	21.57

cleavage plane is formed due to the fragmentation of the coarsened IMC, where cleavage plane is contained in area B of Fig. 4-13. With an increase in the amount of added NiO/T-ZnO_w, a higher density of dimples is appeared, and the depths of dimple also increased, which mean a large degree of plastic deformation of composite solders. The schematic illustration of fracture

behavior of plain solder and composite solder is shown in Fig. 4-14, which clearly explains why the size and depth of the dimples of the composite solder are larger than that of plain solder. In addition, the proportion of the cleavage surface is reduced. Table 4-5 shows the EDS results of areas A and B in Fig. 4-13 (a), which suggests that area A is β-Sn, while area B belongs to the eutectic microstructure. Combining the composition analysis and local fracture morphology, it can be inferred that area A exhibits a microvoid coalescence fracture, whereas the area B exhibits the microvoid coalescence fracture of β-Sn in the eutectic microstructure and cleavage fracture of the IMC (Ag_3Sn and Cu_6Sn_5). With an increase in the NiO/T-ZnO_w contents, the number of dimples increased, the cleavage fracture area decreased, and the degree of fracture deformation increased. This is attributed to the refinement of the microstructure of the composite solder, which had mentioned in Fig. 4-4. Meanwhile, the effective load transfer can be carried out between solder matrix and reinforcements, which allows the composite solder to withstand a higher degree of strain. Therefore, when the amount of reinforcement added reached 0.3 mass% (Fig. 4-13(d)), the fracture surface presents uniform dimples. The fracture mode also transformed from a ductile–brittle mixed fracture consisting of dimples and cleavage planes to the ductile fracture dominated by dimples.

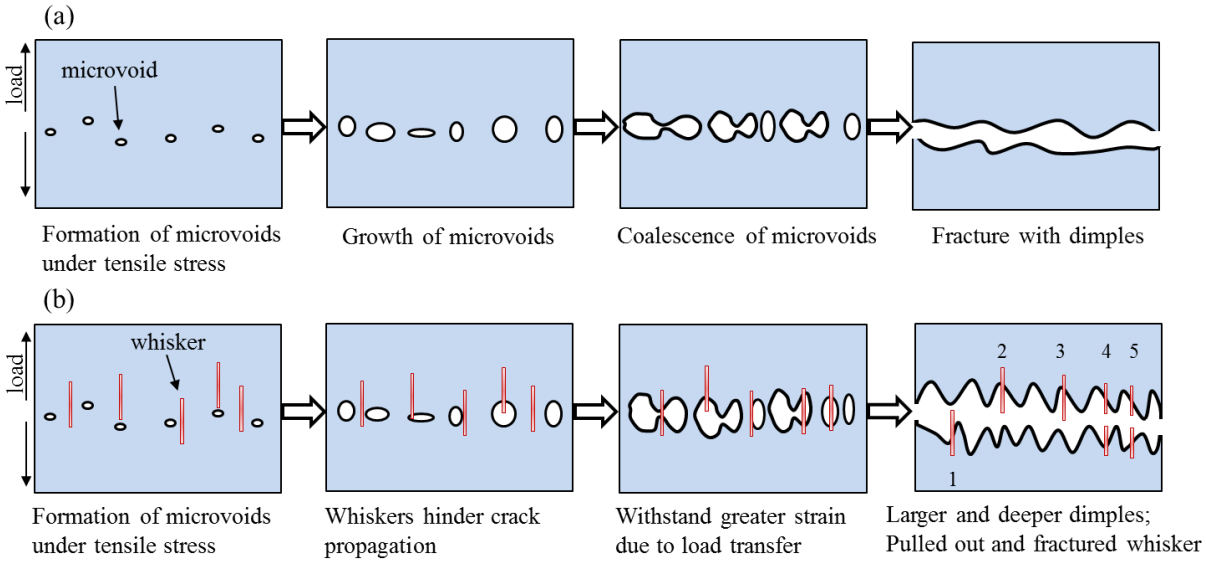

Fig. 4-14 The schematic illustration of fracture behavior of solders. (a) plain Sn1.0Ag0.5Cu solder, (b) composite solder.

However, when the amount of reinforcement added reached 0.5 mass% (Fig. 4-13(e)), the number of dimples significantly decreased, indicating a decrease in the degree of plastic deformation. Fig. 4-13(f) shows the similar phenomenon. In Fig. 4-4, I had mentioned that excessive NiO/T-ZnO_w addition could cause microstructure defects. When the tensile sample is subjected to external loads, stress concentration tends to occur at the defect locations, where cracks are prone to initiation and propagation, leading to a decrease of elongation.

4.6.2 Mechanisms of strengthening and ductility

When developing composite solders, an increase in strength often comes at the expense of ductility. However, high strength and ductility were required simultaneously for the actual service conditions. In this study, both the UTS and elongation of the composite solder were improved compared with the plain solder, which has met the requirements of high strength and ductility. It was mainly attributed to the choice of reinforcement (T-ZnO_w) and the surface modification of T-ZnO_w. A no gaps, no micropores, or new phase formed novel interface between solder matrix and reinforcement was formed, thus generating an effective load transfer effect. The strengthening-ductility mechanism can be systematically proposed as load transfer effect, grain refinement effect, and misfit dislocation effect.

In summary, the above three types of effects improved the mechanical properties of the composite solder. In particular, for carbon nanotube or whisker reinforced composites, the load transfer effect is most effective for improving the strength and ductility [26,27]. Therefore, mechanical properties of the NiO/T-ZnO_w reinforced Sn1.0Ag0.5Cu composite solder might be primarily due to the load transfer, and the key to effective load transfer is the surface modification of T-ZnO_w.

4.7 Conclusions

The effects of NiO/T-ZnO_w addition on the microstructure, melting points and mechanical properties of composite solder were systematically investigated. The major findings are as follows:

1. When the addition content was in the range of 0.05-0.3 mass%, NiO/T-ZnO_w was uniformly distributed in the solder matrix, and most of them existed in the eutectic area. This NiO/T-ZnO_w could act as the heterogeneous nucleation sites to refine the size of IMC and β-Sn. While the addition contents reached 0.5-0.7 mass%, microstructure defects occurred.
2. In the plain Sn1.0Ag0.5Cu solder, granular, short rod-like, and needle-like IMC were distributed inside β-Sn or at the grain boundary. The average IMC size at the grain boundary was larger than that inside β-Sn due to the higher energy at the grain boundary. For the similar reason, IMC located at sharp corner also has a larger size than those at flat locations.
3. For the interface of NiO/T-ZnO_w reinforced Sn1.0Ag0.5Cu composite solder, no gaps, micropores, or new phases were formed, and the atomic interdiffusion occurred at the interface. Hence, the composite interface structure of Sn1.0Ag0.5Cu/NiO/T-ZnO_w was well designed. This novel interface is key in the strengthening and ductility of composite solder.
4. The UTS and elongation of the 0.3 mass% NiO/T-ZnO_w reinforced Sn1.0Ag0.5Cu composite solder were 32.5 MPa and 28.1%, being 19.0% and 35.1% higher than that of plain Sn1.0Ag0.5Cu solder, respectively. The strengthening and ductility mechanism mainly proposed load transfer, grain refinement, and misfit dislocation effects.

References

[1] A.A. El-Daly, T.A. Elmosalami, W.M. Desoky, M.G. El-Shaarawy, A.M. Abdraboh, Tensile deformation behavior and melting property of nano-sized ZnO particles reinforced Sn-3.0Ag-0.5Cu lead-free solder, Mater. Sci. Eng. A. 618 (2014) 389–397. https://doi.org/10.1016/j.msea.2014.09.028.

[2] A. Fawzy, S.A. Fayek, M. Sobhy, E. Nassr, M.M. Mousa, G. Saad, Effect of ZnO nanoparticles addition on thermal, microstructure and tensile properties of Sn-3.5 Ag-0.5 Cu (SAC355) solder alloy, J. Mater. Sci. Mater. Electron. 24 (2013) 3210–3218. https://doi.org/10.1007/s10854-013-1230-2.

[3] H. Ma, A. Kunwar, R. Huang, J. Chen, Y. Wang, N. Zhao, H. Ma, Size effect on IMC growth induced by Cu concentration gradient and pinning of Ag_3Sn particles during multiple reflows, Intermetallics. 90 (2017) 90–96. https://doi.org/10.1016/j.intermet.2017.06.013.

[4] R. Feng, Y. Zhao, C. Zhu, T.J. Mason, Enhancement of ultrasonic cavitation yield by multi-frequency sonication, Ultrason. Sonochem. 9 (2002) 231–236. https://doi.org/10.1016/S1350-4177(02)00083-4.

[5] E. Riedel, M. Liepe, S. Scharf, Simulation of ultrasonic induced cavitation and acoustic streaming in liquid and solidifying aluminum, Metals (Basel). 10 (2020). https://doi.org/10.3390/met10040476.

[6] H. Stange, S. Brunken, D. Greiner, M.D. Heinemann, C.A. Kaufmann, S.S. Schmidt, J.P. Bäcker, M. Klaus, C. Genzel, R. Mainz, Diffusion-induced grain boundary migration as mechanism for grain growth and defect annihilation in chalcopyrite thin films, Acta Mater. 111 (2016) 377–384. https://doi.org/10.1016/j.actamat.2016.03.073.

[7] M. Umehara, Y. Takeda, K. Oh-Ishi, Y. Aoki, T. Motohiro, T. Sakai, R. Maekawa, Energy level diagram around Ge-rich grain boundaries in Cu2Sn1-xGexS3 (CTGS) thin-film solar cells, Sol. Energy Mater. Sol. Cells. 134 (2015) 1–4. https://doi.org/10.1016/j.solmat.2014.11.024.

[8] J.W. Xian, G. Zeng, S.A. Belyakov, Q. Gu, K. Nogita, C.M. Gourlay, Anisotropic thermal expansion of Ni_3Sn_4, Ag_3Sn, Cu_3Sn, Cu_6Sn_5 and β-Sn, Intermetallics. 91 (2017) 50–64. https://doi.org/10.1016/j.intermet.2017.08.002.

[9] F. Wang, M. O'Keefe, B. Brinkmeyer, Microstructural evolution and tensile properties of Sn-Ag-Cu mixed with Sn-Pb solder alloys, J. Alloys Compd. 477 (2009) 267–273. https://doi.org/10.1016/j.jallcom.2008.10.141.

[10] J.G. Maveety, P. Liu, J. Vijayen, F. Hua, E.A. Sanchez, Effect of cooling rate on microstructure and shear strength of pure Sn, Sn-0.7Cu, Sn-3.5Ag, and Sn-37Pb solders, J. Electron. Mater. 33 (2004) 1355–1362. https://doi.org/10.1007/s11664-004-0165-z.

[11] L. Qi, J. Huang, X. Zhao, H. Zhang, Effect of thermal-shearing cycling on Ag_3Sn microstructural coarsening in SnAgCu solder, J. Alloys Compd. 469 (2009) 102–107. https://doi.org/10.1016/j.jallcom.2008.01.108.

[12] D.A. Shnawah, M.F.M. Sabri, I.A. Badruddin, S.B.M. Said, M.B.A. Bashir, N.M. Sharif, M.H. Elsheikh, Study on coarsening of Ag_3Sn intermetallic compound in the Fe-modified Sn-1Ag-0.5Cu solder alloys, J. Alloys Compd. 622 (2015) 184–188. https://doi.org/10.1016/j.jallcom.2014.10.042.

[13] Y. Wen, X. Zhao, Z. Chen, Y. Gu, Y. Wang, Z. Chen, X. Wang, Reliability enhancement of Sn-1.0Ag-0.5Cu nano-composite solders by adding multiple sizes of TiO_2 nanoparticles, J. Alloys Compd. 696 (2017) 799–807. https://doi.org/10.1016/j.jallcom.2016.12.037.

[14] C.R. He, W.G. Wang, J. Wang, Y. Xue, Effect of alumina on the curvature, Young's modulus, thermal expansion coefficient and residual stress of planar solid oxide fuel cells, J. Power Sources. 196 (2011) 7639–7644. https://doi.org/10.1016/j.jpowsour.2011.05.025.

[15] L.C. Sim, S.R. Ramanan, H. Ismail, K.N. Seetharamu, T.J. Goh, Thermal characterization of Al_2O_3 and ZnO reinforced silicone rubber as thermal pads for heat dissipation purposes, Thermochim. Acta. 430 (2005) 155–165. https://doi.org/10.1016/j.tca.2004.12.024.

[16] Y.D. Han, S.M.L. Nai, H.Y. Jing, L.Y. Xu, C.M. Tan, J. Wei, Development of a Sn-Ag-Cu solder reinforced with Ni-coated carbon nanotubes, J. Mater. Sci. Mater. Electron. 22 (2011) 315–322. https://doi.org/10.1007/s10854-010-0135-6.

[17] C. Villada, F. Jaramillo, J.G. Castaño, F. Echeverría, F. Bolívar, Design and development of nitrate-nitrite based molten salts for concentrating solar power applications, Sol. Energy. 188 (2019) 291–299. https://doi.org/10.1016/j.solener.2019.06.010.

[18] A. Bonk, S. Sau, N. Uranga, M. Hernaiz, T. Bauer, Advanced heat transfer fluids for direct molten salt line-focusing CSP plants, Prog. Energy Combust. Sci. 67 (2018) 69–87. https://doi.org/10.1016/j.pecs.2018.02.002.

[19] A.A. El-Daly, A.E. Hammad, G.S. Al-Ganainy, M. Ragab, Influence of Zn addition on the microstructure, melt properties and creep behavior of low Ag-content Sn-Ag-Cu lead-free solders, Mater. Sci. Eng. A. 608 (2014) 130–138. https://doi.org/10.1016/j.msea.2014.04.070.

[20] G. Chen, F. Wu, C. Liu, V. V. Silberschmidt, Y.C. Chan, Microstructures and properties of new Sn-Ag-Cu lead-free solder reinforced with Ni-coated graphene nanosheets, J. Alloys Compd. 656 (2016) 500–509. https://doi.org/10.1016/j.jallcom.2015.09.178.

[21] Y.D. Han, S.M.L. Nai, H.Y. Jing, L.Y. Xu, C.M. Tan, J. Wei, Development of a Sn-Ag-Cu solder reinforced with Ni-coated carbon nanotubes, J. Mater. Sci. Mater. Electron. 22 (2011) 315–322. https://doi.org/10.1007/s10854-010-0135-6.

[22] A.A. El-Daly, T.A. Elmosalami, W.M. Desoky, M.G. El-Shaarawy, A.M. Abdraboh, Tensile deformation behavior and melting property of nano-sized ZnO particles reinforced Sn-3.0Ag-0.5Cu lead-free solder, Mater. Sci. Eng. A. 618 (2014) 389–397. https://doi.org/10.1016/j.msea.2014.09.028.

[23] A.A. El-Daly, A. Fawzy, S.F. Mansour, M.J. Younis, Novel SiC nanoparticles-containing Sn-1.0Ag-0.5Cu solder with good drop impact performance, Mater. Sci. Eng. A. 578 (2013) 62–71. https://doi.org/10.1016/j.msea.2013.04.022.

[24] R. Abbaschian, M.D. Lipschutz, Eutectic solidification processing via bulk melt undercooling, Mater. Sci. Eng. A. 226–228 (1997) 13–21. https://doi.org/10.1016/s0921-5093(97)80022-6.

[25] R.K. Chinnam, C. Fauteux, J. Neuenschwander, J. Janczak-Rusch, Evolution of the microstructure of Sn-Ag-Cu solder joints exposed to ultrasonic waves during solidification, Acta Mater. 59 (2011) 1474–1481. https://doi.org/10.1016/j.actamat.2010.11.011.

[26] S.I. Cha, K.T. Kim, K.H. Lee, C.B. Mo, S.H. Hong, Strengthening and toughening of carbon nanotube reinforced alumina nanocomposite fabricated by molecular level mixing process, Scr. Mater. 53 (2005) 793–797. https://doi.org/10.1016/j.scriptamat.2005.06.011.

[27] J. Li, F. Wang, C. Shi, E. Liu, C. He, N. Zhao, High strength-ductility synergy of $MgAlB_4$ whisker reinforced aluminum matrix composites achieved by in situ synthesis, Mater. Sci. Eng. A. 799 (2021) 140127. https://doi.org/10.1016/j.msea.2020.140127.

Chapter 5 Microstructure and properties of NiO/ZrO_2 and NiO/T-ZnO_w hybrid reinforced Sn1.0Ag0.5Cu composite solders

5.1 Introduction

In chapter 3, NiO/ZrO_2 reinforced Sn1.0Ag0.5Cu composite solder was prepared via ultrasonic stirring method. The effect of NiO/ZrO_2 on the microstructure and properties of composite solder were systematically investigated. In chapter 4, NiO/T-ZnO_w reinforced Sn1.0Ag0.5Cu composite solder was also prepared via ultrasonic stirring method. And the effect of NiO/T-ZnO_w on the microstructure and properties of composite solder were systematically investigated.

In this chapter, NiO/ZrO_2 and NiO/T-ZnO_w hybrid reinforced Sn1.0Ag0.5Cu composite solder with different Zn:Zr ratios were prepared with ultrasonic stirring. The microstructure evolution of composite solders was systematically investigated. The interface between reinforcement and solder matrix was also explored. Moreover, the mechanical properties of composite solders were also investigated.

5.2 Experimental procedure

5.2.1 Materials

The reinforcement of NiO/ZrO_2 was prepared with the ball milling-pyrolysis method. And the reinforcement of NiO/T-ZnO_w was prepared with pyrolysis method based on the self-assembly. The detailed fabrication process and morphology of the kinds of reinforcements are shown in chapter 2. So this chapter would not elaborate. The commercial Sn1.0Ag0.5Cu solder bar was provided by Senju Metal Industry Co. Ltd. Japan.

5.2.2 Fabrication of NiO/ZrO_2 and NiO/T-ZnO_w hybrid reinforced Sn1.0Ag0.5Cu composite solders

In chapters 3 and 4, the effects of NiO/ZrO_2 and NiO/T-ZnO_w additions on the mechanical properties of composite solders were explored respectively. The result is shown in Fig. 5-1.

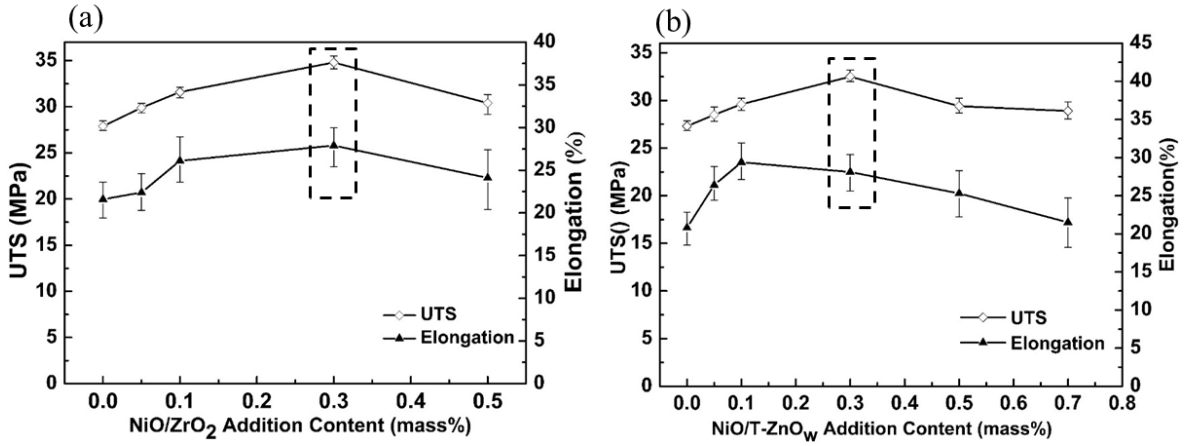

Fig. 5-1 Mechanical properties of single reinforcement reinforced composite solders. (a) NiO/ZrO_2 reinforced composite solders, (b) $NiO/T\text{-}ZnO_w$ reinforced composite solders.

Table 5-1 Composition of reinforcements

Reinforcement	1# (mass%)	2#	3#	4#	5#	6#
NiO/ZrO_2	0.30	0.24	0.18	0.12	0.06	0
$NiO/T\text{-}ZnO_w$	0	0.06	0.12	0.18	0.24	0.30
Total contents	0.30	0.30	0.30	0.30	0.30	0.30
Zn: Zr ratios	-	1: 4	2: 3	3: 2	4: 1	-

For the single NiO/ZrO_2 reinforced composite solder, UTS and elongation reached the maximum values simultaneously when the addition amount reached 0.3 mass%, suggesting that the optimal addition amount of NiO/ZrO_2 was 0.3 mass%. For the single $NiO/T\text{-}ZnO_w$ reinforced composite solder, UTS and elongation did not reach the maximum values simultaneously. The composite solder can also obtain good comprehensive mechanical properties when the $NiO/T\text{-}ZnO_w$ addition reached 0.3 mass%. Therefore, the optimal addition amount of $NiO/T\text{-}ZnO_w$ is also selected as 0.3 mass%. Therefore, for the NiO/ZrO_2 and $NiO/T\text{-}ZnO_w$ hybrid reinforced composite solders, the total content of the reinforcement is a constant value of 0.3 mass%, while the mixing ratio of the two reinforcements is different. For convenience, these components are labeled as different Zn: Zr ratios. The specific reinforcement phase components are shown in Table 5-1.

Like previous chapters, firstly, a commercial Sn1.0Ag0.5Cu solder bar was melted at 380 °C in a furnace. Subsequently, NiO/ZrO_2 and $NiO/T\text{-}ZnO_w$ reinforcement with different Zn:

Zr ratios were added to the molten solder, respectively. Due to the surface tension of the molten solder, the reinforcement could not be well dispersed in it, ultrasonic vibration-assisted stirring was applied to the mixture at the ultrasonic power and duration of 80 W and 4 min, respectively. Afterwards, the oxide film on the surface of the molten solder was removed and quickly cast molten into a stainless steel mold with the size of 50 mm × 10 mm × 5 mm (L × W × H).

5.2.3 Characterization and testing

Scanning electron microscopy (SEM, SU-70, Hitachi, Japan) equipped with energy-dispersive X-ray spectroscopy (EDS) was used to observe the microstructure and fracture surface of the composite solders. The interface between reinforcement and solder matrix were investigated using transmission electron microscopy (TEM, JEOL JEM 2100F) equipped with EDS. The acceleration voltage of TEM was 200 kV. The TEM samples of the composite solder were prepared with the focused ion beam (FIB, HITACHI FB-2000A).

These composite solder bars were formed into the tensile test samples using an electrical discharge machine (AG360L). The schematic diagram of the tensile test sample is shown in Fig. 5-2. The sample gauge length was 10 mm, and the width and thickness were 2 mm and 1 mm, respectively. The tensile tests were performed using a universal electrical tensile tester (Autograph AG-X Shimazu, Japan) with a strain rate of 0.0005/s. The experimental results are the average values of four tensile samples.

To investigate the thermal stability of newly developed composite solder, thermal aging test of the composite solder was conducted. The samples were performed for 168 h, 504 h and 1008 h in an oil bath at 150 ℃. The oil bath was used to prevent the potential oxidation of

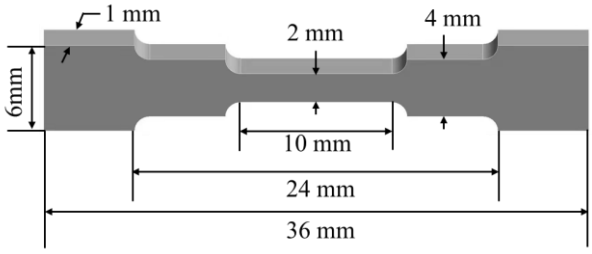

Fig. 5-2 The schematic diagram of the tensile test sample.

the alloys during thermal aging. Plain Sn1.0Ag0.5Cu and Sn3.0Ag0.5Cu solders were also performed as the reference. The tensile test condition is the same as above.

5.3 Microstructure evolution of hybrid reinforced composite solders

Fig.5-3 shows the microstructure of NiO/ZrO_2 and NiO/T-ZnO_w hybrid reinforced composite solder with different Zn: Zr ratios (total contents of reinforcement of 0.3 mass%). As seen from Fig. 5-3(a), the microstructure is composed of β-Sn and eutectic structure. The formation of β-Sn and eutectic structures had been systematically described in previous chapters. And for a single NiO/ZrO_2 reinforced composite solder, NiO/ZrO_2 was located in the eutectic areas, which had mentioned in chapter 3. But these nano-sized reinforcements are not visible in the SEM image due to the low magnification compared to the TEM image.

When the Zn: Zr ratio = 1: 4 (Fig. 5-3(b)), a small amount of NiO/T-ZnO_w can be observed in the eutectic area, suggesting that NiO/T-ZnO_w is effectively added to the solder matrix. When the Zn: Zr ratio changes to 2: 3 (Fig. 5-3(c)), more NiO/T-ZnO_w can be observed, and the proportion of the eutectic structure increases, which is beneficial to improve the strength of the composite solders, and the IMC size in the eutectic structure is almost the same as in Fig. 5-3(a). However, coarsening of eutectic microstructure occurs when the Zn: Zr ratio reaches 3: 2 (Fig. 5-3 (d)), where the size of IMC is larger than that of Fig. 5-3 (a) and (c). This is due to the decrease of NiO/ZrO_2 ratio in the hybrid enhancement phase. For the two reinforcements, NiO/ZrO_2 and NiO/T-ZnO_w, the former belongs to nano-scale materials, while the latter belongs to micro-scale materials. For the same mass (volume), NiO/ZrO_2 contains more quantity, indicating more nucleation sites. Therefore, reducing the ratio of NiO/ZrO_2 means that the number of nucleation sites in the composite solder is reduced, which leads to an increase in the IMC size compared to Fig. 5-3(c). When the Zn:Zr ratio reaches 4: 1 (Fig. 5-3(e)), NiO/T-ZnO_w (black phases) is evenly distributed in the solder matrix with different shapes. And the ratio of the eutectic structure slightly decreased. When the reinforcement of the composite solder is a single NiO/T-ZnO_w with 0.3 mass% addition (Fig. 5-3(f)), a similar phenomenon can be observed.

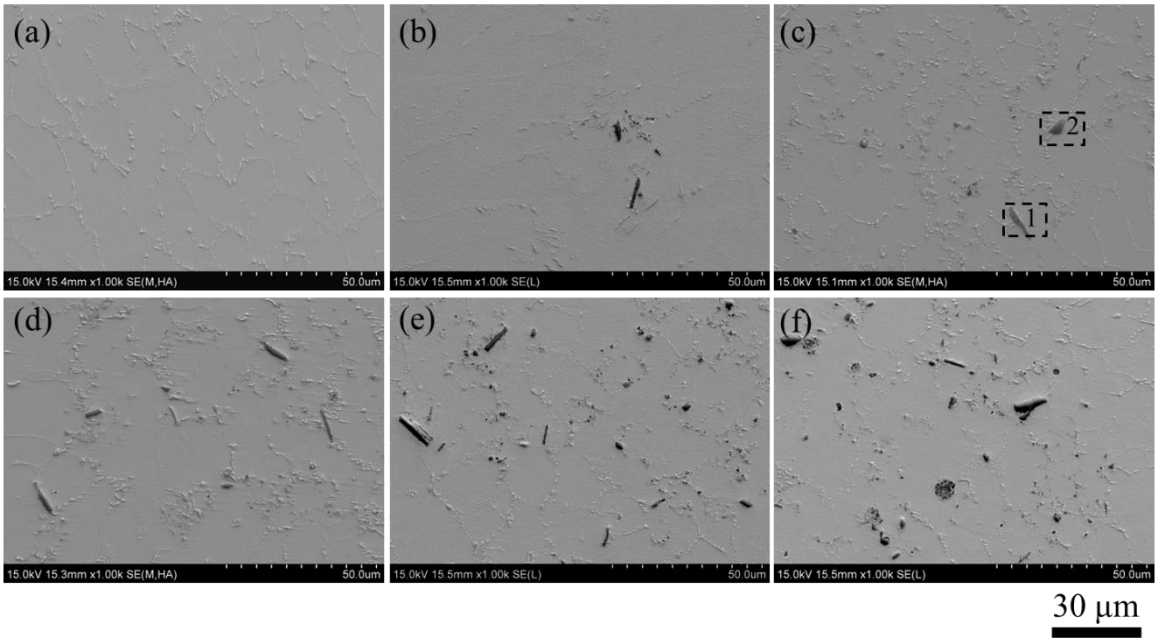

Fig. 5-3 Microstructure of NiO/ZrO_2 and $NiO/T\text{-}ZnO_w$ hybrid reinforced composite solder with different Zn: Zr ratios (total contents of reinforcements is 0.3 mass%). (a) 0.30 mass% NiO/ZrO_2 (b) Zn: Zr=1: 4; (c) Zn: Zr=2: 3; (d) Zn: Zr=3: 2; (e) Zn: Zr=4: 1; (f) 0.30 mass% $NiO/T\text{-}ZnO_w$.

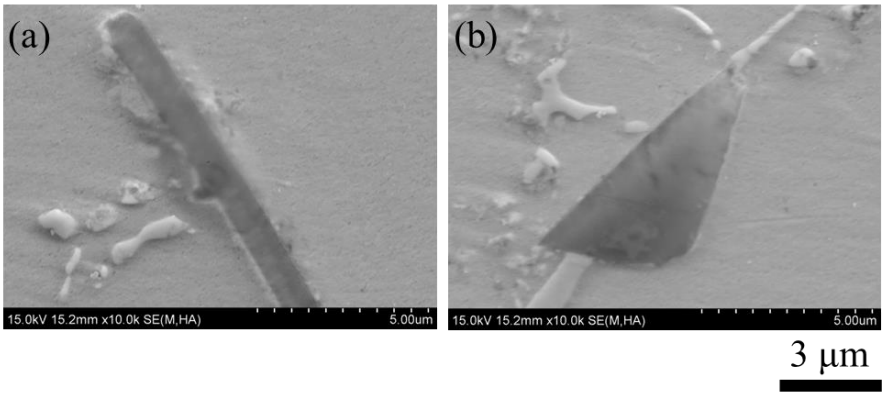

Fig. 5-4 High magnification view of (a) area 1, and (b) area 2 in Fig. 5-3.

Fig. 5-4 (a) and (b) show the high magnification view of areas 1 and 2 in Fig. 5-3, respectively. As seen from Fig. 5-3(a) and (b), $NiO/T\text{-}ZnO_w$ reinforcements are tightly embedded in the solder matrix, neither gaps nor pores are observed. This indicates that the reinforcements and the solder matrix are well bonded at the micrometer scale. In addition, some IMC particles can be observed near the reinforcements, indicating that the reinforcements can act as the nucleation sites of these IMCs during the solidification process. And the similar phenomenon had also been observed in previous chapters.

5.4 Interface of hybrid reinforced Sn1.0Ag0.5Cu composite solder

The interface between the reinforcements and solder matrix is the key issue for composite solder. Therefore, TEM observation was conducted to further explore the interfacial relationship between the solder matrix and reinforcement at the nanometer scale and to inspect whether new phase was formed at the interface. In part 5.4, hybrid composite solder with Zn: Zr ratios of 2: 3 was used to prepare the TEM sample. Since there are two reinforcements in the composite solder, I will investigate the interface relationship between the two reinforcements and the solder matrix respectively.

5.4.1 Interface between NiO/ZrO_2 and solder matrix

Fig. 5-5 shows the TEM and EDS mapping images of the distribution of NiO/ZrO_2 in the solder matrix. According to Fig. 5-5(a) and (b), it can be inferred that dispersed ZrO_2 (marked with the white dashed circles) are existed in Fig. 5-5(a), which belongs to the eutectic area. And many dislocations can be observed here. To further confirm the existence of the phase, SAED was conducted. Fig. 5-5(c) shows the SAED result of area 1 in Fig. 5-5(a), where a set of diffraction points and a set of diffraction rings can be observed simultaneously. One set of diffraction points can be assigned to the (101), ($\bar{1}$01), and (012) planes of ZrO_2 along the [12$\bar{1}$] axis, while the diffraction rings can be indexed as the (012) and (104) planes of NiO. The SAED results indicate that NiO is still attached to the ZrO_2 surface, forming the Sn1.0Ag0.5Cu/NiO/ZrO_2 interface system.

In addition, the reinforcements are relatively dispersed in the solder matrix, and no holes or gaps are found at the interface between the reinforcement and solder matrix. The good results

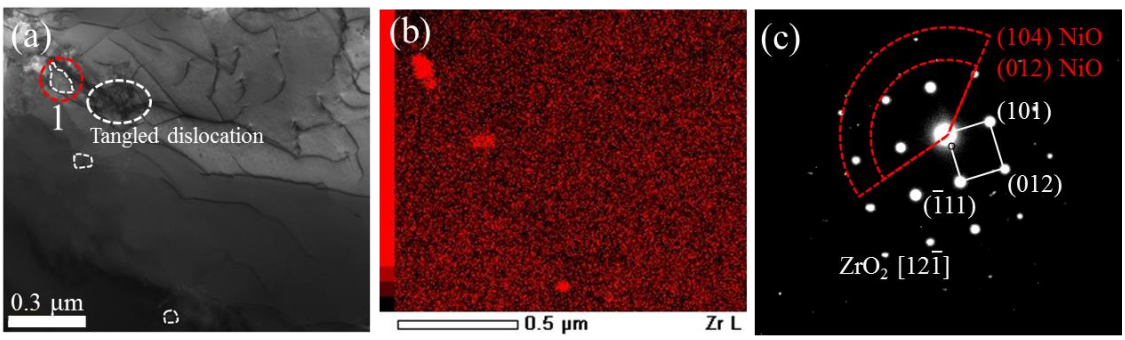

Fig. 5-5 Dispersed NiO/ZrO_2 in hybrid reinforced SAC105 composite solder.

can be attributed to two aspects. First, the ultrasonic stirring introduced during the preparation of composite solder could disperse the agglomerated nanoparticles. Second, the surface modification of ZrO_2 is conducted with NiO. As mentioned in previous chapter, NiO can be solid solute with ZrO_2 and Sn simultaneously, acting as a transition layer to improve the wetting between the ZrO_2 and solder matrix. The above two reasons make the reinforcements dispersed in the solder matrix and achieve a good interface between the solder matrix and reinforcements. In addition, these dispersed nano reinforcements can produce an Orowan strengthening effect, which is one of the reasons for the improved mechanical properties of the composite solders. This part will be discussed later.

5.4.2 Interface between NiO/ T-ZnO_w and solder matrix

Fig. 5-6 shows the TEM, EDS, and SAED images of the interface between NiO/T-ZnO_w and solder matrix. In Fig. 5-6(a)–(d), the phase on the left side is the solder matrix, the right side is T-ZnO_w, and a thin NiO transition layer exists between them. The thickness of the transition layer was approximately 16 nm, which is basically consistent with the results observed in previous chapter. Additionally, neither nanogaps nor nanopores were found at the interface. Fig. 5-6(e) shows the overlay of Sn, Zn, and Ni mappings, indicating that both Sn and Zn elements existed in the NiO layer area. Thus, atomic inter-diffusion occurred at the interface, constituting an effective way of bonding. In addition, NiO can be found at the interface of the composite solder, indicating its relative stability during the preparation process of the composite solder, as well as suggesting good bonding between NiO and T-ZnO_w.

An ideal interface needs to avoid not only gaps and pores but also the reaction between NiO/T-ZnO_w and the solder matrix to form brittle IMC at the interface, which can deteriorate the performance of the composite solder. SEAD was conducted to detect whether new phase was formed. First, the selected area aperture was located at the Sn zone (area 1 of Fig. 5-6 (a)) to obtain diffraction spots. Then the selected area was continuously moved until it passed through the interface and reached the T-ZnO_w area. Three representative zones (area 1, area 2, and area 3 of Fig. 5-6(a)) are displayed here. Fig. 5-6(g) shows the pattern of area 1 in Fig. 5-

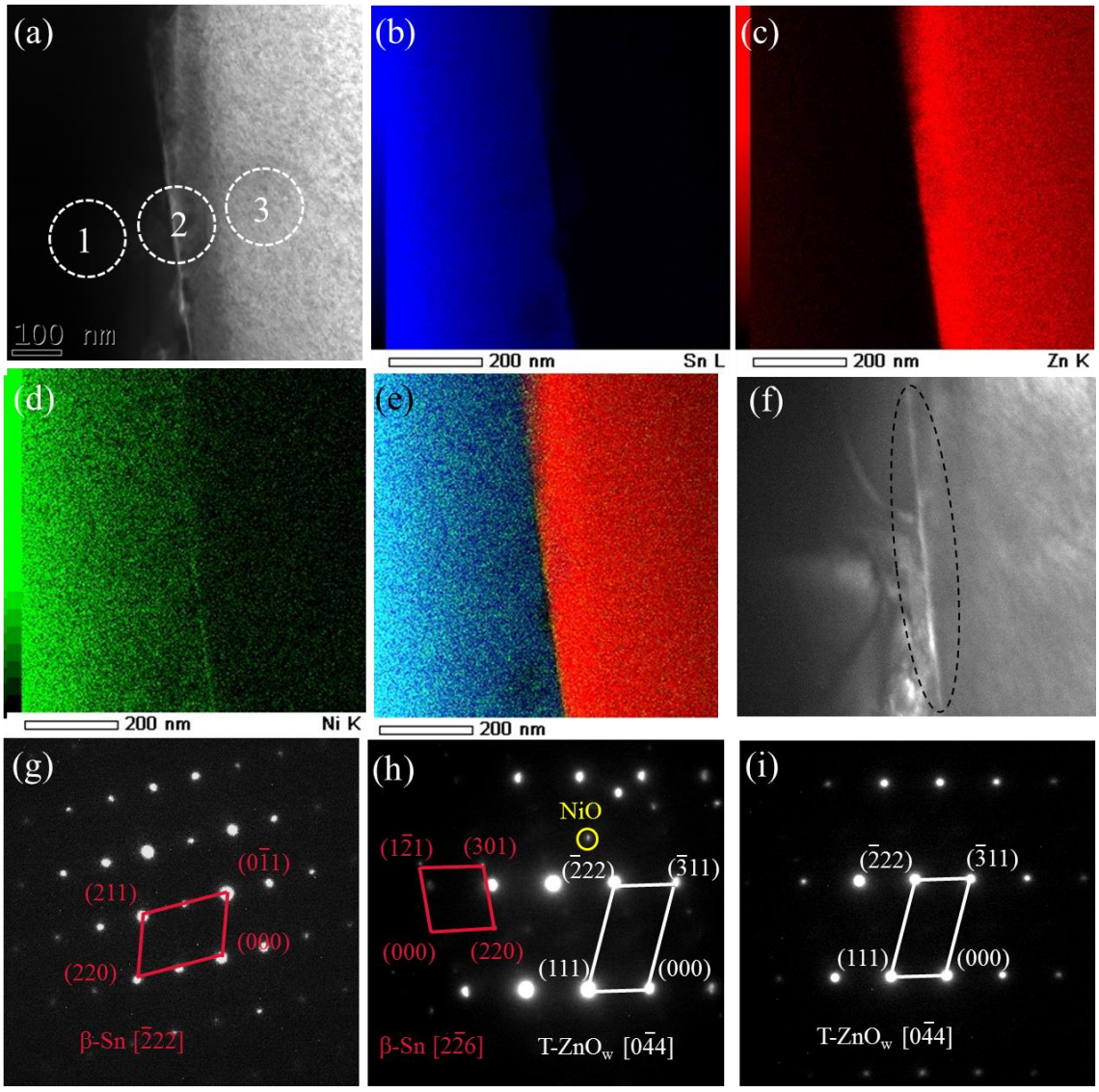

Fig. 5-6 TEM images of (a) the interface between NiO/T-ZnOw and Sn1.0Ag0.5Cu solder matrix. EDS maps of (b) Sn, (c) Zn, (d) Ni, and (e) the overlay of Sn, Zn, and Ni. (f) the dark field phase of NiO. SAED patterns of (g) area 1, (h) area 2, and (i) area 3 in Fig. 5-6(a).

6(a), which can be calibrated as β-Sn (220), (0$\bar{1}$1), and (211) planes with the [$\bar{2}$2$\bar{2}$] axis. The SAED pattern of area 2 is shown in Fig. 5-6(h), through which three phases, T-ZnO$_w$, β-Sn, and NiO, can be identified. Especially, the diffraction spot of NiO was marked with yellow-coloured circle. The dark-field phase of NiO is shown in Fig .5-6(f), which shows a bright streak (marked with a dotted frame). The result is consistent with the EDS result in Fig. 5-6(d), which further validates the presence of NiO at the interface. Similarly, the SAED pattern of area 3 shows the (111), ($\bar{3}$11), and ($\bar{2}$22) planes of T-ZnO$_w$ along with the [0$\bar{4}$4] axis. According

to the SAED results, it can be inferred that no other phases were detected except for Sn1.0Ag0.5Cu, NiO, T-ZnO_w. In other words, no new phases were generated, and the clean interface was obtained. In summary, no gaps, no micropores, and no new phases were generated at the interface between NiO/T-ZnO_w and solder matrix, suggesting that the Sn1.0Ag0.5Cu/NiO/T-ZnO_w composite interface structure was well designed. This interface is an important factor in the strengthening and ductility of the composite solder.

5.5 Strengthening-ductility behavior of NiO/ZrO_2 and NiO/T-ZnO_w hybrid reinforced Sn1.0Ag0.5Cu composite solders

5.5.1 Tensile properties and fracture surface

Tensile tests were conducted to study the mechanical properties of composite solders. Fig. 5-7(a) shows the representative stress-strain curves of samples, and Fig. 5-7(b) shows the UTS and elongation of NiO/ZrO_2 and NiO/T-ZnO_w hybrid reinforced composite solders with different Zn: Zr ratios. The leftmost and rightmost data in Fig. 5-7(b) represent the mechanical properties of the composite solder reinforced by the single reinforcement, respectively. The UTS and elongation of 0.3 mass% NiO/ZrO_2 reinforced Sn1.0Ag0.5Cu composite solder are 34.8 MPa and 27.9%, respectively. At 0.3 mass% NiO/T-ZnO_w reinforced composite solder, UTS and elongation are 32.5 MPa and 28.1%, respectively. These data had mentioned in chapter 2 and 3. When the Zn: Zr ratio = 1: 4, the elongation of the composite solder increases to 29.8%, while the UTS decreases slightly (32.8 MPa). The increased elongation is due to the addition of NiO/T-ZnO_w, which has better load transfer efficiency compared to NiO/ZrO_2; while the decrease of UTS is due to defects in the microstructure (shown in Fig. 5-3 (b)), which will induce cracks and eventually lead to the fracture of the solder. When the Zn: Zr ratio reaches 2: 3, UTS and elongation reached the maximum values simultaneously, which were 35.9 MPa and 31.4%, respectively.

The synergistic improvement of mechanical properties can be explained by the microstructure in Fig. 5-3. On the one hand, the increase of the eutectic structure improves the UTS of the composite solder, and the the IMC size in the eutectic structure remains fine. On

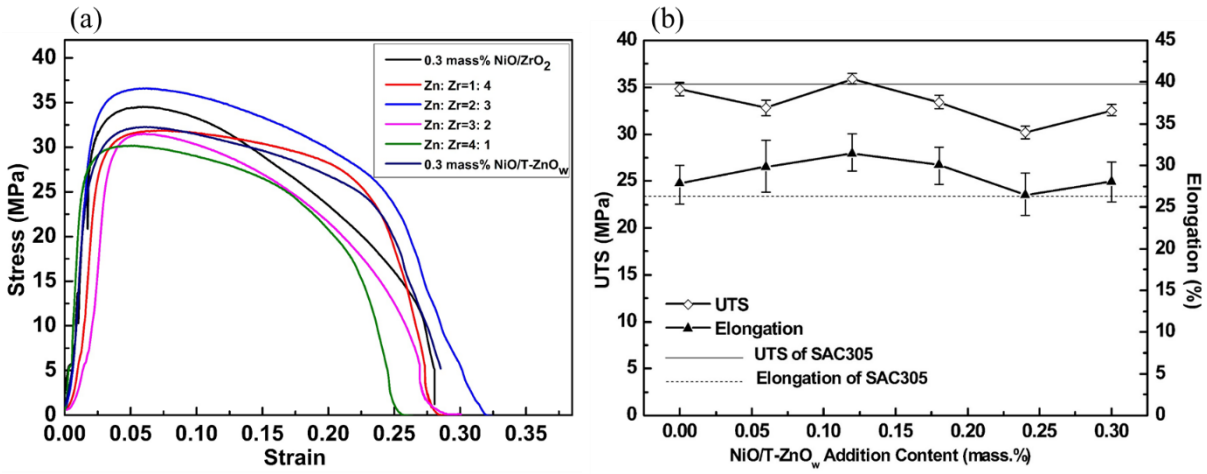

Fig. 5-7 Mechanical properties of NiO/ZrO_2 and $NiO/T\text{-}ZnO_w$ hybrid reinforced composite solders with various Zn: Zr ratios. (a) Representative stress-strain curves, (b) UTS and elongation.

the other hand, the increase of $NiO/T\text{-}ZnO_w$ ratio in the two reinforcements improves the load transfer efficiency of the composite solder, increasing the elongation of the composite solder. However, the UTS and elongation of the composite solder decrease at the same time when the Zn: Zr ratio changes to 3: 2. The outcome is due to the coarsening of the eutectic structure at this composition. In addition, the continuous decrease of NiO/ZrO_2 percentage also weakens the strengthening effect in the composite solder. The above two factors reduce the mechanical properties of the hybrid reinforced composite solder. Similarly, when the Zn: Zr ratio changes to 4: 1, the mechanical properties are further decreased, even lower than the composite solder reinforced by a single reinforcement.

In summary, for the design of multi-phase and multi-scale hybrid reinforced composite solders, in addition to selecting the appropriate reinforcements and constructing an ideal interface, the ideal mixing ratio is also one of the important factors for obtaining high-performance composite solders. Inappropriate mixing ratio (Zn: Zr= 1: 4) cannot guarantee the synergistic improvement of UTS and elongation, and may even reduce the overall mechanical properties (such as Zn: Zr= 4: 1). Only a proper mixing ratio can guarantee the synergistic enhancement of UTS and elongation. As mentioned above, when the mixing ratio of Zn: Zr was 2: 3, the synergistic improvement of UTS and elongation can be obtained, which were 35.9 MPa and 31.4%, respectively. The results are better than Sn1.0Ag0.5Cu composite solder in

reference [1]. In addition, Sn3.0Ag0.5Cu solder was prepared with the same process as a benchmark, and its UTS and elongation were 35.4 MPa and 26.1%, respectively. The performance of the NiO/ZrO_2 and $NiO/T\text{-}ZnO_w$ hybrid reinforced Sn1.0Ag0.5Cu composite solder is higher than that of Sn3.0Ag0.5Cu, in which a high strength-ductility composite solder is obtained.

To better understand the evolution of mechanical properties and fracture behavior of composite solders, fracture surfaces were observed. Fig. 5-8 shows the photographs of NiO/ZrO_2 and $NiO/T\text{-}ZnO_w$ hybrid reinforced composite solders with various Zn: Zr ratios after tensile tests. Fig. 5-9 shows the fracture surface of hybrid reinforced composite solders with different Zn: Zr ratios. Fig. 5-9(a) shows the fracture surface of single NiO/ZrO_2 reinforced composite solder. Many dimples can be observed at the surface, exhibiting a typical ductile fracture. When the Zn: Zr ratio reaches to 1: 4 (Fig. 5-9(b)), ductile fracture characteristics also show. Unlike Fig. 5-9(a), some large and small-sized dimples are distributed alternately in Fig. 5-9(b). It is known that the larger the dimple size and the deeper the depth, the greater the degree of deformation of the composite solder. Therefore, Fig. 5-9(b) shows a greater plastic deformation degree than Fig. 5-9(a). When the Zn: Zr ratio reaches 2: 3 (Fig. 5-9(c)), the proportion of large dimples is further increased, indicating the greater plastic deformation degree, which is attributed to the reasonable Zn: Zr mixing ratio. At this mixing ratio, while ensuring refined grain size, effective load transfer can be obtained, so that the composite solder exhibits good strength-ductility. However, when the mixing ratio is changed to 3: 2, the number of large-size dimples is slightly reduced, indicating the decreased ductility of the composite solder. The decline in ductility is due to the decrease of NiO/ZrO_2 percentage, weakening the grain refinement effect, resulting in the coarsening of IMC, which leads to the decrease of elongation. When the mixing ratio is increased to 4: 1, the roughness of the fracture surface is further reduced, corresponding to the declined number of dimples. When a single 0.3 mass% $NiO/T\text{-}ZnO_w$ is added, the plastic deformation degree of the fracture is increased, but it is still lower than that of the composite solder with the Zn: Zr ratio of 2: 3.

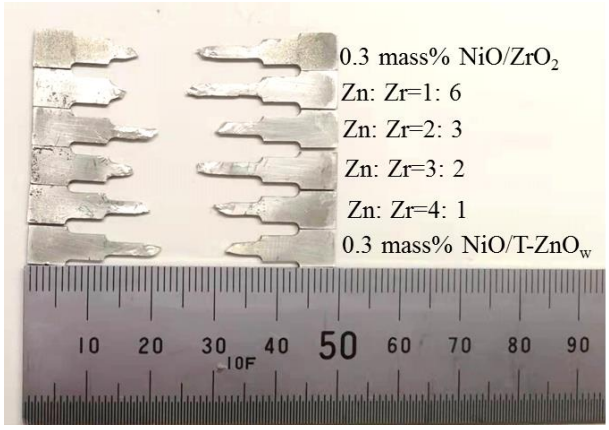

Fig. 5-8 Photographs of the NiO/ZrO_2 and $NiO/T\text{-}ZnO_w$ hybrid reinforced composite solders with various Zn: Zr ratios after tensile tests.

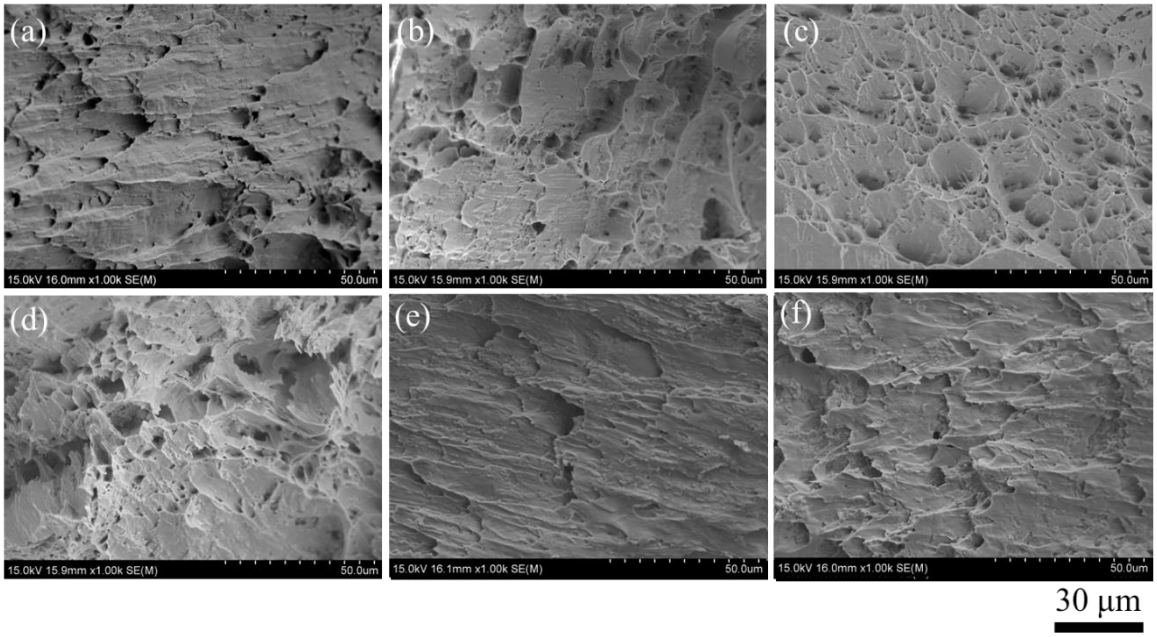

Fig. 5-9 Fracture surfaces of NiO/ZrO_2 and $NiO/T\text{-}ZnO_w$ hybrid reinforced composite solders with various Zn: Zr ratios. (a) 0.30 mass% NiO/ZrO_2 (b) Zn: Zr=1: 4; (c) Zn: Zr=2: 3; (d) Zn: Zr=3: 2; (e) Zn: Zr=4: 1; (f) 0.30 mass% $NiO/T\text{-}ZnO_w$.

In summary, for the NiO/ZrO_2 and $NiO/T\text{-}ZnO_w$ hybrid reinforced composite solder, different mixing ratios affect the fracture morphology of the composite solder. The fracture of composite solder with a suitable mixing ratio exhibits uniform and dense dimples. Overall, the microstructure, properties and fracture morphology of composite solders show a consistent correlation during the hybrid regulation process of reinforcements.

5.5.2 Mechanisms of strengthening and ductility

When developing composite solders, an increase in strength often comes at the expense of ductility. However, high strength and ductility were required simultaneously for the actual service conditions. In this study, both the UTS and elongation of the composite solder were improved compared with the plain Sn1.0Ag0.5Cu solder, and the results also higher than that of commercial Sn3.0Ag0.5Cu solder. It was mainly attributed to the design of multi-phase and multi-scale hybrid reinforcement system and the surface modification of reinforcements. A no gaps, no micropores, or new phase formed novel interface between solder matrix and reinforcements was formed. The strengthening-ductility mechanism can be systematically proposed as follows: (1) Orowan strengthening effect (2) load transfer effect, (3) grain refinement effect, (4) misfit dislocation effect, and (5) synergy effect of two reinforcements.

(a) Orowan strengthening effect

It has mentioned that, in Fig. 5-6, NiO/ZrO_2 is dispersed in the solder matrix. These dispersed reinforcements can hinder the movement of the dislocations, improving the mechanical properties of composite solders. The schematic diagram of dislocations bypassing the second phase particles had mentioned in Fig. 1-4 of chapter 1. In addition, NiO/ZrO_2 can act as heterogeneous nucleation sites for IMC (Ag_3Sn and Cu_6Sn_5). Therefore, the IMC size in the composite solder is refined when the Zn: Zr ratio is 2: 3, which has mentioned in Fig. 5-3. These refined IMCs, which belong to the hard particles, can also hinder the movement of the dislocations, and exhibit a better strengthening effect than the coarse IMC in plain solder. This can be qualitatively explained by Eq. (5-1) [2],

$$\sigma_{Orowan} = \frac{0.13 G_m b}{d_p[(1/2V_p)-1]} \cdot ln\left(\frac{d_p}{2b}\right) \quad (5\text{-}1)$$

where σ_{Orowan} is the strengthening effect caused by the Orowan strengthening mechanism, G_m is the shear modulus of the solder matrix alloy, d_p is the particle size of reinforcements, b is the Burgers vector of the solder matrix, and V_p is the volume fraction of reinforcements.

(b) Load transfer effect

For the particle and whisker hybrid reinforced composite solder, load transfer is considered one of the most important strengthening and ductility mechanisms. During the

composite solder is subjected to the external tensile load, the strain first occurs in the solder matrix. With the continuation of the tensile, the stress is transferred from the solder matrix to the whiskers through the interface. Because the whiskers are characterized by high strength and high modulus, they can withstand higher stress loads, which is one of the reasons for the higher strength of the composite solder. However, the brittle T-ZnO_w breaks when the external tensile load exceeds a critical value. Subsequently, the load returns to the solder matrix, and a continued external load eventually leads to the sample fracture. Moreover, due to the presence of whiskers, the crack tip could be blunted and deflected during crack propagation. Additional energy is required for forming and growing new cracks, which enhances the ductility of the composites [3,4]. In addition, in the process of whiskers being pulled out, in addition to bear part of the tensile load, it can also act as a "bridge" to inhibit rapid fracture of the sample. Fig. 5-10(a) and (b) show two typical strengthening and ductility modes of load transfer, where Fig. 5-10(a) and (b) shows the fractured and pulled-out whiskers. And a schematic illustration of the strengthening and ductility mechanism caused by load transfer of the whiskers is shown in Fig. 5-10(c), where (A) presents the fracture, and (B) presents the pulled-out whisker. The added NiO/T-ZnO whiskers not only bore the load but also hindered the propagation of microcracks, contributing to the simultaneous improvement of strength and ductility.

In addition, for the NiO/ZrO_2 doped into the solder matrix, the NiO nanoparticles are uniformly attached to the ZrO_2 surface after surface modification, resulting in the increased roughness of the ZrO_2 surface. This rough surface could increase the contact area between the solder matrix and reinforcements. Meanwhile, the protruding NiO nanoparticles could act as wedges, which are conductive to the formation of micro-mechanical locking between the

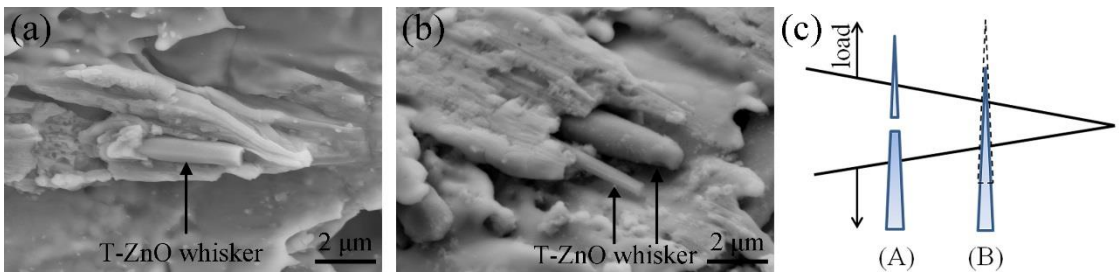

Fig. 5-10 Strengthening and ductility models of load transfer. (a) Fractured whisker, (b) pulled-out whisker, and (c) schematic illustration of the strengthening and ductility mechanism.

NiO/ZrO_2 and solder matrix. Both of the two factors can improve the load transfer efficiency of the NiO/ZrO_2 reinforcements in solder matrix.

The shear-lag model [5] (Eq. (5-2)) can be used to evaluate the strengthening effect of the NiO/T-ZnO whiskers.

$$\Delta\sigma_{L.T\ 1} = 0.5 \cdot \sigma_m \cdot V_r \cdot \frac{l}{d} \tag{5-2}$$

where $\Delta\sigma_{L.T\ 1}$ is the strengthening effect caused by load transfer, σ_m is the strength of the solder matrix, V_r is the volume fraction of reinforcement phase, and $\frac{l}{d}$ is the aspect ratio of the whiskers.

This model assumes that all whiskers are parallel to the tensile direction. However, whiskers with the three-dimensional spatial structure were randomly distributed in the Sn1.0Ag 0.5Cu solder matrix instead. This problem of distribution directions is also known for other whiskers reinforced composite materials [6]. To accurately understand the strengthening effect of the whiskers, a modified shear-lag model (Eq. (5-3)) was proposed by Ryu [7]:

$$\Delta\sigma_{L.T\ 2} = 0.5 \cdot \sigma_m \cdot V_r \cdot [\left(\frac{l}{d}\right) cos^2\theta + (\frac{3\pi-4}{3\pi})(1+\frac{d}{l})sin^2\theta] \tag{5-3}$$

where θ is the angle between the whisker and the loading direction.

For the T-ZnO_w, the angle between any of its two needles is 109 °. If one needle is parallel to the loading direction, then the other three needles point away from the loading direction at an angle of 34.4 °.

When θ = 34.4°, the above equation is equivalent to Eq. (5-4)

$$\Delta\sigma_{L.T\ 3} = 0.5 \cdot \sigma_m \cdot V_r \cdot [0.68\left(\frac{l}{d}\right) + 0.18(1+\frac{d}{l})] \tag{5-4}$$

In summary, for T-ZnO_w, when one needle is parallel to the stretching direction and other three needles are at 34.3 °from this direction. The final strengthening equation is expressed by Eq. (5-5).

$$\Delta\sigma_{L.T\ 4} = \sigma_{L.R\ 1} + 3\sigma_{L.R\ 3} \tag{5-5}$$

(c) Grain refinement effect

It has been mentioned in Fig. 5-3 that the grain size in the composite solder is refined when the Zn: Zr ratio is 2: 3. The smaller the grain size, the greater the number of grains per

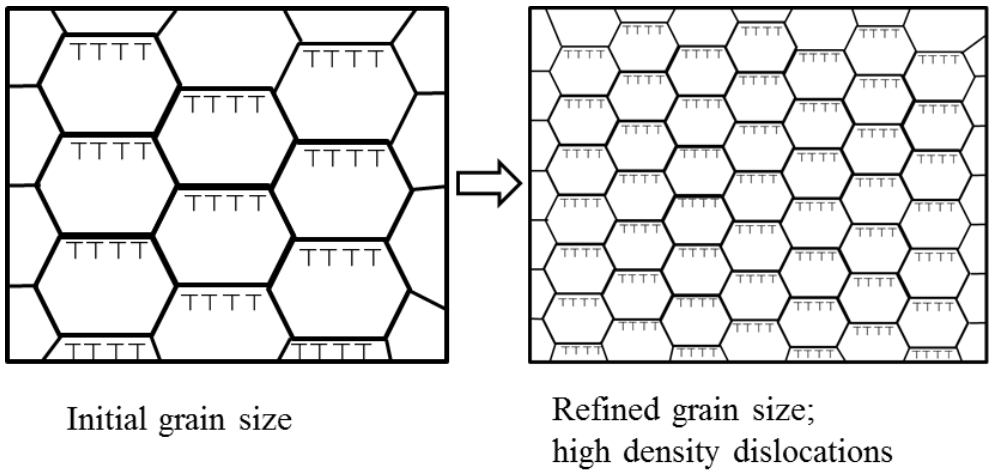

Fig. 5-11 Schematic illustration of the grain refinement effect.

unit volume of the material. The schematic illustration of the grain refinement effect is shown in Fig. 5-11. This corresponds to a larger grain boundary area that increased the plastic deformation resistance of the material. On the one hand, dislocations were blocked at the grain boundaries, and the slip band was also terminated near the grain boundaries during tensile deformation of the samples [8]. Meanwhile, multiple slips took place to coordinate the deformation due to different grain orientations, and dislocation intercross occurred during the multiple slips [9]. The above two aspects increased the resistance of dislocation movement, thereby increasing the strength of the composite solder.

At the same time, better plasticity can be obtained when the grain sizes were fine and uniform. The smaller the grains size, the much the number of grains in a certain volume. Under the same deformation degree, the deformation is dispersed in much grain, resulting in much uniform deformation and less stress concentration, which made it possible to withstand a larger amount of deformation before breaking. This is the one of the reasons for the increased elongation for the composite solder. Additionally, the smaller grain size also indicates the more tortuous grain boundary, which is not conducive to the propagation of cracks along the grain boundary. As a result, more energy can be absorbed during the fracture process, leading to good ductility of the composite solder.

Grain refinement effects can be evaluated using the Hall-Petch formula (Eq. (5-6)) [10].

$$\Delta\sigma_{G.R} = k(d^{-0.5} - {d_0}^{-0.5}) \tag{5-6}$$

where $\Delta\sigma_{G.R}$ is the strengthening effect caused by grain refining, *k* is a constant, *d* is the average grain size of the composite solder, and d_0 is the average grain size of the plain solder.

(d) Misfit dislocation effect

Thermal misfit dislocations can be observed near the interface between the reinforcement and Sn1.0Ag0.5Cu, and they were caused by the different CTE values. The misfit dislocation effect is also one of the reasons for the increased strength in the composite solder. The strengthening effect can be expressed with Eq. (5-7) [11].

$$\Delta\sigma_{T.M} = k \cdot G_m \cdot b\sqrt{\frac{12\Delta\alpha \cdot \Delta T \cdot V_p}{b \cdot d_p(1-V_p)}} \quad (5\text{-}7)$$

where $\Delta\sigma_{T.M}$ is the strengthening effect caused by the thermal effect, k is a constant, G_m is the shear modulus of the solder matrix, b is the Burgers vector, $\Delta\alpha$ is the difference in CTE between the reinforcement and matrix, ΔT is the temperature difference between materials preparation and testing, V_p is the volume fraction of the reinforcement, and d_p is the size of reinforcement.

(e) synergy effect of two reinforcements

In chapters 3 and 4, I had prepared single NiO/ZrO_2 reinforced composite solder and single NiO/T-ZnO_w reinforced composite solder, respectively, and systematically analyzed their strengthening-ductility mechanism. For the former, its strengthening-ductility mechanism mainly includes Orowan strengthening effect, grain refinement effect, and misfit dislocation effect (shown in Table 5-2). Among them, Orowan strengthening mechanism was the main strengthening mechanism in improving the mechanical properties of composite solders. The effective implementation of the Orowan strengthening mechanism is mainly attributed to the appropriate choice of reinforcement and its dispersed distribution, and the novel interface design between reinforcement and solder matrix. For the latter (whisker reinforced composite solder), its strengthening mechanism mainly includes load transfer effect, grain refinement effect, and misfit dislocation effect (shown in Table 5-2). Among them, the load transfer effect is most effective for improving the strength and ductility. Its effective implementation mainly depends on the choice of T-ZnO_w and the design of the clean interface of the T-

ZnO_w/NiO/SnAgCu sandwich structure, thereby realizing the isotropic-based load transfer effect and effectively improving the ductility of the composite solder.

Based on the above systematic analysis, in order to obtain high strength-ductility composite solder, I first proposed the design concept of multi-phase and multi-scale hybrid reinforced composite solder. The schematic diagram of hybrid reinforced composite solder is shown in Fig. 5-12. In this design concept, NiO/T-ZnO whisker act as the skeleton role of composite solder, thereby constructing a discontinuous three-dimensional network space structure. On the basis of this spatial structure, NiO/ZrO_2 nanoparticles are dispersed in the matrix, which plays the role of strengthening particle due to the Orowan strengthening effect.

Table 5-2 Strengthening-ductility mechanism of ZrO_2 particle and T-ZnO whisker hybrid reinforced composite solder.

Reinforcemnts / Mechanism	ZrO_2 particle	T-ZnO whisker
Orowan strengthening effect	√	-
Grain refinement effect	√	√
Misfit dislocation effect	√	√
Load transfer effect	-	√
Synery effect	Combined of them	

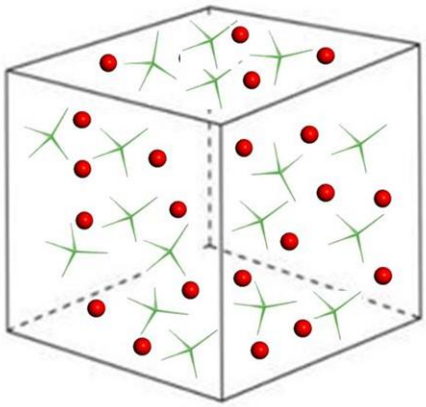

Fig. 5-12 Schematic diagram of hybrid reinforced composite solder.

In addition, the two kind of reinforcements and solder matrix are well bonded. Therefore, the hybrid system can synergistically produce effective load transfer effect and Orowan strengthening effect, grain refinement effect, and misfit dislocation effect. Under the synergy effect, a novel lead-free composite solder with high strengthen-ductility is obtained. This design concept could provide new ideas for designing high-performance lead-free composite solders. I also hope that this could provide some support for the improvement of design criterion and principle of composite solder.

5.6 Thermal stability of hybrid reinforced composite solders

In above parts, I systematically studied the microstructure and mechanical properties of composite solders with different Zn: Zr mixing ratios, and determined the optimal mixing ratio of composite solders. However, SnAgCu system composite solders are widely used in electronic packaging. This not only requires the solder to have good mechanical properties, but also good reliability during long-term service. Among several reliability issues, thermal aging is the most widespread, which had mentioned in chapter 1. Therefore, thermal aging test was conducted systematically to evaluate hybrid reinforced composite solders. In this section, the optimal composition of the composite solder, with the Zn: Zr ratio of 2: 3, was selected. In addition, plain Sn1.0Ag0.5Cu, commercial Sn3.0Ag0.5Cu, and 0.3 mass% NiO/ZrO_2 reinforced Sn1.0Ag0.5Cu composite solder were also selected as references.

5.6.1 Microstructure evolution during thermal aging

Fig. 5-13 shows the SEM images of plain Sn1.0Ag0.5Cu and Sn3.0Ag0.5Cu sold bulk with different thermal aging times. Fig, 5-13(a) presents the cast of plain Sn1.0Ag0.5Cu solder bulk, typical microstructure, consisting of β-Sn + eutectic phase, can be observed. The size of the phase is defined as the intercept across them, which had mentioned in chapter 3 and chapter 4. The average size of IMCs in eutectic is 0.5 μm. Their formation process has been systematically explained in the previous chapter. After 168 h thermal aging (Fig. 5-13(b)), the eutectic phase began to dissolve, and the coarsening of IMC also occurred. Similar phenomena also appeared in the literature [12]. During the thermal aging process, the coarsening of IMCs

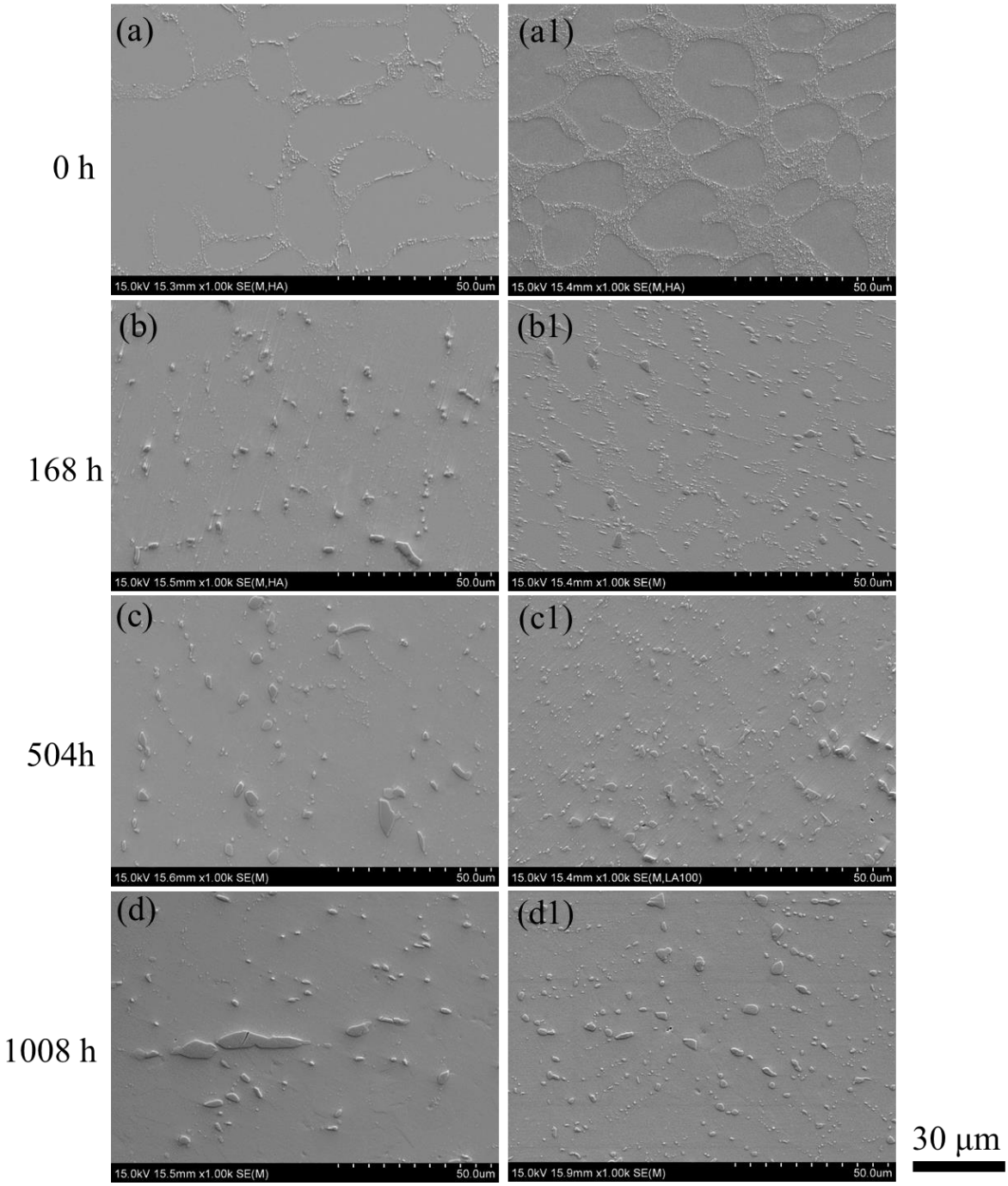

Fig. 5-13 SEM images of plain Sn1.0Ag0.5Cu and Sn3.0Ag0.5Cu solder bulk with different thermal aging times. (a) 0 h, (b) 168 h, (c) 504 h, and (d) 1008 h thermal aging of plain Sn1.0Ag0.5Cu; (a1) 0 h, (b1) 168 h, (c1) 504 h, and (d1) 1008 h thermal aging of plain Sn3.0Ag0.5Cu.

can be attributed to two aspects. The coarsening of IMC is due to Ostwald ripening, which is defined as the growth of large particles at the expense of small ones of a dispersed phase in a matrix, is driven by the tendency of a system to reduce the total interfacial energy [13].

Therefore, during the aging process, the small IMCs (Ag_3Sn, Cu_6Sn_5) are gradually merged by the adjacent large-sized IMCs, which eventually leads to the coarsening of the IMCs. On the other hand, the solidification process of composite solder belongs to non-equilibrium solidification, in which partial of Ag and Cu are over-dissolved in Sn. These over-solid-solution Ag and Cu gradually precipitate and form new IMCs with Sn during the aging process. When the thermal aging time reaches 504 h, the net-like eutectic phase almost disappears, and only IMC particles with different sizes are dispersed in the solder matrix. At this time, the average particle size of IMC is 0.87 μm. When the thermal aging time reaches 1008 h, the microstructure continues to be coarsened, and some of the IMC is abnormally coarse, which also can be explained by Ostwald ripening. At this time, the average size of the IMC is 0.95 μm.

Fig. 5-13(a1)-(d1) show the SEM images of plain Sn3.0Ag0.5Cu solder bulk with different thermal aging times. Fig. 5-13(a1) exhibits the as-cast microstructure; the average size of IMC particles is 0.27 μm. The ratio of the eutectic phase is higher than that of plain Sn1.0Ag0.5Cu solder due to the high Ag content. With the increase of aging time, the eutectic structure gradually dissolves. When aging time reaches 504 h (Fig. 5-13(c1)), the network structure disappeared and the IMC size grew to 0.89 μm. When thermal aging time reaches 1008 h (Fig. 5-13(d1)), coarse IMC is dispersed in the solder with an average size of 1.01μm.

Fig. 5-14(a)-(d) shows the SEM images of 0.3 mass% NiO/ZrO_2 reinforced Sn1.0Ag0.5Cu composite solder with different thermal aging times. In the initial stage (Fig. 5-14(a)), the microstructure is composed of β-Sn and eutectic structures. The formation of β-Sn and eutectic structures has systematically described in previous chapters. And for a single NiO/ZrO_2 reinforced composite solder, NiO/ZrO_2 was located in the eutectic areas mentioned in chapter 3. When the thermal aging time reaches 168 h (Fig. 5-14(b)), part of the eutectic structure is dissolved, but the network structure remaines. And the IMC size of composite solder is 0.63 μm, which is slightly higher than that of casting state (Fig. 5-14(a)). Unlike plain solder, the net-like eutectic phase almost disappeared after 504 h thermal aging, NiO/ZrO_2 reinforced composite solder still retained the reticular eutectic structure after 504 h aging. And

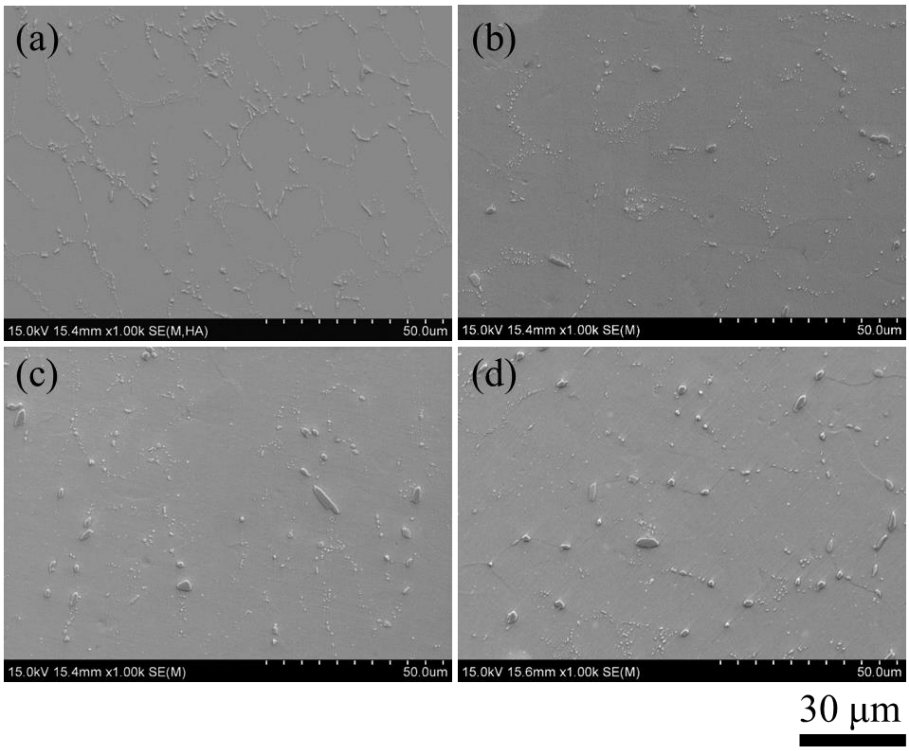

Fig. 5-14 SEM images of 0.3 mass% NiO/ZrO_2 reinforced Sn1.0Ag0.5Cu composite solder bulk with different thermal aging times. (a) 0 h, (b) 168 h, (c) 504 h, and (d) 1008 h.

the size of the IMC has just increased slightly. When the aging time reaches 1008 h (Fig. 5-14(d)), the IMC size shows a coarse trend, and the reticular eutectic structure basically disappears, but the IMC size of composite solder (0.80 μm) is still smaller than that of plain solder. In summary, 0.3 mass% NiO/ZrO_2 reinforced Sn1.0Ag0.5Cu composite solder exhibit better microstructure stability than that of plain solder.

Fig 5-15 shows the SEM images of hybrid reinforced Sn1.0Ag0.5Cu composite solder bulk with Zn: Zr ratio of 2: 3 at different thermal aging times. In the initial stage (Fig. 5-15(a)), the microstructure is also composed of β-Sn and eutectic structure, while the ratio of eutectic structure is higher than that of plain Sn1.0Ag0.5Cu solder due to the reasonable mixing ratio of the two reinforcements. And the average size of the IMC particles is 0.32 μm, which is smaller than that of plain Sn1.0Ag0.5Cu solder. In addition, $NiO/T\text{-}ZnO_w$ can be observed in the eutectic area, which indicates that $NiO/T\text{-}ZnO_w$ is effectively added to the solder matrix. Moreover, I also had proved that NiO/ZrO_2 was dispersed in the solder in Fig. 5-6. When the thermal aging time reaches 168 h (Fig. 5-13(b)), the proportion of eutectic phase is decreased,

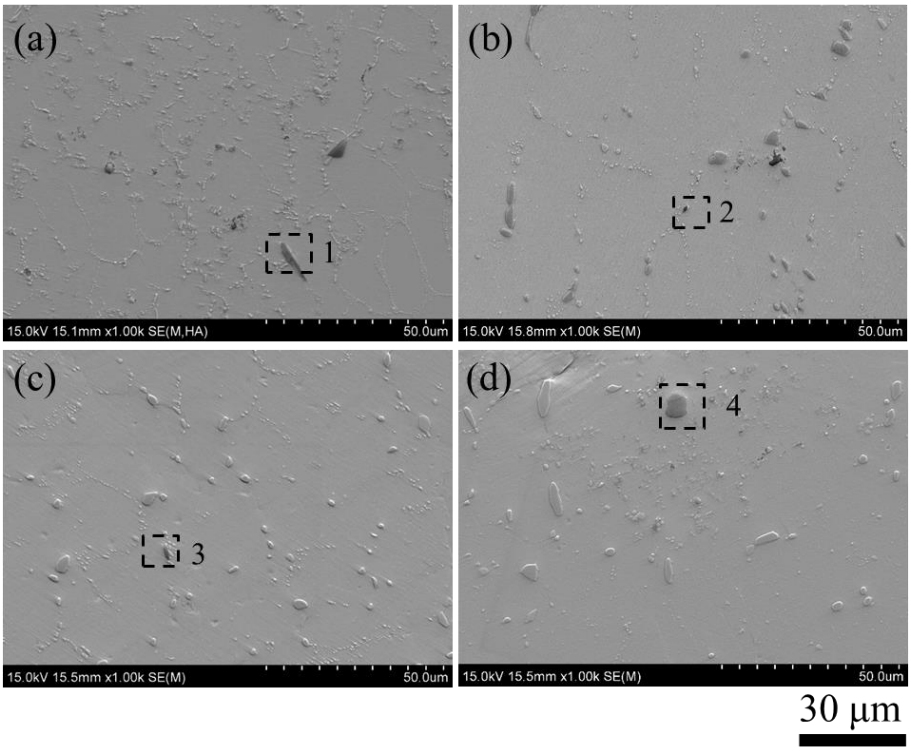

Fig. 5-15 SEM images of hybrid reinforced SAC105 composite solder bulk with Zn: Zr ratio of 2: 3 at different thermal aging times. (a) 0 h, (b) 168 h, (c) 504 h, and (d) 1008 h.

part of the eutectic phase is dissolved, but the network structure is still remained. At the same time, coarsening of IMC is occurred, which is attributed to the similar reasons mentioned in Fig. 5-13(b). Unlike plain Sn1.0 AG0.5Cu solder, the net-like eutectic phase almost disappeared after 504 h thermal aging, composite solder still retained the reticular eutectic structure after 504 h aging. And the size of the IMC has increased slightly. It is known that the growth of grain is controlled by the diffusion behavior during thermal aging process [12]. The continuous migration and merging of grain boundaries eventually lead to the coarsening of the grains. After adding suitable reinforcements, the pinning effect can be produced, thereby inhibiting the migration of grain boundaries during the aging process, and finally exhibiting better structural stability compared with plain Sn1.0Ag0.5Cu solder, the size of the IMC is 0.61 μm after 504 h aging, which is smaller than that of Fig.5-13(c). When the aging time reaches 1008 h, the IMC size shows a coarse trend, and the reticular eutectic phase basically disappears, but no unusually thick IMC appears.

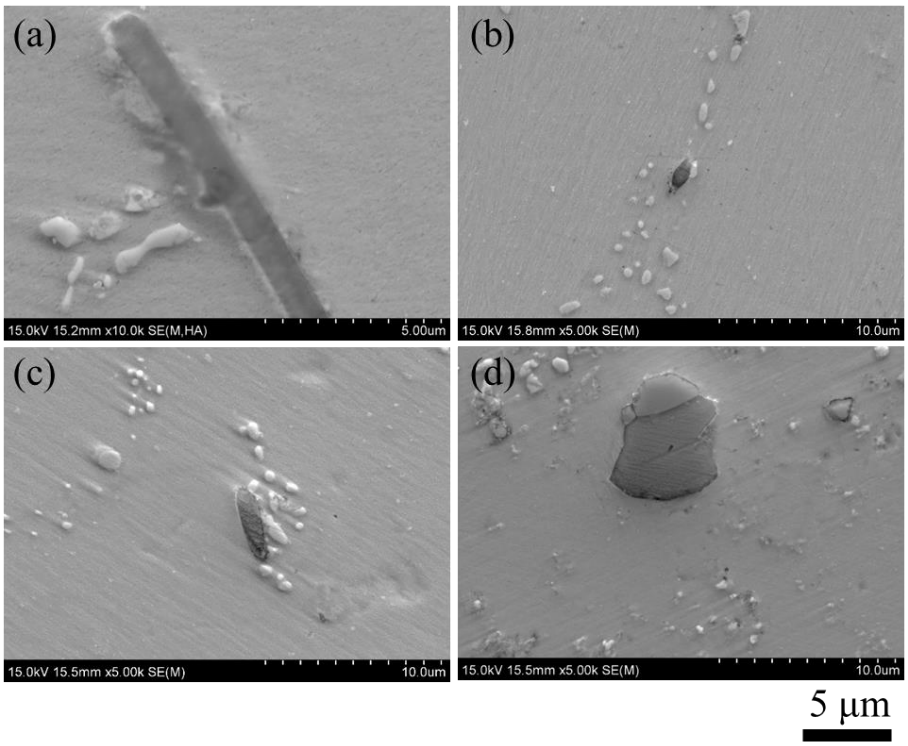

Fig. 5-16 High magnification SEM images of hybrid reinforced SAC105 composite solder bulk with different thermal aging times. (a) 0 h, high magnification view of area 1 in Fig. 5-15(a), (b) 168 h, high magnification view of area 2 in Fig. 5-15(b), (c) 504 h, high magnification view of area 3 in Fig. 5-15(c), (d) 1008 h, high magnification view of area 4 in Fig. 5-15(d).

Fig. 5-16 shows the high magnification SEM images of hybrid reinforced Sn1.0Ag0.5Cu composite solder with different thermal aging times. As seen from Fig. 5-16(a)-(d), NiO/T-ZnO_w existed in the solder matrix, and located in the eutectic areas. On the one hand, NiO/T-ZnO_w can act as the heterogeneous nucleation sites of IMC. On the other hand, the reinforcements produce a pinning effect, which inhibits the growth of IMC and exhibits better microstructure stability. For example, the size of IMC has little difference when aging is 168 h (Fig.5-16 (b)) and 504 h (Fig.5-16 (c)).

To quantitatively analyze the growth of the IMC of the four kinds of solder during the thermal aging process, the function curves of IMC size and thermal aging time was conducted. Fig. 5-17(a) shows the IMC size function to thermal aging times. The four curves represent plain Sn1.0Ag0.5Cu solder, Sn3.0Ag0.5Cu solder, 0.3 mass% NiO/ZrO_2 reinforced Sn1.0Ag0.5Cu composite solder, and hybrid reinforced Sn1.0Ag0.5Cu composite solder,

respectively. Overall, the growth rate of IMC in the four solders alloy is relatively high in 0-156 h, due to the small IMC size and the large specific surface area, which is easy to coarsen. As the aging time increases, the growth rate decreases. In addition, compared to plain Sn1.0Ag0.5Cu solder and Sn3.0Ag0.5Cu solder, two kinds of composite solder exhibit a relatively flat growth curve, indicating that the growth rate of IMC in the composite solder is lower during the thermal aging. The reason had mentioned in Fig. 5-14 and Fig. 5-15. Therefore, when the aging time reaches 1008 h, the IMC size of the hybrid reinforced composite solder is 0.70 μm, which is smaller than that of plain Sn1.0Ag0.5Cu solder, Sn3.0Ag0.5Cu solder, and 0.3 mass% NiO/ZrO_2 reinforced Sn1.0Ag0.5Cu composite solder (0.95 μm, 1.01 μm, and 0.80μm, respectively).

It is known that the growth of IMC is controlled by the diffusion mechanism during the thermal aging process [14]. Therefore, the average size and aging time of IMC can be expressed as the following Eq. (5-8) [15].

$$X=(Dt)^{0.5} \tag{5-8}$$

$$\Rightarrow: X^2=Dt \tag{5-9}$$

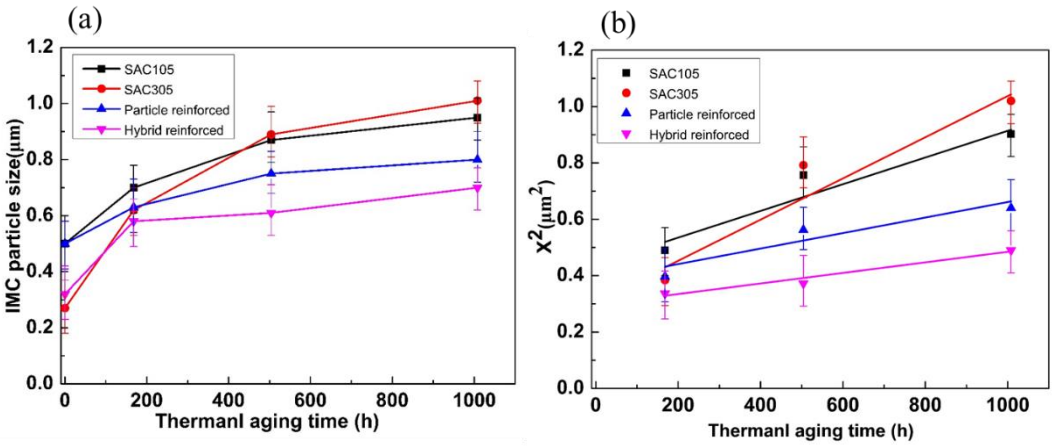

Fig. 5-17 The function curves of IMC size and thermal aging times. (a) IMC size and (b) square of IMC size function to thermal aging times.

Table 5-3 The diffusion coefficient D of four kinds of solder

Materials	Sn1.0Ag0.5Cu	Sn3.0Ag0.5Cu	NiO/ZrO_2 reinforced composite solder	Hybrid reinforced composite solder
D (10^{-19} m^2/s)	1.32	2.03	0.76	0.52

Based on the data in Fig. 5-17 (a) and Eq. (5-9), four fitting lines can be obtained, which are shown in Fig. 5-17(b). The slope of these straight lines represent the diffusion coefficient *D*, and the diffusion coefficient *D* of the four solders are shown in Table 5-3. Hybrid reinforced composite solder shows the smallest *D* values among them, that is, the smallest growth rate during the thermal aging. The results suggest that reasonable mixing of NiO/ZrO_2 and NiO/T-ZnO_w can effectively inhibit the coarsening of the microstructure, thereby improving the thermal stability of the composite solder. In addition, the D value of Sn3.0Ag0.5Cu solder is higher than that of Sn1.0Ag0.5Cu solder, which is attributed to the high Ag contents. The result is consistent with [16].

5.6.2 Mechanical properties evolution during thermal aging

To evaluate the mechanical properties of composite solders during thermal aging, tensile test was conducted. Fig. 5-18(a)-(d) shows the representative stress-strain curves of four kinds of solders, and Fig. 5-18(e) and (f) shows the UTS and elongation of four kinds of solders with different thermal aging times respectively. On the whole, UTS shows a decreasing trend with the increase of aging time. Especially after 168 h of aging, UTS significantly decreased and then tended to be stable. This result is consistent with the literature [10]. In the initial stage (as cast), the UTS of Sn1.0Ag0.5Cu, Sn3.0Ag0.5Cu, 0.3 mass% NiO/ZrO_2 reinforced Sn1.0Ag0.5Cu, and hybrid reinforced Sn1.0Ag0.5Cu composite, are 27.9 MPa, 35.4 MPa, 34.8 MPa, and 35.9 MPa, respectively. After 1008 h of aging, UTS reduced to 16.6 MPa, 22.3 MPa, 19.6 MPa, and 21.7 MPa, respectively. The UTS of hybrid reinforced composite solder was still higher than that of plain Sn1.0Ag0.5Cu solder and single NiO/ZrO_2 reinforced Sn1.0Ag0.5Cu composite solder, and almost equal to the commercial Sn3.0Ag0.5Cu solder. Fig. 5-18(f) shows the elongation evolution with different thermal aging times. The elongation of Sn1.0Ag0.5Cu, Sn3.0Ag0.5Cu, 0.3 mass% NiO/ZrO_2 reinforced Sn1.0Ag0.5Cu, and hybrid reinforced Sn1.0Ag0.5Cu composite, are 21.6%, 26.1%, 27.9% and 31.4% at the initial stage (as cast). After 504 h thermal aging, they increase to 27.8%, 32.8%, 32.4% and 33.2%, respectively. However, in the range of 504-1008 h, the elongation of plain Sn1.0Ag0.5Cu, Sn3.0Ag0.5Cu, and 0.3 mass% NiO/ZrO_2 reinforced Sn1.0Ag0.5Cu decrease to 24.0%, 25.0%,

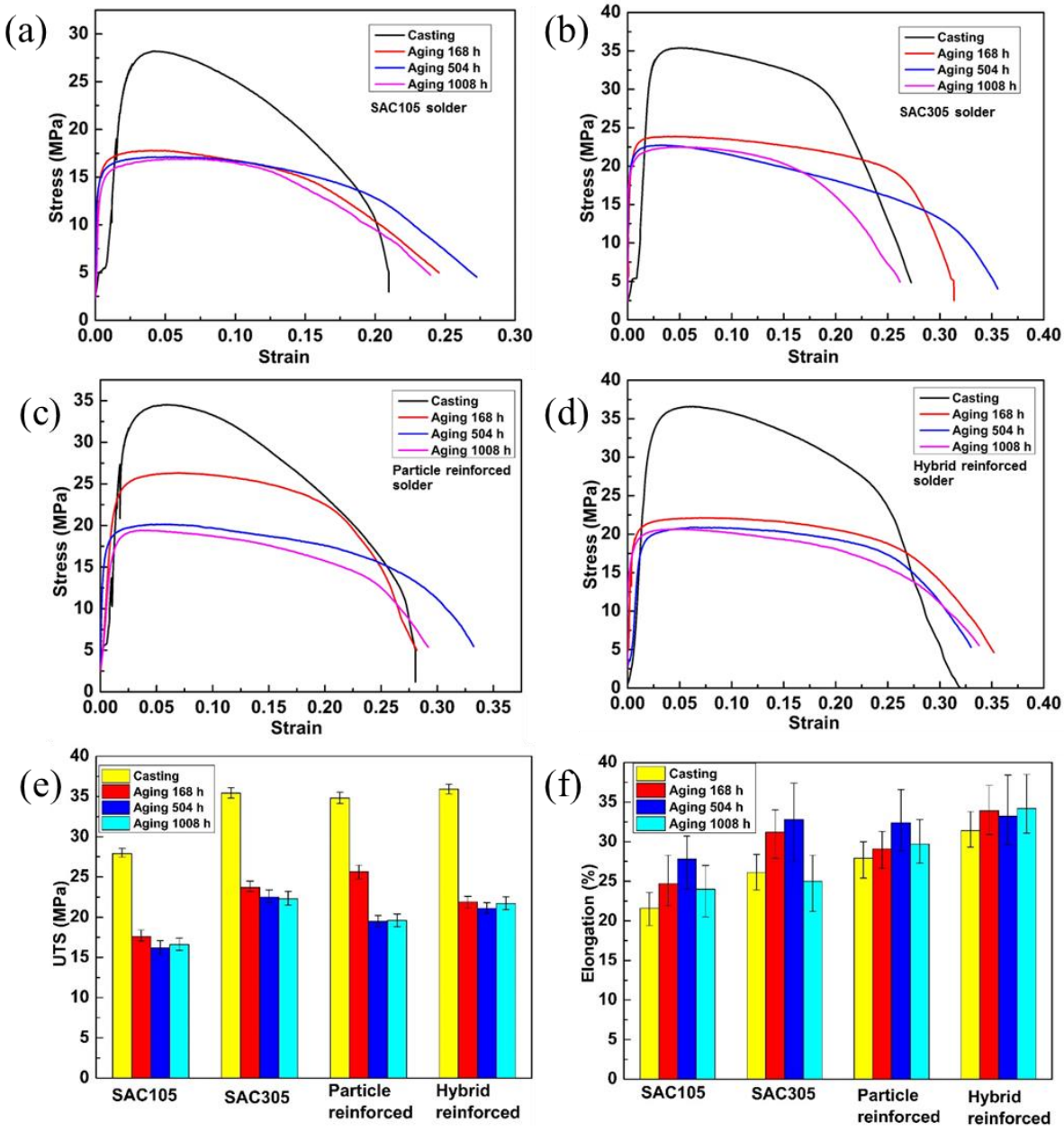

Fig. 5-18 Mechanical properties of four kinds of solders with different thermal aging times. Representative stress-strain curves of (a) plain Sn1.0Ag0.5Cu, (b) plain Sn1.0Ag0.5Cu, (c) 0.3 mass% NiO/ZrO_2 reinforced Sn1.0Ag0.5Cu composite solder, (d) hybrid reinforced Sn1.0Ag0.5Cu composite solder. (e) UTS, (f) elongation.

and 29.7%, respectively. While the elongation of hybrid reinforced composite solder increases to 34.2%, which still is maintained in a high ductility state. This result indicates that the ductility of the composite solder is better than that of plain Sn1.0Ag0.5Cu and Sn3.0Ag0.5Cu after long-term thermal aging.

The decrease of UTS is attributed to the coarsening of the IMC size during thermal aging. In the initial stage, small IMC can act as the hard second phase, producing the Orowan strengthening effect. However, as the aging time increases, these IMC sizes are coarsened, resulting in Orowan strengthening effect being weakened. Moreover, as seen from Fig.5-17(a), IMC coarsened fast during 0-156 h. Corresponding, the UTS also decreased rapidly. However, when IMC coarse to the critical size, it has little influence on UTS, which is also the reason why UTS tends to be stable in the later stage. And for the change of elongation during the aging process, it can be explained using microstructure evolution. As can be seen from Figs. 5-13 to 5-16, the proportion of eutectic structure gradually decreases during thermal aging, and the corresponding β-Sn proportion increases, which belongs to the soft phase, thus improving the elongation of solders. However, for plain Sn1.0Ag0.5Cu and Sn3.0Ag0.5Cu, due to the excessive growth of IMC during long-term thermal aging, obvious IMC coarsening, cracks, and pores occurred. Moreover, due to the coarsening of the microstructure, the coordination deformability between the grains is reduced. Both of the two factors lead to a decrease in elongation. For hybrid reinforced composite solder, when the thermal aging time reaches 1008 h, the grain size is smaller than the other solders, indicating better thermal stability. They are also the reason why the composite solder still maintains a high elongation after long-term thermal aging. In addition, compared with 0.3 mass% NiO/ZrO_2 reinforced Sn1.0Ag0.5Cu, the hybrid reinforced composite solder still shows better microstructure stability and mechanical properties after long-term thermal aging. The results suggest that a reasonable hybrid of reinforcements could improve the properties of composite solder.

In conclusion, hybrid reinforced composite solder shows the best mechanical properties among them after casting. And after 1008 h, it maintains the best among them. The results show that the hybrid reinforced composite solder has good microstructure and mechanical stability during thermal aging.

To better understand the evolution of mechanical properties and fracture behavior of composite solders, fracture surfaces were observed. Fig. 5-19 shows the photographs of four kinds of solders with different thermal aging times after tensile tests. Fig. 5-20 shows the

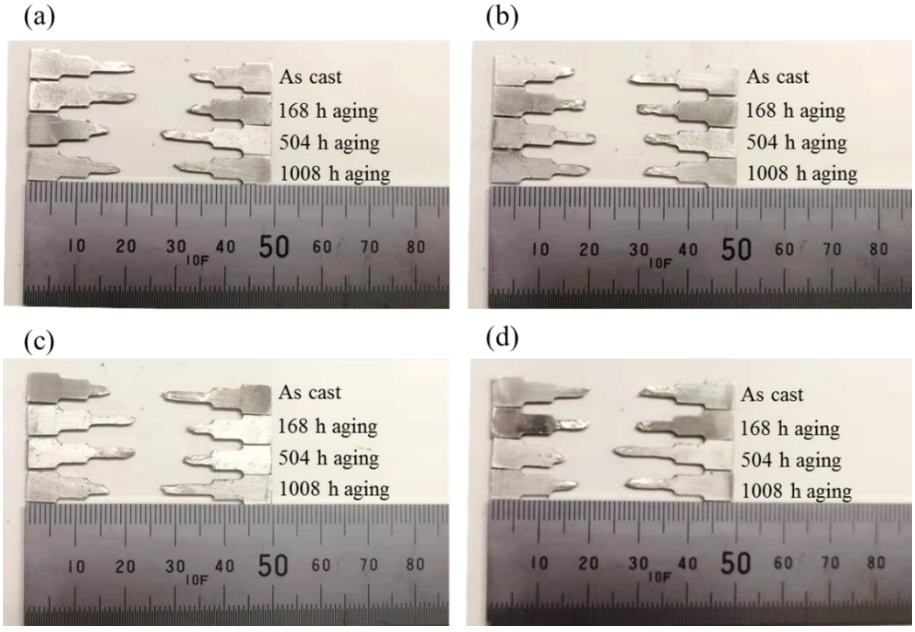

Fig. 5-19 Photographs of four kinds of solders with different thermal aging times after tensile tests. (a) plain Sn1.0Ag0.5Cu, (b) Sn3.0Ag0.5Cu, (c) 0.3 mass% NiO/ZrO_2 reinforced Sn1.0Ag0.5Cu composite solder, and (d) hybrid reinforced Sn1.0Ag0.5Cu composite solder.

fracture surface of them. For the fracture surface of as-cast solders (Fig. 5-20(a), (b), (c)and (d)), which had mentioned in previous parts. Among them, the surface of the hybrid reinforced composite solder presents more dimples, indicating the best plasticity. With the increase of thermal aging time, the fracture surfaces become rougher. In the range of 0-504 h, larger size and deeper dimples are observed in the fracture surface of four kinds of solders, which represents a greater degree of plastic deformation. However, when the thermal aging time reaches 1008 h, the fracture roughness of plain Sn1.0Ag0.5Cu (Fig. 5-20(a3)), Sn3.0Ag0.5Cu (Fig. 5-20(b3)), and 0.3 mass% NiO/ZrO_2 reinforced Sn1.0Ag0.5Cu composite solder (Fig. 5-20(c3)) are decreased, indicating that their ductility decreased. As for the hybrid reinforced composite solder (Fig. 5-20(d3)), it still maintains a high degree of plastic deformation after 1008 h thermal aging. The evolution of the fracture surface during the aging process is consistent with the results in Fig.5-18(f).

To further explore the reasons for the difference in elongation of these solders at 1008 h, I observed the high-magnification fractures. Fig. 5-21(a) shows a high magnification fracture of plain Sn1.0Ag0.5Cu. Coarse IMC (marked with dotted frame) has appeared on the fracture

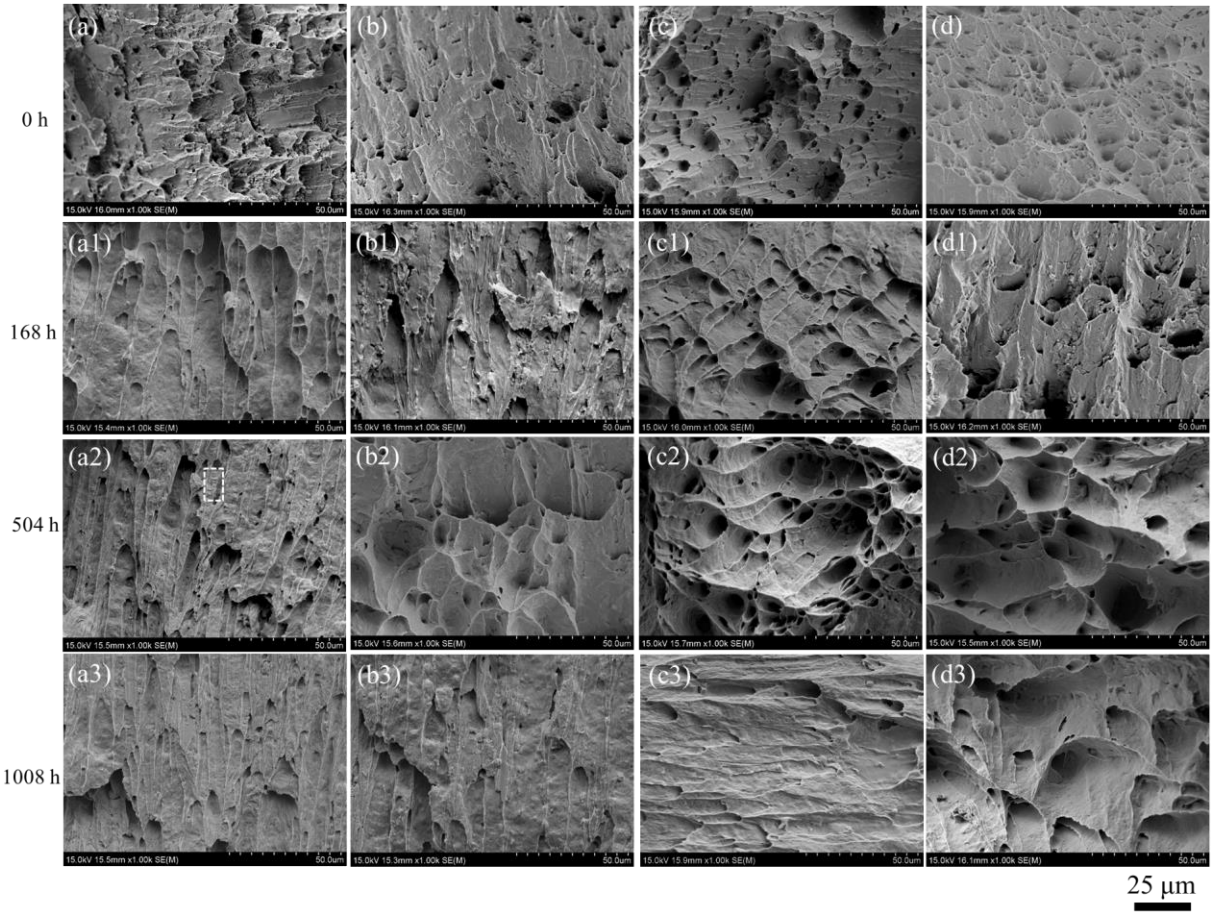

Fig. 5-20 Fracture surface of four kinds of solders with different thermal aging times. (a) plain Sn1.0Ag0.5Cu, (b) Sn3.0Ag0.5Cu, (c) 0.3 mass% NiO/ZrO_2 reinforced Sn1.0Ag0.5Cu composite solder, and (d) hybrid reinforced Sn1.0Ag0.5Cu composite solder. 1, 2, and 3 represent the thermal aging time of 168 h, 504 h, and 1008 h, respectively.

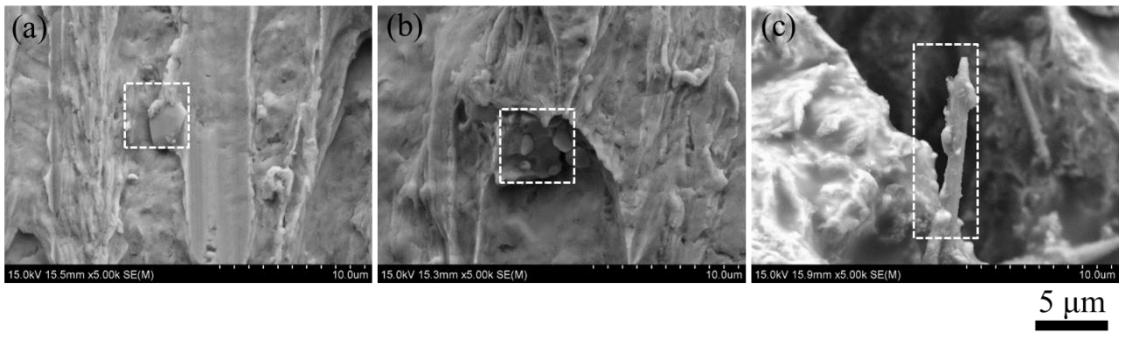

Fig. 5-21 Magnified fracture surface of solders. (a) plain Sn1.0Ag0.5Cu, (b) Sn3.0Ag0.5Cu, and (c) hybrid reinforced composite solder.

surface. IMC is a hard-brittle phase, which could reduce the elongation of solder. Similarly, for Sn3.0Ag0.5Cu solder (Fig. 5-21(b)), many IMC particles (marked with dotted frame) also

appeared on the bottom of the dimple. Therefore, when aging time reaches 1008 h, the decrease in elongation of plain Sn1.0Ag0.5Cu and Sn3.0Ag0.5Cu was attributed to the coarsening of IMC. The result is consistent with the SEM images of microstructure, which had mentioned in Fig. 5-13. For the high magnification fracture surface of the hybrid reinforced composite solder (Fig. 5-21(c)), no coarse IMC was observed, which is due to the reasonable doping of the reinforcements to refine the microstructure. Moreover, the pulled-out NiO/T-ZnO_w was observed (marked with dotted frame), and the pulled-out solder was attached to the surface of the whiskers, which indicates that the solder matrix and the reinforcement phase are well bonded, thereby ensuring effective load transfer effect. And this is also one of the reasons why the hybrid reinforced composite solder exhibit good ductility.

5.7 Conclusions

The NiO/ZrO_2 and NiO/T-ZnO_w hybrid reinforced Sn1.0Ag0.5Cu composite solder with different Zn: Zr ratios were prepared. The microstructure and mechanical properties of composite solder were systematically investigated, as well as the interfaces between reinforcements and solder matrix. The major findings are as follows:

1. NiO/ZrO_2 and NiO/T-ZnO_w were successfully added into the solder matrix, and dispersed in the solder matrix, which can act as the nuclear sites of eutectic. The microstructure evolution occurred with different Zn: Zr ratios. A high proportion of eutectic without coarse IMC was obtained when the Zn: Zr ratio reached 0.12: 0.18.
2. For the interface between NiO/ZrO_2, NiO/T-ZnO_w and Sn1.0Ag0.5Cu, no gaps, micropores, or new phases were formed, and the atomic inter-diffusion occurred at the interface. Hence, the composite interface structure of Sn1.0Ag0.5Cu/NiO/reinforcements was well designed. This novel interface is key in the strengthening and ductility of composite solder.
3. The UTS and elongation of composite solder can be improved synergistically with reasonable hybrid ratios. When the NiO/T-ZnO_w and Ni/ZrO_2 addition contents reached 0.12 mass% and 0.18 mass%, maximum UTS and elongation of composite solder were 35.9MPa and 31.4%, which were higher than the SAC 305. that is, a high strength-

ductility composite solder is obtained. This design concept of multi-phase and multi-scale hybrid reinforced composite solder could provide new ideas for designing high-performance lead-free composite solders.

4. During the thermal aging, hybrid reinforced composite solder showed a lighter degree of coarsening than others solders, which attributed to the suitable reinforcements doping. After 1008 h of thermal aging, composite solder remained the best results among them, indicating good microstructure and mechanical stability during thermal aging.

References

[1] A.A. El-Daly, A. Fawzy, S.F. Mansour, M.J. Younis, Novel SiC nanoparticles-containing Sn–1.0Ag–0.5Cu solder with good drop impact performance, Mater. Sci. Eng. A. 578 (2013) 62–71. https://doi.org/10.1016/j.msea.2013.04.022.

[2] Z.Y. Hu, X.W. Cheng, S.L. Li, H.M. Zhang, H. Wang, Z.H. Zhang, F.C. Wang, Investigation on the microstructure, room and high temperature mechanical behaviors and strengthening mechanisms of the (TiB+TiC)/TC4 composites, J. Alloys Compd. 726 (2017) 240–253. https://doi.org/10.1016/j.jallcom.2017.08.017.

[3] W. Huang, D. Restrepo, J.Y. Jung, F.Y. Su, Z. Liu, R.O. Ritchie, J. McKittrick, P. Zavattieri, D. Kisailus, Multiscale Toughening Mechanisms in Biological Materials and Bioinspired Designs, Adv. Mater. 31 (2019) 1–37. https://doi.org/10.1002/adma.201901561.

[4] Z. Xia, L. Riester, W.A. Curtin, H. Li, B.W. Sheldon, J. Liang, B. Chang, J.M. Xu, Direct observation of toughening mechanisms in carbon nanotube ceramic matrix composites, Acta Mater. 52 (2004) 931–944. https://doi.org/10.1016/j.actamat.2003.10.050.

[5] H.L. Cox, The elasticity and strength of paper and other fibrous materials, Br. J. Appl. Phys. 3 (1952) 72–79. https://doi.org/10.1088/0508-3443/3/3/302.

[6] F. Wang, J. Li, C. Shi, E. Liu, C. He, N. Zhao, In-situ synthesis of $MgAlB_4$ whiskers as a promising reinforcement for aluminum matrix composites, Mater. Sci. Eng. A. 764 (2019) 138229. https://doi.org/10.1016/j.msea.2019.138229.

[7] H.J. Ryu, S.I. Cha, S.H. Hong, Generalized shear-lag model for load transfer in SiC/Al metal-matrix composites, J. Mater. Res. 18 (2003) 2851–2858. https://doi.org/10.1557/JMR.2003.0398.

[8] M.T. Andani, A. Lakshmanan, M. Karamooz-Ravari, V. Sundararaghavan, J. Allison, A. Misra, A quantitative study of stress fields ahead of a slip band blocked by a grain boundary in unalloyed magnesium, Sci. Rep. 10 (2020) 1–8. https://doi.org/10.1038/s41598-020-59684-y.

[9] Y. Guangyin, W. Qudong, D. Wenjiang, High temperature deformation behavior of permanent casting AZ91 alloy with and without Sb addition, J. Mater. Sci. 37 (2002) 127–132. https://doi.org/10.1023/A:1013114412378.

[10] J.A. Sharon, Y. Zhang, F. Mompiou, M. Legros, K.J. Hemker, Discerning size effect strengthening in ultrafine-grained Mg thin films, Scr. Mater. 75 (2014) 10–13. https://doi.org/10.1016/j.scriptamat.2013.10.016.

[11] O.B. Bembalge, S.K. Panigrahi, Development and strengthening mechanisms of bulk ultrafine grained AA6063/SiC composite sheets with varying reinforcement size ranging from nano to micro domain, J. Alloys Compd. 766 (2018) 355–372. https://doi.org/10.1016/j.jallcom.2018.06.306.

[12] S.L. Allen, M.R. Notis, R.R. Chromik, R.P. Vinci, Microstructural evolution in lead-free solder alloys: Part I. Cast Sn-Ag-Cu eutectic, J. Mater. Res. 19 (2004) 1417–1424. https://doi.org/10.1557/JMR.2004.0190.

[13] A.M. Gusak, G. V. Lutsenko, K.N. Tu, Ostwald ripening with non-equilibrium vacancies, Acta Mater. 54 (2006) 785–791. https://doi.org/10.1016/j.actamat.2005.09.035.

[14] R. Mayappan, I. Yahya, N.A.A. Ghani, H.A. Hamid, The effect of adding Zn into the Sn-Ag-Cu solder on the intermetallic growth rate, J. Mater. Sci. Mater. Electron. 25 (2014) 2913–2922. https://doi.org/10.1007/s10854-014-1959-2.

[15] L. Xu, L. Wang, H. Jing, X. Liu, J. Wei, Y. Han, Effects of graphene nanosheets on interfacial reaction of Sn-Ag-Cu solder joints, J. Alloys Compd. 650 (2015) 475–481. https://doi.org/10.1016/j.jallcom.2015.08.018.

[16] P. Kumar, B. Talenbanpour, U. Sahaym, C.H. Wen, I. Dutta, Microstructural evolution and some unusual effects during thermo-mechanical Cycling of Sn-Ag-Cu alloys, Intersoc. Conf. Therm. Thermomechanical Phenom. Electron. Syst. ITHERM. d (2012) 880–887. https://doi.org/10.1109/ITHERM.2012.6231519.

Chapter 6 Microstructure and shear strength of NiO/ZrO_2 and $NiO/T\text{-}ZnO_w$ hybrid reinforced Sn1.0Ag0.5Cu composite solder/Cu joints

6.1 Introduction

In previous chapter, NiO/ZrO_2 and $NiO/T\text{-}ZnO_w$ hybrid reinforced Sn1.0Ag0.5Cu composite solder with different Zn: Zr ratios were prepared with ultrasonic stirring. The microstructure evolution of composite solders was systematically investigated. The interface between reinforcement and solder matrix was also explored. Moreover, the mechanical properties of composite solders also were studied. After systematic research, the optimal mixing ratio of NiO/ZrO_2 and $NiO/T\text{-}ZnO_w$ was determined. To further evaluate the newly developed composite solder, the solderability of composite solder and the reliability of solder joint are further studied.

In this chapter, the wettability of the composite solder was studied, and then the soldering test of the composite solder was conducted. The microstructure evolution and mechanical properties of solder joints were systematically investigated after reflow and thermal aging.

6.2 Experimental procedure

6.2.1 Materials

The reinforcement of NiO/ZrO_2 was prepared with ball milling-pyrolysis method. And the reinforcement of $NiO/T\text{-}ZnO_w$ was prepared with pyrolysis method based on the self-assembly. The detailed fabrication program and morphology of the two kinds of reinforcements are shown in chapter 2. So this chapter would not elaborate. The commercial Sn1.0Ag0.5Cu solder bar was provided by Senju Metal Industry Co. Ltd. Japan. Oxygen-free Cu plate and pillar were used for the wetting test and preparation of solder joints.

6.2.2 Wetting, soldering and thermal aging process

In chapter 5, I had explored the effects of NiO/ZrO_2 and $NiO/T\text{-}ZnO_w$ ratios on the mechanical properties of composite solders, the optimal mixing ratio of NiO/ZrO_2 and NiO/T-

ZnO_w was Zn: Zr=2: 3. Therefore, in chapter 6, the hybrid reinforced composite solder with optimal Zn: Zr ratio was used.

The wettability is an important index to evaluate the performance of the solder [1], so the wetting tests were conducted. The wettability of four kinds of solders (plain Sn1.0Ag0.5Cu, 0.3 mass% NiO/ZrO_2 reinforced Sn1.0Ag0.5Cu, 0.3 mass% $NiO/T\text{-}ZnO_w$ reinforced Sn1.0Ag0.5Cu, hybrid reinforced Sn1.0Ag0.5Cu with Zn: Zr ratio of 2: 3) were studied. These solder bulks were first processed into round foil samples with the diameter of 4 mm and thickness of 100 μm. The samples were placed on oxygen-free Cu plate (15 × 15 × 0.5 mm) with flux (SR-12, SMIC, Japan), and then heated in the reflow furnace (SK-5000 SMTScope, Sanyoseiko, Japan) with N_2 atmosphere. The oxygen concentration in the reflow furnace was controlled below 1000 ppm. The reflow profile is shown in Fig. 6-1. After reflow, wetting angle were measured with CAXA software. Three samples of each composition were prepared for wettability test. The left and right side wetting angles of each sample were measured from the cross-section image. So the experimental results were the average of six measured values.

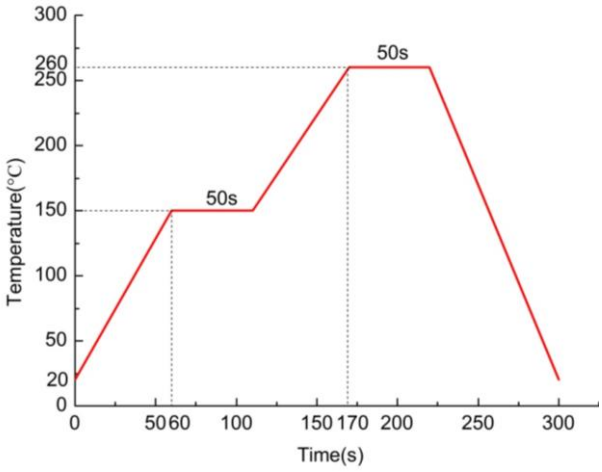

Fig. 6-1The reflow profile of wetting test.

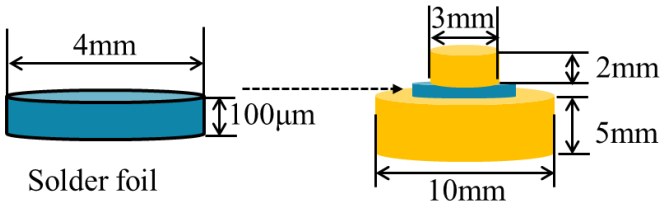

Fig. 6-2 The schematic diagram of the shear test sample.

The schematic illustration of a solder joint was displayed in Fig. 6-2, where the dimensions of the solder foil and the oxygen-free Cu substrate are mentioned in detail. The reflow curve and the curve of the wettability experiment are the same, as well as the experimental conditions. For reference, solder joints of Sn1.0Ag0.5Cu and commercial Sn3.0Ag0.5Cu solders were also prepared.

Thermal aging test of the composite solder was conducted to investigate the reliability of newly developed composite solder. The as-reflowed solder joint samples were performed for 168 h, 504 h and 1008 h in an oil bath at 150 ℃. The oil bath was used to prevent potential oxidation of the samples during the thermal aging.

6.2.3 Characterization and testing

Scanning electron microscopy (SEM, SU-70, Hitachi, Japan) equipped with energy-dispersive X-ray spectroscopy (EDS) was used to observe the microstructure and fracture surface of the solder joints. The thickness of interfacial IMC was calculated using CAXA software, Fig. 6-3(a) shows the typical example used for the measurement of interfacial IMC thickness. Three SEM images were selected for each composition, and about 50 interfacial IMC phases were measured for each composition. In order to observe the top view of interfacial IMC, deep corrosion was conducted. The composition of the corrosion solution was 15 vol.% HNO_3+85 Vol.% deionized H_2O, and the corrosion time was about 13 min. The size of these IMC particles were measured with Nano Measurer software. Fig. 6-3(b) shows the typical example used for the measurement of IMC grain size. Similarly, three SEM images were selected for each composition, and about 150 interfacial IMC phases were measured for each composition. The results are the average of the measured values.

The shear tests of as-flowed and thermal aging samples were performed using a universal electrical shear tester (Rhesca STR-1000) with a 1 mm/min shear rat. The experimental results are the average values of four samples.

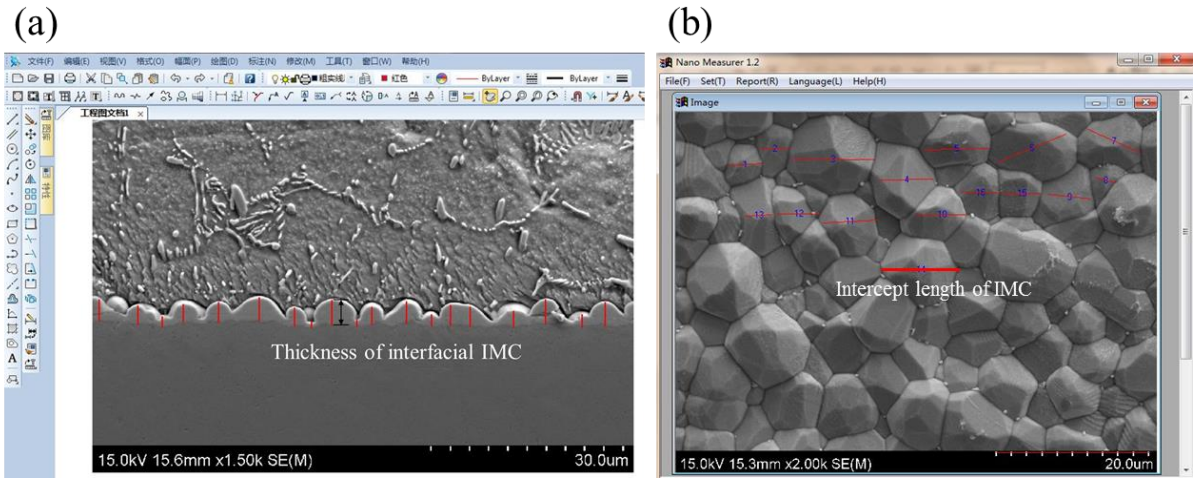

Fig. 6-3 Typical example used for the measurement of interfacial IMC. (a) thickness of interfacial IMC, (b) intercept length of top view IMC.

6.3 Wettability

The wettability is an important performance of the solders. To evaluate the wettability of the new developed composite solder, wetting tests were conducted. Fig. 6-4 show the appearance of spread samples of the four kinds of solders, respectively. The spread solders exhibit the regular circular shape, indicating good wettability of them. Fig. 6-5(a)-(b) show the cross-section images of spread samples of four kinds of solders, respectively, and the measured wetting angle are shown in Fig. 6-5(e). The average wetting angle of plain Sn1.0Ag0.5Cu solder was 11.1°. After addition of NiO/T-ZrO_2, NiO/T-ZnO_w, and hybrid of them, the average wetting angle reduced to 8.1°, 8.4°, and 8.9°, respectively. The results indicated that the wettability was improved after the reinforcements addition. The wetting behavior between molten solder and Cu substrate related to the interfacial reaction. Previous chapters mentioned the reinforcements located in the eutectic area and attached to the Ag_3Sn and Cu_6Sn_5 IMC for the composite solder. It could decrease the surface energy of Ag_3Sn and Cu_6Sn_5 crystal plane. A local steep surface energy gradient is generated, which promotes the instability of the film and accelerates the interfacial turbulence during the wetting process according to the Gibbs-Marangoni effect [2], which is conducive to the spreading of molten on the Cu plate. On the other hand, the NiO/T-ZnO_w remains in the solid-state during the wetting process, acting as a framework. The framework could improve the wettability through capillary action [3].

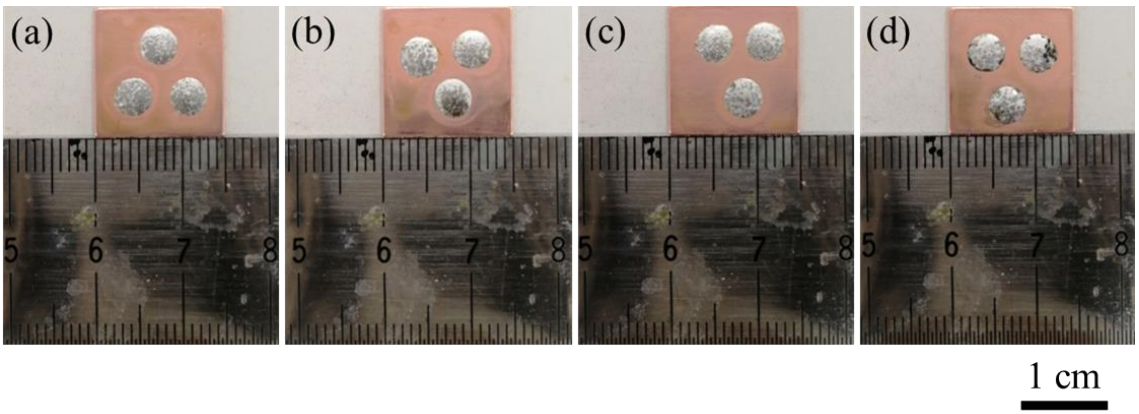

Fig. 6-4 Appearance of spread samples. (a) plain Sn1.0Ag0.5Cu solder, (b) NiO/T-ZrO_2 reinforced Sn1.0Ag0.5Cu composite solder (c) NiO/T-ZnO_w reinforced Sn1.0Ag0.5Cu composite solder, and (d) hybrid reinforced Sn1.0Ag0.5Cu composite solder.

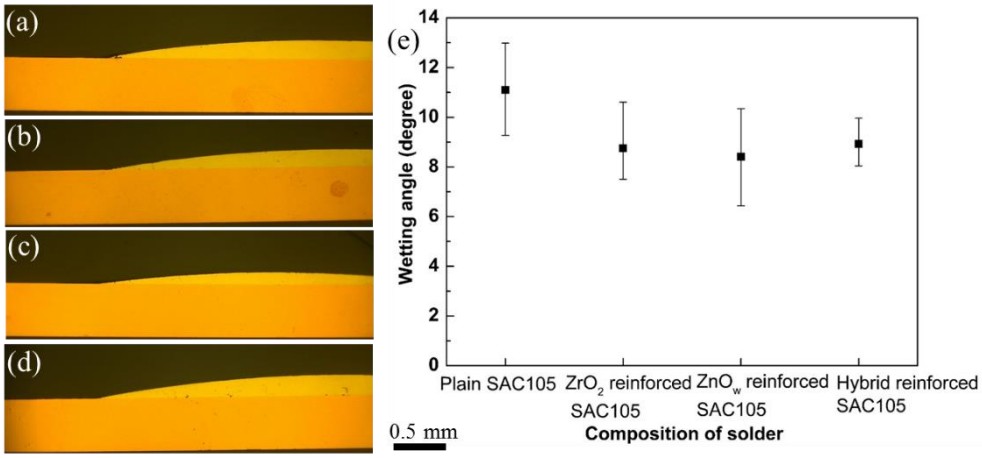

Fig. 6-5 Cross section images of spread samples. (a) plain Sn1.0Ag0.5Cu solder, (b) NiO/T-ZrO_2 reinforced Sn1.0Ag0.5Cu composite solder (c) NiO/T-ZnO_w reinforced Sn1.0Ag0.5Cu composite solder, and (d) hybrid reinforced Sn1.0Ag0.5Cu composite solder. (e)Wetting angle of these solders.

6.4 Microstructure of composite solder/Cu joints after reflow

To investigate the effect of reinforcements on the microstructure evolution of solder/Cu joints during reflow, the microstructure was observed. Fig. 6-6 exhibits the representative side view of solder joint. It is noted that the sound and dense solder joint is obtained. The middle side (marked with dotted frame in Fig. 6-6) is the key part for the solder joint. To better understand the microstructure of solder joint, the observation by high magnified SEM images were conducted. Fig. 6-7 shows the high magnified SEM images of solder joints of plain Sn1.0Ag0.5Cu, hybrid reinforced Sn1.0Ag0.5Cu, and Sn3.0Ag0.5Cu after reflow. As seen

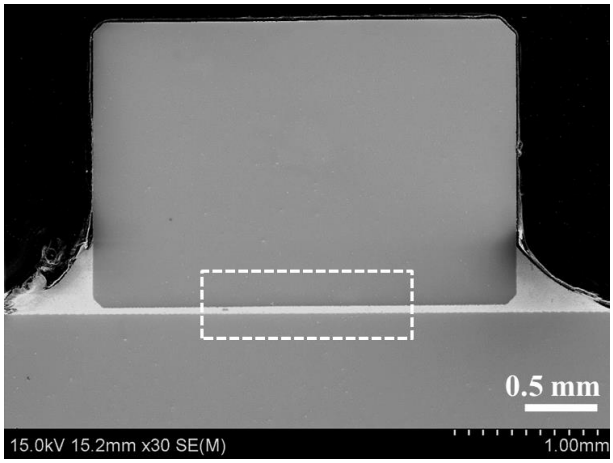

Fig. 6-6 Representative side view of solder joint.

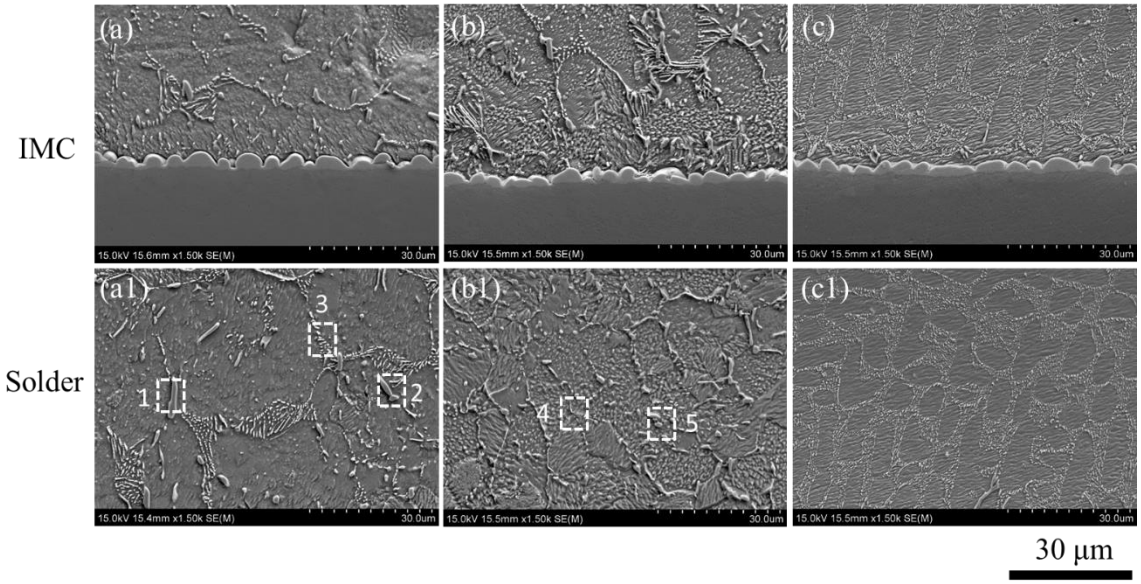

Fig. 6-7 SEM images of (a), (a1) plain Sn1.0Ag0.5Cu, (b), (b1) hybrid reinforced Sn1.0Ag0.5Cu, (c), (c1) plain Sn3.0Ag0.5Cu after reflow.

from Fig. 6-7, the solder joint comprise solder, interfacial IMC, and Cu substrate. As an important part of solder joint, the shape and size of IMC are closely related to the reliability of solder joints [4]. The interfacial IMC belongs to a hard brittle phase, and there are different CTE among Cu substrate, solder, and IMC. An excessive interfacial IMC thickness can cause stress concentration, reducing the reliability of the solder joint [5]. From the Gibbs free energy curve of the Cu-Sn binary system, it is known that the free energy of the system is the smallest when the atomic ratio of Cu:Sn is 6:5 [6]. Therefore, at the initial stage of soldering, the Sn atoms in the liquid solder and the Cu atoms in the Cu substrate react rapidly to form Cu_6Sn_5, and its growth is controlled by the reaction rate of Sn and Cu atoms. When a continuous layer

Table 6-1. EDS results of Fig. 6-7 (at. %)

Location	Sn	Ag	Cu	Possible phase
1	48.14	-	51.86	Cu_6Sn_5
2	47.56	-	52.55	Cu_6Sn_5
3	82.18	12.41	5.41	Cu_6Sn_5, Ag_3Sn
4	61.57	14.59	23.84	Cu_6Sn_5, Ag_3Sn
5	63.55	3.30	33.15	Cu_6Sn_5, Ag_3Sn

of Cu_6Sn_5 is formed, the growth of the interfacial IMC is controlled by the atomic diffusion rate [7]. The statistical results show that the average thickness of the interfacial IMC in Fig. 6-7(a)-(c) is 2.72 μm, 2.39 μm, and 2.25 μm, respectively. The above results show that, after reflow, the interfacial IMC thickness of composite solder joint is less than that of plain Sn1.0Ag0.5Cu solder joint. This is because the reinforcements segregate at the interface during the soldering process, which blocks the Cu and Sn atoms diffusion channel and hinders the growth of interfacial IMC. A similar result was appeared in [8].

The solder layer of the three kinds of joints is composed of β-Sn and eutectic structures, which include granular binary eutectic consisting of β-Sn + Cu_6Sn_5, acicular binary eutectic consisting of β-Sn + Ag_3Sn, and ternary eutectic consisting of β-Sn + Cu_6Sn5 + Ag_3Sn [9]. While the morphology and size of β-Sn and eutectic structures are different. Fig. 6-7(a1)-(c1) show the solder microstructure of three kinds of solders joints. For the plain Sn1.0Ag0.5Cu solder joint, the size of β-Sn is relatively large, and coarse IMC exists in the eutectic structure. The EDS results (Table 6-1) of areas 1, 2, and 3 in Fig. 6-7(a1) show that these coarse phases in the eutectic structure are Cu_6Sn_5, while the refined IMC in eutectic structure (area 3) is a mixture of Cu_6Sn_5 and Ag_3Sn. As for the solder structure of composite solder joint (Fig. 6-7(b1)), β-Sn presents a smaller size, as well as eutectic structure, and almost no coarse IMC is detected. This result can be explained from two aspects. On the one hand, it is attributed to the reasonable addition of the reinforcements, which can act as heterogeneous nucleation sites during the solidification of the solder joint, thereby refining the joint microstructure. On the other hand, these reinforcing phases can hinder the inter-diffusion of Cu atoms in the Cu

substrate and Sn atoms in the solder, reducing the amount of Cu atoms of Cu substrate into the solder. Therefore, compared with the plain Sn1.0Ag0.5Cu solder joint, coarse Cu_6Sn_5 is hardly found in the composite solder joint. Fig. 6-7(c1) shows the microstructure of Sn3.0Ag0.5Cu solder joint. Compared with Fig. 6-7(a1) and (b1), the proportion of eutectic structure is significantly increased, which is attributed to the high Ag content. It is beneficial to improve the strength of the solder.

To further investigate the morphology of interfacial IMC of three kinds of solder joints, top view of IMC was observed. Fig. 6-8(a)-(c) show IMC top view after reflow. As seen from Fig. 6-8(a), the overall top view of IMC interface shows a rough plane composed of irregular polyhedrons with different sizes. These IMC particles are closely arranged, with an average particle size of 2.8 μm. For the hybrid reinforced Sn1.0Ag0.5Cu solder joint with an average IMC particle size of 3.1 μm, the morphology of interfacial IMC is similar with Fig. 6-8(a), while exhibit flatter profile compared with Fig. 6-8(a). The result is consistent with the cross-section view of interfacial IMC, shown in Fig. 6-7. Similar result was also appeared in Fig. 6-8(c), where the IMC particle size is 2.9 μm. Fig. 6-8(a1)-(c1) show the highly magnified view of areas 1, 2, and 3 in Fig. 6-8(a)-(c), respectively, where the top area shows the smooth surface.

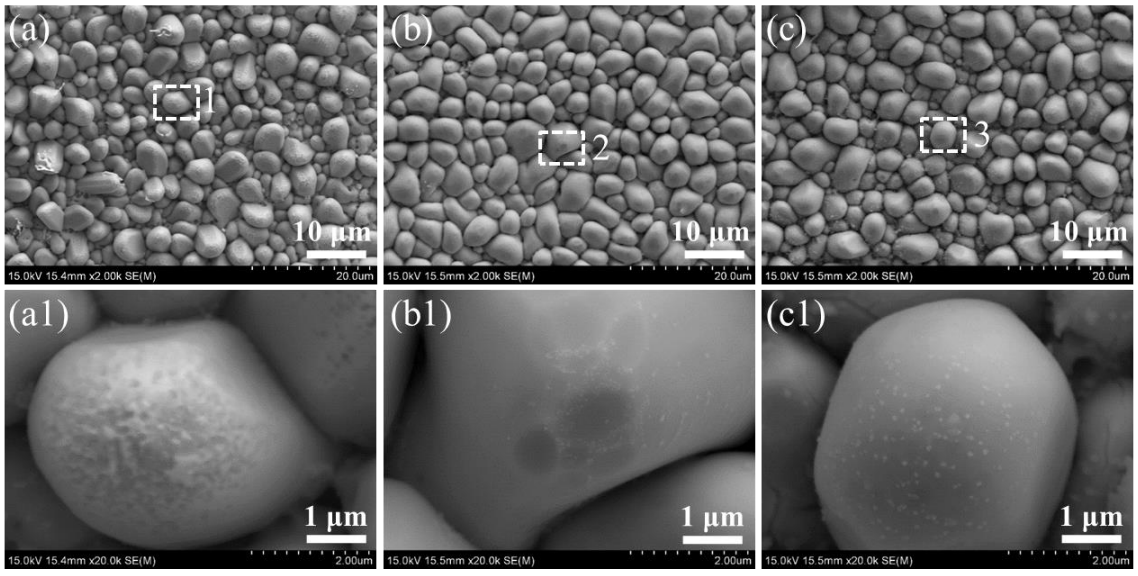

Fig. 6-8 IMC top view of three kinds of solder joints. (a) plain Sn1.0Ag0.5Cu, (b) hybrid reinforced Sn1.0Ag0.5Cu, and (c) plain Sn3.0Ag0.5Cu after reflow. (a1), (b1), and (c1) high magnified view of area 1, 2, and 3, respectively.

In addition, some nano-sized Ag_3Sn particles are attached to the surface. In particular, Fig. 6-8(c1) exhibits relatively large amount of nano-sized Ag_3Sn particles, which is attributed to the high Ag content (3.0 mass%) compared with Fig. 6-8(a1) and (c1). During the soldering process, the Sn atoms in the molten solder at the interface react with the Cu in the substrate, so that the Ag atoms in the solder are enriched at the interface. These enriched Ag atoms react with Sn in the solidification process to form the nano-sized Ag_3Sn, dispersed on the interfacial IMC surface. Tsao [10] reported that these dispersed Ag_3Sn could inhibit the growth of interfacial IMC during service.

6.5 Microstructure evolution of composite solder/Cu joints during thermal aging

The microstructure stability of solder joint is essential to the reliability of electronics. To evaluate the microstructure stability of solder joints, the microstructure evolution of solder joints during thermal aging were investigated. Fig. 6-9 shows the SEM images of plain Sn1.0Ag0.5Cu solder joint with different thermal aging times. The upside presents the evolution of the interfacial IMC, and the downside is the evolution of the solder microstructure. As seen from Fig. 6-9(a)-(c), with the increase of aging time, the morphology of interfacial IMC gradually changes from scallop-like after reflow to layered shape, and the average

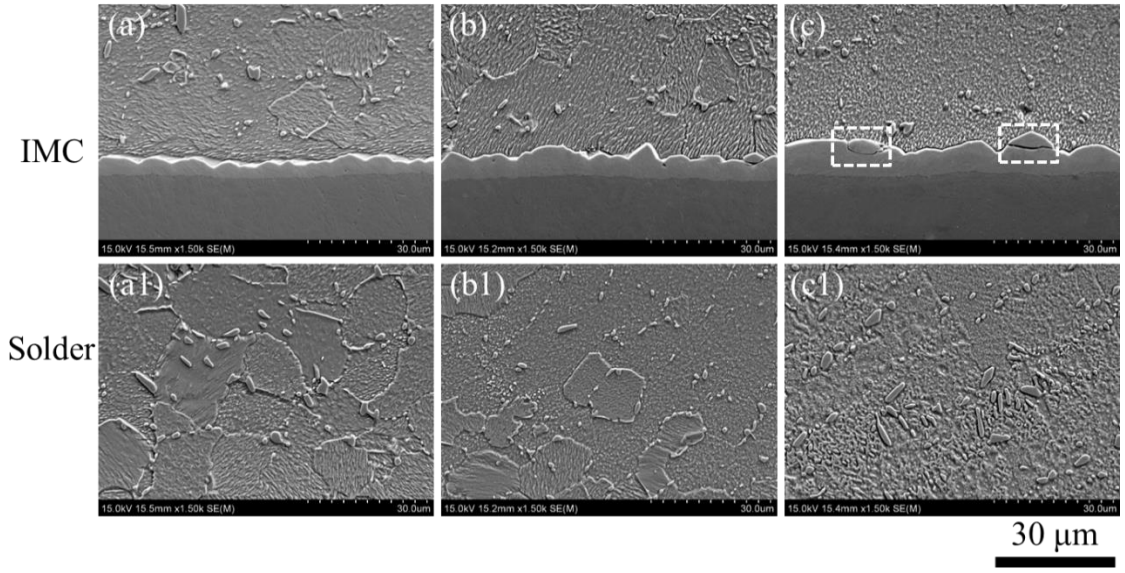

Fig. 6-9 SEM images of plain Sn1.0Ag0.5Cu solder joint with different thermal aging times. (a), (a1) 168 h, (b), (b1) 504 h, (c), (c1) 1008 h.

thickness of IMC increases. When the thermal aging time reaches 168 h (Fig. 6-9(a)), the roughness of the interfacial IMC is significantly reduced compared with Fig. 6-7(a). The average thickness of IMC is 4.05 μm. In the corresponding solder structure (Fig. 6-9(a1)), the number of coarsened IMC particles is increased compared to Fig. 6-7(a1), while the network eutectic structure is still maintained. The coarsening of the solder structure is due to the coarsening of the eutectic structure itself during the aging process; on the other hand, the diffusion of Cu in the Cu substrate into the solder regions, also leading to more IMC formation. With the increase of thermal aging time, the thickness of the interfacial IMC layer gradually increases, and the network eutectic structure in the solder regions gradually dissolves. When the aging time reaches 1008 h (Fig. 6-9(c)), the thickness of the IMC increases to 7.89 μm. From Fig. 6-9, it can be seen that the interfacial IMC can be divided into two layers. From the reference [11], the light-coloured Cu_6Sn_5 near the solder and the dark-coloured Cu_3Sn close to the Cu substrate. During the soldering process, Cu_6Sn_5 with lower activation energy is formed first (Eq. (6-1)), which had mentioned in part 6.4. With the increase of the thickness of Cu_6Sn_5 IMC, the diffusion of Sn atoms to the Cu substrate side is gradually hindered. When the Sn atom supply on the copper substrate side is insufficient, the unstable Cu_6Sn_5 could react with excess Cu atoms to form Cu_3Sn (Eq. (6-2)) [12]. In addition, micro-crack is also found at the interfacial IMC in Fig. 6-9(c), which would reduce the reliability of the joint. The interfacial IMC belongs to the hard brittle phase, and there are different CTE among Cu substrate, solder, and IMC. In the long-term thermal aging, excessively thick interfacial IMC produces stress concentration, eventually leading to cracks. Similar phenomenon has also occurred in [13]. Fig. 6-9(c1) shows the microstructure of solder after1008 h thermal aging. The network eutectic structure is almost completely dissolved, and the coarse IMC is dispersed in the solder.

$$6Cu+5Sn= Cu_6Sn_5 \quad (6\text{-}1)$$

$$Cu_6Sn_5+9Cu= 5Cu_3Sn \quad (6\text{-}2)$$

To further investigate the microstructure evolution of interfacial IMC during thermal aging, top view of IMC was observed. Fig. 6-10(a)-(c) show the IMC top view of plain Sn1.0Ag0.5Cu solder joint with different thermal aging times. As shown in Fig. 6-10(a), the

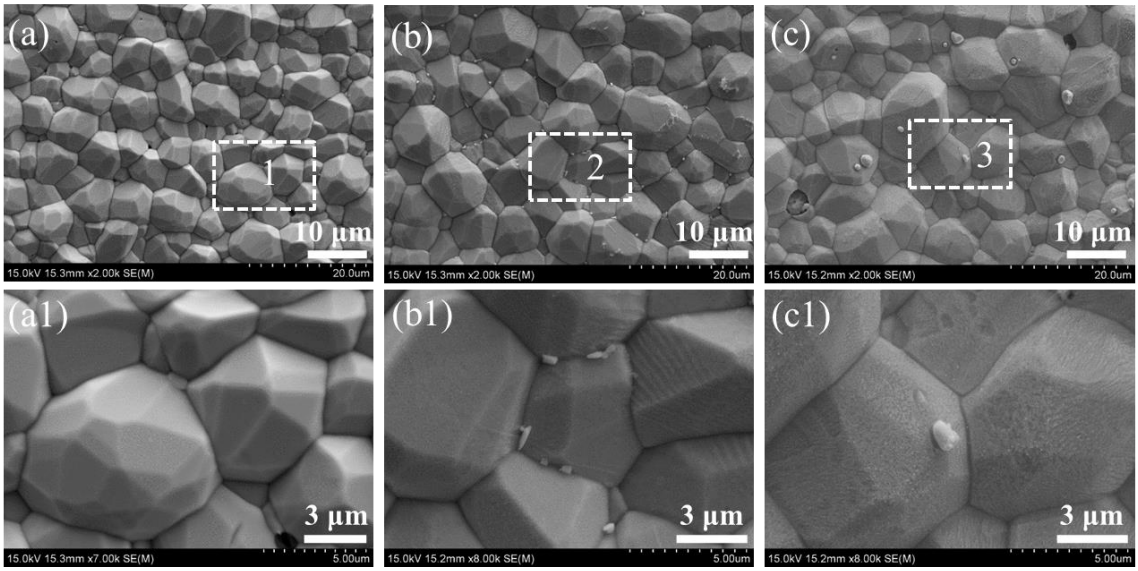

Fig. 6-10 IMC top view of plain Sn1.0Ag0.5Cu solder joint with different thermal aging times. (a) 168 h, (b) 504 h, (c) 1008 h. (a1), (b1), and (c1) high magnified view of area 1, 2, and 3, respectively.

overall top view of IMC interface shows a rough plane composed of irregular polyhedrons with different sizes.These IMC particles are closely arranged, with an average particle size of 4.5 μm. With the increase of thermal aging times, the average size of interfacial IMC particles gradually increases. At the same time, some smaller IMC particles appeared due to the maturation process of IMC particles. In addition, some bright Ag_3Sn particles were found on the surface of Cu_6Sn_5 IMC, and similar results were reported in [14]. When the thermal aging time increase to 1008 h (Fig. 6-10(c)), the average IMC size increase slightly (6.1 μm), but the difference in particle size is obvious. And the attached Ag_3Sn particles also increase. Fig. 6-10(a1)-(c1) show the highly magnified view of areas 1, 2, and 3 in Fig. 6-10(a)-(c), respectively. Three adjacent particles form an angle of 120 °with each other. The surface of the particle is not a smooth transitional curved surface, but a combination of multiple planes, which may be due to the preferential growth of Cu_6Sn_5 on a certain crystal plane. In addition, it is observed that on the surface of the IMC particles in Fig. 6-10(a1), some nano-sized Ag_3Sn particles are attached. The reason for the formation of nano-sized Ag_3Sn has been mentioned in part 6.4. However, with the increase of the aging time, these Ag_3Sn particles did not maintain the nanoscale level, but gradually grew up (shown in Fig. 6-10(b2) and (c2)), and the corresponding effect of inhibiting the growth of IMC also weakened.

In summary, combined with Fig. 6-9 and 6-10, the IMC thickness of the plain Sn1.0Ag0.5Cu solder joint gradually increase during the aging process, as well as the IMC particle size, thereby causing cracks to occur. Moreover, the eutectic structure of solder is continuously dissolved during the aging process, and the IMC in the eutectic structure also continuously coarsening. These deteriorated microstructures could reduce the reliability of solder joints.

Fig. 6-11 shows the SEM images of hybrid reinforced Sn1.0Ag0.5Cu composite solder joint with different thermal aging times. The upside presents the evolution of the interfacial IMC, and the downside is the evolution of the solder microstructure. As shown from Fig. 6-11(a)-(c), with the increase of aging time, the morphology of interfacial IMC gradually changes from scallop-like after reflow to layered shape, and the average thickness of IMC shows an increasing trend. This evolution trend is consistent with plain Sn1.0Ag0.5Cu solder joint. Especially, the morphology evolution from scallop to layered shape can be explained as follows [15-17]. First, a scallop-shaped IMC is formed after reflow, which has a larger surface area and higher surface energy from the thermodynamic perspective. It needs to be transformed into a layered shape to reduce its surface energy, thereby ensuring the stability of the interface system.

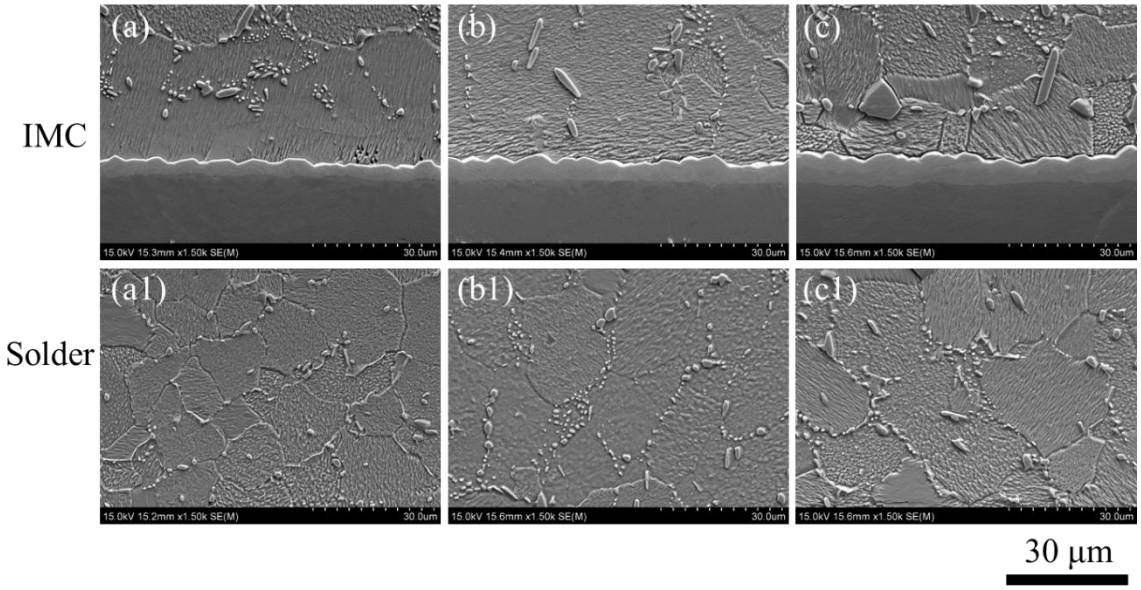

Fig. 6-11 SEM images of hybrid reinforced Sn1.0Ag0.5Cu composite solder joint with different thermal aging times. (a), (a1) 168 h, (b), (b1) 504 h, (c), (c1) 1008 h.

Second, When the profile of IMC interface is rough, the distance between the tip of IMC particles and the Cu substrate is obviously larger than the distance between the groove of IMC particles and the Cu substrate. In this case, the Cu atoms in the substrate preferentially diffused into the groove between IMC particles during the thermal aging process, which made the thin IMC layer grow rapidly, and finally caused the integral IMC layer tends to be flat. Third, the groove between the interface IMC belongs to a near-interface zone, which often accumulates high-density vacancies, dislocations and other defects [18]. These areas are non-stable regions; they can be used as a channel for Cu atoms to dissolve and diffuse into the solder quickly. The above three factors change the morphology of interfacial IMC from scallop to layered shape.

When the thermal aging time reaches 168 h (Fig. 6-11(a)), the average thickness of interfacial IMC is 3.59 μm, lower than that of plain Sn1.0Ag0.5Cu solder joint. The network eutectic phase is still maintained for the corresponding solder structure (Fig. 6-11(a1)). As the aging time increases, the thickness of the interface IMC layer gradually increases. When the aging time reaches 1008 h (Fig. 6-11(c)), the interfacial IMC can be divided into two layers, the light-coloured Cu_6Sn_5 near the solder and the dark-coloured Cu_3Sn close to the Cu substrate, the result is consistent with reference [11]. The corresponding interfacial IMC thickness increase to 6.40 μm, also lower than that of plain Sn1.0Ag0.5Cu solder joint. Fig. 6-11(c1) shows the microstructure of solder with 1008 h thermal aging times, the IMC in the eutectic structure has grown slightly, but its size is still lower than that of plain Sn1.0Ag0.5Cu solder joint. And the network eutectic structure has not been dissolved, which indicates that the composite solder joint has good microstructure stability during the thermal aging. This is attributed to the reasonable addition of reinforcements, so that the pinning effect can be produced, thereby inhibiting the migration of grain boundaries during thermal aging.

Fig. 6-12(a)-(c) show the IMC top view of composite solder joint with different thermal aging times. As seen from Fig. 6-12(a), the overall top view of IMC interface shows a rough plane, which is composed of irregular polyhedrons with different sizes. These IMC particles are closely arranged, with an average particle size of 3.8 μm. With the increase of thermal aging times, the average size of interfacial IMC particles gradually increases. When the thermal aging

time reaches 1008 h (Fig. 6-12(c)), the average particle size of interfacial IMC is 5.2 μm. This result is smaller than that of plain Sn1.0Ag0.5Cu solder joint.

Fig. 6-12(a1)-(c1) shows the highly magnified view of areas 1, 2, and 3, respectively. As seen from them, some small sized Ag_3Sn (bright particles) were attached to the Cu_6Sn_5 IMC surface. And the size of these Ag_3Sn particles remained stable during the thermal aging, and no obvious growth occurred. In the above, I have mentioned that the dispersed Ag_3Sn can inhibit the growth of the interfacial IMC during the service. For the composite solder joints, these Ag_3Sn particles keep the stable size during the whole aging process, so the corresponding inhibition effect of interfacial IMC growth is also maintained. This is also one of the reasons why the interfacial IMC of composite solder joint is refined. The reinforcing phase in the composite solder joint is also one of the factors that inhibit the growth of interfacial IMC [19]. Fig. 6-13 shows IMC top view of hybrid reinforced Sn1.0Ag0.5Cu composite solder joint with 504h thermal aging. Fig. 6-13(a) illustrate that the whisker enhancement phase exists near the interfacial IMC. On the one hand, these reinforcing phases can hinder the mutual diffusion of Cu atoms from the Cu substrate and Sn atoms from the solder. On the other hand, it can also produce the pinning effect and inhibit the merging effect between interfacial IMC particles [20].

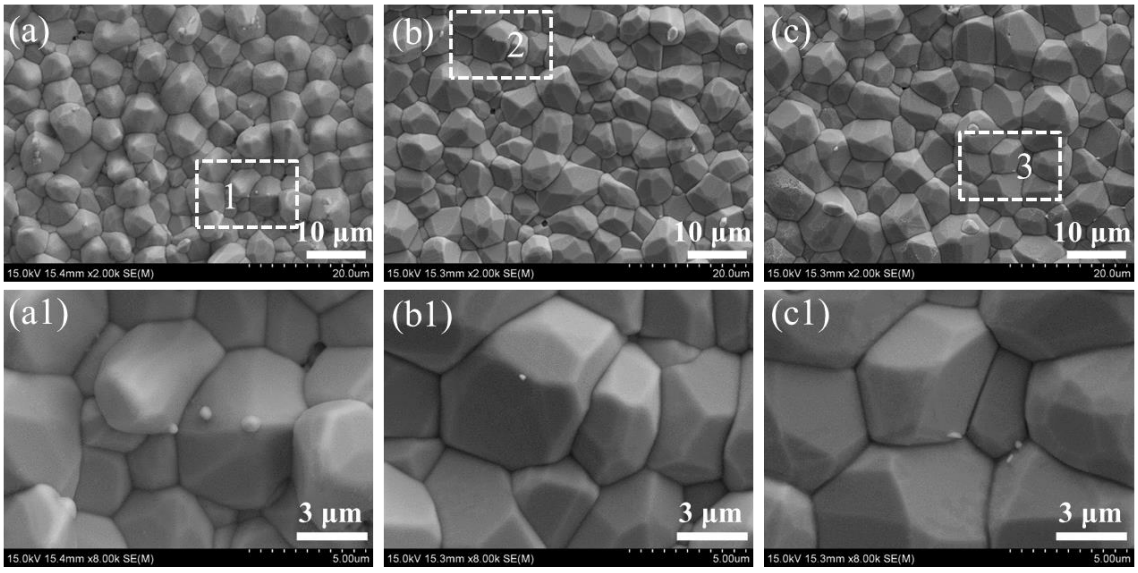

Fig. 6-12 IMC top view of hybrid reinforced Sn1.0Ag0.5Cu composite solder joint with different thermal aging times. (a) 168 h, (b) 504 h, (c) 1008 h. (a1), (b1), and (c1) high magnified view of area 1, 2, and 3, respectively.

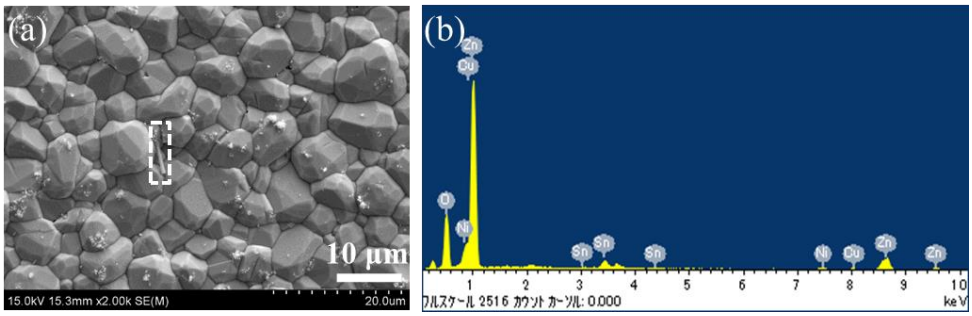

Fig. 6-13 IMC top view of hybrid reinforced Sn1.0Ag0.5Cu composite solder joint with 504h thermal aging. (a) Whisker located near the interface, (b) EDS result of selected area in (a).

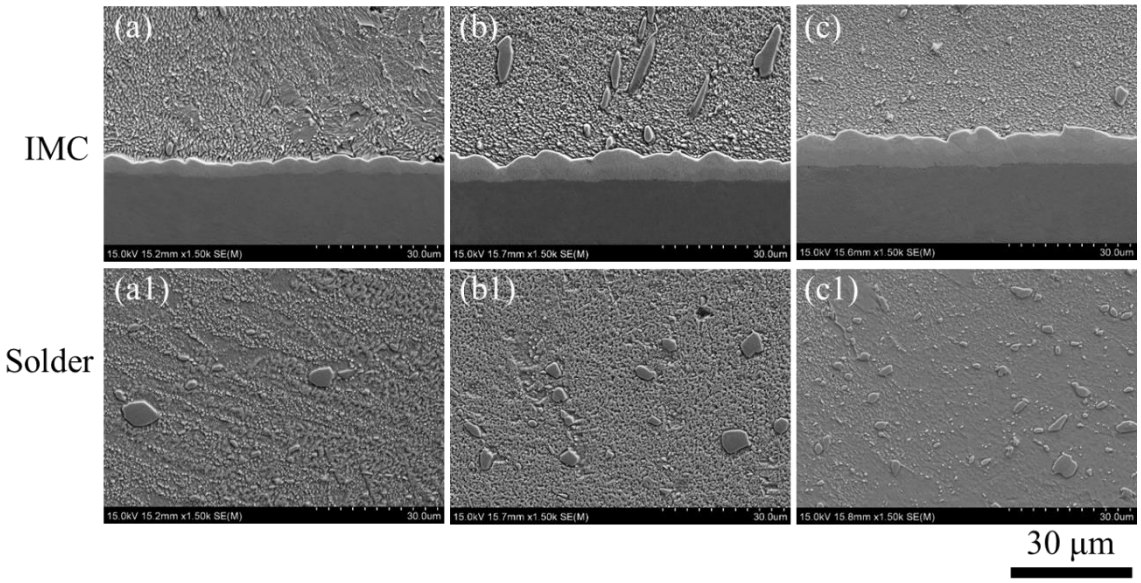

Fig. 6-14 SEM images of plain Sn3.0Ag0.5Cu solder joint with different thermal aging times. (a), (a1) 168 h, (b), (b1) 504 h, (c), (c1) 1008 h.

Fig. 6-14 shows the SEM images of plain Sn3.0Ag0.5Cu solder joint with different thermal aging times. Similar to Fig. 6-9 and 6-11, the morphology of the interfacial IMC gradually changes from the scallop shape after reflow to the layered shape with the increased thermal aging time, and the average thickness of the interfacial IMC gradually increases. The reason had mentioned in above. When the thermal aging time reaches 1008 h (Fig.6-14(c)), the average thickness of interfacial IMC is 8.09 μm, which is higher than those of plain Sn1.0Ag0.5Cu and composite solder joints. For the solder evolution, when the aging time reaches 168 h (Fig. 6-14(a1)), the eutectic structure is partially dissolved, but the network structure is still maintained. In addition, a small amount of coarse Cu_6Sn_5 IMC particles are observed. With the increase of the aging time, there are more and more such coarse IMC

particles, which is mainly due to the rapid diffusion of Cu atoms in the Cu substrate into the solder. When thermal aging time reaches 1008 h (Fig.6-14(c1)), the network eutectic structure is dissolved, and the coarse IMC is dispersed in the solder.

Fig. 6-15(a)-(c) show IMC top view of plain Sn3.0Ag0.5Cu solder joint with different thermal aging times. As seen from Fig. 6-15(a), the overall top view of IMC interface shows a rough plane, which is composed of irregular polyhedrons with different sizes. These IMC particles are closely arranged, with an average particle size of 4.9 μm. With the increase of thermal aging times, the average size of interfacial IMC particles gradually increases. However, unlike Fig. 6-10 and 6-12, many Ag_3Sn particles are attached to the interfacial IMC surface in Fig. 6-15(a1), mainly attributed to the high Ag content of Sn3.0Ag0.5Cu solder. And as the thermal aging time increases, the size of Ag_3Sn increases significantly, which could weaken the inhibition effect on the growth of interfacial IMC.

To quantitatively analyze the growth of the interfacial IMCs during the thermal aging, the interfacial IMC thickness and grain size as a function of time are conducted. Fig. 6-16 shows the effect of thermal aging time on interfacial IMC. The curves represent plain Sn1.0Ag0.5Cu solder, hybrid reinforced composite solder, and Sn3.0Ag0.5Cu solder, respectively. On the whole, in the early stage of thermal aging (0-156 h), the slope of the curve is large, indicating

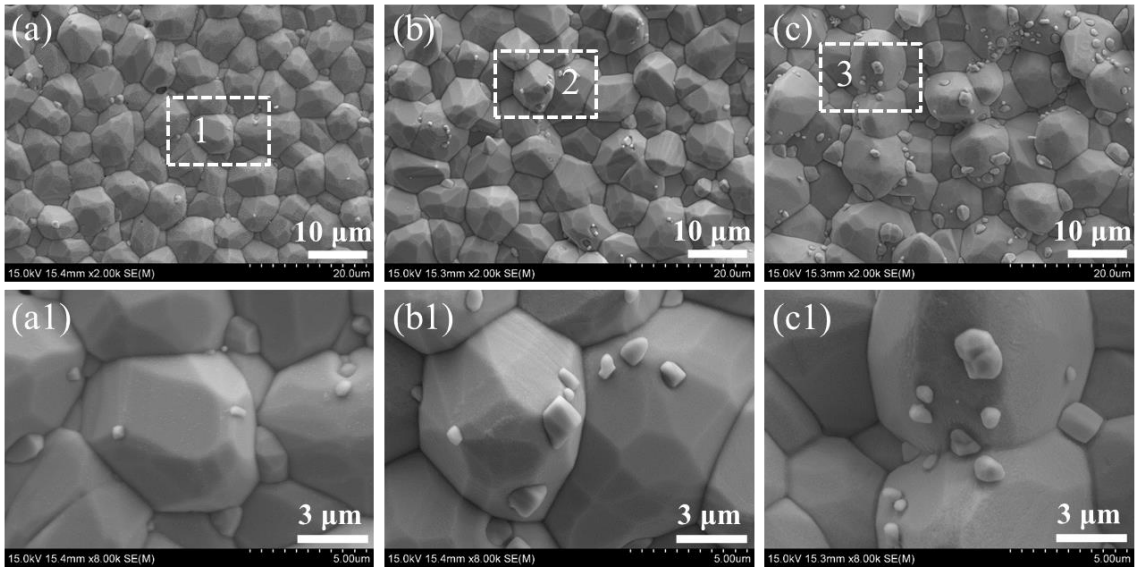

Fig. 6-15 IMC top view of plain Sn3.0Ag0.5Cu solder joint with different thermal aging times. (a) 168 h, (b) 504 h, (c) 1008 h. (a1), (b1), and (c1) high magnified view of area 1, 2, and 3, respectively.

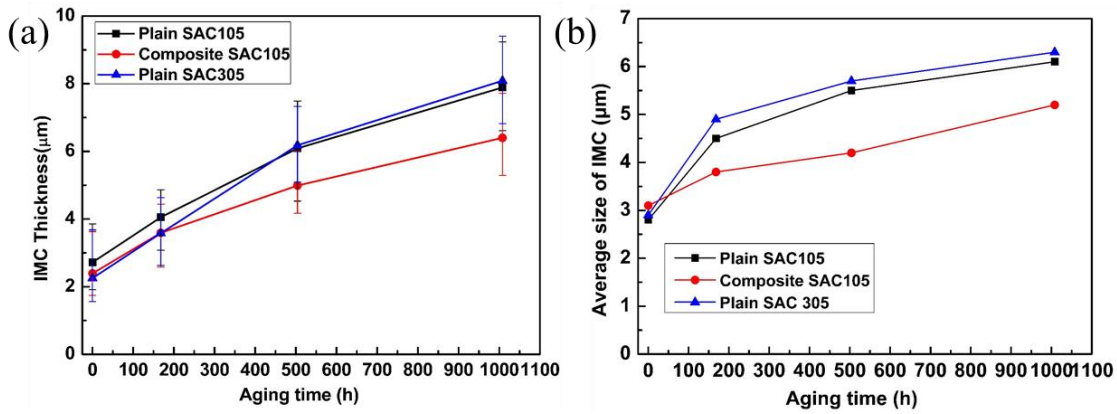

Fig. 6-16 Effect of thermal aging time on interfacial IMC. (a) thickness and (b) grain size.

the high growth rate of interfacial IMC. This is because the Cu source is more readily available for the interfacial IMC layer at the early stage of thermal aging. On the one hand, the supersaturated Cu atoms dissolved in the solder near the interface can be precipitated, and then react with the Sn atoms to form Cu_6Sn_5 IMC [21]. On the other hand, the interfacial IMC is relatively thin in the early stage, indicating that the resistance of Cu atoms in the Cu substrate to cross the IMC barrier is relatively small. Both of them make interfacial IMC grow faster in the early stage of thermal aging. At the later stage of aging, supersaturated Cu atoms have been consumed, so the Cu source of interfacial IMC growth is mainly from Cu substrate. The thickening IMC increases the diffusion resistance of Cu atoms, so the growth rate slows down at the later stage of thermal aging. In addition, compared with these three curves, the composite solder joint has a thin interfacial IMC thickness, due to the reasonable addition of the reinforcements hinders the inter-diffusion of Cu and Sn atoms. The detailed reason had mentioned in Fig. 6-11 to Fig. 6-13. Therefore, when the thermal aging time reaches 1008 h, the average size of the interfacial IMC is 6.40 μm, which is smaller than that of plain Sn1.0Ag0.5Cu and Sn3.0Ag0.5Cu solder joints (7.89 μm and 8.09 μm, respectively). Similarly, for the grain size of the interfacial IMC (Fig. 6-16(b)), the interfacial IMC grain size of the composite solder joint also exhibits the smallest among them after the aging time of 1008 h.

In summary, after long-term thermal aging, the interfacial IMC of hybrid reinforced composite solder joint presents the minimum thickness and gain size, and the refined microstructure of solder. This result indicates that reasonable doping of NiO/ZrO_2 and NiO/T-

ZnO_w reinforcements can effectively inhibit the growth of interfacial IMC and the coarsening of solder, thereby improving the microstructure stability of solder joint.

6.6. Shear strength and fracture behavior of solder joints after reflow and thermal aging

6.6.1 Shear strength of solder joints after reflow and thermal aging

The above, I mentioned the microstructure evolution during reflow and long-term thermal aging. Actually, not only microstructure stability, but also mechanical properties stability are also important for the reliability of electronics. Therefore, in this part, the mechanical behavior of solder joints during reflow and long-term thermal aging was systemically investigated. Fig.6-17 shows the shear strength of three kinds of solder joints with different thermal aging times. The shear strength of the Sn3.0Ag0.5Cu solder joint was 54.3 MPa after reflow, which was higher than that of plain Sn1.0Ag0.5Cu and composite solder joints (37.4 and 42.8, respectively). The thickness of interfacial IMC is relatively thin after reflow, and its function is mainly effective metallurgical bonding, where fracture occurs mainly in the solder zone [22]. Therefore, the shear strength of solder joints mainly depends on the strength of the solder, which is related to the microstructure of the solder. It can be seen from Fig. 6-7(a1)-(c1) that the proportion of eutectic structure in Sn3.0Ag0.5Cu solder joint (Fig. 6-7(c1)) is higher than that of Fig. 6-7(a1) and (b1). So the corresponding shear strength of Sn3.0Ag0.5Cu solder joint

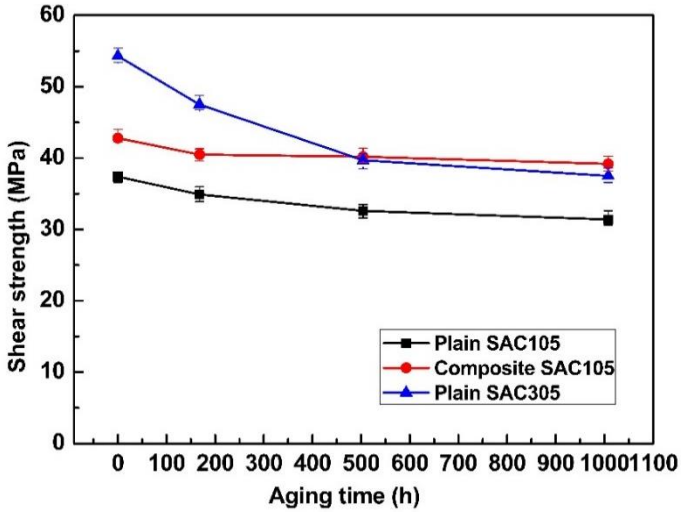

Fig. 6-17 Shear strength of solder joints with different thermal aging times.

was also the highest among them. For the plain Sn1.0Ag0.5Cu and composite solder joints, the microstructure of the composite solder joint is refined, and the proportion of eutectic structure also increased. This is attributed to the reasonable addition of the reinforcements. Moreover, the added NiO/ZrO_2 and NiO/T-ZnO_w can produce effective Orowan strengthening and load transfer effect, respectively, which had mentioned in previous chapters. Therefore, the shear strength of composite solder joint was greater than that of plain Sn1.0Ag0.5Cu solder joint. As the aging time increases, the shear strength of solder joints gradually decrease, which was mainly due to the coarsening of the joint microstructure. The shear strength of Sn3.0Ag0.5Cu solder joint decreased the most among them, while the composite solder joint decreased slightly, indicating the good mechanical property stability of the composite solder joint. When the thermal aging time reached 504 h, the shear strength of the composite solder joint was 40.2 MPa, which has already higher than that of plain Sn1.0Ag0.5Cu and Sn3.0Ag0.5Cu solder joints. Continue to extend the thermal aging time, the shear strength is slightly reduced, but still maintains the maximum value among them. When the thermal aging time reaches 1008 h, the shear strength of the composite solder joint was 39.2 MPa. In summary, the composite solder joint exhibits good performance stability during long-term thermal aging.

6.6.2 Fracture behavior of solder joints after reflow and thermal aging

To better understand the changes in shear strength and fracture behavior of the solder joints during thermal aging, the cross-section and surface morphology of the fracture are systematically analyzed.

Fig. 6-18 shows the cross-section of fracture of plain Sn1.0Ag0.5Cu solder joint with different thermal aging times. Fig. 6-18(a)-(d) exhibit the overall images of the cross section of fractures. Fig. 6-18(a) presents the cross section of fracture after reflow; it can be divided into three parts. The upper side is the mounted polymer, the middle is the solder, and the lower side is the Cu substrate. According to Fig. 6-18(a)-(d), the fracture of plain Sn1.0Ag0.5Cu solder joint occurs in solder regions during the whole thermal aging. While the profile of the facture is changed from rough to relatively flat. To further investigate the evolution of fracture behavior, high magnified images were conducted. Fig. 6-18(a1)-(d1) show the high magnified

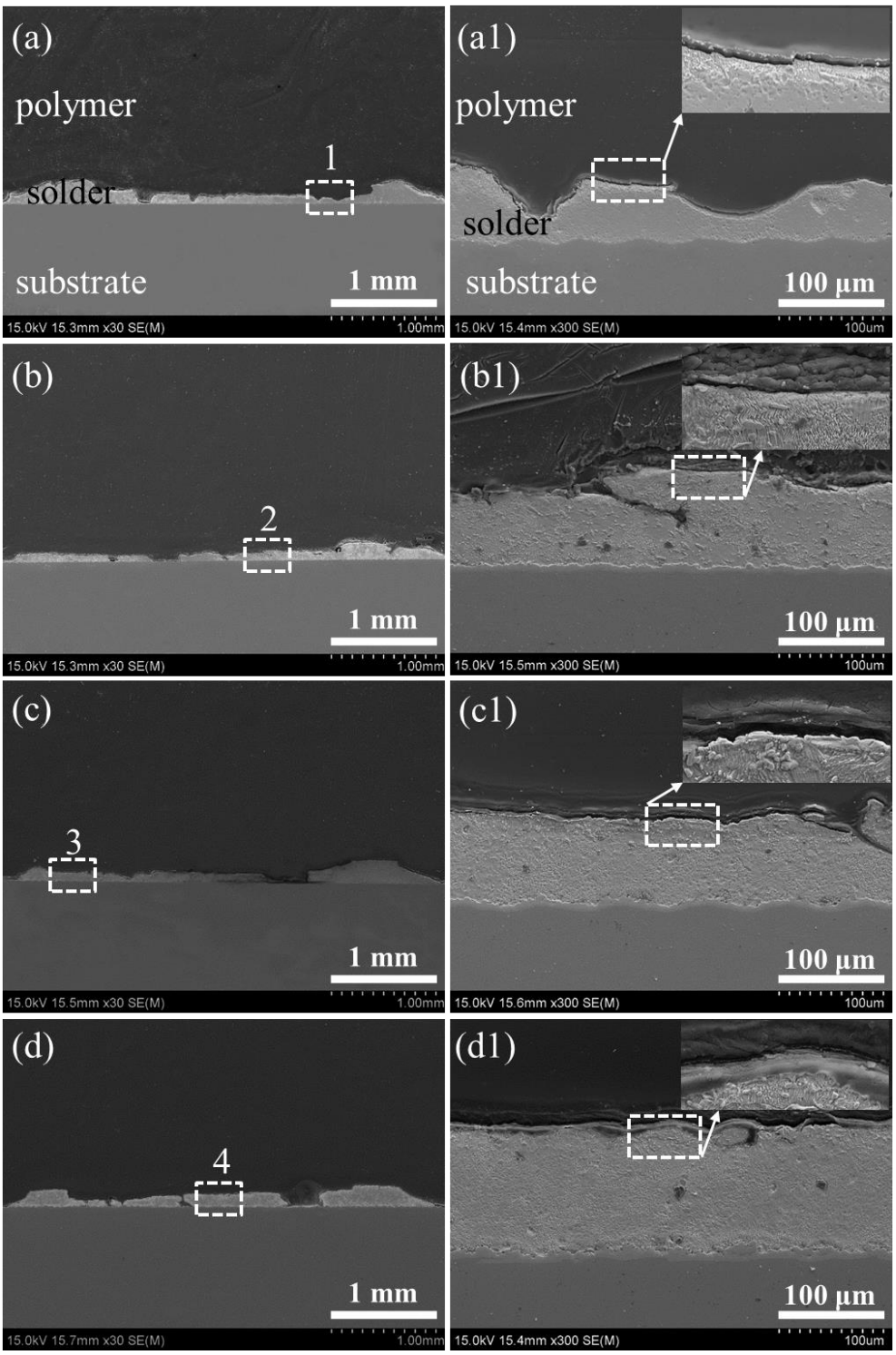

Fig. 6-18 Cross section of fracture of plain Sn1.0Ag0.5Cu solder joint with different thermal aging times. (a)-(d) overall images of the cross section of fractures. (a1)-(d1) high magnified view of area 1, 2, 3, and 4 of Fig. 6-18(a)-(d), respectively. (a), (a1) 0 h; (b), (b1) 168 h; (c), (c1) 504 h; (d), (d1) 1008 h.

view of areas 1, 2, 3, and 4 of Fig. 6-18(a)-(d), respectively. In addition, the upper right corner is the higher magnified view of the highest position of the fracture (marked with dotted frame), where the fracture can be clearly observed. The profile of the fracture is tortuous in the initial stage (Fig. 6-18(a1)). With the increase of thermal aging time, the curvature degree of contour decreases gradually. When the aging time reaches 1008 h (Fig. 6-18(d1)), and the profile is relatively flat. It is known that the more tortuous the fracture profile, the more energy absorbed during the fracture process, and the slower the crack propagation, so that the joint exhibits good toughness [23]. The fracture profile of the joint changed from tortuous to relatively flat, indicating that the toughness of the plain Sn1.0Ag0.5Cu solder joint decreased during the thermal aging. In addition, during the entire thermal aging process, fractures always occur in the solder area, which suggest that the strength of the plain Sn1.0Ag0.5Cu solder needs to be improved. This is also one of the reasons why composite solder is developed.

According to the cross section of fracture (Fig. 6-18), the fracture pathway of Sn1.0Ag0.5Cu solder joint was analyzed, and then the fracture mechanism and mode are investigated through the high magnified fracture surfaces. Fig. 6-19 shows the fracture surfaces of plain Sn1.0Ag0.5Cu solder joint with different thermal aging times. In initial stage (Fig. 6-19(a)), the fracture surface shows uniform dimples; the fracture mechanism is the microvoid coalescence fracture and the fracture mode belongs to ductile fracture. As the thermal aging time increases, the number of dimples decreases, and broken IMC can be observed (marked with red circle in Fig. 6-19(c)). This is mainly due to the coarsening of the solder. The fracture mechanism at this time includes the microvoid coalescence fracture of β-Sn and the cleavage fracture of the IMC in solder, and the corresponding fracture mode is ductile-brittle mixed fracture. When the thermal aging time reaches 1008 h (Fig. 6-19(d)), the number of dimples is further reduced and the surface roughness also decreases, indicating a low toughness of plain solder joint.

Fig. 6-20 shows the cross section of fracture of hybrid reinforced Sn1.0Ag0.5Cu composite solder joint with different thermal aging times. Fig. 6-20(a)-(d) exhibit the overall images of the cross section of fractures, where the fracture of composite solder joint occurs in

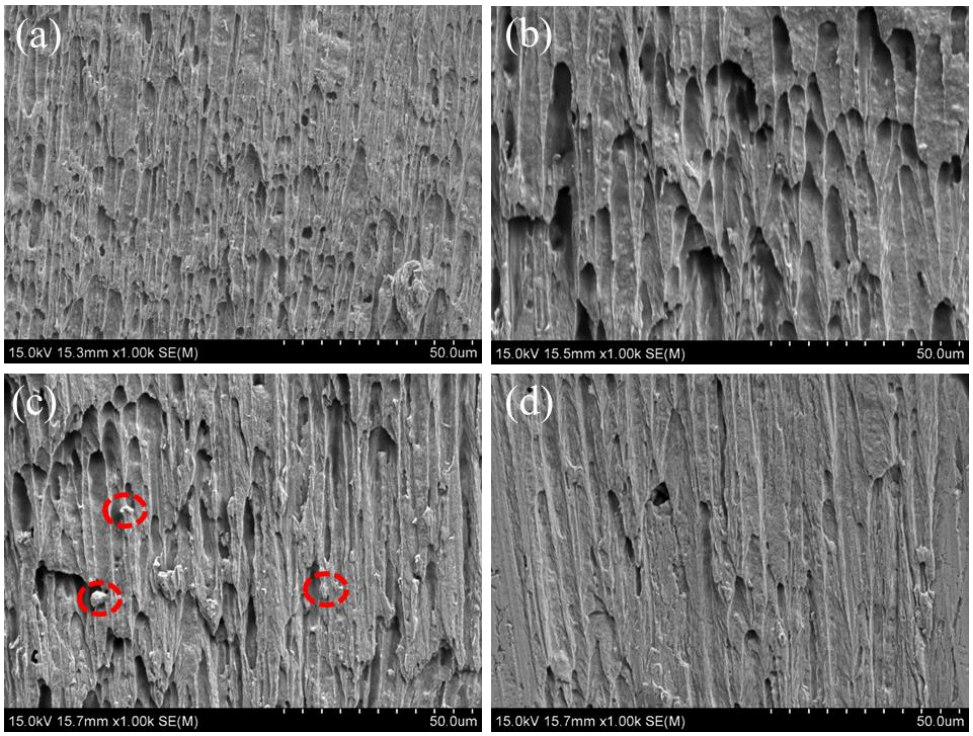

Fig. 6-19 Fracture surfaces of plain Sn1.0Ag0.5Cu solder joint with different thermal aging times. (a) 0 h, (b) 168 h, (c) 504 h, (d) 1008 h.

solder regions during the whole thermal aging. And the profile of the facture shows slight changes. To further investigate the evolution of fracture behavior, high magnified images were conducted. Fig. 6-20(a1)-(d1) show the high magnified view of areas 1, 2, 3, and 4 of Fig. 6-20(a)-(d), respectively. In addition, the upper right corner is the higher magnified view of the highest position of the fracture (marked with dotted frame), where the fracture can be clearly observed. In the initial stage (Fig. 6-20(a1)), the profile of the fracture is tortuous. With the increase of thermal aging time, the curvature degree of contour slightly decreases. However, at the same thermal aging time, composite solder joint exhibits more tortuous profile than plain Sn1.0Ag0.5Cu solder joint, which indicates a better toughness of composite solder joint. This good result of composite solder joint can be attributed to two aspects. The first one is the refined and stable microstructure of the composite solder joint, which had mentioned in Fig. 6-11. For the refined microstructure, under the same deformation degree, the deformation is dispersed in much grains, resulting in much uniform deformation and less stress concentration, making it possible to withstand a large amount of deformation failure. On the other hand, the composite

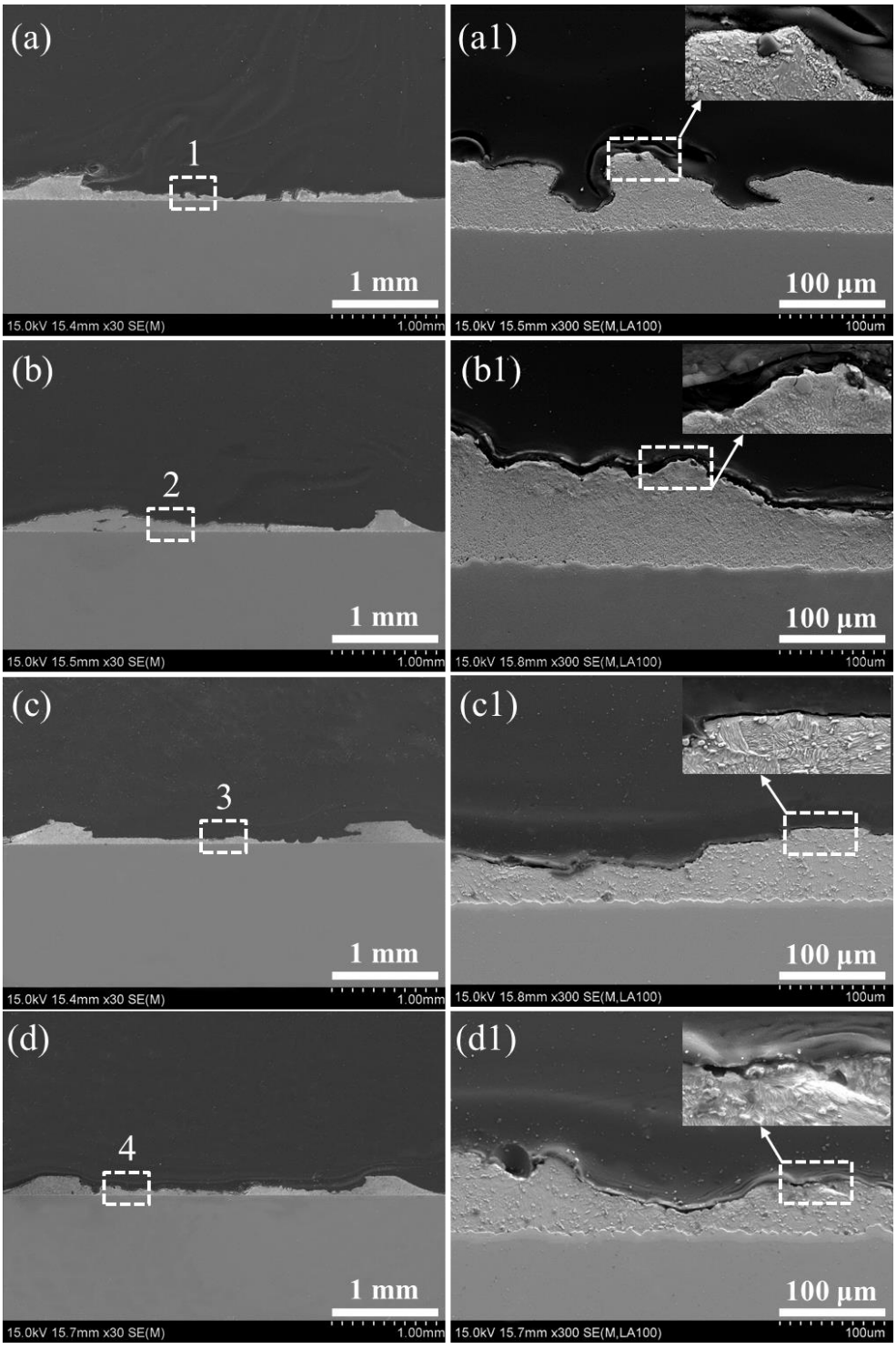

Fig. 6-20 Cross section of fracture of hybrid reinforced Sn1.0Ag0.5Cu composite solder joint with different thermal aging times. (a)-(d) overall images of the cross section of fractures. (a1)-(d1) high magnified view of area 1, 2, 3, and 4 of Fig. 6-20(a)-(d), respectively. (a), (a1) 0 h; (b), (b1) 168 h; (c), (c1) 504 h; (d), (d1) 1008 h.

solder contains a certain proportion of whisker reinforcement. It can produce effective load transfer effect, which had also mentioned in previous chapter.

Fig. 6-21 shows the fracture surfaces of hybrid reinforced Sn1.0Ag0.5Cu composite solder joints with different thermal aging times. In the initial stage (Fig. 6-21(a)), the fracture surface of the composite solder joint is rougher than that of plain Sn1.0Ag0.5Cu solder joint. The fracture surface is composed of dimples, the fracture mechanism is the microvoid coalescence fracture, and the fracture mode belongs to ductile fracture. With the increase of aging time, the fracture morphology changes slightly, but it is still dominated by dimples. When the aging time reaches 504 h (Fig. 6-21(c)), dimples still exist with large numbers, and the fractured coarse IMC is not observed. This is due to the good structural stability of the composite solder joint. The fracture mechanism at this time is the microvoid coalescence fracture, and the fracture mode also belongs to ductile fracture. When the thermal aging time reaches 1008 h (Fig. 6-21(d)), the corresponding fracture mode still belongs to ductile fracture dominated by dimples.

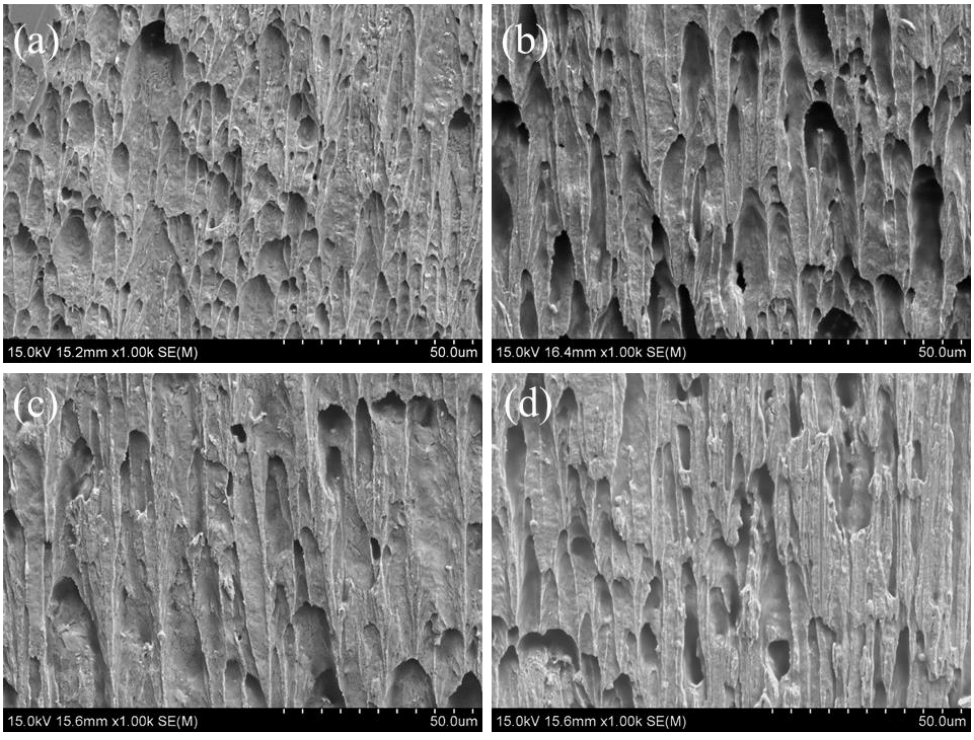

Fig. 6-21 Fracture surfaces of hybrid reinforced Sn1.0Ag0.5Cu composite solder joint with different thermal aging times. (a) 0 h, (b) 168 h, (c) 504 h, (d) 1008 h.

Fig. 6-22 shows the cross section of fracture of Sn3.0Ag0.5Cu solder joint with different thermal aging times. Fig. 6-22(a)-(d) exhibit the overall images of the cross section of fractures. Different from plain Sn1.0Ag0.5Cu and composite solder joints, which fracture location occurs in solder area during the whole thermal aging. However, the fracture position of Sn3.0Ag0.5Cu solder joint changes from solder region to interfacial IMC layer. To further investigate the evolution of fracture behavior, high magnified images were conducted. Fig. 6-22(a1)-(d1) show the high magnified view of areas 1, 2, 3, and 4 of Fig. 6-22(a)-(d), respectively. In addition, the upper right corner is the higher magnified view of the highest or lowest position of the fracture (marked with dotted frame), where the fracture can be clearly observed. In the initial stage (Fig. 6-22 (a1)), fracture occurs in the solder regions, and the profile of the fracture is tortuous, exhibiting good toughness of solder joint in the initial stage. This is because the thickness of the interfacial IMC is moderate after reflow, and the eutectic structure in the solder is refined. With the increase of the thermal aging time, the fracture position moves from the solder area to the interfacial IMC direction. When the aging time reaches 168 h (Fig. 6-22(b1)). The fracture occurs at the solder near the interface, and the degree of tortuosity decreases. On the one hand, due to the high Ag content and the coarsening of the solder structure during the thermal aging, the coordinated deformation ability of the grains in solder area is weaken. On the other hand, the thickness of interface IMC increases during thermal aging. Due to the CTE difference between interfacial IMC and solder, it is easy to produce stress concentration near the interface. Therefore, under the application of external load, the fracture occurs at the solder near the interface. As the aging time increases, the fracture position further migrates to the interface. From Fig. 6-22(c1) and the embedded high-magnification image, it can be seen that part of the fracture occurs at the interface between the interfacial IMC solder, where the interfacial IMC itself does not break, and the rest occurs in the solder regions. When the aging time reaches 1008 h (Fig. 6-22(d1)), part of the fracture occurs in the interfacial IMC and the other part occurs in the solder area. After a long-term thermal aging, the thickness of brittle IMC is larger and the proportion of IMC in the joint is increased. On the other hand, the Kirkendall effect would occur in IMC after long-term aging, producing defects such as holes

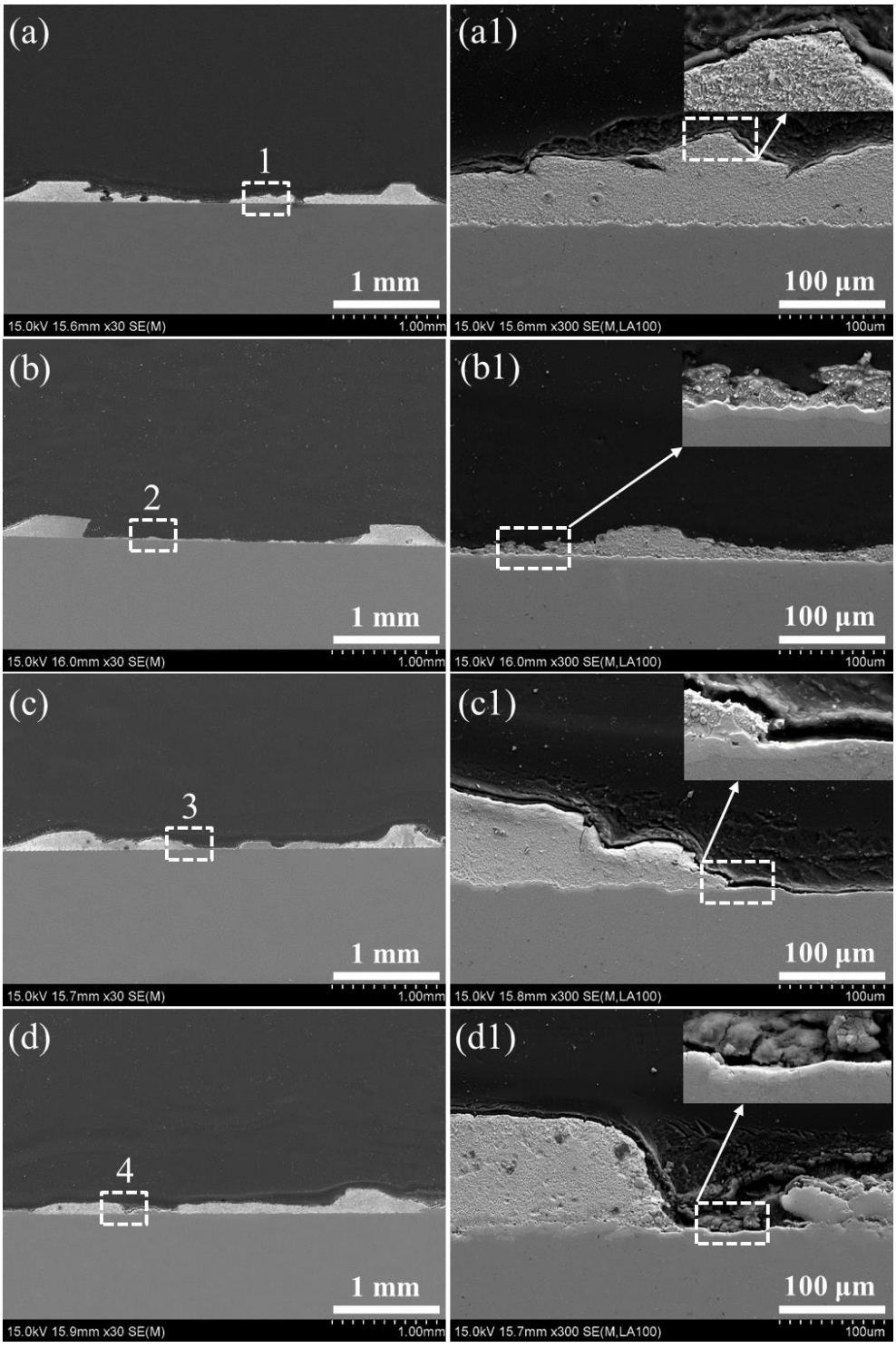

Fig. 6-22 Cross section of fracture of Sn3.0Ag0.5Cu solder joint with different thermal aging times. (a)-(d) overall images of the cross section of fractures. (a1)-(d1) high magnified view of area 1, 2, 3, and 4 of Fig. 6-22(a)-(d), respectively. (a), (a1) 0 h; (b), (b1) 168 h; (c), (c1) 504 h; (d), (d1) 1008 h.

[24]. Under the application of external load, stress concentration is prone to occur at this place, leading to the initiation and propagation of cracks. Finally, cracks occur in interfacial IMC.

Fig. 6-23 shows the fracture surfaces of Sn3.0Ag0.5Cu solder joint with different thermal aging times. After reflow (Fig. 6-23(a)), the fracture surface showed a typical ductile fracture mode with uniform dimples distributed. As the aging time increases, the degree of plastic deformation gradually decreases. When thermal aging time reaches 504 h (Fig. 6-23(c)), fracture morphology changes significantly, which can be divided into two parts (divide by red dotted line). The left side is composed of dimples, accompanied by broken IMC (marked with red dotted circle); while the right side is the slid surface, which is less deformed than the left side. Moreover, the exposed interface IMC in area 1 of Fig. 6-23(c) can be observed, where the high magnified view of area 1 is shown in Fig. 6-23(e). This indicates that part of the fracture occurred at the interface between the solder and the interfacial IMC. This result is consistent with Fig. 6-22(c). The fracture mechanism at this time includes the microvoid coalescence fracture in the solder zone, the cleavage fracture of IMC in the eutectic structure, and the slip fracture in the near-interface zone. The corresponding fracture mechanism belongs to ductile-brittle mixed fracture. When the aging time is increased to 1008 h (Fig. 6-23(d)), new fracture phenomena is found. In addition to dimples and slip surfaces, a large area of cleavage plane was also observed in the upper left corner; the high magnified view of area 2 is shown in Fig. 6-23(f). This indicates that the fracture occurs in the solder zone, the near-interface zone, and

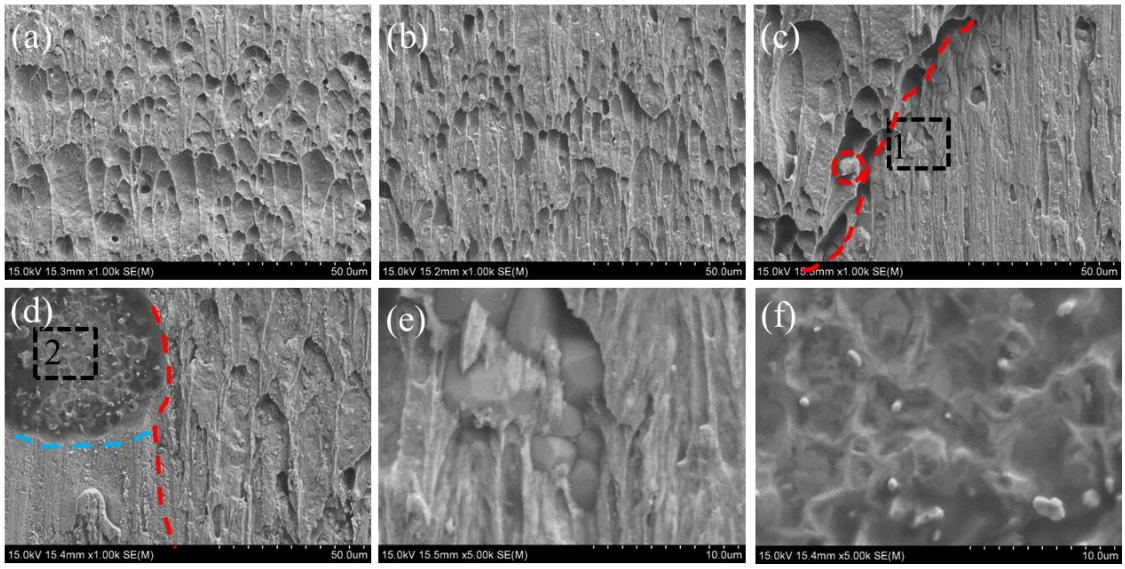

Fig. 6-23 Fracture surfaces of Sn3.0Ag0.5Cu solder joint with different thermal aging times. (a) 0 h, (b) 168 h, (c) 504 h, (d) 1008 h, (e) high magnified view of area 1, and (f) high magnified view of area 2.

the interfacial IMC at the same time. The result is consistent with the Fig. 6-22(d). The fracture mechanism at this time includes the microvoid coalescence fracture of the solder zone, the slip fracture of the near-interface zone, and the cleavage fracture of interfacial IMC. The corresponding fracture mechanism belongs to ductile-brittle mixed fracture.

The above systematically describe the evolution of fracture behavior of three kinds of solder joints during thermal aging, the summarized schematic illustration of fracture behavior of solder joints is shown in Fig. 6-24. In the initial stage (Fig. 6-24(a1), (b1), (c1)), fracture of three kinds of solder joints occur in the solder regions, and the profile of the fracture are tortuous. The fracture mode at this time belongs to ductile fracture dominated by dimples. For plain Sn1.0Ag0.5Cu and composite solder joint, as the aging time increases, the fracture still occurs in the solder area, but the fracture profile of the plain Sn1.0Ag0.5Cu solder joint is flatter. The fracture mode of plain Sn1.0Ag0.5Cu solder joint gradually changed from ductile fracture dominated by dimples to ductile-brittle mixed fracture; while composite solder joint maintains ductile fracture mode dominated by dimples during the whole thermal aging. For Sn3.0Ag0.5Cu solder joint, the fracture position gradually moves to the interfacial IMC direction as the aging time increases. When the thermal aging time reaches 1008 h (Fig. 6-

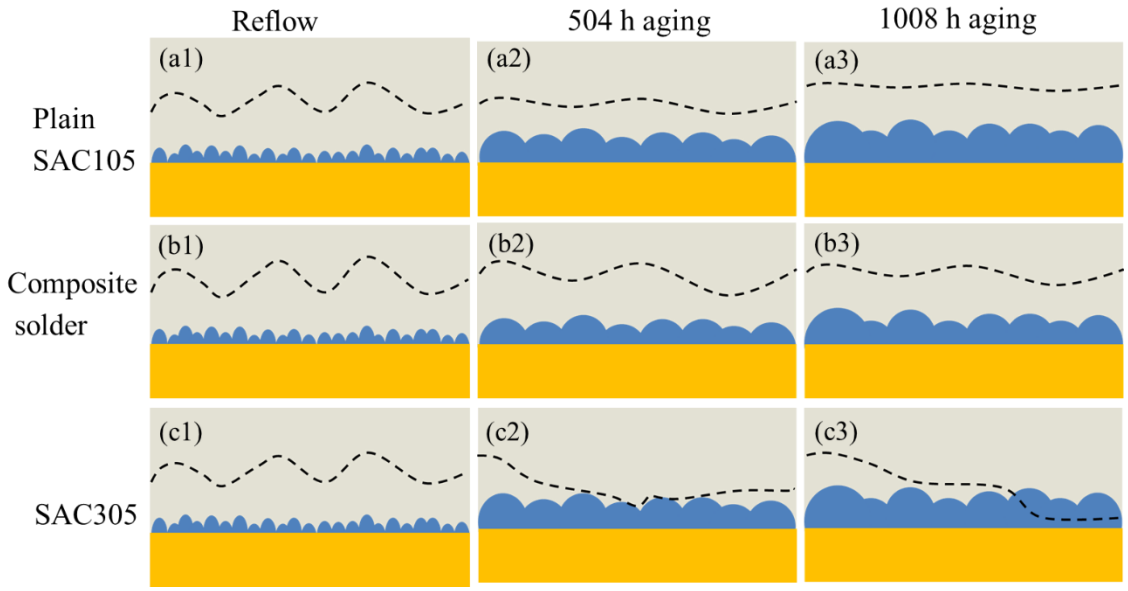

Fig. 6-24 Schematic illustration of fracture behavior of solder joints. (a) plain Sn1.0Ag0.5Cu, (b) composite solder, (c) Sn3.0Ag0.5Cu.

24(c3)), the fracture occurs in the solder zone, the near-interface zone, and the interfacial IMC at the same time. The fracture mechanism at this time includes the microvoid coalescence fracture of the solder zone, the slip fracture of the near-interface zone, and the cleavage fracture of interfacial IMC. And the corresponding fracture mechanism belongs to ductile-brittle mixed fracture.

6.7 Conclusions

The soldering tests of the composite solder was conducted. The microstructure evolution and mechanical properties of solder joints are systematically investigated after reflow and thermal aging. In addition, the shear strength and fracture behavior of solder joints after reflow and thermal aging also studied. The major findings were as follows:

1. The wettability of composite solders was improved with the suitable addition of reinforcements, which was attributed to the decreased surface energy of molten composite solder and capillary action.
2. The interfacial IMC of hybrid reinforced composite solder joint presented the minimum thickness and gain size after long-term thermal aging, as well as the refined microstructure of solder. This result indicates that reasonable doping of NiO/ZrO_2 and $NiO/T\text{-}ZnO_w$ reinforcements can effectively inhibit the growth of interfacial IMC and the coarsening of solder, thereby improving the microstructure stability of solder joint.
3. Composite solder joint presented good mechanical property stability during the long-term service. The shear strength of composite solder joint was 42.8 MPa after reflow, which was higher than that of plain Sn1.0Ag0.5Cu, while lower than that of Sn3.0Ag0.5Cu solder joint. After 1008 h thermal aging, shear strength of the composite solder joint is 39.2 MPa, which has already higher than that of plain Sn1.0Ag0.5Cu and Sn3.0Ag0.5Cu solder joints. The high strength and high reliability composite solder joint was obtained.
4. During the thermal aging, the composite solder joint maintains ductile fracture mode dominated by dimples during the whole thermal aging. And the fracture position of composite solder joint occurs in the solder regions with tortuous fracture profile,

indicating a good toughness of composite solder joint. This good result was attributed to the refined and stable microstructure of the composite solder joint.

References

[1] M.I.I. Ramli, M.A.A. Mohd Salleh, H. Yasuda, J. Chaiprapa, K. Nogita, The effect of Bi on the microstructure, electrical, wettability and mechanical properties of Sn-0.7Cu-0.05Ni alloys for high strength soldering, Mater. Des. 186 (2020) 108281. https://doi.org/10.1016/j.matdes.2019.108281.

[2] T. Gambaryan-Roisman, Marangoni convection, evaporation and interface deformation in liquid films on heated substrates with non-uniform thermal conductivity, Int. J. Heat Mass Transf. 53 (2010) 390–402. https://doi.org/10.1016/j.ijheatmasstransfer.2009.09.017.

[3] H. Wang, K. Zhang, M. Zhang, Fabrication and properties of Ni-modified graphene nanosheets reinforced Sn-Ag-Cu composite solder, J. Alloys Compd. 781 (2019) 761–772. https://doi.org/10.1016/j.jallcom.2018.12.080.

[4] D.Q. Yu, L. Wang, The growth and roughness evolution of intermetallic compounds of Sn-Ag-Cu/Cu interface during soldering reaction, J. Alloys Compd. 458 (2008) 542–547. https://doi.org/10.1016/j.jallcom.2007.04.047.

[5] R. Tian, C. Hang, Y. Tian, L. Zhao, Growth behavior of intermetallic compounds and early formation of cracks in Sn-3Ag-0.5Cu solder joints under extreme temperature thermal shock, Mater. Sci. Eng. A. 709 (2018) 125–133. https://doi.org/10.1016/j.msea.2017.10.007.

[6] F.J. Wang, F. Gao, X. Ma, Y.Y. Qian, Depressing effect of 0.2wt.%Zn addition into Sn-3.0Ag-0.5Cu solder alloy on the intermetallic growth with Cu substrate during isothermal aging, J. Electron. Mater. 35 (2006) 1818–1824. https://doi.org/10.1007/s11664-006-0163-4.

[7] Y. Qiao, H. Ma, N. Zhao, Diffusion anisotropy induced uneven regional growth of Cu_6Sn_5 IMC in Cu/SAC305/Cu micro solder joints under temperature gradient, J. Alloys Compd. 886 (2021). https://doi.org/10.1016/j.jallcom.2021.161221.

[8] N.S.M. Zaimi, M.A.A.M. Salleh, A.V. Sandu, M.M.A.B. Abdullah, N. Saud, S.Z.A. Rahim, P. Vizureanu, R.M. Said, M.I.I. Ramli, Performance of Sn-3.0Ag-0.5Cu

composite solder with kaolin geopolymer ceramic reinforcement on microstructure and mechanical properties under isothermal ageing, Materials (Basel). 14 (2021) 1–19. https://doi.org/10.3390/ma14040776.

[9] F. Huo, Z. Jin, D. Le Han, K. Zhang, H. Nishikawa, Interface design and the strengthening-ductility behavior of tetra-needle-like ZnO whisker reinforced Sn1.0Ag0.5Cu composite solders prepared with ultrasonic agitation, Mater. Des. 210 (2021) 110038. https://doi.org/10.1016/j.matdes.2021.110038.

[10] L.C. Tsao, Evolution of nano-Ag3Sn particle formation on Cu-Sn intermetallic compounds of Sn3.5Ag0.5Cu composite solder/Cu during soldering, J. Alloys Compd. 509 (2011) 2326–2333. https://doi.org/10.1016/j.jallcom.2010.11.010.

[11] M. Shang, C. Dong, J. Yao, C. Wang, H. Ma, H. Ma, Y. Wang, Competitive growth of Cu_3Sn and Cu_6Sn_5 at Sn/Cu interface during various multi-reflow processes, J. Mater. Sci. Mater. Electron. 32 (2021) 22771–22779. https://doi.org/10.1007/s10854-021-06711-x.

[12] Y. Ding, F. Wang, Y. Li, K. Wang, Effect of Different Ag Content on the Structural and Mechanical Properties of Sn15Bi Solder, ES Mater. Manuf. (2020) 65–71. https://doi.org/10.30919/esmm5f1045.

[13] J. Shen, M. Zhao, P. He, Y. Pu, Growth behaviors of intermetallic compounds at Sn-3Ag-0.5Cu/Cu interface during isothermal and non-isothermal aging, J. Alloys Compd. 574 (2013) 451–458. https://doi.org/10.1016/j.jallcom.2013.05.156.

[14] X. Liu, M. Huang, Y. Zhao, C.M.L. Wu, L. Wang, The adsorption of Ag_3Sn nano-particles on Cu-Sn intermetallic compounds of Sn-3Ag-0.5Cu/Cu during soldering, J. Alloys Compd. 492 (2010) 433–438. https://doi.org/10.1016/j.jallcom.2009.11.131.

[15] H. Gao, F. Wei, Y. Sui, J. Qi, Growth behaviors of intermetallic compounds on the Sn-0.7Cu-10Bi-xCo/Co interface during multiple reflow, Mater. Des. 174 (2019) 107794. https://doi.org/10.1016/j.matdes.2019.107794.

[16] D. Taneja, M. Volpert, F. Hodaj, Further insight into interfacial interactions in nickel/liquid Sn–Ag solder system at 230–350 ℃, J. Mater. Sci. Mater. Electron. 28 (2017) 18366–18378. https://doi.org/10.1007/s10854-017-7783-8.

[17] H.F. Zou, H.J. Yang, Z.F. Zhang, Morphologies, orientation relationships and evolution of Cu_6Sn_5 grains formed between molten Sn and Cu single crystals, Acta Mater. 56 (2008) 2649–2662. https://doi.org/10.1016/j.actamat.2008.01.055.

[18] H. Kim, K. Tu, Kinetic analysis of the soldering reaction between eutectic SnPb alloy and Cu accompanied by ripening, Phys. Rev. B - Condens. Matter Mater. Phys. 53 (1996) 16027–16034. https://doi.org/10.1103/PhysRevB.53.16027.

[19] L. Xu, L. Wang, H. Jing, X. Liu, J. Wei, Y. Han, Effects of graphene nanosheets on interfacial reaction of Sn-Ag-Cu solder joints, J. Alloys Compd. 650 (2015) 475–481. https://doi.org/10.1016/j.jallcom.2015.08.018.

[20] W. qing Xing, X. ye Yu, H. Li, L. Ma, W. Zuo, P. Dong, W. xian Wang, M. Ding, Effect of nano Al_2O_3 additions on the interfacial behavior and mechanical properties of eutectic Sn-9Zn solder on low temperature wetting and soldering of 6061 aluminum alloys, J. Alloys Compd. 695 (2017) 574–582. https://doi.org/10.1016/j.jallcom.2016.11.136.

[21] S. Shang, Y. Wang, Y. Wang, H. Ma, A. Kunwar, Enhancement of hardness of bulk solder by doping Cu nanoparticles at the interface of Sn/Cu solder joint, Microelectron. Eng. 208 (2019) 47–53. https://doi.org/10.1016/j.mee.2019.01.009.

[22] C. Cao, K. Zhang, B. Shi, H. Wang, D. Zhao, M. Sun, C. Zhang, The interface microstructure and shear strength of Sn2.5Ag0.7Cu0.1RExNi/Cu solder joints under thermal-cycle loading, Metals (Basel). 9 (2019). https://doi.org/10.3390/met9050518.

[23] P. Darbandi, T.R. Bieler, F. Pourboghrat, T.K. Lee, The effect of cooling rate on grain orientation and misorientation microstructure of SAC105 solder joints before and after impact drop tests, J. Electron. Mater. 43 (2014) 2521–2529. https://doi.org/10.1007/s11664-014-3176-4.

[24] M.P.C. Roma, S. Kudtarkar, O. Kierse, D. Sengupta, J. Cho, Aging Studies of Cu–Sn Intermetallics in Cu Micropillars Used in Flip Chip Attachment onto Cu Lead Frames, J. Electron. Mater. 47 (2018) 1694–1704. https://doi.org/10.1007/s11664-017-5872-3.

Chapter 7 Conclusions and future work

7.1 Summary

In this dissertation, the design concept of multi-phase and multi-scale hybrid reinforced composite solder was proposed to develop a high strength-ductility lead-free solder. In addition, a new surface modification method, ball milling-pyrolysis method also proposed. In this study, I systematically illustrated the surface modification of the reinforcements, preparation of the composite solder, the interface regulation between the reinforcements and solder matrix, the strengthening-ductility behavior of composite solders, and the reliability of composite solder joints. The major findings in each chapter are summarized below.

In chapter 2, a new surface modification method, the ball milling-pyrolysis method based on self-assembly, was proposed. And successfully applied to the surface modification of ZrO_2 nanoparticles and T-ZnO_w.

The NiO/ZrO_2 successfully prepared using the ball milling-pyrolysis method, and the synthesis of NiO/ZrO_2 can be regulated by controlling ball milling time and Ni/Zr molar ratio. As the the ball milling time increased, the surface defects of ZrO_2 were increased, facilitating the attachment of NiO nanaoparticles. I drived an expression to describe the relationship between the NiO particle size (y) and the ball milling time (t), $y = 10.310t^{-0.076}$. Meanwhile, as the Ni/Zr molar ratio increased in the range of 5–20 %, the NiO particle size slighly increased. The transformation from precursor/ZrO_2 into NiO/ZrO_2 under beam irradiation was explored by in-situ TEM. Initially, the precursor was attached to ZrO_2 surface as a result of a self-assembly reaction with ZrO_2. Subsequently, it decomposed into intermediate $NiCO_3$/$Ni(OH)_2$ products. With continuous irradiation, these intermediate products merged, grew, and finally transformed into NiO. The mismatch of the typical interfaces was found to be 0.029–0.054, indicating semi-coherent and coherent interfaces.

Similarly, T-ZnO_w was successfully modified by NiO nanoparticles via a pyrolysis method based on self-assembly. When the Ni/Zn molar ratio reached 10%, NiO nanoparticles were densely and evenly distributed on the surface of T-ZnO_w. The interfacial relationship between T-ZnO_w (100) and NiO (101) plane was semi-coherent interface with the misfit of 0.145,

indicating the good adhesion. In-situ TEM observation showed that NiO attached to the surface of T-ZnO_w in a stacked manner.

In chapter 3, NiO/ZrO_2 reinforced Sn1.0Ag0.5Cu composite solder was prepared with ultrasonic stirring. The microstructure evolution and refinement mechanism of composite solders were systematically investigated.

An appropriate addition amount (0–0.3 mass%) of NiO/ZrO_2 can improve the microstructure of composite solders, which the eutectic and β-Sn were refined. The refinement mechanism of NiO/ZrO_2 on the microstructure was investigated with the TEM observation. NiO/ZrO_2 were relatively dispersed and uniformly distributed in the eutectic microstructure area, which can act as the heterogeneous nuclear sites in eutectic area. On the other hands, reinforcements distributed at the grain boundary can hinder the migration of grain boundary by the pinning effect. Moreover, a micro-mechanical lock and non-micropored clean interface was formed between NiO/ZrO_2 and Sn1.0Ag0.5Cu solder matrix. The Sn/NiO/ZrO_2 interface system based on mutual solid solution was ingenious designed.

In a certain addition range of NiO/ZrO_2 (0–0.3mass%), the mechanical properties of the composite solder gradually increased with the NiO/ZrO_2 addition. The fracture mechanism also transformed from a ductile–brittle mixed fracture consisting of dimples and cleavage planes to the ductile fracture dominated by dimples. When the NiO/ZrO_2 addition reached 0.3 mass%, the maximum tensile strength and elongation of 34.8 MPa and 27.9%, respectively, were obtained. This result is an increase of 24.7% and 29.2% respectively compared to that of the plain Sn1.0Ag0.5Cu solder.

In chapter 4, NiO/T-ZnO_w reinforced Sn1.0Ag0.5Cu composite solder was prepared with ultrasonic stirring. The microstructure evolution mechanical propereties of composite solders was systematically investigated. The interface between reinforcement and solder matrix was also explored.

When the addition content was in the range of 0.05-0.3 mass%, NiO/T-ZnO_w was uniformly distributed in the solder matrix, and most of them existed in the eutectic area. This NiO/T-ZnO_w could act as the heterogeneous nucleation sites to refine the size of IMC and β-Sn. While the addition contents reached 0.5-0.7 mass%, microstructure defects were occurred.

For the interface of NiO/T-ZnOw reinforced Sn1.0Ag0.5Cu composite solder, no gaps, micropores, or new phases were formed, and the atomic inter-diffusion occurred at the interface. Hence, the composite interface structure of Sn1.0Ag0.5Cu/NiO/T-ZnOw was well designed. This novel interface is key in the strengthening and ductility of composite solder.

The UTS and elongation of the 0.3 mass% NiO/T-ZnOw reinforced Sn1.0Ag0.5Cu composite solder were 32.5 MPa and 28.1%. Both UTS and elongation were higher than that of plain Sn1.0Ag0.5Cu solder, respectively. The strengthening and ductility mechanism were mainly proposed as load transfer, grain refinement, and misfit dislocation effects.

In chapter 5, The NiO/ZrO_2 and NiO/T-ZnO_w hybrid reinforced Sn1.0Ag0.5Cu composite solder with different Zn: Zr ratios were prepared. The microstructure and mechanical properties of composite solder were systematically investigated, as well as the interfaces between reinforcements and solder matrix.

NiO/ZrO_2 and NiO/T-ZnO_w were successfully added into the solder matrix, and dispersed in the solder matrix, which can act as the nuclear sites of eutectic. The microstructure evolution occurred with different Zn: Zr ratios. When the Zn: Zr ratio reached 2: 3, high proportion of eutectic without coarse IMC was obtained. For the interface between NiO/ZrO_2, NiO/T-ZnO_w and Sn1.0Ag0.5Cu, no gaps, micropores, or new phases were formed, and the atomic inter-diffusion occurred at the interface. Hence, the composite interface structure of Sn1.0Ag0.5Cu/NiO/reinforcements was well designed. This novel interface is key in the strengthening and ductility of composite solder.

The UTS and elongation of composite solder can be improved synergistically with reasonable hybrid ratios. When the NiO/T-ZnO_w and Ni/ZrO_2 addition contents reached 0.12 wt.% and 0.18 wt.%, maximum UTS and elongation of composite solder were 35.9MPa and 31.4%, which were higher than the SAC305, that is, a high strength-ductility composite solder is obtained. In addition, composite solder showed the lighter degree of coarsening compared to others solder during the thermal aging, which attributed to the suitable reinforcements doping. After 1008 h thermal aging, composite solder still remained the best results among them. It indicated good microstructure and mechanical stability of composite solder during thermal aging. This design concept of multi-phase and multi-scale hybrid reinforced composite solder

could provide new ideas for designing high-performance lead-free composite solders.

In chapter 6, the wettability of the composite solder was studied, and then the soldering tests of the composite solder was conducted. The microstructure evolution and mechanical properties of solder joints were systematically investigated after reflow and thermal aging.

The wettability of composite solders was improved with the suitable addition of reinforcements, which is attributed to the decreased surface energy of molten composite solder and capillary action. The interfacial IMC of hybrid reinforced composite solder joint presented the minimum thickness and gain size after long-term thermal aging, as well as the refined microstructure of solder seam. This result indicated that reasonable doping of NiO/ZrO_2 and NiO/T-ZnOw reinforcements can effectively inhibit the growth of interfacial IMC and the coarsening of solder seam, thereby improving the microstructure stability of solder joint.

Composite solder joint presented good mechanical property stability during the long-term service. The shear strength of composite solder joint was 42.8 MPa after reflow, which is higher than that of plain Sn1.0Ag0.5Cu, while lower than that of Sn3.0Ag0.5Cu solder joint. After 1008 h thermal aging, shear strength of the composite solder joint was 39.2 MPa, which has already higher than that of plain Sn1.0Ag0.5Cu and Sn3.0Ag0.5Cu solder joints. The high strength and high reliability composite solder joint was obtained. Composite solder joint maintained ductile fracture mode dominated by dimples during the whole thermal aging. And the fracture position of composite solder joint occurred in the solder seam regions with tortuous fracture profile, indicating a good toughness of composite solder joint. This good result was attributed to the refined and stable microstructure of the composite solder joint.

7.2 Future work

7.2.1 Quantitative analysis of mechanical properties improvement

In chapter 3, chapter 4 and chapter 5, the composite solder reinforced with single and hybrid reinforcing phases were prepared, respectively. The strengthening-ductility mechanism was systematically investigated, and the improvement of UTS was qualitatively analyzed. However, I hope to explain the improvement in mechanical properties more accurately. Therefore, in future work, I am committed to a quantitative analysis of the improvement of

mechanical properties. For the quantitative analysis of mechanical properties, I need to build a constitutive model based on the phase composition and distribution of the composite solder. Unfortunately, the system of SnAgCu composite solder is too complicated. In the solder matrix, it contains not only β-Sn, but also Cu_6Sn_5 and Ag_3Sn with different shapes and sizes. And the mechanical performance of these phases are also different. This makes it very difficult to build an accurate model. Therefore, firstly, my plan is to use pure Sn as the matrix to build a single reinforcement enhanced composite solder model, and evaluate the matching degree between the experimental result and the mathematical model. Subsequently, the solder matrix becomes a binary solder, such as Sn-Ag or Sn-Cu solder, and then related mathematical model is constructed and the matching degree is evaluated. Similar to this, step by step, until a model of NiO/ZrO_2 and NiO/T-ZnO_w hybrid reinforced Sn1.0A0.5Cu composite solder is accurately constructed. This process is complicated and time consuming. But I think it is very meaningful and worth a long time to accomplish.

7.2.2 Reliability study of multi-field coupling

In this study, I developed the multiple-phases and multi-scale hybrid reinforced Sn1.0Ag0.5Cu composite solder, and evaluated the thermal aging behavior of the solder and its joint. In chapter 1, it had mentioned that the reliability of joints includes several kinds [1-4], such as thermal aging, electric migration, thermal fatigue, creep and so on. To better evaluate the new developed composite solder, not only thermal aging experiments, but also other reliability tests also need to be carried out. Moreover, in actual IC service, these reliability problems do not exist in isolation, but in synergy. Therefore, in the reliability test, the reliability study of multi-field coupling is particularly important. Therefore, I will conduct other kinds of reliability tests and their coupling in future work. Regarding the reliability test of multi-field coupling, the design of the experimental device is a problem that needs to be solved first.

7.2.3 Cross-scale simulation of reliability studies

For the reliability test of a single field or multi-field coupling, only the results of different experimental stages can be obtained, but can’t get the real-time data of stress field and temperature field during the experimental process. And these real-time data are important for

analyzing the cause of joint failure. Therefore, the effective application of simulation methods is also very important in reliability study. In particular, in the reliability test of thermal aging or thermal shock, there is not only thermal stress (due to the CTE difference in materials), but also microstructure stress due to the microstructure evolution. The CTE, modulus and thermal conductivity of the interface IMC are different from those of the Cu substrate and solder seam. Moreover, the size and shape of the interfacial IMC are constantly changing during the service process. Therefore, to include the evolution of the microstructure in the reliability simulation, it is necessary to resort to more micro-scale simulation software, such as molecular dynamics software. Based on the above cross-scale reliability simulation, it is helpful to understand the reliability failure problem of the solder joint at a deeper level.

References

[1] M.A. Rabiatul Adawiyah, O. Saliza Azlina, Comparative study on the isothermal aging of bare Cu and ENImAg surface finish for Sn-Ag-Cu solder joints, J. Alloys Compd. 740 (2018) 958–966. https://doi.org/10.1016/j.jallcom.2018.01.054.

[2] X. Long, X. He, Y. Yao, An improved unified creep-plasticity model for SnAgCu solder under a wide range of strain rates, J. Mater. Sci. 52 (2017) 6120–6137. https://doi.org/10.1007/s10853-017-0851-x.

[3] P. Borgesen, L. Wentlent, S. Hamasha, S. Khasawneh, S. Shirazi, D. Schmitz, T. Alghoul, C. Greene, L. Yin, A Mechanistic Thermal Fatigue Model for SnAgCu Solder Joints, J. Electron. Mater. 47 (2018) 2526–2544. https://doi.org/10.1007/s11664-018-6121-0.

[4] H. Madanipour, Y.R. Kim, C.U. Kim, D. Mishra, P. Thompson, Study of electromigration in Sn-Ag-Cu micro solder joint with Ni interfacial layer, J. Alloys Compd. 862 (2021) 158043. https://doi.org/10.1016/j.jallcom.2020.158043.

Research achievement

I List of publication

1. **Fupeng Huo**, Zhi Jin, Duy Le Han, Keke Zhang, Hiroshi Nishikawa. Interface design and the strengthening and toughening behavior of tetra-needle like ZnO whisker reinforced Sn1.0Ag0.5Cu composite solders prepared with ultrasonic agitation. **Materials & Design**, 210 (2021) 110038.

2. **Fupeng Huo**, Zhi Jin, Duy Le Han, Jiahui Li, Keke Zhang, Hiroshi Nishikawa. Novel interface regulation of Sn1.0Ag0.5Cu composite solders reinforced with modified ZrO_2: Microstructure and mechanical properties. **Journal of Materials Science & Technology**, 125 (2022) 157–170.

3. **Fupeng Huo**, Yu-An Shen, Siliang He, Keke Zhang, Hiroshi Nishikawa. Fabrication of NiO/ZrO_2 nanocomposites using ball milling-pyrolysis method. **VACUUM**, 191 (2021) 110370.

4. Zhi Jin, Yu-An Shen, **Fupeng Huo**, Y. C. Chan, Hiroshi Nishikawa. Electromigration behavior of silver thin film fabricated by electron-beam physical vapor deposition. **Journal of Materials Science**, 56, (2021) 9769.

5. Jianhao Wang, XundaLiu, **Fupeng Huo**, Kento Kariya, Noriyuki Masago, Hiroshi Nishikawa. Novel transient liquid phase bonding method using In-coated Cu sheet for high-temperature die attach. **Materials Research Bulletin**, 149, (2022), 111713.

6. Duy Le Han, Yu-An Shen, **Fupeng Huo**, Hiroshi Nishikawa. Microstructure Evolution and Shear Strength of Tin-Indium-xCu/Cu Joints. **Metals**. 12, (2022), 13.

Ⅱ List of conference

1. **Fupeng Huo**, Keke Zhang, Hiroshi Nishikawa. Surface Modification of Tetra-needle like ZnO (T-ZnO) and Characterization of Interface Between Sn1.0Ag0.5Cu and NiO Decorated T-ZnO. **International Conference of Electronic Packaging (ICEP) 2021**, dio: 10.23919/ICEP51988.2021.9451909. Tokyo, Japan. (Oral)

2. **Fupeng Huo**, Keke Zhang, Hiroshi Nishikawa. Microstructure and the strengthening-ductility behavior of Sn1.0Ag0.5Cu composite solders reinforced with modified nano ZrO_2. **IIW 74th On-line Annual Assembly and International Conference**. (Oral)

Acknowledgment

Time flies, three years are fleeting, and my PhD program is coming to the end. In the past three years, with the help of supervisor and classmates, I have gradually grown from a master student to a doctoral student with preliminary independent scientific research ability. During this period, I experienced confusion, failure, self-doubt, as well as a sense of accomplishment after overcoming these difficulties. These experiences remind me of an old Chinese saying, “Every cloud has a silver lining”, which is the treasure of my life.

My deepest thanks to my supervisor, Prof. Hiroshi Nishikawa, for his earnest teaching and careful guidance over the past three years. In terms of research, Prof. Nishikawa flexibly practiced the philosophy of the whole and the parts. On the one hand, establish an overall view of the field, and then carry out precise overall control of the research topic. On the other hand, the delicate handling of specific matters. “Detail is important”, which he often said, has been deeply branded in my mind. The combination of the above two aspects makes the logic very clear when doing research. This philosophy has served me well throughout my life. Moreover, Prof. Nishikawa is the most industrious person in our lab, and his work attitude has also set a good example for our young people.

In addition to my supervisor, I express my great thanks to Prof. Yasuo Takahashi and Prof. Keke Zhang. Thanks for their highly recommendation during Ph.D applications. Without their help, I would not have the opportunity to study at Osaka University. Many thanks to Mr. Takeshi Murakami, he patiently taught me to operate FIB and TEM equipment, which is essential to my research. I appreciate Dr. Xinxin Wei from the Institute of Metals, Chinese Academy of Sciences. She has given me a lot of help in the theory of TEM. I hope she has a bright future.

Moreover, I would like to thank the kind and helpful members and alumni of the Nishikawa Lab, especially Associate Prof. Hiroaki Tatsumi, Dr. Kishichi Sasaki, Dr. Takuya Naoe, Ms. Aiko Yonezawa, Ms. Yuko Sakata, Dr. Yu-An Shen, Dr. Shiqi Zhou, Dr. Siliang He, Dr. Runhua Gao, Dr. Zhi Jin, Dr. Duy Le Han, Mr. Jiahui Li, Mr. Byungho Park, Mr. Xunda Liu, Mr. Seongwoo Pak, Mr. Sijie Huang and Mr. Laizhou Zhou. Without their support and

advice, it would have been impossible to accomplish this research.

In addition, I acknowledge the China Scholarship Council (CSC) for the financial support to my studies as a Ph. D student.

Most sincere thanks to Ms. Min Yang for her invaluable support, patience, and love.

I would like to express the great gratitude and respect to my family for the perpetual personal support and encouragement through all the years. Without them, I would not pursue my dream.

April 2022

Fupeng Huo

Joining and Welding Research Institute

Osaka University